ATOMIC STRUCTURE AND NON-ELECTRONIC PROPERTIES OF SEMICONDUCTORS

Indium layers in low-temperature gallium arsenide: structure and how it changes under annealing in the temperature range 500–700 °C

N. A. Bert, A. A. Suvorova, and V. V. Chaldyshev

A. I. Ioffe Physicotechnical Institute, Russian Academy of Sciences, 194021 St. Petersburg, Russia

Yu. G. Musikhin

A. I. Ioffe Physicotechnical Institute, Russian Academy of Sciences, 194021 St. Petersburg, Russia; Max Planck Institut für Mikrostrukturphysik, D-5120 Halle, Germany

V. V. Preobrazhenskiĭ, M. A. Putyato, and B. R. Semyagin

Institute of Semiconductor Physics, Russian Academy of Sciences, Siberian Branch, 630090 Novosibirsk, Russia

R. Werner

Max Planck Institut für Mikrostrukturphysik, D-05120 Halle, Germany
(Submitted December 29, 1997; accepted for publication December 31, 1997)
Fiz. Tekh. Poluprovodn. **32**, 769–774 (July 1998)

Transmission electron microscopy is used to study the microstructure of indium δ layers in GaAs(001) grown by molecular beam epitaxy at low temperature (200 °C). This material, referred to as *LT*-GaAs, contains a high concentration ($\approx 10^{20}$ cm^{-3}) of point defects. It is established that when the material is δ-doped with indium to levels equivalent to 0.5 or 1 monolayer (ML), the roughness of the growth surface leads to the formation of InAs islands with characteristic lateral dimensions <10 nm, which are distributed primarily within four adjacent atomic layers, i.e., the thickness of the indium-containing layer is 1.12 nm. Subsequent annealing, even at relatively low temperatures, leads to significant broadening of the indium-containing layers due to the interdiffusion of In and Ga, which is enhanced by the presence of a high concentration of point defects, particularly V_{Ga}, in *LT*-GaAs. By measuring the thickness of indium-containing layers annealed at various temperatures, the interdiffusion coefficient is determined to be $D_{\mathrm{In-Ga}} = 5.1\times 10^{-12}\exp(-1.08\ \mathrm{eV}/kT)$ cm^2/s, which is more than an order of magnitude larger than $D_{\mathrm{In-Ga}}$ for stoichiometric GaAs at 700 °C. © *1998 American Institute of Physics.* [S1063-7826(98)00107-0]

INTRODUCTION

Gallium arsenide grown by molecular beam epitaxy (MBE) at low (about 200 °C) temperatures (so-called *LT*-GaAs) has aroused great interest since it was first described in papers at the end of the 1980's.[1–3] This interest is due to two unique properties of *LT*-GaAs: high resistivity and very short carrier lifetimes (about 100 fs). As shown in Refs. 2 and 3, these properties are caused by the presence of excess arsenic (of order 1 at. %) in the *LT*-GaAs host. The excess arsenic forms clusters that incorporate into the GaAs host with practically no defects when the material is annealed at temperatures above 500 °C. The concentration, size, and spatial distribution of these arsenic clusters play a key role in shaping the properties of the material. Usually the concentration and size of the arsenic precipitates are controlled by varying the growth conditions and the annealing temperature of the material. It has been shown[4–6] that the spatial distribution of the clusters can be controlled by introducing thin layers of InGaAs into the *LT*-GaAs or by isovalently δ doping the latter with indium during low-temperature MBE. During subsequent annealing, the indium-containing layers act as regions which accumulate excess arsenic. This makes it possible to obtain two-dimensional layers of arsenic clusters and to form As/GaAs heterostructures.

It is obvious that annealing not only gives rise to the diffusion and precipitation of excess arsenic, but also to the interdiffusion of indium and gallium, which leads to broadening and spreading of the indium-containing layers and can thus influence how effectively they accumulate arsenic clusters. In addition, on a more global scale, this concentration disordering alters the electronic and optical properties of the material. For this reason, the self-diffusion processes in semiconductor III–V compounds and their solid solutions are a subject of intense investigation (see, for example, the review in Ref. 7). The few papers on diffusion in *LT*-GaAs have revealed that the huge concentration of point defects in the material, particularly gallium vacancies,[8,9] leads to a de-

 © 1998 American Institute of Physics

crease in the activation energy for the diffusion of Al[10–12] and to an increase in the diffusion coefficient by one to two orders of magnitude.[9] Unfortunately, there are practically no data on the diffusion of indium in low-temperature GaAs. However, it has been observed[13] in ordinary gallium arsenide near a layer of *LT*-GaAs, which serves as a source of V_{Ga}, that the activation energy for In-Ga interdiffusion is greatly decreased and that the effective diffusion coefficient in the temperature range $T = 700-1000$ °C exceeds that of Al-Ga by one to two orders of magnitude. For this reason, investigation of the behavior of thin layers of InAs in a *LT*-GaAs host during annealing is a subject of considerable current interest.

This paper describes an investigation of the structure of indium δ layers in *LT*-GaAs and how it changes during annealing in the temperature range 500–700 °C. This research was performed using transmission electron microscopy (TEM), which has proven to be an effective tool[14,15] for studying interdiffusion at the atomic level.

EXPERIMENT

The experimental samples were grown by MBE in a two-chamber Katun' system on semi-insulating GaAs(001) substrates containing an 85 nm thick buffer layer of stoichiometric undoped gallium arsenide (grown at 600 °C) and a layer of *LT*-GaAs with a thickness of about 1 μm. The *LT*-GaAs was grown at a temperature of 200 °C at a rate of 1 μm/h under an As_4 vapor pressure $P = 7 \times 10^{-4}$ Pa. Indium-containing δ layers were created in *LT*-GaAs by interrupting the Ga flux and depositing indium for 4 or 8 sec, which ensured nominal In layer thicknesses of 0.5 and 1 monolayer (ML), respectively. The distance between δ layers varied from 20 to 60 nm.

The samples grown were divided into four parts, one of which was not subjected to further procedures (the as-grown sample). The other three were annealed in the growth chamber under an arsenic vapor pressure for 15 min, each at a different temperature: 500, 600, or 700 °C.

For the TEM studies a series of samples was prepared in the form of (110) transverse sections using mechanical polishing and a final milling by Ar^+ ions with an energy of 4 keV at grazing angles on a Gatan Duo-Mill 600 machine. In order to minimize the radiation damage, the sample was cooled during the ion sputtering. In addition, a parallel series of samples was prepared in the form of (100) transverse section by cleaving.[16] Two transmission electron microscopes were used in these studies: a JEM4000EX microscope with an accelerating voltage of 400 kV, and an EM420 microscope operating with an accelerating voltage of 100 or 120 kV.

RESULTS AND DISCUSSION

Because strong contrast is needed in imaging epitaxial layers of semiconducting heterostructures with a sphalerite type of lattice, we chose a technique that is widely used for this type of image generation: dark-field electron microscopy using the (002) reflection, whose amplitude is proportional to the difference between the average atomic scattering factors of the *A* and *B* sublattices and is highly sensitive to the chemical composition of the material. Figure 1 shows the dark-field image in the (020) reflection of a (100) transverse section of an unannealed sample of *LT*-GaAs with indium δ layers having a nominal thickness of 0.5 ML.

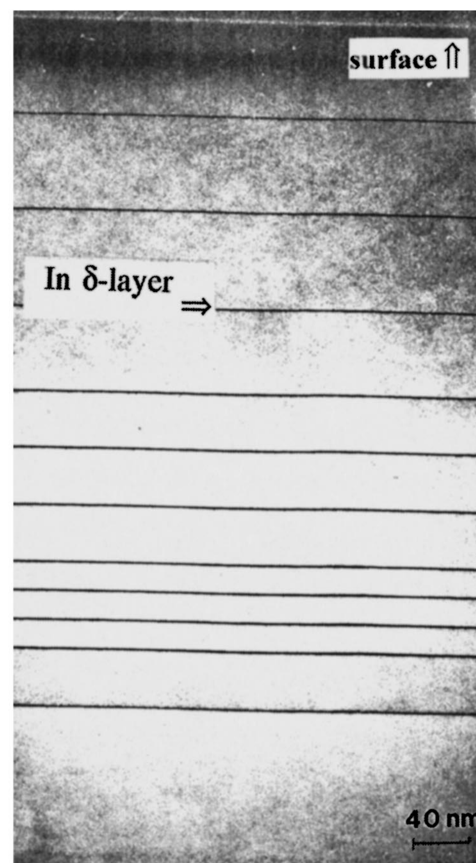

FIG. 1. Dark-field (020) TEM image of a transverse section of a (100) layer of *LT*-GaAs δ-doped with In to a nominal concentration of 0.5 ML.

Thin layers with dark contrast, whose spatial positions in the structure correspond to the positions of indium δ layers assigned by the growth regime, are clearly observed. The thickness of a δ layer in an unannealed sample measured from this image turns out to equal 1.2 ± 0.1 nm. In order to decrease the possibility of errors arising from the influence of the sample thickness on the contrast of the layer images, we also determined these thicknesses from dark-field images of cleaved samples using the (002) reflection with the sample tilted relative to the axis perpendicular to the growth direction to achieve conditions for two-beam diffraction. This situation is illustrated schematically in Fig. 2a. In this case, the observed thickness of the layer varies with the sample thickness. At thicknesses small compared to the extinction length, the contrast on the layer ceases to depend on thickness; therefore, a value for the layer thickness is obtained by extrapolating the dependence of the measured layer thickness on sample thickness to zero sample thickness (Fig. 2b). The thickness values obtained in this way for indium-containing layers in an unannealed sample equaled 1.1 ± 0.1 nm. Samples were also studied in a high-resolution regime. The thicknesses of indium-containing layers on transverse sec-

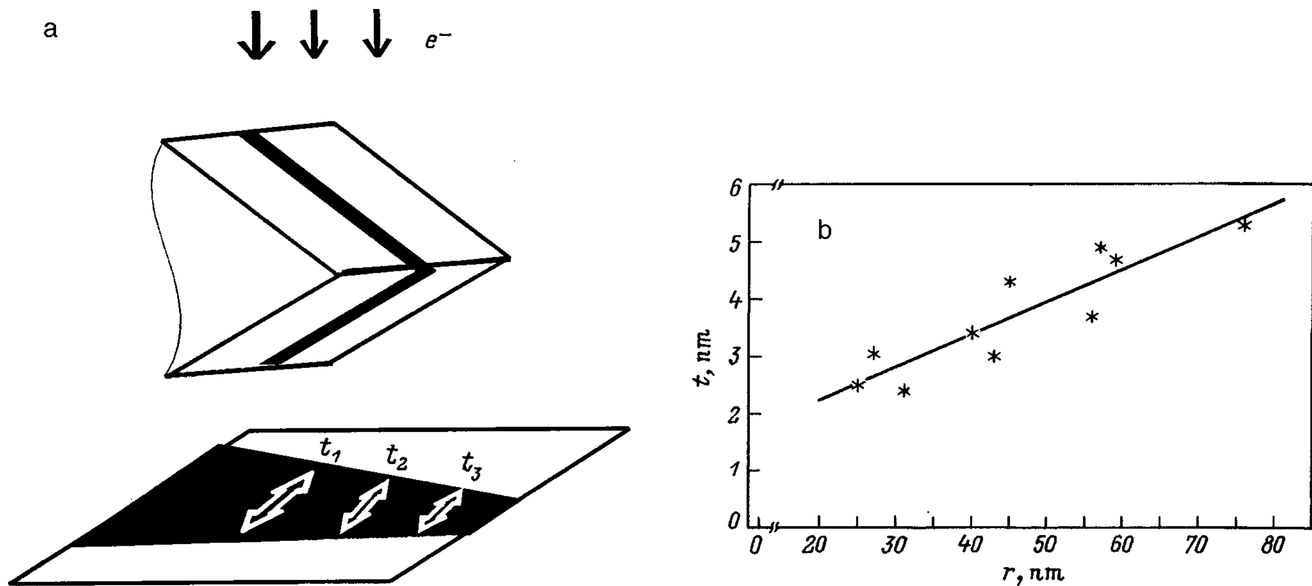

FIG. 2. Schematic representation of the formation of an image in projection along a [100] transverse section of a sample prepared by cleaving (a) and plot of the measured thickness of a layer with a nominal In concentration of 0.5 ML versus the distance to the edge of the sample (b), * — experimental values, straight line — least-squares averaging.

tions of *LT*-GaAs samples were determined from high-resolution [100] zone axis images. Under these conditions an image is formed by four (220) beams and four ''chemically sensitive'' (200) beams. This allowed us to change the relative contributions of the spatial frequencies by choosing the thickness of the portion of the sample being imaged and the degree of defocusing to thereby obtain markedly different images for layers of diverse chemical composition. Figure 3*a* shows a high-resolution image of an unannealed sample of *LT*-GaAs with indium δ layers having a nominal thickness of 0.5 ML and clearly demonstrates that most of the indium atoms are actually distributed in four adjacent (002) atomic planes, i.e., the observed thickness of the indium-containing layer is 4 ML or 1.12 nm.

Analogous studies of an unannealed sample with a nominally deposited amount of indium equivalent to 1 ML show that the real thickness of a δ layer is also 4 ML.

Thus, the deposition of indium during growth in amounts equivalent to 0.5 or 1 ML leads in both cases to the formation of indium-containing layers, whose thickness turns out to equal 4 ML. The spreading of thin layers and interfaces in heteroepitaxial structures observed in the electron microscope is difficult to interpret and is widely discussed in the literature. Even when additional processing of the images is used, as a rule it is not possible to determine unambiguously whether this spreading is a result of interdiffusion or is caused by interface morphologies whose characteristic lateral dimensions are smaller than the sample thickness in the direction of the electron beam, because high-resolution images are in reality projections of the atomic structure averaged over the sample thickness along the direction of the electron beam. Under our conditions, the epitaxial growth temperature is quite low (200 °C), the interdiffusion of Ga and In atoms is very improbable, and the observed broadening of

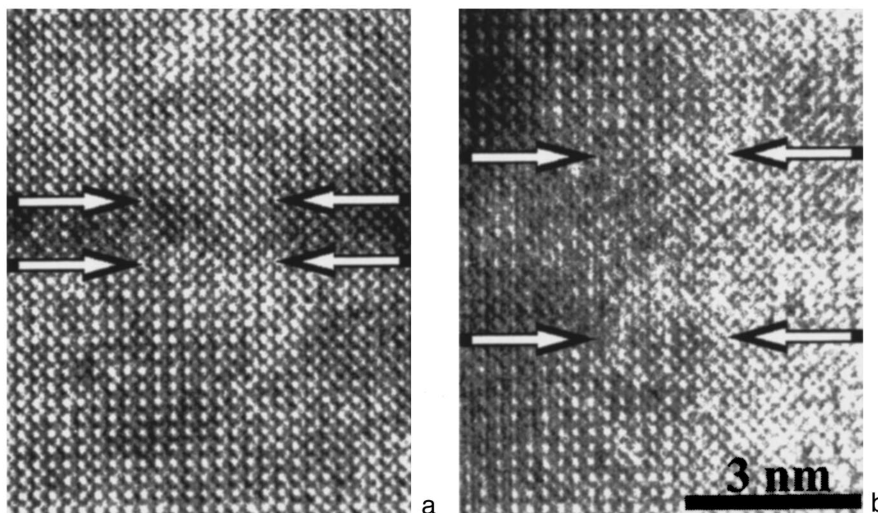

FIG. 3. High-resolution electron photomicrographs of *LT*-GaAs layers along [100] exhibiting layers with a nominal In concentration of 0.5 ML in the following samples: a — unannealed, b — annealed at 600 °C for 15 min. The arrows show the boundaries of the In-containing layer.

the layers must be related to the morphology of the growth front. Additional confirmation of the small role played by interdiffusion in the broadening of the δ layers is provided by the fact that their thicknesses in the two unannealed samples are the same, despite the considerable, twofold, difference between the nominal indium concentrations (1 and 0.5 ML). Step-like interface morphologies with an amplitude of several atomic layers and a characteristic lateral dimension of 1–5 nm along [010] have been observed previously in electron-microscopic studies of transverse sections of GaAlAs/GaAs,[17] GaInAs/AlInAs,[14] and CdHgTe/CdTe[18] heterostructures using the high-resolution technique in projections along [100]. The structures investigated in Refs. 14,17, and 18 were grown by MBE at ordinary temperatures (600–680 °C) on substrates oriented precisely along (001); nevertheless, even under these conditions the growth front can have bumps with heights as large as 4–5 ML, which are not smoothed by interdiffusion, despite the fact that the samples studied in Ref. 14 were additionally annealed at 700–900 °C. Decreasing the epitaxial growth temperature to 200 °C, as we have done in this work, significantly suppresses the migration of deposited atoms over the growth surface, and thus the formation of steps or bumps with a height of several atomic layers at the growth surface is far more natural. From this we conclude that the δ layers probably consist of InAs islands in GaAs, which are distributed primarily within four adjacent atomic layers.

An investigation of the samples annealed for 15 min at 500 °C reveals a considerable increase in the thickness of the δ layers beyond the initial 4 ML. After annealing samples with a nominal indium content of 0.5 and 1 ML, indium is observed in layers 6 ML thick, i.e., 1.7 nm, and 8 ML thick, i.e., 2.24 nm, respectively.

Annealing at 600 °C has the consequence of further increasing the thickness of the indium-containing layers. In Fig. 3b we show a photomicrograph obtained using the high-resolution technique of a sample with a nominal indium content of 0.5 ML. The indium-containing layer occupies 12 ML (3.4 nm). In a sample with a nominal indium content of 1 ML, the experimental thickness comes to 15 ML (4.2 nm).

When the anneal temperature is increased to 700 °C and the δ layers spread further, their visualization in the high-resolution regime turns out to be impossible due to the strong decrease in the indium concentration. The thickness of the δ layers in samples with a nominal indium content of 0.5 ML determined from dark-field (002) images is estimated to be 6 nm. The results of measuring the thickness of the δ layers in samples with nominal indium contents of 0.5 and 1 ML for various anneal temperatures are listed in Table I.

Thus, in the temperature range 500–700 °C we investigated, *LT*-GaAs exhibits significant interdiffusion of indium and gallium, which leads to an increase in the thickness of the δ layers and, evidently, spreads the InAs islands into a $In_xGa_{1-x}As$ solid solution. Starting from measured values of the thickness of the indium-containing layers for various anneal temperatures, we can determine the In-Ga interdiffusion coefficient in *LT*-GaAs. We represent the initial profile of the indium concentration in an unannealed sample as follows:

TABLE I. Measured values of the thickness of an indium-containing layer and diffusion constants.

Nominal In content, ML	Thickness of In-containing layer, nm			
	as-grown	500 °C	600 °C	700 °C
0.5	1.1	1.7	3.4	6
1	1.1	2.2	4.2	⋯
Nominal In content, ML	**Diffusion coefficient $D_{\text{In-Ga}}$, cm²/s**			
0.5	⋯	3.6×10^{-19}	2.6×10^{-18}	1.2×10^{-17}
1	⋯	6.2×10^{-19}	3.5×10^{-18}	⋯

$$c_{\text{In}}(z)=\frac{c_0}{\sqrt{2\pi}\sigma_0}\exp\left(-\frac{z^2}{2\sigma_0^2}\right), \tag{1}$$

where c_0 is the nominal indium concentration, σ_0 is the standard deviation, and z is the coordinate in the growth direction. In this case the solution to the diffusion equation

$$\frac{\partial}{\partial t}c_{\text{In}}(z,t)=D_{\text{In-Ga}}\frac{\partial^2}{\partial z^2}c_{\text{In}}(z,t) \tag{2}$$

will be a Gaussian, whose standard deviation σ is related to the diffusion coefficient $D_{\text{In-Ga}}$ by

$$2D_{\text{In-Ga}}t=\sigma^2-\sigma_0^2. \tag{3}$$

When experimental values of the layer thickness are used to determine the diffusion coefficient, it is necessary to establish the indium concentration level at which the layer boundary is observed. In order to determine this level we investigated samples of *LT*-GaAs containing δ layers with various indium concentrations from 0.5 down to 0.006 ML. The (002) dark-field image of such a sample is shown in Fig. 4, from which it is clear that the smallest nominal concentration of InAs in a δ layer that can be reliably measured is 1.8 mole %. Taking into account that the thickness of the δ layer in an unannealed sample is at least 4 ML, the lowest indium concentration that can be detected in a (002) dark-field image is estimated to be 0.5 mole %. Solving Eq. (2) numerically with allowance for the fact that the thickness of an indium-containing layer deduced from electron-microscopic images corresponds to a width of the Gaussian distribution at an absolute level of 0.5 mole % In, we obtain the values of the effective diffusion coefficients for the anneal temperatures used. The effective diffusion coefficients determined in this way for indium in *LT*-GaAs at 500, 600, and 700 °C are listed in Table I. A plot of the temperature dependence of the effective diffusion coefficient in log ($D_{\text{In-Ga}}$) versus $1/T$ coordinates is shown in Fig. 5. Because the diffusion coefficient depends exponentially on temperature, i.e.,

$$D_{\text{In-Ga}}=D_0\exp(-Q/kT), \tag{4}$$

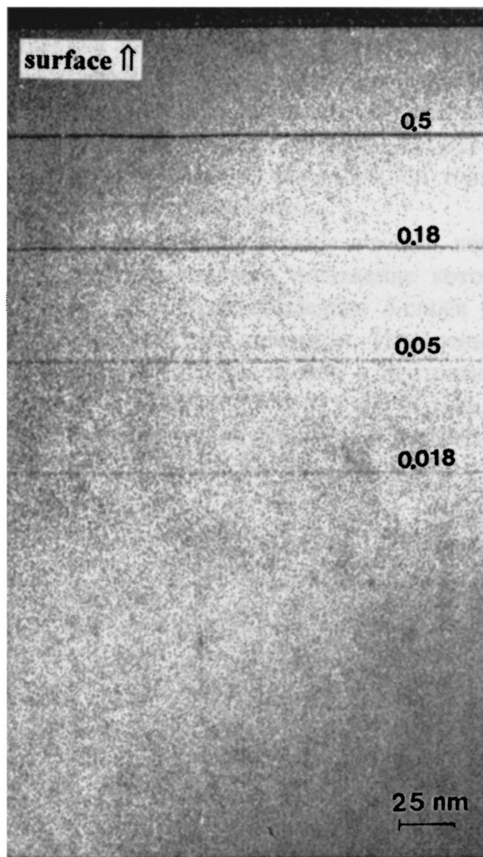

FIG. 4. Dark-field (002) image of a (110) transverse section of a LT-GaAs layer containing In δ layers with various indium contents.

we can use an Arrhenius plot to find the pre-exponential factor D_0 and the effective activation energy for diffusion Q. They turn out to equal 5.1×10^{-12} cm^2/s and 1.1 ± 0.3 eV, respectively.

The activation energy for In-Ga interdiffusion in ordinary gallium arsenide found experimentally in Ref. 13 is 1.9 eV. In the same paper it was shown that the activation energy drops to 1.6 eV when there is an excess concentration of Ga vacancies supplied by a layer of LT-GaAs at a distance of 0.17 μm from the indium-containing layer.

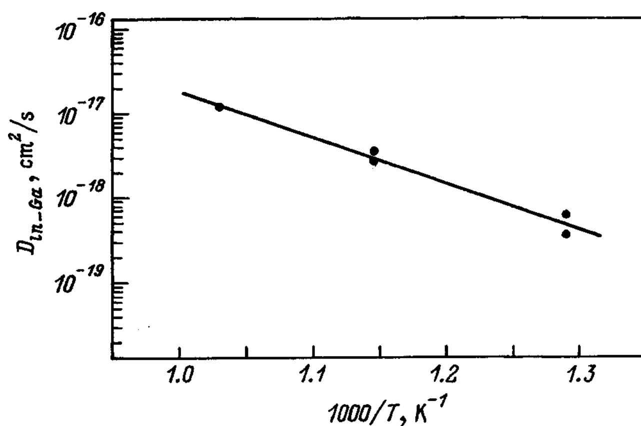

FIG. 5. Plot of the interdiffusion coefficient of In and Ga versus the reciprocal temperature.

The value of the effective activation energy that we obtain is considerably smaller than either of these values. In our view there are two fundamental reasons for this. First, Gebauer *et al.*[19] used experiments involving the annihilation of slow positrons to establish that LT-GaAs grown at 200 °C contains gallium vacancies with a density of $(1-2)\times10^{18}$ cm^{-3}, which exceeds their thermodynamic equilibrium concentration in ordinary GaAs at 600 °C by almost two orders of magnitude. The migration of V_{Ga} should be assumed to play a decisive role in the interdiffusion of In and Ga atoms in LT-GaAs, enhancing it considerably. Unlike Tsang *et al.*,[13] we studied interdiffusion directly in LT-GaAs, where the concentration of V_{Ga} is obviously higher than it is at some distance away. Second, in addition to V_{Ga}, LT-GaAs contains a huge number of other point defects, particularly As_{Ga}, whose concentration reaches 10^{20} cm^{-3} in our samples.[6] The interaction of these defects with gallium vacancies and among themselves can turn out to have a strong influence on the interdiffusion processes. Thus, in Ref. 20 Feng *et al.* established that lowering the growth temperature of LT-GaAs from 400 to 270 °C with a resultant increase in the concentration of point defects in the latter leads to a decrease in the activation energy for the interdiffusion of Al and Ga from 4.15 to 0.39 eV. The samples we investigated were grown at 200 °C and obviously contain close to the maximum concentration of point defects for LT-GaAs, which can result in a low value of the effective activation energy.

CONCLUSION

Our electron-microscopic investigations of LT-GaAs layers grown at 200 °C and δ-doped by indium have revealed that the thickness of the indium-containing layers is 4 ML, i.e., 1.1 nm, regardless of whether the nominal indium content is 0.5 or 1 ML. Because the diffusion of indium from the surface into the bulk of a growing layer is highly improbable at 200 °C, this observation implies that during the MBE of LT-GaAs the growth front has a profile with an amplitude of 4 ML and characteristic lateral dimensions less than 10 nm, and the deposition of indium leads to the formation of InAs islands located in four adjacent atomic layers.

Annealing for 15 min at $T=500-700$ °C gives rise to a considerable broadening of the indium-containing layers from the original thickness due to In-Ga interdiffusion, which is enhanced by the presence of a high concentration of point defects, particularly V_{Ga}, in LT-GaAs. The temperature dependence of the In-Ga interdiffusion coefficient is faithfully described by the expression

$$D_{In-Ga}=5.1\times10^{-12}\exp(-1.08\text{ eV}/kT)\text{ cm}^2/\text{s} \qquad (5)$$

and turns out to be more than an order of magnitude higher than D_{In-Ga} for stoichiometric GaAs in the neighborhood of 700 °C.

This work was supported by the Russian Fund for Fundamental Research, the Ministry of Science of the Russian Federation (under the ''Fullerenes and Atomic Clusters'' program) and the German Scientific Research Society.

We are grateful to R. V. Zolotareva for her careful and high-quality preparation of the TEM samples and to A. E. Kunitsyn for making the optical measurements.

[1] F. N. Smith, A. R. Calawa, C. L. Chen, M. J. Manfra, and L. J. Mahoney, IEEE Trans. Electron Devices **9**, 77 (1988).
[2] M. Kaminska, E. R. Weber, Z. Liliental-Weber, R. Leon, and Z. Rek J. Vac. Sci. Technol. **7**, 710 (1989).
[3] M. R. Melloch, D. C. Miller, and B. Das, Appl. Phys. Lett. **54**, 943 (1989).
[4] M. R. Melloch, N. Otsuka, K. Mahalingam, C. L. Chang, P. D. Kircher, J. Woodall, and A. C. Warren, Appl. Phys. Lett. **61**, 177 (1992).
[5] N. A. Bert, V. V. Chaldyshev, D. I. Lubyshev, V. V. Preobrazhenskiĭ, and V. R. Semyagin, Fiz. Tekh. Poluprovodn. **29**, 2242 (1995) [Semiconductors **29**, 1170 (1995)].
[6] N. A. Bert, V. V. Chaldyshev, A. E. Kunitsyn, Yu. G. Musikhin, N. N. Faleev, V. V. Tretyakov, V. V. Preobrazhenskii, M. A. Putyato, and B. R. Semyagin, Semicond. Sci. Technol. **12**, 51 (1997).
[7] U. Gösele, T. U. Tan, M. Schultz, U. Egger, P. Werner, R. Scholz, and O. Breitenstein, Defect Diffus. Forum **143–147**, 1079 (1997).
[8] X. Liu, A. Prasad, J. Nishio, E. R. Weber, Z. Liliental-Weber, and W. Walukiewicz, Appl. Phys. Lett. **67**, 279 (1995).
[9] C. Kisielovski, A. R. Calawa, and Z. Liliental-Weber, J. Appl. Phys. **80**, 156 (1996).
[10] J. C. P. Chang, J. M. Woodal, M. R. Melloch, I. Lahiri, D. D. Nolte, N. Y. Li, and C. W. Tu, Appl. Phys. Lett. **67**, 3491 (1995).
[11] I. Lahiri, D. D. Nolte, J. C. P. Chang, J. M. Woodal, and M. R. Melloch, Appl. Phys. Lett. **67**, 1244 (1995).
[12] I. Lahiri, D. D. Nolte, M. R. Melloch, J. M. Woodal, and W. Walukiewicz, Appl. Phys. Lett. **69**, 239 (1996).
[13] J. C. Tsang, C. P. Lee, S. H. Lee, K. L. Tsai, C. M. Tsai, and J. C. Fan, J. Appl. Phys. **79**, 644 (1994).
[14] R. E. Mallard, N. J. Long, G. R. Booker, E. G. Scott, M. Hockly, and M. Taylor, J. Appl. Phys. **70**, 182 (1991).
[15] J.-L. Rouviere, Y. Kim, J. Cunningham, J. A. Rentscsler, A. Bourett, and A. Ourmazd, Phys. Rev. Lett. **68**, 2798 (1992).
[16] M. P. A. Viegers, A. F. de Jong, and M. R. Leys, Spectrochim. Acta B **40**, 835 (1985).
[17] A. Ourmazd, J. Cryst. Growth **98** 72 (1989).
[18] Y. Kim, A. Ourmazd, M. Bode, and D. Feldman, Phys. Rev. Lett. **63**, 636 (1989).
[19] J. Gebauer, R. Krause-Rehberg, S. Eichler, M. Luysberg, H. Sohn, and E. R. Weber, Appl. Phys. Lett. **71**, 638 (1997).
[20] W. Feng, F. Chen, W. Q. Cheng, Q. Huang, and J. M. Zhou, Appl. Phys. Lett. **71**, 1676 (1997).

Translated by Frank J. Crowne

Features of the electrical compensation of bismuth impurities in PbSe

S. A. Nemov, T. A. Gavrikova, V. A. Zykov, P. A. Osipov, and V. I. Proshin

St. Petersburg State Technical University, 195251 St. Petersburg, Russia
(Submitted January 12, 1998; accepted for publication January 14, 1998)
Fiz. Tekh. Poluprovodn. **32**, 775–777 (July 1998)

Self-compensation is studied in bulk samples of PbSe : (Bi, Se_{ex}) prepared by a metal-ceramic method. The dependence of the carrier concentration on the amount of excess selenium is investigated for various bismuth concentrations. Comparison of the experimental data with calculated data shows that the donorlike activity of bismuth accommodated in the cation sublattice is compensated by doubly ionized lead vacancies. Nonmonotonic behavior of the dependence of the carrier concentration on the selenium excess is observed in some series of samples due to the incorporation of Bi atoms into both the cation and anion sublattices.
© *1998 American Institute of Physics.* [S1063-7826(98)00207-5]

This paper describes our studies of the phenomenon of self-compensation in PbSe doped by the amphoteric impurity bismuth. The essence of self-compensation can be stated as follows: when an electrically active impurity is introduced into a crystal, it is generally energetically advantageous for the crystal to change the concentration of electrically active intrinsic defects which compensate the doping action of the new impurity.

Previous studies of self-compensation in lead selenide focused on material doped with thallium[1] and chlorine[2] impurities. Thallium exhibits acceptor properties in lead selenide and produces one hole in the valence band per impurity atom. In samples with the maximum level of compensation achievable in experiment, the typical electron and hole concentrations are $n,p \approx (1-3)\times 10^{18}$ cm^{-3}. In maximally compensated samples the type of conduction depends on the thallium content N_{Tl} and undergoes a very abrupt change near $N_{Tl}=0.23$ at. %. These peculiarities make the PbSe : (Tl, Pb_{ex}) system less than promising from the point of view of photoelectric applications.[1)] A detailed comparison of the experimental data with computations shows that the acceptorlike activity of thallium in PbSe is compensated by doubly ionized intrinsic donorlike defects.

In lead selenide doped with the donor impurity chlorine, a higher level of self-compensation is observed, and compensated samples have been obtained with carrier concentrations of $(2-5)\times 10^{17}$ cm^{-3}, i.e., an order of magnitude lower than for PbSe : (Tl, Pb_{ex}). The dependence of the carrier concentration in the compensated samples on the amount of chlorine N_{Cl} is a gently sloping curve with a point of complete compensation at $N_{Cl}\approx 0.7$ at. %. Theoretical calculations show that the compensation mechanism is complicated and that the high self-compensation level can be explained only if we take into account not only single vacancies, but also the formation of complexes.

In this study we chose to investigate the impurity bismuth, because bismuth can exhibit amphoteric properties in lead selenide. Lead selenide is a type IV–VI semiconductor; therefore, thallium, a group-III element, exhibits acceptorlike properties in lead selenide, while chlorine, a group-VII element, exhibits donorlike properties. We should expect that atoms of bismuth (a group-V element) should exhibit either donor- or acceptorlike properties in PbSe, depending on the conditions of incorporation. When bismuth atoms are accommodated in the cation sublattice, they display donorlike properties and donate one electron to the conduction band per impurity atom.[3,4] However, in samples with excess lead, bismuth can also be accommodated in the anion sublattice, where it should exhibit acceptorlike properties and contribute holes to the valence band. Thus, when a bismuth atom moves from the cation to the anion sublattice, a donor should disappear and an acceptor should appear; therefore, we should expect additional compensation of the electrically active behavior of bismuth due to the transfer of some atoms to the opposite sublattice.

The self-compensation in film samples of PbSe : Bi prepared by vacuum sputtering was investigated in Ref. 5. In this study, we established experimentally that bismuth impurities can redistribute between the sublattices. We showed that excess selenium and lead determine the number of vacant sites in the cation and anion sublattices and, therefore, permit the effective redistribution of bismuth between the sublattices. However, it should be noted that the interpretation of data in film samples is complicated by the high concentration of nonequilibrium defects ($\sim 10^{19}$ cm^{-3}). A detailed study of the behavior of bismuth impurities in equilibrium bulk samples of lead selenide has not been made before.

In this study we investigated bulk samples of PbSe : Bi prepared by a metal-ceramic method with grain sizes $d\sim 0.1$ mm. The samples were subjected to a homogenizing anneal for 100 hours at a temperature of 650 °C. We assume that this time is long enough for thermodynamic equilibrium to be established in these samples. The bismuth impurities and excess selenium were introduced directly into the melt during the synthesis of the material. The composition of the samples corresponded to the chemical formula $Pb_{1-x}Bi_xSe_{1+y}$ with the ranges of variation $x=0.075-1.0$ at. % and $y=0-2$ at. %. The carrier concentrations were determined from measurements of the Hall coefficient

 © 1998 American Institute of Physics

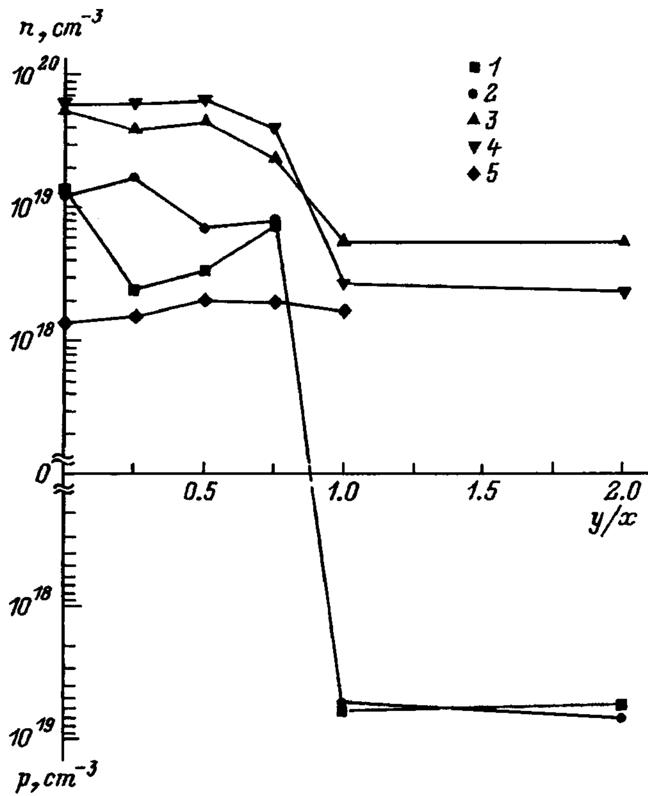

FIG. 1. Dependence of the carrier concentration on the excess concentration of selenium in samples of $Pb_{1-x}Bi_xSe_{1+y}$. N_{Bi}, at. %: *1* — 0.075, *2* — 0.1, *3* — 0.3, *4* — 0.5, *5* — 0.75.

R at room temperature according to the expression $n,p=(eR)^{-1}$.

The experiment provided the dependence of the carrier concentration on the content of bismuth and excess selenium in samples of PbSe : (Bi, Se_{ex}), which is shown in Fig. 1. In our experiments on compensated samples, the typical carrier concentrations were $(2-7)\times 10^{18}$ cm^{-3}, i.e., of the same order of magnitude as in PbSe : Tl and an order of magnitude larger than in PbSe : Cl. This fact leads us to conclude that self-compensation takes place predominantly through isolated vacancies in PbSe : Bi and that complexation processes do not play as important a role as it does in PbSe : Cl. Let us estimate the carrier concentration in maximally compensated samples of PbSe : Bi within the self-compensation theory developed in Ref. 6, assuming that the compensation of bismuth takes place via doubly ionized lead vacancies. According to Ref. 6, in this case the theory has one fitting parameter—the point of complete self-compensation N^*_{Bi}, which is unambiguously determined from experiment. The dependence of the carrier concentration on the impurity concentration N_{Bi} is given by the expression

$$\frac{N_{Bi}}{N^*_{Bi}}=1-\Delta+\frac{\Delta^2}{2\delta^2}-\frac{\Delta}{\delta}\sqrt{1+\frac{\Delta^2}{4\delta^2}},$$

in which $\Delta=(p-n)/N^*_{Bi}$, $\delta=n_i/N^*_{Bi}$, and n_i is the intrinsic carrier concentration. Assuming in accordance with the experimental data that $N^*_{Bi}\approx 0.2$ at.%, and taking into account that at 650 °C we have $n_i=3.5\times 10^{18}$ cm^{-3}, for $N_{Bi}=0.5$ at. % a we obtain a conduction-band electron concentration of $n=3\times 10^{18}$ cm^{-3}, whereas the experimental value is $n=2.3\times 10^{18}$ cm^{-3}. Thus, there is good agreement between the experimental data and the results of calculations within the model of impurity self-compensation via isolated doubly ionized vacancies.

Let us examine the experimental data in more detail. From Fig. 1 it is clear that for bismuth concentrations in PbSe less than 0.75 at. % the introduction of excess selenium lowers the carrier concentration and that for bismuth concentrations up to 0.3 at. % this trend can even lead to a change in the type of conduction. This is evidence that the donorlike behavior of Bi is compensated by acceptorlike Pb vacancies. We note also that the carrier concentration corresponds approximately to the amount of bismuth introduced into samples not containing excess selenium. Nevertheless, at small bismuth concentrations ($N_{Bi}<0.1$ at. %), the plot of $n,p=f(N_{Se_{ex}})$, where $N_{Se_{ex}}$ is the excess concentration of Se, exhibits a region of nonmonotonicity in which the concentration of electrons in the conduction band increases with increasing excess selenium (which leads to acceptorlike behavior in PbSe).

We note that at high bismuth concentrations, e.g., $N_{Bi}=0.75$ at. %, our series of samples exhibits a higher level of compensation than follows from the self-compensation theory. The carrier concentration $n\approx(2-3)\times 10^{18}$ cm^{-3} in our series of samples turns out to be an order of magnitude smaller than the amount of bismuth introduced and is practically independent of the amount of excess selenium. These features of the experimental data can be explained if we assume that not all of the bismuth introduced resides in the cation sublattice and exhibits donorlike properties, i.e., the bismuth atoms introduced redistribute between the cation and anion sublattices with mutual compensation of their doping action.

Thus, by performing these experiments we have established that at small bismuth concentrations ($N_{Bi}\sim 0.1$ at. %) the bismuth atoms are accommodated predominantly in the cation sublattice, and the doping action of bismuth is compensated by doubly ionized acceptorlike lead vacancies. Conversely, at high bismuth concentrations ($N_{Bi}>0.5$ at. %) some of the bismuth atoms are apparently accommodated in the anion sublattice. In this case, in addition to the self-compensation of bismuth in the cation sublattice, an important role is played by the mutual compensation of bismuth atoms in both sublattices of lead selenide.

[1)]Here and in what follows, the subscript ''ex'' denotes an excess amount of the respective component.

[1]L. I. Bytenskiĭ, V. I. Kaĭdanov, R. B. Mel'nik, S. A. Nemov, and Yu. I. Ravich, Fiz. Tekh. Poluprovodn. **14**, 74 (1980) [Sov. Phys. Semicond. **14**, 40 (1980)].
[2]S. A. Nemov, M. K. Zhitinskaya, and V. I. Proshin, Fiz. Tekh. Poluprovodn. **25**, 114 (1991) [Sov. Phys. Semicond. **25**, 67 (1991)].
[3]Yu. I. Ravich, B. A. Efimov, and I. A. Smirnov, *Semiconducting Lead Chalcogenides* [Plenum Press, New York, 1970; Nauka, Moscow, 1968].

[4] N. Kh. Abrikosov and L. E. Shelimova, *IV–VI Semiconducting Materials* [in Russian] (Nauka, Moscow, 1975).
[5] V. A. Zykov, T. A. Gavrikova, and S. A. Nemov, Fiz. Tekh. Poluprovodn. **29**, 309 (1995) [Semiconductors **29**, 154 (1996)].
[6] V. I. Kaĭdanov, S. A. Nemov, and Yu. I. Ravich, Fiz. Tekh. Poluprovodn. **28**, 369 (1994) [Semiconductors **28**, 223 (1994)].

Translated by Frank J. Crowne

Effect of isovalent indium doping on excess arsenic in gallium arsenide grown by molecular-beam epitaxy at low temperatures

V. V. Chaldyshev, A. E. Kunitsyn, V. V. Tret'yakov, and N. N. Faleev

A. I. Ioffe Physicotechnical Institute, Russian Academy of Sciences, 194021 St. Petersburg, Russia

V. V. Preobrazhenskiĭ, M. A. Putyato, and B. R. Semyagin

Institute of Semiconductor Physics, Russian Academy of Sciences, Siberian Branch, 630090 Novosibirsk, Russia

(Submitted April 21, 1998; accepted for publication April 23, 1998)
Fiz. Tekh. Poluprovodn. **32**, 778–781 (July 1998)

X-ray spectral microanalysis, optical transmission measurements at near-infrared wavelengths, and x-ray diffractometry are used to show that the isovalent indium doping of gallium arsenide during molecular-beam epitaxy at low temperatures leads to an increase in the concentration of excess arsenic trapped in the growing layer. © *1998 American Institute of Physics.* [S1063-7826(98)00307-X]

A fundamental feature of gallium arsenide layers grown by molecular-beam epitaxy at low (down to 250 °C) temperatures (so-called *LT*-GaAs) is the large excess of arsenic trapped in the crystal during epitaxial growth.[1–3] In subsequent thermal processing, the excess arsenic forms clusters ranging in size from a few nanometers to tens of nanometers.[4] A material obtained in this way exhibits high resistivity (up to $10^8 \Omega \cdot$cm) and extremely small charge-carrier lifetimes (less than 1 ps).[5] These unique properties of *LT*-GaAs are already used in a number of GaAs-based semiconductor devices. There are examples of the successful use of this material as a buffer layer in field-effect transistors and as the active layer in ultrahigh-speed photodetectors. Since the properties of *LT*-GaAs are largely determined by the amount of excess arsenic trapped in the material during growth, the ability to control this concentration is extremely important. It is known that decreasing the growth temperature of the epitaxial layer or increasing the As/Ga flux ratio leads to an increase in the concentration of excess arsenic in *LT*-GaAs.[3,6] However, the use of either of these methods leads to a considerable degradation of the crystal perfection of the epitaxial film: the formation of a surface relief, the appearance of twinning, stacking faults, dislocations, and other extended defects. For this reason, there is interest in developing alternative approaches and possible ways to increase the concentration of excess arsenic in *LT*-GaAs.

In this paper we show that the concentration of excess arsenic in *LT*-GaAs can be increased by isovalent doping with indium. The indium-doped epitaxial layers are found to have higher crystallinity than undoped layers of *LT*-GaAs. We also examine how doping low-temperature gallium arsenide with shallow Si donors and shallow Be acceptors affects the concentration of excess arsenic.

Layers of *LT*-GaAs were grown in a Katun' molecular beam epitaxy machine on a (100)-oriented substrate of semi-insulating gallium arsenide 40 mm in diameter. The procedure for pregrowth sample preparation of the substrate was described in Ref. 3. A buffer layer of GaAs with a thickness of 85 nm was grown on the substrate at a temperature of 580 °C. Then the substrate temperature was lowered to 200 °C, and a layer of *LT*-GaAs was grown under an arsenic pressure of 7×10^{-4} Pa at a rate of 1 μm/h. Both undoped layers and layers doped with the isovalent impurity In, the shallow donor impurity Si, and the shallow acceptor impurity Be were grown. The concentration of electrically active impurities was 7×10^{17} cm^{-3}. The concentration of indium, which was monitored by x-ray spectral microanalysis, was 0.2 and 0.04 at. %. The samples were annealed in the molecular beam epitaxy machine at 500, 600, 700, or 810 °C for 15 min under an arsenic pressure.

For a direct estimate of the excess arsenic concentration we used x-ray microanalysis. The x-ray diffraction studies were made using a double-crystal diffractometer. An asymmetric crystal of Ge was used as a monochromator-collimator, which ensured that the primary beam for the (004) Cu $K_{\alpha1}$ reflection had a divergence of $1.0-1.2$ arc sec. The concentration of As_{Ga} antisite defects was determined by measuring the optical absorption in the near-infrared region at 300 K using Martin's calibration.[7]

The x-ray spectral microanalysis measurements showed that the concentration of excess arsenic in the layers was in the range 0.2–0.4 at. % and increased as the sample was doped with indium. However, the low accuracy of this measurement technique (the concentration of excess arsenic is close to the detection limits) prevented us from arriving at quantitative estimates with sufficient accuracy. In order to make more accurate and quantitative measurements of the concentration of excess arsenic and the extent to which it is influenced by isovalent doping with indium, we undertook high-resolution x-ray diffraction and optical absorption measurements in the near-infrared (near-IR) region.

Figure 1 shows x-ray diffraction curves for unannealed samples of *LT*-GaAs and samples annealed at various temperatures. Some samples were doped only with silicon (a), some with silicon combined with indium (b). The two strong peaks observed in the unannealed samples correspond to a

 © 1998 American Institute of Physics

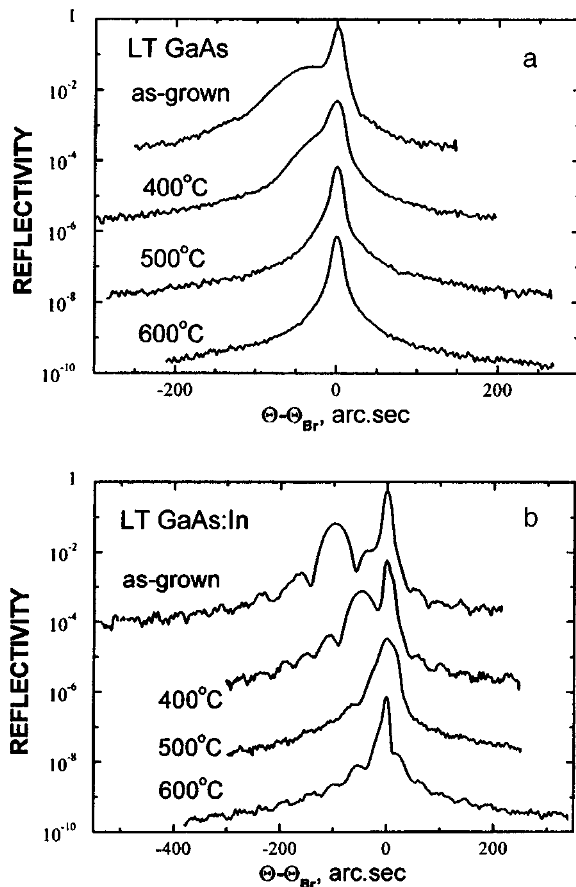

FIG. 1. X-ray diffraction curves for undoped (a) and indium-doped (b) samples of *LT*-GaAs grown at 200 °C and then either left unannealed or annealed at various temperatures. The indium concentration in the doped samples was 0.04 at. %.

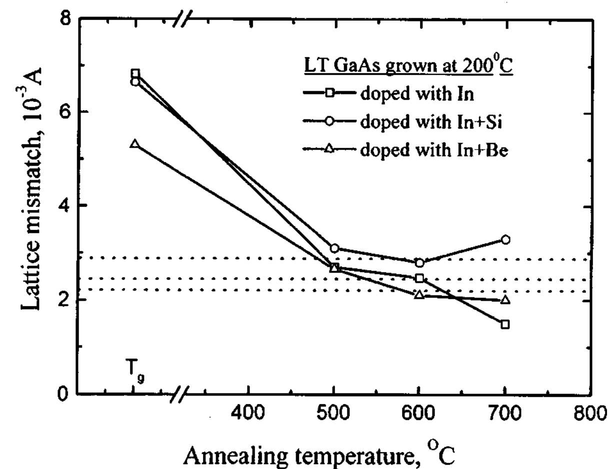

FIG. 2. Lattice parameter mismatch between epitaxial layers of *LT*-GaAs doped with indium (0.2 at. %), as well as In + Be and In + Si, and the GaAs substrate as a function of the anneal temperature. The horizontal curves show the contribution of indium doping to the increase in the lattice parameter of the materials.

diffraction reflection from the GaAs substrate and from the *LT*-GaAs epitaxial layer. It is clear from the figure that the doping of *LT*-GaAs(Si) with indium leads to a considerable increase in the angular distance between the maxima of the peaks. It is known that the trapping of excess arsenic in an epitaxial layer leads to an increase in the lattice parameter of GaAs.[3] Furthermore, doping with indium also has an influence on the lattice parameter due to the difference between the diameters of the gallium and indium atoms. However, because the mismatch between the crystal lattices of GaAs and InAs is only 7%, and the concentration of indium in the samples whose x-ray diffraction spectra are shown in Fig. 1 is only 0.04 at. %, we infer that the replacement of gallium atoms by indium atoms can cause only a tenth of the effect observed. Therefore, we can conclude that the increase in the lattice parameter of *LT*-GaAs is due primarily to an increase in the trapping of arsenic in the epitaxial layer during growth.

In contrast to samples doped only with silicon, samples with additional indium doping exhibit not only the principal peak, but also an interference pattern, which attests to the improved quality of the surface and boundary between the substrate and the *LT*-GaAs epitaxial film. A further indication of the better crystallinity of the *LT*-GaAs(In) layer is the smaller half-width of the principal peaks in the rocking curves.

The amount of lattice parameter mismatch between the *LT*-GaAs epitaxial layer and the GaAs substrate associated with In_{Ga} replacement can be determined by analyzing data from x-ray diffraction studies of the annealed *LT*-GaAs samples. It is known that the excess arsenic forms precipitates during annealing,[4] and that thermal processing at temperatures above 500 °C removes the strain in the crystal lattice caused by excess arsenic almost completely (see Fig. 1). Figure 2 shows how the lattice parameter mismatch between the *LT*-GaAs epitaxial layer and the GaAs substrate depends on the anneal temperature for epitaxial layers doped with indium (in amounts of 0.2 at. %), In+Be, and In+Si. In marked contrast to doping with indium, when the layers are doped with the shallow donor Si or the shallow acceptor Be, the lattice parameter mismatch in the unannealed samples caused by excess arsenic decreases. Similar results were reported previously in Ref. 8. For layers annealed at a temperature greater than 500 °C, the difference between the lattice parameters is determined almost completely by the amount of dopants in the epitaxial layer.

Figure 3a shows the near-infrared optical absorption spectra of undoped samples, both unannealed and annealed at various temperatures, and Fig. 3b shows the spectra of similar samples doped with indium. It is clear that indium doping leads to a considerable increase (by more than a factor of 2 for the unannealed samples) in the characteristic absorption associated with As_{Ga} antisite defects.[9] Conversely, samples doped with the donor impurity Si or the acceptor impurity Be have smaller optical absorption in this wavelength range than do the undoped samples (Fig. 4 shows the spectra of the unannealed samples). Based on optical absorption data at a wavelength of 1 μm and the calibration introduced in Ref. 7, we determined the concentration of As_{Ga} antisite defects for all the samples (see Table I). These data reveal that the As_{Ga} concentration in undoped

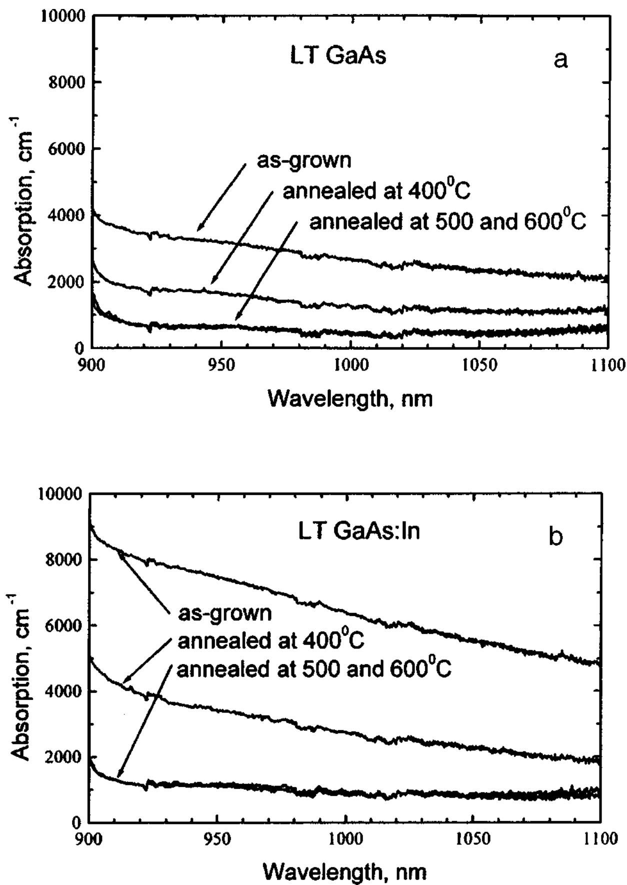

FIG. 3. Optical absorption spectra of undoped (a) and doped (b) *LT*-GaAs samples unannealed and annealed at various temperatures after being grown at 200 °C.

LT-GaAs grown at 200 °C comes to 5.7×10^{19} cm^{-3}. Indium doping leads to a ~15% increase in the concentration of excess arsenic trapped in the epitaxial layer compared to the undoped material. When *LT*-GaAs is doped with Si donors or Be acceptors, the concentration of excess arsenic in the layer decreases by 10 and 25%, respectively. Comparing the parameters of the material doped with indium and grown at a temperature of 200 °C with the undoped *LT*-GaAs obtained at 150 °C, we conclude that isovalent doping with In

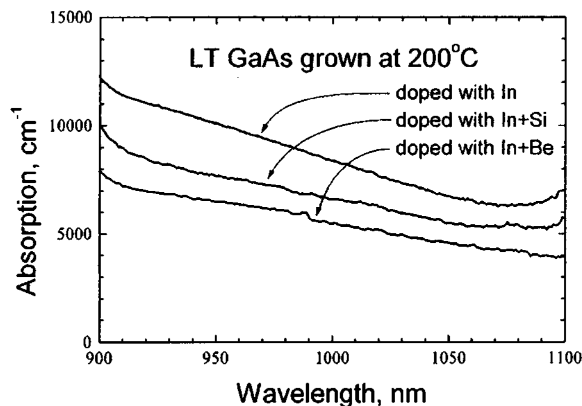

FIG. 4. Optical absorption spectra of undoped *LT*-GaAs samples grown at 200 °C and doped with In, In + Si, and In + Be.

TABLE I.

T_g, °C	Doping	Optical absorption coefficient at a wavelength of 1 μm, cm^{-1}	Concentration of As_{Ga}, 10^{19} cm^{-3}
150	None	10 400	8.0
200	None	7300	5.7
200	In	8400	6.5
200	In, Si	6600	5.1
200	In, Be	5500	4.3

to a concentration of 0.2 at. % is equivalent to decreasing the growth temperature by 20 °C while improving the crystallinity of the material.

As the anneal temperature is increased, the optical absorption of the material falls to values characteristic of stoichiometric gallium arsenide. This effect is known to be associated with the decrease in the concentration of As_{Ga} due to precipitation of the excess arsenic.[4] Our transmission electron microscopy studies showed that the concentration of clusters was higher and their sizes larger in samples doped with indium than in samples that were not doped with In, which also confirms the increase in the trapping of arsenic in the epitaxial layer during indium doping.

Thus, independent investigations all have shown that isovalent doping with indium leads to an increase in the concentration of excess arsenic in *LT*-GaAs. We offer the following possible explanation for this effect. It is known that the distance between nearest-neighbor atoms in bulk arsenic is ~2.4% larger than the distance between gallium and arsenic atoms in gallium arsenide, while calculations show[10,11] that the As_{Ga}–As bond length in GaAs exceeds the Ga–As bond length by an amount of order 8% (similar results were also obtained in Ref. 9 for *LT*-GaAs under the assumption that the increased lattice parameter of the material is caused by the presence of As_{Ga} antisite defects). The isovalent impurity In also increases the In_{Ga}–As bond length in comparison to Ga–As. Thus, doping with indium can ensure a smaller energy of formation for As_{Ga} defects during the growth of *LT*-GaAs. Since the In concentrations used here are comparable to the concentration of As_{Ga} antisite defects, they can have a very strong effect. Conversely, the Coulomb interaction between As_{Ga} antisite defects and shallow Si donors or shallow Be acceptors can increase the energy of formation of As_{Ga} during the growth of the epitaxial layer, thereby hindering the trapping of arsenic in *LT*-GaAs.

Thus, we have shown that isovalent doping with indium leads to an increase in the concentration of excess arsenic trapped in gallium arsenide grown by molecular-beam epitaxy at low temperatures, whereas doping with Si donors or Be acceptors has the opposite effect and decreases the amount of excess arsenic in *LT*-GaAs. This effect is probably associated with the different mechanisms by which these impurities interact with As_{Ga} antisite defects. In contrast to the traditional methods for controlling the concentration of excess arsenic in *LT*-GaAs by varying the growth temperature or the As/Ga flux ratio, the use of isovalent indium doping to increase the concentration of excess arsenic

shows great promise, since it also provides a way to avoid degrading the crystallinity of the epitaxial layer and to improve the quality of the boundary between the substrate and the *LT*-GaAs layer.

This work was carried out with the support of the Russian Ministry for Science (the ''Fullerenes and Atomic Clusters'' and ''Physics of Solid-State Nanostructures'' programs) and the Russian Fund for Fundamental Research.

We are grateful to N. A. Bert for the electronmicroscopic studies.

[1] F. W. Smith, A. R. Calawa, C. L. Chen, M. J. Manfra, and L. J. Mahoney, Electron. Dev. Lett. **9**, 77 (1988).
[2] M. Kaminska, Z. Liliental-Weber, E. R. Weber, T. George, J. B. Kortright, F. W. Smith, B. Y. Tsaur, and A. R. Calawa, Appl. Phys. Lett. **54**, 1831 (1989).
[3] N. A. Bert, A. I. Veĭnger, M. D. Vilisova, S. I. Goloshchapov, I. V. Ivonin, S. V. Kozyrev, A. E. Kunitsyn, L. G. Lavrent'eva, D. I. Lubyshev, V. V. Preobrazhenskiĭ, B. R. Semyagin, V. V. Tret'yakov, V. V. Chaldyshev, and M. P. Yakubenya, Fiz. Tverd. Tela (St. Petersburg) **35**, 2609 (1993) [Phys. Solid State **35**, 1289 (1993)].
[4] M. R. Melloch, N. Otsuka, J. M. Woodall, A. C. Warren, and J. L. Freeouf, Appl. Phys. Lett. **57**, 1531 (1990).
[5] S. Gupta, M. Y. Frankel, J. A. Valdmanis, J. F. Wittaker, G. A. Mouron, F. W. Smith, and A. R. Calawa, Appl. Phys. Lett. **59**, 3276 (1991).
[6] Z. Liliental-Weber, W. Swider, K. M. Yu, J. Kortright, F. W. Smith, and A. R. Calawa, Appl. Phys. Lett. **58**, 2153 (1991).
[7] G. M. Martin, Appl. Phys. Lett. **39**, 747 (1981).
[8] R. E. Prichard, S. A. McQuaid, L. Hart, R. C. Newman, J. Makinen, H. J. von Bardeleben, and M. Missous, J. Appl. Phys. **78**, 2411 (1995).
[9] X. Liu, A. Prassad, J. Nishio, E. R. Weber, Z. Liliental-Weber, and W. Walukiewicz, Appl. Phys. Lett. **67**, 279 (1995).
[10] J. Dobrowski and M. Scheffler, Phys. Rev. Lett. **60**, 2183 (1988).
[11] J. D. Chadi and K. J. Chang, Phys. Rev. Lett. **60**, 2187 (1988).

Translated by Frank J. Crowne

ELECTRONIC AND OPTICAL PROPERTIES OF SEMICONDUCTORS

Stabilization of the physical properties of $Cd_xHg_{1-x}Se$ solid solutions doped with iron

O. S. Romanyuk, S. Yu. Paranchich, L. D. Paranchich, and V. N. Makogonenko

Yu. Fed'kovich Chernovytsy State University, 274012 Chernovytsy, Ukraine
(Submitted June 30, 1997; accepted for publication November 10, 1997)
Fiz. Tekh. Poluprovodn. **32**, 782–785 (July 1998)

The electrical and galvanomagnetic properties of $Cd_xHg_{1-x}Se$ crystals ($x=0.23$) doped with iron in various concentrations are investigated in the temperature range $77-400$ K and in magnetic fields up to 1.6 T. It is established that iron introduced into the crystal host stabilizes its physical properties. It is shown that annealing the samples in selenium vapor has only a small effect on their physical characteristics. © *1998 American Institute of Physics.* [S1063-7826(98)00407-4]

A new group of gapless and narrow-gap, dilute magnetic semiconductors with the formula $A^{II}_{1-x}Fe_xB^{VI}$, in which the magnetic ions are iron, has generated much interest in recent years.[1–3] However, only crystals of $Fe_xHg_{1-x}Se$ have been thoroughly investigated. Fe^{2+} ($3d^6$) ions are substitutional impurities in the HgSe lattice and act as neutral donors. In contrast to Mn^{2+} ions, they form a donor level in the conduction band of HgSe at a depth of ~ 0.235 eV below the bottom of the band. The solid solutions $Fe_xHg_{1-x}Se$ display a whole spectrum of ''anomalous'' properties, which according to Mycielski's ideas[1] arise from Coulomb correlation between the trivalent Fe^{3+} ions that form as the result of the autoionization of Fe^{2+} ions. This correlation leads to ordering of the Fe^{3+} ions, i.e., to the formation of a localized Wigner crystal of charged ions. Spatial ordering of the ionized donors strongly influences the scattering of carriers, thereby giving rise to anomalous increases in mobility at low temperatures.

The kinetic and magnetotransport properties of the solid solutions $Zn_xHg_{1-x}Se:Fe$ and $Mn_xHg_{1-x}Se:Fe$ have been investigated over a wide range of temperatures ($T=4.2-300$ K) and compositions, where the Fe^{2+} level is located in the conduction band.[4] These investigations showed that spatial correlation of donors analogous to HgSe:Fe occurs in these systems as well. Studies of the absorption spectra of $Hg_{1-x-y}Cd_yFe_xSe$ ($y=0.5$; $x=0.05$) at 4.2 K (Ref. 1) reveal that for energies in the range $170-230$ meV there is a clearly marked threshold associated with transitions between the Fe^{2+} level and the conduction band. Between 300 and 450 meV absorption caused by the $^5E(^4D)\rightarrow {}^5T_2(^5D)$ transition between internal crystal-field levels is characteristic of all II-VI compounds containing Fe^{2+}. At energies in the range $770-780$ meV transitions are observed from the valence band to the conduction band.

The goal of this work is to study how the presence of iron atoms and an Fe^{2+} level affects the physical properties of the narrow-gap solid solutions $Cd_xHg_{1-x}Se$.

This paper describes our investigations of the transport properties of $Cd_xHg_{1-x}Se:Fe$ crystals with compositions such that the Fe^{2+} level is located near the bottom of the conduction band in the temperature range $77-400$ K and in magnetic fields up to 1.6 T. We investigated the variation of physical properties over the length of an as-grown crystal of $Cd_xHg_{1-x}Se:Fe$, as well as how thermal annealing in selenium vapor affects these properties.

Mercury selenide with the sphalerite structure and cadmium selenide with the wurtzite structure form $Cd_xHg_{1-x}Se$ solid solutions with one another over a comparatively wide range of values of x.[5] According to Ref. 6, there is a solubility gap in the range $x=0.77-0.81$. Figure 1 shows the change in band structure as we go from HgSe to CdSe at 77 K. These energy-composition curves were calculated from the dependence of E_g on x given in Ref. 7. The figure shows the position of the iron level in $Cd_xHg_{1-x}Se$ crystals with various compositions, taking into account its values for the pure components (0.23 eV above the bottom of the conduction band in HgSe and 0.64 eV above the top of the valence band in CdSe).[1] From this plot it is clear that the iron level is close to the bottom of the conduction band in the composition range $x=0.23-0.28$.

Single crystals of $Cd_xHg_{1-x}Se:Fe$ (with $x=0.23$ and the Fe concentrations $N_{Fe}=2\times 10^{18}$ and 5×10^{19} cm^{-3}) having the zinc blende structure were grown by a modified Bridgman method at a growth rate of 1.2 mm/h and a temperature gradient at the crystallization front of 30 °C/cm. The samples used for the measurements had dimensions $1.5\times 2.5\times 10$ mm^3 and were cut perpendicularly to the growth direction. After mechanical processing the samples were chemically etched with a 5% solution of bromine in methyl alcohol. The contacts consisted of copper wire electrodes soldered to the samples with indium. The values of the free-carrier concentration n_e and the mobility μ were determined as $n_e=1/|R|e$ and $\mu=R\sigma$, respectively, where R is the Hall coefficient and σ the conductivity; the Hall factor was chosen to equal 1.

Table I shows the electrical parameters of the $Cd_xHg_{1-x}Se$ samples ($x=0.23$) doped with Fe to a concentration $N_{Fe}=5\times 10^{19}$ cm^{-3} at $T=77$ and 300 K. The

 © 1998 American Institute of Physics

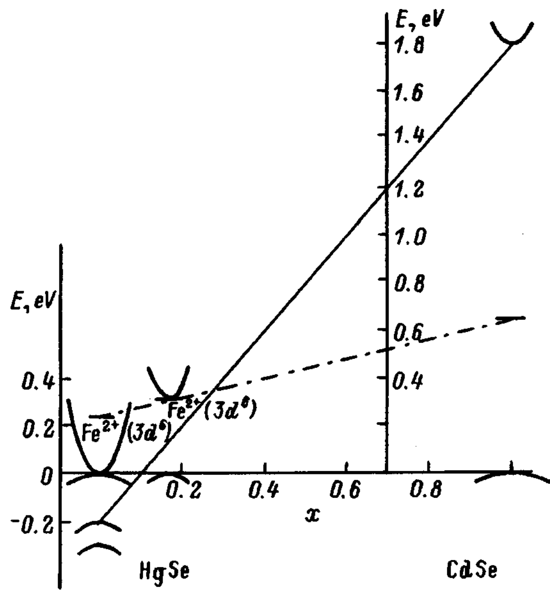

FIG. 1. Variation of the band structure of $Cd_xHg_{1-x}Se$ solid solutions containing a donor Fe^{2+} level as we pass from HgSe to CdSe at 77 K.

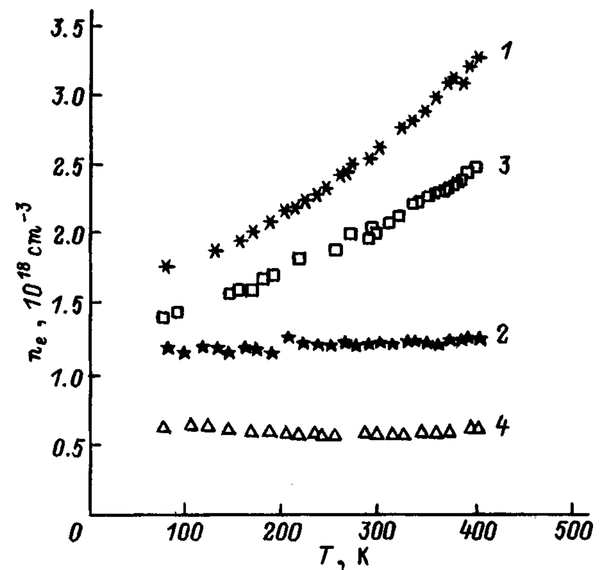

FIG. 2. Temperature dependence of the free-carrier concentration in $Cd_xHg_{1-x}Se:Fe$ ($x=0.23$) with $N_{Fe}=5\times10^{19}$ cm^{-3} [sample 15 (*1, 3*)] and $N_{Fe}=2\times10^{19}$ cm^{-3} [sample 8 (*2, 4*)]: *1, 2* — before annealing, *3, 4* — after annealing in Se vapor.

samples were cut from various portions of a single crystal (the samples are numbered according to crystallization direction). As follows from the table, samples taken from the initial portion of the crystal ($\sim$1/3 of its length) had a carrier concentration of about $(5-8)\times10^{17}$ cm^{-3}, while for the rest of the samples (from the other 2/3 of the crystal) the carrier concentration stabilized at a level of $(1.5-1.8)\times10^{18}$ cm^{-3}.

Figure 2 shows the temperature dependence of the free-carrier concentration n_e for samples of $Cd_xHg_{1-x}Se$ ($x=$ 0.23) with various iron concentrations. It is clear that this dependence is similar to those for $Zn_xHg_{1-x}Se:Fe$ and $Mn_xHg_{1-x}Se:Fe$ (see Ref. 4), i.e., for the samples (both annealed and unannealed) with $N_{Fe}=5\times10^{19}$ cm^{-3} the free-carrier concentration increases with temperature, whereas for the samples with $N_{Fe}=2\times10^{18}$ cm^{-3} it is practically independent of temperature. In this case the Hall coefficient varies only slightly with magnetic field, having a tendency to increase with increasing field for the samples with an iron concentration $N_{Fe}=5\times10^{19}$ cm^{-3}.

Figure 3 shows temperature dependences of the conduc-

TABLE I. Variation of the electron concentration n_e, the conductivity σ, and the mobility μ of samples of $Cd_xHg_{1-x}Se$ ($x=0.23$) along a crystal for $N_{Fe}=5\times10^{19}$ cm^{-3}.

Sample No.	77 K			300 K		
	n_e, 10^{18} cm^{-3}	σ, $10^3\Omega^{-1}\cdot$cm^{-1}	μ, 10^3 cm^2/V·s	n_e, 10^{18} cm^{-3}	σ, $10^3\Omega^{-1}\cdot$cm^{-1}	μ, 10^3cm^2/V·s
2	0.64	0.515	5.02	1.04	0.291	1.74
3	0.562	0.305	3.39	0.575	0.173	1.88
4	0.415	0.364	5.48	0.798	0.062	0.486
5	0.869	1.31	9.42	1.33	0.572	2.7
6	0.579	0.607	6.5	0.88	0.255	1.8
7	0.979	0.791	5.05	1.45	0.429	1.84
8	0.556	6.35	7.14	0.932	0.713	3.7
10	0.816	1.65	13.0	1.19	0.713	3.7
12	1.75	1.87	4.3	2.71	0.808	2.87
13	1.56	2.45	9.8	1.97	0.998	3.15
15	1.77	2.48	8.75	1.85	1.0	2.34
16	1.7	2.49	9.2	2.4	0.996	2.58
19	1.55	2.02	8.15	2.3	0.908	2.5
20	1.55	2.06	8.3	2.56	0.845	2.06
21	1.51	2.94	12.4	2.2	1.13	3.2
22	1.58	2.93	8.7	1.8	1.18	2.78
25	2.87	7.13	1.55	3.12	2.38	4.7
26	1.47	2.64	11.2	2.17	1.08	3.09
27	1.72	3.7	13.4	2.31	1.44	3.89
28	3.54	3.55	17.4	4.62	9.89	4.79

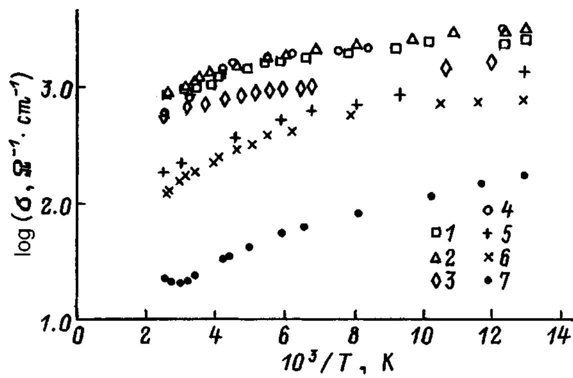

FIG. 3. Temperature dependence of the conductivity of $Cd_xHg_{1-x}Se:Fe$ ($x=0.23$) with $N_{Fe}=5\times10^{19}$ cm^{-3} [samples 15 (*1, 3*) and 22 (*2*)], $N_{Fe}=2\times10^{18}$ cm^{-3} (*4, 5*), and $N_{Fe}=0$ (*6, 7*): *1, 2, 4, 6* — before annealing, *3, 5, 7* — after annealing in Se vapor.

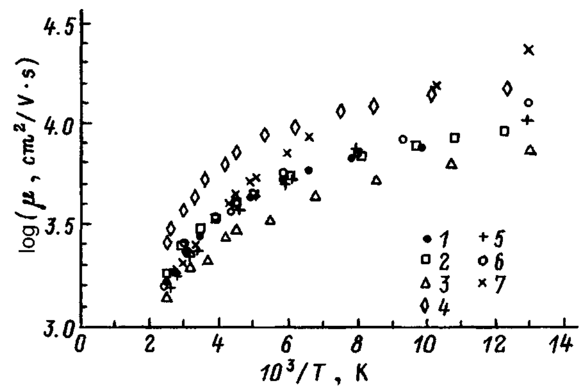

FIG. 4. Temperature dependence of the mobility of $Cd_xHg_{1-x}Se:Fe$ with $N_{Fe}=5\times10^{19}$ cm^{-3} [sample 15 (*1, 3*) and 22 (*2*)], $N_{Fe}=2\times10^{18}$ cm^{-3} (*4, 5*), and $N_{Fe}=0$ (*6, 7*): *1, 2, 4, 6* — before annealing, *3, 5, 7* — after annealing in Se vapor.

tivity of pure samples of $Cd_xHg_{1-x}Se$ (undoped by Fe), as well as samples of $Cd_xHg_{1-x}Se$ ($x=0.23$) doped with iron ($N_{Fe}=2\times10^{18}$, 5×10^{19} cm^{-3}) before and after thermal annealing in selenium vapor. From the figure it follows that:

a) for all the samples studied the conductivity varies with the temperature as in a semimetal, i.e., the electron gas is strongly degenerate;

b) the values of the conductivity for the unannealed samples practically coincide (curves *1*, *2*, and *4*);

c) thermal annealing in selenium vapor turns out to affect undoped samples most strongly (compare curves *6* and *7*), while the conductivity of samples with iron concentration $N_{Fe}=5\times10^{19}$ cm^{-3} is practically unchanged by annealing (curves *1*, *2*, and *3*).

The carrier mobilities for all the samples studied had the same temperature behavior (Fig. 4), i.e., the mobility decreased with increasing temperature, which is characteristic of mercury chalcogenides with n-type conductivity. For the samples prepared from different portions of a crystal with $N_{Fe}=5\times10^{19}$ cm^{-3} the mobilities practically coincide (curves *1* and *2*). For the samples with carrier concentrations $<5\times10^{19}$ cm^{-3} the mobility is somewhat higher (curve *4*). Annealing of the doped samples in selenium vapor, leads to only a small decrease in mobility (curves *3* and *5*), whereas in the undoped samples of $Cd_xHg_{1-x}Se$ annealing in Se increases μ considerably.

The electrical characteristics of doped and undoped samples of $Cd_xHg_{1-x}Se$, as well as samples annealed in selenium vapor, are shown in Table II. It follows from the table that annealing of the undoped samples can change the carrier concentration by an order of magnitude, whereas in the iron-doped samples of $Cd_xHg_{1-x}Se$ with $N_{Fe}=5\times10^{19}$ cm^{-3} the concentration of free carriers is scarcely altered by annealing.

DISCUSSION AND CONCLUSIONS

Replacing a portion of the mercury atoms in mercury selenide by cadmium atoms decreases the distance between the s- and p-symmetry bands, and the inverted band structure is converted into a direct band structure at a certain Cd content (Fig. 1). For gapless crystals of $Cd_xHg_{1-x}Se$ with iron concentrations sufficient to pin the Fermi level, the electron concentration varies over a certain rather small interval as cadmium is added. This variation in the electron concentration continues until spatial correlation begins to appear between charged donors. In our case, the Fe^{2+} level in $Cd_xHg_{1-x}Se$ ($x=0.23$) is located at the bottom of the conduction band or slightly below it, since the crystal was obtained by the Bridgman method and the initial portion of the crystal is rich in Cd. When this is the case, the Fe ions are in the Fe^{+} state with the same valence, i.e., all the donors are ionized. Since the system of ionized Fe^{3+} donors is not strictly periodic, there is a certain contribution to the scattering of electrons from the disordered distribution of Fe^{3+} ions, so that a decrease in the concentration of these scatter-

TABLE II. Effect of annealing in Se vapor on the electrical properties of $Cd_xHg_{1-x}Se:Fe$ ($x=0.23$).

Sample	N_{Fe}, 10^{19} cm^{-3}	77 K: n_e, 10^{18} cm^{-3}	77 K: σ, 10^3 $\Omega^{-1}\cdot$cm^{-1}	77 K: μ, 10^3 cm^2/V·s	300 K: n_e, 10^{18} cm^{-3}	300 K: σ, 10^3 $\Omega^{-1}\cdot$cm^{-1}	300 K: μ, 10^3 cm^2/V·s
22	5.0	1.58	2.93	8.70	1.80	1.18	2.78
15	5.0	1.77	2.48	8.75	1.85	1.00	2.34
15, anneal in Se	5.0	1.40	1.68	7.45	1.94	0.73	2.30
8	0.2	1.18	2.78	14.7	1.70	0.88	4.26
8, anneal in Se	0.2	0.67	1.36	12.6	0.58	0.26	2.86
6	0.0	0.475	0.81	10.7	0.495	0.19	2.39
6, anneal in Se	0.0	0.048	0.18	23.2	0.0527	0.0235	2.78

ing centers $N_{Fe^{3+}} = n_e$ leaves the carrier mobility almost the same for doped and undoped samples (Fig. 4). We associate the temperature dependence of the carrier concentration, i.e., the increase in the concentration with temperature, with the fact that the iron is predominantly in the Fe^{3+} state. Experimental studies of the magnetic susceptibility have shown[8,9] that the ground state of the Fe^{2+} ion in a tetrahedral crystal field is a magnetic singlet. In this case, no variation in the concentration with temperature should be observed. As for Fe^{3+} ions, EPR measurements[10] show that the ground state consists of an orbital singlet with sixfold spin degeneracy. The local symmetry is cubic, and the spin splittings are clearly expressed. Analysis of the temperature dependence of the width of the EPR lines leads us to conclude that at sufficiently high temperatures the line caused by Fe^{3+} ions is broadened by spin-flip collisions with band electrons.

Our experimental results indicate that the phenomena observed in direct-gap $Cd_xHg_{1-x}Se:Fe$ are not associated with spatial correlation of the impurity ions, but rather with the number of intrinsic defects that form during crystallization. An analysis of the crystal structure and chemical binding allows us to identify the three defects most likely to occur in $Cd_xHg_{1-x}Se$ solid solutions: selenium vacancies (V_{Se}), which are donors, interstitial mercury atoms (Hg_i), which are also donors, and mercury vacancies (V_{Hg}), which are acceptors. Iron that replaces mercury atoms in $Cd_xHg_{1-x}Se$ decreases the number of intrinsic defects (for example, Hg vacancies), as is confirmed by the weak influence of annealing in Se vapor on the transport phenomena (Table II).

Thus, from these results it follows that no spatial ordering of the system of Fe^{3+} donors is observed as the resonant level moves closer to the bottom of the conduction band and that the properties of $Cd_xHg_{1-x}Se$ are stabilized by iron doping because of the decreased number of intrinsic defects.

[1] A. Mycielski, J. Appl. Phys. **63**, 3279 (1988).
[2] W. J. M. Jorge, H. J. M. Swagtent, C. E. P. Gerrits, and A. Twardowski, Semicond. Sci. Technol. **5**, S270 (1990).
[3] A. Twardowski, J. Appl. Phys. **67**, 5108 (1990).
[4] W. Dobrowolski, R. R. Galazka, E. Grodzicka, J. Kossut, and B. Witkowska, Phys. Rev. B **48**, 17 848 (1993).
[5] N. P. Gavaleshko, P. N. Gorleĭ, S. Yu. Paranchich, V. M. Frasunyak, and V. V. Khomyak, Neorg. Mater. **17**, 327 (1983).
[6] A. Kalb and V. Leut, Phys. Status Solidi A **5**, K199 (1971).
[7] C. J. Summersand and J. G. Broerman, Phys. Rev. B **21**, 559 (1980).
[8] Z. Wilatowski, W. Jantsch, and G. Hendorfer, Semicond. Sci. Technol. **5**, S266 (1990).
[9] N. P. Gavaleshko, S. Yu. Paranchich, L. D. Paranchich, and M. F. Rybak, Izv. Vyssh. Uchebn. Zaved., Fiz. **11**, 48 (1990).
[10] V. D. Prozorovskiĭ, I. Yu. Reshidova, S. Yu. Paranchich, and L. D. Paranchich, Fiz. Tverd. Tela (Leningrad) **32**, 3290 (1990) [Sov. Phys. Solid State **32**, 1904 (1990)].

Translated by Frank J. Crowne

Phase states and magnetic structure of superconducting lead inclusions in a narrow-gap PbTe semiconducting host

S. D. Darchuk, L. A. Korovina, and F. F. Sizov

Institute of Semiconductor Physics, Ukrainian National Academy of Sciences, 252028 Kiev, Ukraine

T. Dietl, S. Kolesnik, and M. Sawicki

Institute of Physics, Polish Academy of Sciences, PL02668 Warsaw, Poland
(Submitted June 2, 1997; accepted for publication November 10, 1997)
Fiz. Tekh. Poluprovodn. **32**, 786–790 (July 1998)

Samples of the narrow-gap semiconductor PbTe with n- and p-type conductivities are investigated using a SQUID magnetometer in the temperature range 1.7−20 K and in magnetic fields up to 1 kOe. It is shown that there are microscopic inclusions of superconducting lead with minimum dimensions ~1300 Å containing $\sim(1-5)\times10^{18}$ lead atoms/cm^3 in the lead telluride matrix and that the samples undergo a phase transition that is characteristic of type-II superconductors. © *1998 American Institute of Physics.* [S1063-7826(98)00507-9]

1. INTRODUCTION

There is much interest in investigating interactions in systems of semiconductor-superconductor contacts, both from a scientific and an applications-oriented standpoint, since it may be possible to control the nature of these interactions by an external magnetic field.

Such contacts are quite unlike Josephson contacts, which consist of a thin layer of an insulator (usually a metal oxide with a thickness $d\approx10$ Å) between two superconducting phases. The parameters of this layer are difficult to control and are unstable. In contrast, when a semiconductor is used as the medium that separates the superconducting phases, the thickness of the boundary layer can be greatly increased, and consequently much more control of the junction parameters, as well as improved stability of the junction characteristics, are possible. For this reason, there is interest in efforts to create ultralow-noise semiconductor transistors with a superconducting source and drain. Such transistors have in fact been made, e.g., in structures based on InAs with a Nb source and drain, which utilize the interaction of a tunneling current (of Cooper pairs) with a 2D electron gas.[1]

Conclusions concerning the physical processes and nature of the interaction in a semiconductor-superconductor system in an external magnetic field can be drawn by studying the behavior of a semiconductor host with microscopic superconducting inclusions. The behavior of such a system is of interest in its own right, since the size of the inclusions should play an important role in determining the character of their interaction with the electron subsystem. This is because the ability of the magnetic field to penetrate the inclusions should depend on their size.[2]

The most suitable objects for observing the tunneling of Cooper pairs between superconducting inclusions in a semiconductor host are the narrow-gap semiconductors. This is because these semiconductors are characterized by the presence of inclusions rich in metals (see, e.g., Refs. 3 and 4) due to the relatively small enthalpy of formation of vacancies in metals, as well as, e.g., the concentration supercooling observed when they are grown by the usual methods from a melt or the vapor phase. When the components of the semiconductor include superconducting metals (for example, Hg, Pb, Sn, etc.), it is possible in principle to observe the tunneling of Cooper pairs between superconducting inclusions, as has been done, e.g., in studies of carrier transport in HgSe in a magnetic field,[5] as well as of transport in low-dimensional and epitaxial layers of PbTe.[6,7]

However, investigations of these phenomena tell us nothing about the phase states of the inclusions in a magnetic field at temperatures below the superconducting transition temperature. The achievement of this goal calls for investigations of magnetization processes. Because of the small changes in the diamagnetic component accompanying the passage of microinclusions into the superconducting state and because of their generally low concentration, the only way to probe the phase state and magnetic structure of superconducting microinclusions is by using high-sensitivity apparatus, for example, a SQUID magnetometer.

In this work, we used a SQUID magnetometer[1)] to investigate the behavior of the diamagnetic component of the magnetic susceptibility of microinclusions of lead (whose superconducting transition temperature $T_c=7.15$ K) in undoped PbTe semiconductor hosts with n- and p-type conductivity in the temperature range 1.7–20 K. For these investigations we used crystals grown by the Czochralski and Bridgman methods.[2)]

2. EXPERIMENTAL RESULTS AND DISCUSSION

Figure 1 shows the temperature dependence of the magnetization of one of the single-crystal samples of n-PbTe cut in the (001) plane for various values of the external magnetic field. Because the samples with n-type conductivity were usually grown with a certain excess of the metallic component in the melt, microinclusions of Pb in the host are generally observed. In Fig. 1 the plots of $M=f(T)$ exhibit an

 © 1998 American Institute of Physics

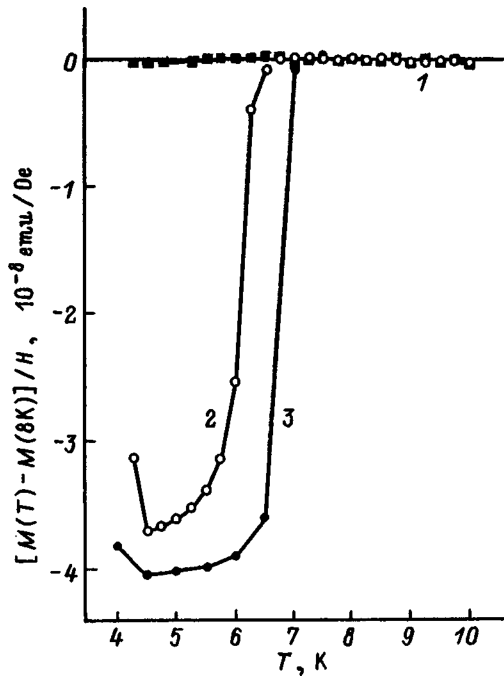

FIG. 1. Dependence of the magnetization M of a single-crystal sample of n-PbTe on temperature T for the following values of the external magnetic field H, Oe: *1* — 600, *2* — 200, *3* — 80.

abrupt increase in the diamagnetic signal against the background of constant diamagnetism from the PbTe host in the vicinity of $T \approx 7$ K in relatively weak external magnetic fields $H < 600$ Oe, which is due to the transition of the lead inclusions to the superconducting state.

It is worth noting that the diamagnetic contribution decreases smoothly as the magnetic field increases, which is characteristic of second-order phase transitions, even though lead is a type-I superconductor. This kind of change in the type of transition is associated with the decrease in the dimensionality (the thickness of the superconductor in the direction perpendicular to the magnetic field direction; see, e.g., Ref. 8). In order to confirm this assertion, we investigated the magnetic-field dependence of the magnetization at various temperatures (Fig. 2a), from which we obtained the dependence of the diamagnetic contribution on magnetic field (Fig. 2b, curve *1*). This in its turn allowed us to determine the value of the second critical field $H_{c2} \approx 950$ Oe at $T = 4.2$ K and the region for the existence of the mixed state in the interval from 480 to 950 Oe. As is clear from the figure, the values of the first and second critical fields increase as the temperature decreases. Curve *2* in Fig. 2b also shows a plot of $M = f(T)$ for a relatively thick (≈ 0.5 mm) sample of pure Pb. Knowing the volume of the Pb and PbTe samples, as well as the absolute values of the diamagnetic signals, we can estimate the concentration of Pb atoms in the PbTe host, which turns out to equal $N \approx (1-5) \times 10^{18}$ cm^{-3} for the samples under investigation.

When we differentiate the curve *1* shown in Fig. 2b, we discover a region $H'_{c1} \approx 190$ Oe $< H < H_{c1} \approx 480$ Oe in which the $M = f(T)$ curve is not typical of a type-II superconductor (due to the presence of a kink at the point H'_{c1}). This is probably due to a size dispersion of the inclusions; consequently, the real region for the existence of the mixed state should lie within the range $H'_{c1} < H < H_{c2}$. In order to prove this assertion we investigated the hysteresis of the magnetization in the system (Fig. 3a). The difference between the magnetization curves as the magnetic field is first increased ($H\uparrow$) and then decreased ($H\downarrow$) describes the dynamics of the trapping of magnetic flux (Fig. 3b), and from it we can infer the existence of three regions: 1 — a region with a superconducting phase ($0 < H < H'_{c1}$), 2 — a region with a superconducting phase and the mixed state ($H'_{c1} < H < H_{c1}$), and 3 — a region with the mixed state ($H_{c1} < H < H_{c2}$).

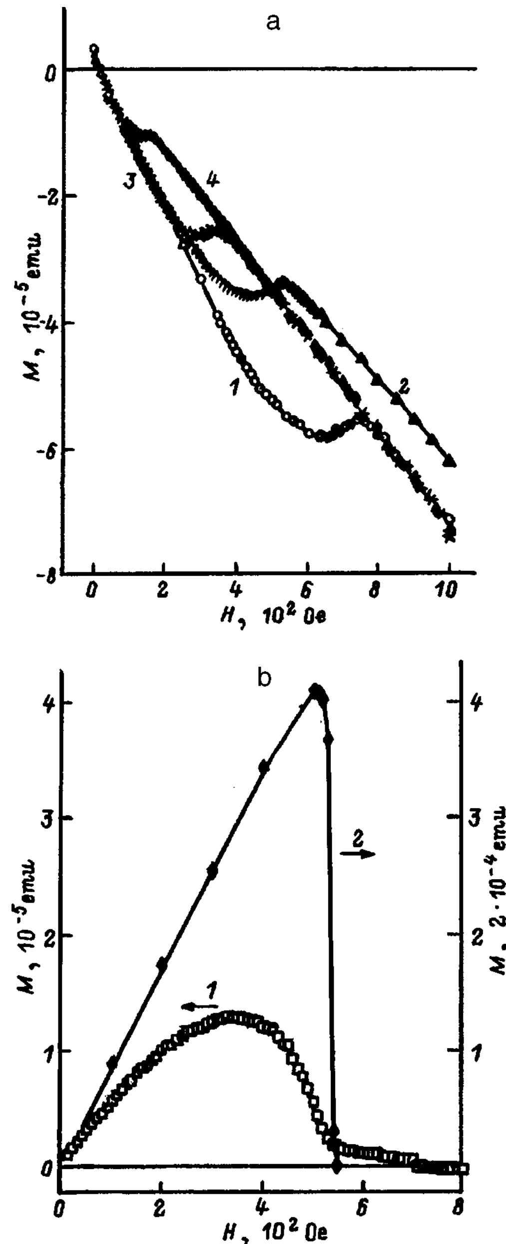

FIG. 2. a — Magnetic-field dependence of the magnetization of a single-crystal sample of n-PbTe at various temperatures T, K: *1* — 1.7, *2* — 4.2, *3* — 5.5, *4* — 6.5; b — dependence of the diamagnetic correction to the magnetization M on magnetic field H at $T = 4.2$ K for the following samples: *1* — n-PbTe, *2* — Pb.

The first critical field H'_{c1} is assigned to inclusions of minimum size, while H_{c1} is assigned to those of maximum

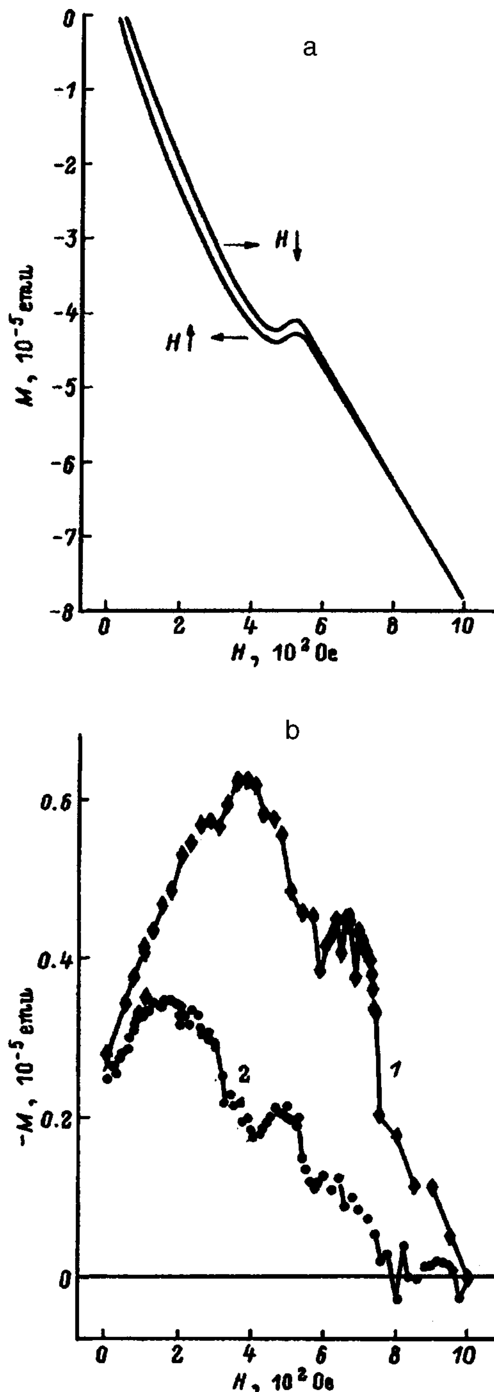

FIG. 3. a — Dependence of the magnetization M of a n-PbTe sample on the magnitude of H and the direction of variation of the magnetic field at $T=4.2$ K; b — difference between the increasing-field and decreasing-field magnetization curves M for a sample of n-PbTe as a function of the magnitude of the external magnetic field H at two temperatures T, K: *1* — 1.7, *2* — 4.2.

size. Additional confirmation of this was obtained by investigating PbTe samples with p-type conductivity, which were grown from stoichiometric melts. These samples usually have an insufficiency of the metallic component in the host compared to the chalcogen. Therefore, the concentration of microinclusions in them should be considerably lower than in samples of n-PbTe, and we could expect a predominance of small-size inclusions. Microinclusions of lead are initiated in the host by the low enthalpy of formation of Schottky vacancies in the metallic sublattice of PbTe ($\Delta H_v^M \cong 0.45$ eV; see Ref. 4). And indeed, in this case the magnetic-field dependence of the magnetization exhibits only one value for the first critical field $H_{c1}\approx 190$ Oe and the value $H_{c2}\approx 950$ Oe, in agreement with the assumptions made above.

The illustrations that follow apply to inclusions of minimum size, since in this case we can use a rather simple mathematical expression for our estimates. This expression is used to describe phenomena in type-II superconductors:[8]

$$H_{c2}=H_b[1-(2\lambda/d)\tanh(d/2\lambda)]^{-1/2},$$

where H_b is the critical magnetic field for the bulk material, in which a first-order phase transition takes place [in the case of lead, $H_b(T=4.2\,K)=350$ Oe], and λ is the penetration depth of a magnetic field into the superconductor (for lead $\lambda\approx 500$ Å).[9] Knowing the value of H_{c2}, we can determine how thick the inclusions of minimum size are in the direction perpendicular to the magnetic field; in our case it turns out to equal $d\approx 1300$ Å. Because there is no variation of the course of the magnetic-field dependences as a function of the orientation of the magnetic field relative to the crystallographic axes of the crystal, we can assert that the inclusions consist of objects of either spherical or filamentary structure.

As we know, the penetration of a magnetic field into a superconductor in the region of the mixed state occurs in the form of quantized vortex filaments. Each of these filaments (or vortices) has a normal core in the form of a long thin normal cylinder having a radius of the same order as the coherence length ξ and extending along the direction of the external magnetic field. An undamped superconducting current flows around this normal cylinder, embracing a region with a radius of order λ. We can estimate the value of the coherence length ξ from the expression[9]

$$H_{c2}=1.69\sqrt{2}(\lambda/\xi)H_b.$$

In this case $\xi\approx 650$ Å; consequently, the diameter of the normal core of a vortex filament is $2\xi\approx 1300$ Å. Vortices that penetrate into the superconductor are separated from one another by a distance of order λ and form a regular triangular lattice (or rectangular lattice) in a transverse section. Thus, in our case a one-dimensional chain of vortices, each of which carries a single magnetic flux quantum Φ_0, forms in the mixed-state region.

In view of the small dimensions of the inclusions ($d\approx 1300$ Å), the system can exhibit effects that are characteristic of two-dimensional or one-dimensional systems. For example, the Kosterlitz–Thouless theory[2] predicts the formation of antiparallel pairs of fluxons in such systems. One way to identify such effects is to analyze the dependence of the period of the one-dimensional vortex lattice on the magnetic induction B. It is known[10] for a lattice with a single magnetic flux quantum per filament having translational symmetry corresponding to a square lattice that the relation between the induction and the lattice period L is fairly simple: $B=\Phi_0/L^2$. Taking into account this relation and the fact that at H_{c2} the distance between nearest-neighbor vortices, i.e., the lattice period, is of order ξ, we can obtain the function

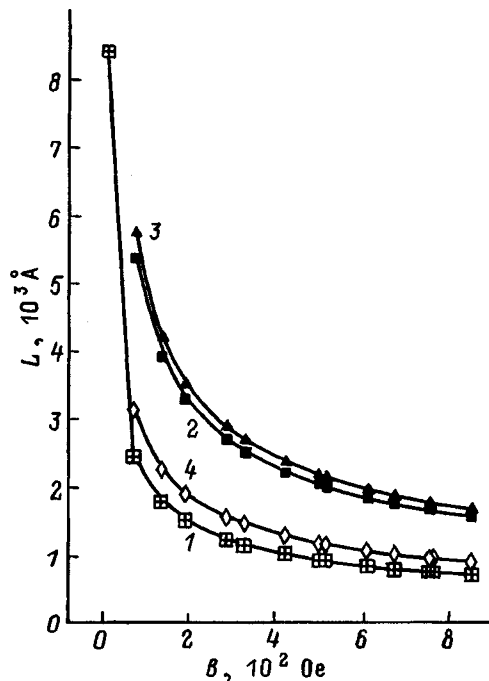

FIG. 4. Dependence of the period L of a one-dimensional lattice of vortex filaments on the magnetic induction B: *1* — experimental data, *2* — calculation for a square lattice, *3* — calculation for a triangular lattice; *4* — curve corresponding to the expression $B=\Phi_0/3L^2$.

$L=f(B)$ from experimental data. This function is shown in Fig. 4 (curve *1*). This figure also shows the theoretical dependences for square (curve *2*) and triangular (curve *3*) lattices. From Fig. 4 it is clear that the theoretical curves *2* and *3* are considerably higher than the experimental curve *1*. This disparity can be attributed to the formation of antiparallel fluxon pairs. In this case there is only one magnetic flux quantum directed along the field for every three vortex filaments, and the actual value of the induction is decreased by a factor of 3. Curve *4* in Fig. 4, which was plotted in accordance with the relation $B=\Phi_0/3L^2$, gives a rather good description of the data obtained in the experiment.

3. CONCLUSION

We have shown that, regardless of the type of conductivity or the presence of an excess or a shortage of the metallic component in the melt, PbTe single-crystal hosts contain inclusions of superconducting Pb. The minimum size of these microscopic Pb inclusions is roughly 1300 Å, and the concentration of Pb atoms in them is $(1-5)\times10^{18}$ cm^{-3}. The behavior of the diamagnetic component of the magnetic susceptibility of the Pb microinclusions is characterized by a phase transition that is characteristic of type-II superconductors (although extended Pb objects are characterized by first-order phase transitions). The Pb microinclusions are organized into one-dimensional chains of quantized vortex filaments in the region of the mixed-state of superconducting and normal phases with dimensions of the normal filament core of order 1300 Å.

[1)]The investigations of the diamagnetic contribution of superconducting inclusions of Pb to the overall magnetic susceptibility of a single-crystal PbTe host were carried out in the Institute of Physics of the Polish Academy of Sciences.

[2)]The authors are grateful to V.M. Lakeenkov for providing several crystals for our study.

[1]T. Kawakami and H. Takayanagi, Jpn. J. Appl. Phys. **26-3**, 2059 (1987).
[2]T. Matsuda, S. Hasegawa, M. Igarashi, T. Kobayashi, M. Naito, H. Kajiyama, J. Endo, N. Odakabe, A. Tonomura, and R. Aoki, Phys. Rev. Lett. **62**, 2519 (1989).
[3]T. T. Dedegkaev, V. A. Moshnikov, D. B. Chesnokova, and D. A. Yas'kov, Pis'ma Zh. Tekh. Fiz. **6**, 1030 (1980) [Sov. Tech. Phys. Lett. **6**, 443 (1980)].
[4]F. F. Sizov and S. V. Plyatsko, J. Cryst. Growth **92**, 571 (1988).
[5]A. Lenard, T. Dietl, M. Sawicki, W. Dobrowolski, K. Dybko, T. Skoskiwicz, S. Miotkowska, A. Witek, W. Plesiewicz, and A. Mycielski, J. Low Temp. Phys. **80**, 15 (1990).
[6]O. A. Mironov, B. A. Savitskiĭ, A. Yu. Sipatov, A. I. Fedorenko, A. N. Chirkin, S. V. Chistyakov, and L. P. Shpakovskaya JETP Lett. **48**, 106 (1988).
[7]S. Takaoka, T. Sugita, and K. Murase, Jpn. J. Appl. Phys. **26-3**, 1345 (1987).
[8]*The Physics of Superconductors: Introduction to Fundamentals and Applications*, edited by V. V. Schmidt, P. Muller, and A. V. Ustinov (Springer, New York, 1997).
[9]D. R. Tilley and J. Tilley, *Superfluidity and Superconductivity* (Van Nostrand Reinhold, 1974).
[10]D. Saint-James, G. Sarma, and E. J. Thomas, *Type II Superconductivity* (Pergamon Press, 1969).

Translated by Frank J. Crowne

Properties of manganese-doped gallium arsenide layers grown by liquid-phase epitaxy from a bismuth melt

K. S. Zhuravlev, T. S. Shamirzaev,*) and N. A. Yakusheva

Institute of Semiconductor Physics, Russian Academy of Sciences, Siberian Branch, 630090 Novosibirsk, Russia

(Submitted November 3, 1997; accepted for publication November 17, 1997)
Fiz. Tekh. Poluprovodn. **32**, 791–798 (July 1998)

The electrical and photoluminescence properties of p-GaAs : Mn(100) layers grown by liquid-phase epitaxy from a bismuth solvent at various temperatures are investigated. It is shown that such layers have a low concentration of background impurities and a low degree of electrical compensation up to a hole concentration of $p=1\times10^{18}$ cm^{-3} at 295 K. As the concentration of manganese in the liquid phase increases, the concentration of donors in the GaAs : Mn layers increases superlinearly, while the concentration of ionized acceptors increases sublinearly. This leads to an increase in the compensation factor. The donor and acceptor concentrations, as well as the degree of compensation, increase more slowly with increasing temperature. Reasons for the donor compensation are discussed from a crystal-chemical point of view, and it is shown that the preassociation of manganese and arsenic atoms in the liquid phase could be responsible for generating these compensated donors. It is postulated that the compensating donors are nonradiative recombination centers, whose concentration increases with increasing doping level more rapidly than does the concentration of Mn_{Ga} acceptors.
© *1998 American Institute of Physics.* [S1063-7826(98)00607-3]

1. INTRODUCTION

Gallium arsenide doped with manganese is a promising material for creating a number of semiconductor devices (photodetectors in the infrared region, resistive thermometers, etc.).[1–3] Improving the sensitivity of GaAs : Mn photodetectors requires not only a high concentration of Mn_{Ga} (manganese at a gallium site) acceptors, but also a low concentration of residual impurities and defects, which act as recombination centers, since these centers decrease the carrier lifetime and hence degrade the sensitivity of the photodetector.[1] In our view, the optimal method for obtaining an improved material might be liquid-phase epitaxy (LPE) from a bismuth melt, because the use of bismuth in the LPE of GaAs as an alternative metallic solvent to gallium makes it possible to grow high-purity low-compensation epitaxial layers with a lower content of residual impurities.[4] Moreover, impurities that incorporate into the Ga-sublattice of gallium arsenide[5] (in this case, Mn) are more soluble in bismuth. However, there is no information in the literature on the properties of GaAs : Mn epitaxial layers obtained by liquid-phase epitaxy from a bismuth melt.

In a previous article,[6] we established that radiative and nonradiative recombination centers form in GaAs : Mn grown by LPE from a bismuth melt in addition to Mn_{Ga} acceptors. The binding energy of charge carriers on the radiative recombination centers, which are probably impurity-defect complexes, was determined to be 41 ± 2 meV. Furthermore, it was shown that the concentration of these centers increases more rapidly than the concentration of Mn_{Ga} acceptors as the doping level increases.

In this paper we investigate the electrical properties of epitaxial layers of manganese-doped GaAs obtained by LPE from a bismuth melt. In addition, photoluminescence data are presented to confirm the results of Hall measurements.

2. EXPERIMENTAL METHOD

The GaAs : Mn layers investigated were grown on substrates of semi-insulating (100)-oriented GaAs in a stream of purified hydrogen at temperatures from 800 to 750 °C and from 700 to 640 °C by the method described previously.[4] For brevity, we shall indicate below only the initial growth temperature T_G. The dopant used was MN-00 elemental manganese, whose atomic fraction in the liquid phase X_{Mn} was varied from 4×10^{-5} to 1×10^{-2}. At higher manganese concentrations, the morphology of the surface layers degrades strongly, preventing removal of the solution-melt from it. All the layers doped with manganese had hole-type conductivity, whereas undoped GaAs layers obtained under analogous conditions were electronic conductors. The free-carrier concentration and mobility were determined from van der Pauw measurements of the resistivity and Hall constant. The Hall scattering factor for n-type conductivity layers was taken equal to unity, while for p-type layers it was set equal to 2.66 in accordance with the calculations carried out in Ref. 7 using a model that takes into account the expression for the light- and heavy-hole bands at the center of the Brillouin zone.

Steady-state photoluminescence spectra were measured on a setup built around a CDL-1 monochromator with a 600-line grating (the focal length was 600 mm, and the spectral resolution no worse than 0.2 meV). The photoluminescence was detected using a photomultiplier with an S-1 photocath-

 © 1998 American Institute of Physics

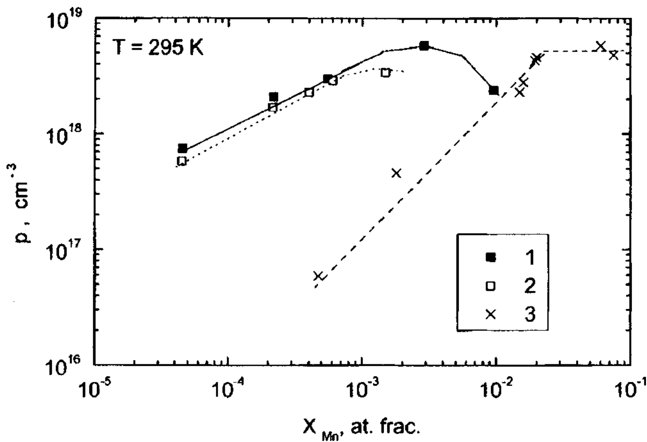

FIG. 1. Dependence of the hole concentration in GaAs : Mn layers at room temperature on manganese content in the liquid phase. T_G, °C: *1* — 700, *2* — 800, *3* — data from Ref. 8.

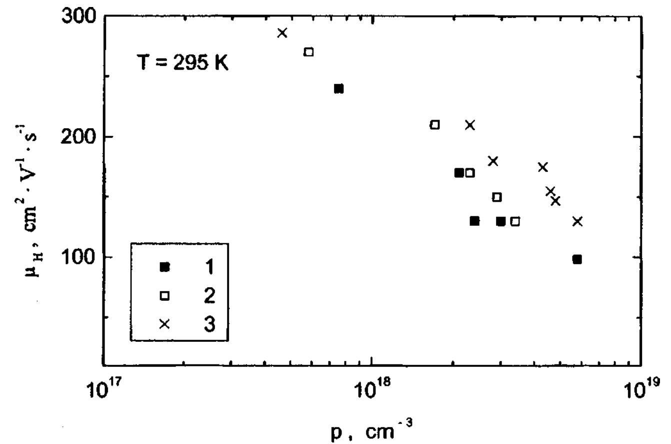

FIG. 2. Dependence of the Hall mobility of holes on their concentration in GaAs : Mn layers at room temperature. T_G, °C: *1* — 700, *2* — 800, *3* — data from Ref. 8.

ode in the photon-counting regime and excited by a He-Ne laser, whose excitation power density was 100 W/cm^2.

3. EXPERIMENTAL RESULTS AND ANALYSIS

Figure 1 shows plots of the dependence of the room-temperature hole concentration p in GaAs : Mn layers on the manganese content in the liquid phase for two series of samples grown at different temperatures. The figure also shows the analogous dependence for GaAs : Mn layers grown by LPE from a gallium melt in the temperature range from 850 to 820 °C, according to the data of P. Kordos *et al.* in Ref. 8.[1)] From this figure it is clear that the plots of $p=f(X_{\mathrm{Mn}})$ for the GaAs : Mn layers grown from a bismuth melt have a sublinear character, whereas the data in Refs. 8, as well as Refs. 7 and 9, indicate that the dependences for the GaAs : Mn layers grown from a gallium melt are nearly linear. The plots of $p=f(X_{\mathrm{Mn}})$ saturate at fairly large values of X_{Mn}; however, in layers obtained from a bismuth melt this saturation takes place at considerably lower values of X_{Mn} than in layers from a gallium melt. Nevertheless, the limiting doping levels are roughly the same in layers from either type of melt ($p\approx 6\times 10^{18}$ cm^{-3} at room temperature). Before the saturation region, the hole concentration in the layers obtained from a bismuth melt exceeds the concentration in the layers obtained from a gallium melt by more than an order of magnitude (for the same value of X_{Mn}). From the figure it is also clear that increasing the growth temperature from $T_G=700$ °C to $T_G=800$ °C increases the hole concentration in the layers grown from bismuth by roughly 20%.

Figure 2 shows the dependence of the Hall mobility μ_H on the hole concentration at room temperature in bismuth-grown layers, along with data from the paper by P. Kordos.[8] It is clear that μ_H decreases considerably more rapidly with increasing doping in the GaAs : Mn layers grown from bismuth than in the layers grown from gallium. In the layers grown from bismuth there is a slight increase (by $8-18\%$) in mobility when the growth temperature is increased from $T_G=700$ °C to $T_G=800$ °C.

The electrical parameters of the bismuth-grown layers are listed in Table I. Along with the values of the parameters determined experimentally (the free-electron concentration n, the hole concentration p, and the electron and hole Hall mobilities at two temperatures), this table also lists values of the concentrations of ionized donors (N_D^+) and acceptors (N_A^-) and the electrical compensation factor $K=N_D^+/N_A^-$ in GaAs : Mn layers at room temperature, which were estimated from the theoretically calculated dependences of the Hall mobility in p-GaAs on the concentration of free holes and impurity ions in Ref. 10. It is clear that K increases with increasing X_{Mn}, and the degree of compensation is lower for the series of samples grown at $T_G=800$ °C.

For clarity, Fig. 3 shows the dependences of N_A^- and N_D^+ (in relative units) on the manganese concentration in the liquid phase. As we see from this figure, the increase in the degree of compensation of the layers investigated here is caused by a superlinear (roughly quadratic) increase in the donor concentration with increasing X_{Mn} combined with a sublinear (roughly as $N_A^-\sim X_{\mathrm{Mn}}^{0.6}$) increase in the acceptor concentration. At higher growth temperatures the concentrations of both donors and acceptors are lower. Because the donor concentration depends more strongly on the growth temperature, the layers grown at $T_G=800$ °C exhibit less compensation.

In contrast to these results, the electrical compensation factor decreases with increasing doping level in the GaAs : Mn layers grown from a gallium melt. This is because the donor concentration varies only slightly[8] or even increases somewhat,[7,9] while the concentration of ionized acceptors increases.[2)]

The increase in the degree of compensation with increasing doping level is also manifested in the exciton photoluminescence spectra shown in Fig. 4. This figure reveals that the dominant feature in the spectrum of an undoped layer is the line for an exciton bound to a shallow neutral donor (D°,X).[11] In addition, we also observe lines for a free exciton polariton X, an exciton bound to a shallow charged donor (D^+,X), an exciton bound to a shallow neutral acceptor (A°,X), and an exciton bound to a donorlike defect (D_C,X).[11] In the spectrum of sample *2*, which has the lowest level of manganese doping, all the lines mentioned above

TABLE I. Electrical parameters of bismuth-grown layers as a function of growth conditions.

Sequence No.	T_G, °C	XMn	$p(n)$, cm^{-3} 77 K	$p(n)$, cm^{-3} 295 K	μ_H, $cm^2/V\cdot s$ 77 K	μ_H, $cm^2/V\cdot s$ 295 K	$K=N_D^+/N_A^-$	N_A^- for $T=295$ K, cm^{-3}	N_D^+ for $T=295$ K, cm^{-3}
1*	700	0	2.0×10^{14}	2.1×10^{14}	89 120	6840	–	$<10^{15}$	$<10^{15}$
2	700	4.53×10^{-5}	9.3×10^{13}	7.5×10^{17}	3340	240	0	7.5×10^{17}	$<10^{15}$
3	700	2.18×10^{-4}	6.5×10^{14}	2.1×10^{18}	1470	170	0.027	2.2×10^{18}	6.6×10^{16}
4	700	5.53×10^{-4}	1.3×10^{15}	3.0×10^{18}	1050	130	0.189	3.7×10^{18}	7.0×10^{17}
5	700	2.90×10^{-3}	1.9×10^{15}	5.8×10^{18}	560	98	0.420	1.0×10^{19}	4.2×10^{18}
6	700	9.58×10^{-3}	3.9×10^{14}	2.4×10^{18}	900	130	0.260	3.3×10^{18}	8.6×10^{17}
7*	800	0	1.4×10^{14}	1.5×10^{14}	117 000	7280	–	$<10^{15}$	$<10^{15}$
8	800	4.50×10^{-5}	1.4×10^{14}	5.8×10^{17}	4860	270	0	5.8×10^{17}	$<10^{15}$
9	800	2.15×10^{-4}	4.6×10^{14}	1.7×10^{18}	2050	210	0	1.7×10^{18}	$<10^{16}$
10	800	3.99×10^{-4}	–	2.3×10^{18}	–	170	0.004	2.3×10^{18}	1.0×10^{16}
11	800	6.02×10^{-4}	6.4×10^{14}	2.9×10^{18}	1040	150	0.033	3.0×10^{18}	1.0×10^{17}
12	800	1.49×10^{-3}	1.1×10^{15}	3.4×10^{18}	950	130	0.171	4.1×10^{18}	7.0×10^{17}

Note:*A sample with n-type conductivity.

remain; however, the relative intensity of the lines for excitons bound to shallow impurities decreases. In the spectrum of the more heavily doped sample *3* the lines for excitons bound to impurities are not resolved and appear only in the form of a long-wavelength shoulder on the *FX* line with a peak energy of 1.515 eV. The intensity of this line increases superlinearly with increasing excitation power density, attesting to its excitonic nature, while its energetic position allows us to associate it with the recombination of free excitons.[12,13] It can also be seen from the figure that the intensity of all of the exciton lines decreases strongly with increasing doping level (by more than two orders of magnitude in layer 3). In more heavily doped layers the exciton photoluminescence intensity decreases so much that it is difficult to say anything definite about its composition.

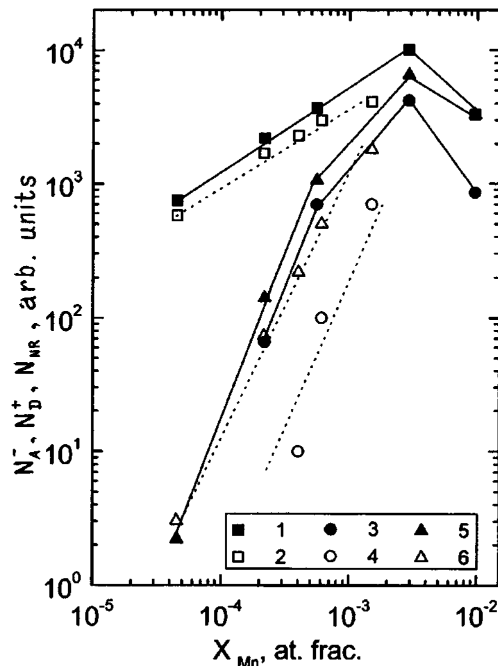

FIG. 3. Dependence of the concentration of acceptors (*1*, *2*) and donors (*3*, *4*) ionized at room temperature, as well as the concentration of nonradiative recombination centers (5,6), on the manganese concentration in the liquid phase. T_G, °C: *1*, *3*, *5* — 700; *2*, *4*, *6* — 800.

One reason why the relative intensity of the lines for excitons bound to shallow impurities decreases with increasing doping level could be the ionization of such excitons under the action of the built-in electric field generated by large-scale fluctuations in the spatial distribution of donors and acceptors. The ionization of excitons by an electric field is observed when the change in potential over a distance equal to the diameter of the exciton orbit [200 Å for $(D°,X)$ and 270 Å for $(A°,X)$ in GaAs; see Refs. 14 and 15] is comparable in order of magnitude to the ionization energy of the excitons,[16] the characteristic size of the built-in field region being larger than the diameter of the exciton orbit. Depending on the type and charge state of the impurity, the ionization energy of a bound exciton in GaAs varies in the range from 0.8 to 3.4 meV (see Refs. 17 and 18), which gives an ionization field E_i of order 200−500 V/cm.

In order to estimate the built-in field intensity in the

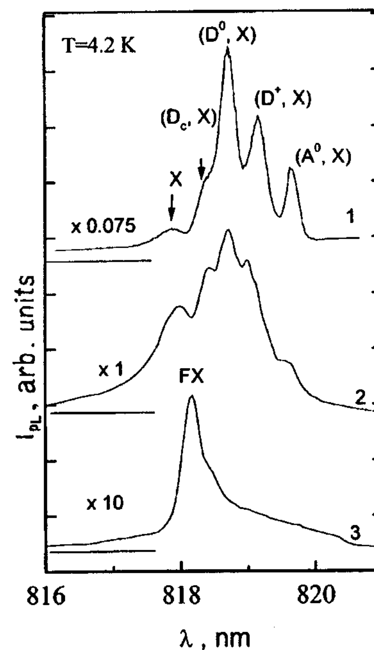

FIG. 4. Exciton portion of the photoluminescence spectra. The spectra are labeled according to the sample numbers in Table I.

bismuth-grown layers, we used the model proposed by Shklovskiĭ and Éfros.[19] The characteristic size of a built-in field region r, which coincides with the fluctuation screening radius, and its intensity E, are related to the total donor (N_D) and acceptor (N_A) concentrations by the following expressions:

$$r=0.58(N_A)^{1/6}/(N_D)^{1/2}, \quad (1)$$

$$E=0.26\cdot E_{\mathrm{Mn}}(N_D/N_A)^{1/4}/(e\cdot r)$$
$$=0.45\cdot E_{\mathrm{Mn}}\cdot N_A^{1/3}(N_D/N_A)^{3/4}/e, \quad (2)$$

where $E_{\mathrm{Mn}}=110$ meV (see Ref. 20) is the ionization energy of a $\mathrm{Mn_{Ga}}$ acceptor, and e is the electron charge.

The bismuth-grown layers have p-type conductivity; therefore, we can assume that $N_D=N_D^+$. Due to the large value of E_{Mn}, the concentration of ionized acceptors is much smaller than the total acceptor concentration even at room temperature. When we estimate the total concentration of acceptors in these layers by substituting the values of E_{Mn}, N_D^+, and p into the electroneutrality equation, we find that the acceptor concentration is approximately equal to $8\cdot N_A^-$ in layers 2 and 3. When this is taken into account, the computed values of the characteristic size of a built-in electric field region and its intensity are $r>300$ Å, $E<50$ V/cm in layer 2 and $r\approx 400$ Å, $E\approx$ 800 V/cm in layer 3, i.e., $E<E_i$ in layer 2 and $E>E_i$ in layer 3, while in both cases the value of r is greater than the diameter of the exciton orbit.

Thus, our estimate shows that the intensity of the built-in field turns out to be insufficient to ionize bound excitons in layer 2 and sufficient to do so in layer 3. This estimate agrees with the experimental results. However, if the degree of compensation for this acceptor concentration were the same in layer 3 as in layer 2, the ionization of acceptors bound to shallow impurities would not take place.

The possible candidates for the role of compensating donors include the radiative centers that we observed in our previous study[6] and nonradiative recombination centers.

We associate the D line in the photoluminescence spectrum of the bismuth-grown layers with the radiative recombination centers (R). This line overlaps strongly with the (e,Mn) line caused by the recombination of nonequilibrium charge carriers via levels of the acceptor $\mathrm{Mn_{Ga}}$. The concentration of R centers, like the concentration of donors, increases with the doping level more rapidly than the concentration of the acceptor $\mathrm{Mn_{Ga}}$. This follows from the increase in intensity of the D line relative to the intensity of the (e,Mn) line with increasing doping level.[6] However, following an increase the growth temperature of the layers, which leads to a considerable decrease in the donor concentration, we do not observe a change in the relative intensity of the D line. This is possibly because the D and (e,Mn) lines in the photoluminescence spectra overlap strongly, hindering any quantitative analysis of the intensities of these lines. Therefore, the question of whether the radiative recombination centers (R) are the donors which determine the electrical compensation in these layers remains open.

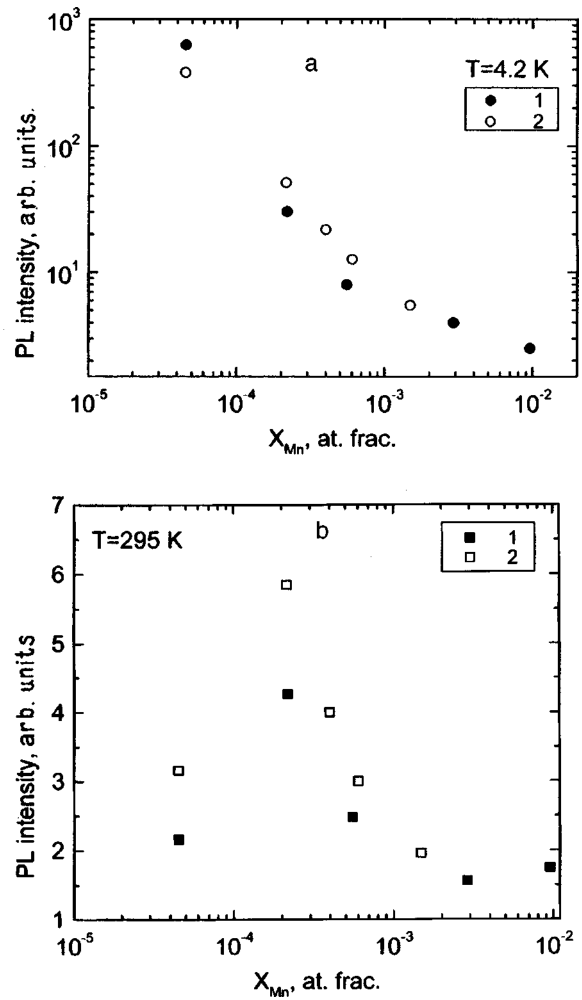

FIG. 5. Dependence of the integrated photoluminescence intensity of GaAs : Mn layers at 4.2 K (a) and 295 K (b) on the manganese concentration in the liquid phase. T_a, °C: *1* — 700, *2* — 800.

The presence of nonradiative recombination centers in the GaAs : Mn layers grown from a bismuth melt is confirmed by the data in Fig. 5a, which shows the dependence of the integrated photoluminescence intensity I_{PL} of the bismuth-grown layers at 4.2 K on manganese concentration in the liquid phase. It is clear that the integrated photoluminescence intensity falls off with increasing X_{Mn} by more than two orders of magnitude. However, at room temperature (see Fig. 5b) I_{PL} varies only by a factor of 3, while the plot of $I_{PL}=f(X_{\mathrm{Mn}})$ has a nonmonotonic character. From Figs. 5a and 5b it is also clear that the value of I_{PL} is higher for the layers grown at $T_G=800$ °C.

In order to determine how the concentration of nonradiative recombination centers (we shall refer to these as *NR* centers) depends on the doping level, we analyzed the concentration dependence of the integrated photoluminescence intensity of the bismuth-grown layers at liquid-helium temperature within the model proposed in Ref. 21.

It is clear from Fig. 1 of Ref. 6 that more than 90% of the integrated radiative recombination intensity in all the GaAs : Mn layers investigated is determined by recombination via levels of the acceptor $\mathrm{Mn_{Ga}}$. If we assume that the nonradiative recombination takes place primarily via *NR*

centers, we can construct the following system of equations to describe the recombination of charge carriers in these layers:

$$I_{NR}=\{C_{nNR}\cdot dn\cdot C_{pNR}(p+dp)N_{NR}\}/\{C_{nNR}\cdot dn + C_{pNR}[(p+dp)+A\cdot \exp(-E_{NR}/kT)]\} \quad (3)$$

for the number of charge carriers recombining via the NR centers per unit volume and

$$I_{\mathrm{Mn}}=\{C_{n\mathrm{Mn}}\cdot dn\cdot C_{p\mathrm{Mn}}(p+dp)N_{\mathrm{Mn}}\}/\{C_{n\mathrm{Mn}}\cdot dn + C_{p\mathrm{Mn}}[(p+dp)+A\cdot \exp(-E_{\mathrm{Mn}}/kT)]\} \quad (4)$$

for the intensity of the (e,Mn) line. In this case

$$L=I_{\mathrm{Mn}}+I_{NR}. \quad (5)$$

Here p is the equilibrium concentration of free holes; dn and dp are the concentrations of nonequilibrium electrons and holes, respectively; L is the number of electron-hole pairs generated per unit time (we take L to equal the integrated photoluminescence intensity at $T=4.2$ K for layer 2, in which the concentration of NR centers is minimal); k is the Boltzmann constant; N_{Mn}, N_{NR}, E_{Mn}, E_{NR}, $C_{n\mathrm{Mn}}$, $C_{p\mathrm{Mn}}$, C_{nNR}, and C_{pNR} are the concentration, binding energy, and capture coefficients of electrons and holes for the $\mathrm{Mn_{Ga}}$ and NR centers, respectively; and A is a constant. Since E_{Mn} and $E_{NR}\gg kT$ at $T=4.2$ K, assuming that $dp=dn\gg p$, we can write the ratio of Eqs. (4) and (3) at this temperature in the following form:

$$I_{\mathrm{Mn}}/I_{NR}=N_{\mathrm{Mn}}\cdot B/N_{NR}, \quad (6)$$

where $B=C_{n\mathrm{Mn}}\cdot C_{p\mathrm{Mn}}(C_{nNR}+C_{pNR})/[C_{nNR}\cdot C_{pNR}(C_{n\mathrm{Mn}}+C_{p\mathrm{Mn}})]$. Taking into account Eqs. (5) and (6), we can write the concentration of NR centers as

$$N_{NR}=N_{\mathrm{Mn}}\cdot B(L-I_{\mathrm{Mn}})/I_{\mathrm{Mn}}. \quad (7)$$

We can estimate the concentration of $\mathrm{Mn_{Ga}}$ from Hall measurement data, taking it to be proportional to the concentration N_A^- of acceptors ionized at room temperature. Then

$$N_{NR}\sim N_A^-\cdot B(L-I_{\mathrm{Mn}})/I_{\mathrm{Mn}}. \quad (8)$$

Figure 3 shows the dependence of the concentration of nonradiative recombination centers calculated from Eq. (8) on the concentration of manganese in the liquid phase. It is clear that the concentration of NR centers increases with increasing doping level more rapidly than the acceptor concentration. This finding is consistent with the nonmonotonic form of the plots of $I_{PL}=f(X_{\mathrm{Mn}})$ at room temperature (see Fig. 5b). At $T=4.2$ K, because the manganese acceptor level lies deep in the band gap, the concentration of holes does not increase with increasing X_{Mn} ($p\ll dp$), and the increase in the concentration of NR centers leads to abrupt quenching of the photoluminescence (see Fig. 5a). Conversely, at 295 K the concentration of holes increases with increasing X_{Mn}, leading to an increase in the integrated photoluminescence intensity at small values of X_{Mn} (there are still few nonradiative recombination centers). However, because the concentration of nonradiative recombination centers increases more rapidly than the concentration of acceptors (holes), as the doping level is further increased, the accompanying abrupt increase in the concentration of NR centers causes I_{PL} to begin to fall off.

Because the plots of $N_{NR}=f(X_{\mathrm{Mn}})$ are nearly quadratic, we can assume that the nonradiative recombination centers are complexes, the concentration of whose components depends on the concentration of manganese in the liquid phase (i.e., impurity-defect complexes). In this case, the concentration of NR centers increases symbatically with the donor concentration as the doping level is increased. Increasing the growth temperature of the layers decreases the concentration of nonradiative recombination centers along with the donor concentration. Thus, the dependences of the concentration of NR centers on the manganese concentration in the liquid phase and the growth temperature indicate that just these centers can be the donors which significantly influence the electrical compensation of the GaAs : Mn layers.

4. DISCUSSION OF RESULTS

As we expected, at a fixed value of X_{Mn} the concentration of holes in the bismuth-grown layers considerably exceeds the concentration of holes[7–9] in layers grown from gallium[3)] (by an order of magnitude or more for $X_{\mathrm{Mn}}\leqslant 10^{-3}$). This is due to the predictable increase in the distribution coefficient of manganese as an impurity incorporated into the Ga sublattice of GaAs when a bismuth solution-melt is used.[5] However, despite this fact, we were unable to obtain GaAs : Mn layers with $p>6\times 10^{18}$ cm^{-3}, i.e., with hole concentrations larger than those present in GaAs : Mn layers grown from a gallium melt. There are three reasons for this: first, the difference between the values of p in layers grown from different melts arising from the different behavior of the plots of $p=f(X_{\mathrm{Mn}})$ is reduced at large values of X_{Mn}; second, saturation of the plots of $p=f(X_{\mathrm{Mn}})$ begins at this doping level; and third, when $X_{\mathrm{Mn}}>1.5\times 10^{-3}$ for $T_G=800$ °C and when $X_{\mathrm{Mn}}>1\times 10^{-2}$ for $T_G=700$ °C, the smoothness of the surface layer is so degraded that it is not possible to completely remove it from the melt.

The presence of well-resolved exciton lines in the photoluminescence spectra of samples 2 and 8 indicates a low concentration of background impurities in the GaAs : Mn layers with $p\leqslant 1\times 10^{18}$ cm^{-3} grown from a bismuth solution-melt. This is in agreement with the high values of the Hall mobility for holes at 77 K and the low values of the compensation factors ($K<10^{-3}$) and donor concentrations ($N_D<10^{15}$ cm^{-3}) in these layers. However, with increasing doping level, the concentration of donors in GaAs : Mn layers undergoes a strong (superlinear) increase, which combines with the sublinear growth in the acceptor concentration to produce an increase in the degree of compensation.

Let us analyze possible reasons for the formation of compensating donors. The quite high purity of the manganese used and the small amount of it in the liquid phase (as a consequence of the high distribution coefficient during the growth of GaAs : Mn from a bismuth melt) with consideration of the values of the distribution coefficient of donor impurities in GaAs[5,22,23] rules out the assumption that the high concentration of donors in these layers at low values of

X_{Mn} is caused by some donor impurity introduced into the solution-melt by the manganese. This assumption is also contradicted by the superlinear (approximately quadratic) dependence of the donor concentration in the layers on the concentration of manganese in the liquid phase.

The doping of GaAs with manganese from a bismuth melt during LPE most likely leads to the formation of defects or impurity-defect complexes of donor type in the crystal lattice. The nearly quadratic character of the plots of $N_D = f(X_{\mathrm{Mn}})$ is also evidence of the formation of complexes. The composition of these impurity-defect complexes cannot be resolved within this work. However, it is obvious that their appearance is caused by specific features not only of the dopant, but also of the ensemble of intrinsic point defects of the crystal lattice that is characteristic of GaAs grown by liquid-phase epitaxy from a bismuth melt and the composition of the liquid phase during growth, because, as far as we know, an increase in the degree of compensation with increasing doping level and the appearance of the *D* line in the photoluminescence spectrum, which we also relate to the formation of impurity-defect complexes,[6] has not been observed in GaAs : Mn obtained by other methods.[20,24,25]

To explain this fact let us consider the processes that take place during the crystallization layers from the crystal-chemical point of view. It is known[26] that the preassociation of atoms that form a chemical compound can occur in the liquid phase. This preassociation becomes important at temperatures equal to the melting point T_F of the given compound, and as the temperature drops the probability of association increases. Manganese forms the following compounds with arsenic, all of whose melting points are above the temperature at which the layers were grown in our experiment: MnAs ($T_F = 935$ °C), $\mathrm{Mn_2As}$ ($T_F = 1029$ °C), and possibly $\mathrm{Mn_3As_2}$ ($T_F > 950$ °C).[27] In the LPE growth of GaAs : Mn from a gallium melt, where the liquid phase is more than 95% gallium atoms, which also form a compound with arsenic (GaAs) more refractory than any of the manganese compounds [T_F(GaAs) = 1238 °C, see Ref. 27], the probability of the association of Mn and As atoms is extremely low because the competing preassociation of As and Ga atoms is far more probable (nevertheless, in Ref. 8 x-ray analysis revealed that a $\mathrm{Mn_2As}$ phase is present in rapidly cooled Ca+GaAs+Mn solution-melts). However, when GaAs : Mn is grown from bismuth, which does not form chemical compounds with arsenic,[27] the concentration of Ga atoms in the liquid phase decreases to a few percent or less and is commensurate with the concentration of Mn atoms at high doping levels.[28] Under these conditions, the probability of the preassociation of Mn and As atoms is considerably increased.

If MnAs molecules are incorporated into the growing GaAs layer, then the Mn atoms obviously occupy positions in the Ga sublattice, where they become acceptors. The probability of incorporating molecules increases as the growth temperature decreases, as a result of which the concentration of acceptors is higher in the layers grown at $T_G = 700$ °C.

With increasing concentrations of manganese in the liquid phase, the probability of forming the more refractory molecules $\mathrm{Mn_2As}$ ($\mathrm{Mn_3As_2}$) in the melt becomes higher than the probability of forming MnAs. This implies that a significant portion of the Mn atoms are diverted to forming these compounds and do not participate in creating acceptor levels. As a result, when GaAs : Mn layers are grown from a bismuth melt, the plots of $p = f(X_{\mathrm{Mn}})$ and $N_A^- = f(X_{\mathrm{Mn}})$ have a sublinear character, in contrast to the LPE of GaAs : Mn from a gallium melt.[4)] This is probably the reason why a decrease in the hole concentration is observed in layer 6 at the highest values of X_{Mn}. Obviously, a considerable fraction of the Mn atoms in the form of $\mathrm{Mn_2As}$ ($\mathrm{Mn_3As_2}$) molecules remain in the liquid phase in this case, and hence the real value of X_{Mn} is lowered.

When molecules of $\mathrm{Mn_2As}$ or $\mathrm{Mn_3As_2}$ incorporate into the crystallizing layer, their incorporation should be accompanied by the generation of point defects in the GaAs crystal lattice or impurity-defect complexes, which also can act as compensating donors. If we assume that the manganese compounds $\mathrm{Mn_2As}$ or $\mathrm{Mn_3As_2}$ are responsible for the formation of donors, i.e., point defects in the lattice or impurity-defect complexes generated by them, then the concentration of donors should decrease with increasing growth temperature of the layers. This is observed in experiment, supporting our assumption. Furthermore, if $\mathrm{Mn_2As}$ or $\mathrm{Mn_2As_2}$ are responsible for the formation of donors, then since they are more refractory than MnAs, and the crystallization temperature of the layers consequently affects the probability of the formation of molecules of these compounds in the liquid phase to a larger extent than that of MnAs, the electrical compensation factor of p-GaAs : Mn layers should increase with decreasing growth temperature, because, according to the logic of our discussion, it is determined by the ratio of the probabilities of the formation of $\mathrm{Mn_2As}$ ($\mathrm{Mn_3As_2}$) and MnAs molecules. This is also observed in experiment.

Thus, it follows from our analysis that the appearance of complexing donors in p-GaAs : Mn layers grown by LPE from a bismuth melt is due to changes in the composition of the liquid phase during the growth of the layer, or, more precisely, to a decrease by almost two orders of magnitude in the concentration of gallium in the solution-melt compared with epitaxy from a gallium melt. As we have said above, the compensating donors obviously consist of impurity-defect complexes and are probably nonradiative recombination centers. To decrease their concentration, the epitaxy temperature of the layers should be raised as much as possible.

5. CONCLUSION

Our studies show that, despite the increased distribution coefficient of the manganese dopant when a gallium solution-melt is replaced by a bismuth solution-melt, we are unable to obtain p-GaAs : Mn layers from a bismuth melt with a higher hole concentration than from the gallium melt. The layers of GaAs weakly and moderately doped with manganese[5)] (up to $p = 1 \times 10^{18}$ cm^{-3} at 395 K) that were grown from a bismuth solution-melt have a low concentration of background impurities and a high degree of electrical compensation. However, with increasing doping levels, the concentration of donors in the GaAs : Mn layers grown from a bismuth melt, in contrast to the GaAs : Mn layers grown

from a gallium melt, undergoes a sharp (superlinear) increase, which, when combined with a sublinear increase in the concentrations of acceptors, leads to an increase in the compensation factor. Increasing the growth temperature decreases the concentration of acceptors, donors, and holes at room temperature, as well as the degree of electrical compensation in GaAs : Mn layers grown from a bismuth melt.

We have analyzed the reasons for the formation of complexing donors, which are obviously impurity-defect complexes, from the crystal-chemical standpoint, and we have shown that the preassociation of manganese and arsenic atoms in the liquid phase could be responsible for their formation. The compensating donors are probably nonradiative recombination centers, whose concentration increases more rapidly as the doping level increases than does the concentration of Mn_{Ga} acceptors.

The authors are grateful to V. G. Pogadaev for help in growing the epitaxial layers.

*)E-mail tim@ns.isp.nsc.ru

1)In determining the hole concentration, Kordos *et al.*[8] set the Hall scattering factor equal to 1 instead of the value of 2.66 that we used. Therefore, the values of the hole concentration taken from Ref. 8 were multiplied by 2.66 before plotting in order to properly compare the two data sets.

2)In the papers cited here, the electrical parameters of the layers were determined from an analysis of the temperature dependences of the resistivity and Hall constant in the interval 60−300 K, which differs from our procedure. Therefore, rather than compare the absolute values of these parameters reported in those papers with our own, we note only the qualitative difference in behavior. We argue that this difference is unrelated to the different methods used to estimate the parameters, since the Hall mobility in our layers falls off more rapidly with increasing doping level than in the layers grown from a gallium melt.

3)In Ref. 8 the authors did not take into account the degeneracy of the valence band in determining the hole concentration; therefore, in comparing the results of Ref. 8 with ours the values of p in Ref. 8 should be multiplied by 2.66.

4)The experimentally observed behavior of these functions in the vicinity of $x=y^{0.5}$ is unrelated to the fact that when GaAs : Mn layers are grown from a bismuth melt the liquid phase is in equilibrium with the bulk of the semiconductor, rather than with its surface,[23] since when GaAs is doped with zinc, which diffuses more rapidly into GaAs as an impurity than does manganese,[29,30] during LPE from a bismuth melt, linear plots of $p=f(X_{Zn})$ are obtained at the same growth temperatures.[31]

5)It is important to remember that because we have included the degeneracy of the valence band, our values of p are 2.66 times larger than they would be if degeneracy is ignored (as in most of the papers cited).

1. V. V. Antonov, A. V. Voĭtsekhovskiĭ, M. A. Krivov, E. V. Malisova, É. N. Mel'chenko, V. S. Morozov, M. P. Nikiforova, E. A. Popova, and S. S. Khludkov, *Semiconductor Doping* (Nauka, Moscow, 1982), p. 32.
2. P. Kordos, L. Jansak, and V. Benc, Cryogenics **5**, 312 (1973).
3. L. Jansak and P. Kordos, Cryogenics **8**, 467 (1974).
4. N. A. Yakusheva, K. S. Zhuravlev, S. I. Chikichev, and O. A. Shegaj, Cryst. Res. Technol. **24**, 235 (1989).
5. N. A. Yakusheva, in *Abstracts from Proceedings of the 6th All-Union Conference on Physical-Chemical Fundamentals of the Doping of Semiconductor Materials* [in Russian] (Nauka, Moscow, 1988), p. 51.
6. K. S. Zhuravlev, T. S. Shamirzaev, and N. A. Yakusheva, Fiz. Tekh. Poluprovodn. **32**, 50 (1998) [Semiconductors **32**, 43 (1998)].
7. L. Gouskov, S. Bilac, J. Pimentel, and A. Gouskov, Solid-State Electron. **20**, 653 (1977).
8. P. Kordos, L. Jansak, and V. Benc, Solid-State Electron. **18**, 223 (1975).
9. S. Bilac, Z. P. Arguello, C. A. Arguello, and R. C. C. Leite, Solid-State Electron. **25**, 755 (1978).
10. V. G. Polovinkin, Preprint 9–84, Novosibirsk, 1984.
11. U. Heim and P. Hiesinger, Phys. Solid State **66**, 461 (1974).
12. J. Lee, E. S. Koteles, M. O. Vassell, and J. P. Salerno, J. Lumin. **34**, 63 (1985).
13. L. Schulthtis and C. W. Tu, Phys. Rev. B **32**, 6978 (1985).
14. F. Dujardin and B. Stebe, Phys. Status Solidi B **140**, K117 (1987).
15. M. Suffczynski and L. Wolniewicz, Phys. Rev. B **40**, 6250 (1989).
16. R. S. Knox, *Theory of Excitons (Solid State Physics, Suppl. 5)* (Academic Press, New York, 1963) [Mir, Moscow, 1966].
17. D. D. Sell, S. E. Stokowski, R. Dingle, and J. V. DiLorenzo, Phys. Rev. B **7**, 4568 (1973).
18. B. M. Ashkinadze, V. V. Bel'kov, and A. G. Krasinskaya, Fiz. Tekh. Poluprovodn. **24**, 883 (1990) [Sov. Phys. Semicond. **24**, 555 (1990)].
19. B. I. Shklovskiĭ and A. A. Éfros, *Electronic Properties of Doped Semiconductors* (Springer-Verlag, New York, 1984) [Nauka, Moscow, 1979].
20. M. Ilegems, R. Dingle, and L. W. Rupp, Jr., J. Appl. Phys. **46**, 3059 (1975).
21. K. D. Glinchuk, A. V. Prokhorovich, V. E. Rodionov, and V. I. Vovnenko, Phys. Status Solidi A **48**, 593 (1978).
22. V. M. Andreev, L. M. Dolginov, and D. N. Tret'yakov, *Liquid-Phase Epitaxy in the Fabrication of Semiconductor Devices* [in Russian] (Sov. Radio, Moscow, 1975).
23. H. C. Casey, Jr. and M. B. Panish, *Heterostructure Lasers, Part B: Materials and Operating Characteristics* (Mir, Moscow, 1981).
24. P. W. Yu and Y. S. Park, J. Appl. Phys. **50**, 1097 (1979).
25. L. Montelius, S. Nilsson, and L. Samuelson, Phys. Rev. B **40**, 5598 (1989).
26. S. A. Stroitelev, *Crystal-Chemical Aspects of Semiconductor Technology* [in Russian] (Nauka, Novosibirsk, 1976).
27. M. Hansen and K. Anderko, *Constitution of Binary Alloys* (McGraw-Hill, New York–Toronto–London, 1958).
28. N. A. Yakusheva and S. I. Chikichev, Izv. Akad. Nauk SSSR, Neorg. Mater. **23**, 1607 (1987).
29. T. D. Dzhafarov, *Defects and Diffusion in Epitaxial Structures* [in Russian] (Nauka, Leningrad, 1978).
30. S. M. Sze, *Physics of Semiconductor Devices*, Vol. 1 (Wiley, New York, 1969) [Mir, Moscow, 1984].
31. V. G. Pogadaev and N. A. Yakusheva, Elektron. Tekh. Mater., **5** (250), 48 (1990).

Translated by Frank J. Crowne

Calculation of the energy levels of shallow acceptors in uniaxially strained germanium

M. A. Odnoblyudov and V. M. Chistyakov

A. I. Ioffe Physicotechnical Institute, Russian Academy of Sciences, 194021 St. Petersburg, Russia
(Submitted October 29, 1997; accepted for publication December 23, 1997)
Fiz. Tekh. Poluprovodn. **32**, 799–802 (July 1998)

A variational method is used to calculate the positions of resonant and localized energy levels of a shallow acceptor impurity in uniaxially compressed germanium in the high-pressure limit. The dependence of the positions of these levels on the applied pressure is presented. © *1998 American Institute of Physics.* [S1063-7826(98)00707-8]

1. INTRODUCTION

The problem of calculating the position of energy levels of shallow acceptors in strained semiconductors has taken on special importance due to the observation of stimulated emission in the far-infrared region from p-Ge subjected to uniaxial compression.[1] It is assumed that the stimulated emission is caused by optical transitions of holes between various states of shallow acceptors and is connected with the formation of resonant acceptor states, i.e., acceptor states that move into the continuous spectrum of the valence band under the action of uniaxial strain. In order to confirm this hypothesis, information is needed about the positions of localized and resonant acceptor levels in strained germanium. The calculations of Ref. 2, which were done within the zero-radius potential model, showed that resonant states exist in this system, and their energies and lifetimes were found. However, the results given by this method are too approximate to describe the real situation with regard to the positions of levels at high pressures. Furthermore, the zero-radius potential method cannot give the energies of excited states. The variational calculations of Ref. 3 make it possible to calculate the energies of localized states with good accuracy; however, they cannot predict even the presence of resonant states. This is probably because the variational method cannot be used to follow the transformation of a localized state into a resonant state.

In this paper we study acceptor levels in the high-strain limit, calculating energies for the ground state and several excited states for both localized and resonant series. We use a variational method that presupposes the existence of resonant states and treats them as if they were localized in the calculation.

2. THEORY

In the spherical approximation with an applied uniaxial strain, the valence band is described by the 4×4 Luttinger Hamiltonian:[4,5]

$$H(\mathbf{k},\zeta)=-\frac{\hbar^2}{2m_0}\begin{bmatrix} a_+ & b & c & 0\\ b^* & a_- & 0 & c\\ c^* & 0 & a_- & -b\\ 0 & c^* & -b^* & a_+\end{bmatrix}, \quad (1)$$

where

$$a_+=-(\gamma_1-2\gamma)k_z^2-(\gamma_1+\gamma)(k_x^2+k_y^2)-\zeta,$$
$$a_-=-(\gamma_1+2\gamma)k_z^2-(\gamma_1-\gamma)(k_x^2+k_y^2)+\zeta,$$
$$b=2\sqrt{3}\gamma(k_x-ik_y)k_z,$$
$$c=\sqrt{3}\gamma(k_x-ik_y)^2,\quad \gamma=(2\gamma_2+3\gamma_3)/5. \quad (1a)$$

In writing Eq. (1) we have chosen the following system of basis Bloch functions:

$$u_{3/2}=\frac{1}{\sqrt{2}}(X+iY)\uparrow,\quad u_{1/2}=\frac{i}{\sqrt{6}}((X+iY)\downarrow-2Z\uparrow),$$
$$u_{-3/2}=\frac{1}{\sqrt{2}}(X-iY)\downarrow,$$
$$u_{-1/2}=\frac{1}{\sqrt{6}}((X-iY)\uparrow+2Z\downarrow). \quad (2)$$

The diagonalization of the Hamiltonian (1) gives us the spectrum of the valence band, which consists of heavy-hole (ε_h) and light-hole (ε_l) subbands, whose peaks are separated in energy by the quantity

$$E_{\text{def}}=\frac{\hbar^2\zeta}{m_0}=bX, \quad (3)$$

where b is the deformation potential and X is the applied pressure. The spectrum of the valence band of the strained crystal has the form

$$\varepsilon_{l,h}(\mathbf{k})=-\frac{\hbar^2}{2m_0}(-\gamma_1(k_x^2+k_y^2+k_z^2) \pm\sqrt{\zeta^2-2\gamma\zeta(k_z^2-k_x^2-k_y^2)+4\gamma^2(k_x^2+k_y^2+k_z^2)^2}). \quad (4)$$

In the high-strain limit, we can ignore terms higher than quadratic in k under the radical and expand the root in a series with respect to the small parameter (k^2/ζ). In this limit we obtain a valence-band spectrum consisting of two independent ellipsoidal subbands:

$$\varepsilon_l(\mathbf{k})=\frac{\hbar^2}{2m_0}((\gamma_1+2\gamma)k_z^2+(\gamma_1-\gamma)(k_x^2+k_y^2)-\zeta),$$

 © 1998 American Institute of Physics

$$\varepsilon_h(\mathbf{k}) = \frac{\hbar^2}{2m_0}((\gamma_1 - 2\gamma)k_z^2 + (\gamma_1+\gamma)(k_x^2+k_y^2)+\zeta). \quad (5)$$

The high-strain limit corresponds to a transition from a four-component basis (2) to two two-component sets of basis Bloch functions, viz.,

$$[u_{+3/2},\ u_{-3/2}], \quad (6a)$$

$$[u_{+1/2},\ u_{-1/2}], \quad (6b)$$

i.e., elimination of the terms in the Hamiltonian (1) that correspond to the interaction of states with different values of the hole spin projection onto the z axis.

When the potential of a shallow acceptor impurity is present in the strained crystal, we have two series of acceptor levels below the bottom of each subband. The states below the bottom of the heavy-hole subband are resonant states. The wave functions of holes localized on shallow acceptors have the form

$$\varphi^l_{3/2}(\mathbf{r}) = f^l(\mathbf{r})u_{3/2}(\mathbf{r}); \quad \varphi^l_{-3/2}(\mathbf{r}) = f^l(\mathbf{r})u_{-3/2}(\mathbf{r});$$

$$\varphi^h_{1/2}(\mathbf{r}) = f^h(\mathbf{r})u_{1/2}(\mathbf{r}); \quad \varphi^h_{-1/2}(\mathbf{r}) = f^h(\mathbf{r})u_{-1/2}(\mathbf{r}); \quad (7)$$

where the labels l and h are used to denote wave functions in the light- and heavy-hole subbands, respectively. The effective-mass equations for determining the wave functions and energy levels of a shallow impurity center written in the basis (6a) for the heavy-hole subband and in basis (6b) for the light-hole subband have the form

$$\left(\frac{\hbar^2}{2m^l_\parallel}\frac{\partial^2}{\partial z^2} + \frac{\hbar^2}{2m^l_\perp}\left(\frac{\partial^2}{\partial x^2}+\frac{\partial^2}{\partial y^2}\right) + \frac{e^2}{\kappa r} + E\right)f^l = 0, \quad (8a)$$

$$\left(\frac{\hbar^2}{2m^h_\parallel}\frac{\partial^2}{\partial z^2} + \frac{\hbar^2}{2m^h_\perp}\left(\frac{\partial^2}{\partial x^2}+\frac{\partial^2}{\partial y^2}\right) + \frac{e^2}{\kappa r} + E\right)f^h = 0. \quad (8b)$$

We introduce the dimensionless parameter $\eta = m_\perp/m_\parallel$, dimensionless coordinates in units of the Bohr radius $a_B = \hbar^2\kappa/m_\perp e^2$, and a dimensionless energy in units of $E_B = m_\perp e^4/2\hbar^2\kappa$ (where κ is the dielectric constant). Then Eq. (8) can be rewritten in the form

$$\left(\eta^{l,h}\frac{\partial^2}{\partial z^2} + \frac{\partial}{\partial x^2} + \frac{\partial^2}{\partial y^2} + \frac{2}{r} + E\right)f^{l,h} = 0. \quad (9)$$

If the internal angular momentum of the hole is ignored, the eigenstates of the Hamiltonian (9) are characterized by the projection of the orbital angular momentum (m) onto the z axis and the parity (i). The problem of finding the eigenvalues of the Hamiltonian (9) was discussed in Ref. 6 in connection with finding the spectrum of shallow donors in silicon and germanium. The high-strain limit, for which Eqs. (8a) and (8b) are valid, can be introduced by assuming that $E_{\rm def} > E$, i.e., the magnitude of the strain-induced splitting of the peaks of the valence band should be larger than the ionization energy of the impurity center.

Following Ref. 6, we used the variational method to calculate the energies of the four lowest localized states below the bottom of the ellipsoidal band, which we denote by $1s$, $2p_{\pm 1}$, $2p_0$, and $2s$, where $1s$ is the state with $m=0$, $i=+1$; $2p_{\pm 1}$ is the state with $m=\pm 1$, $i=-1$; $2p_0$ is the state with $m=0$, $i=-1$; and $2s$ is the state with $m=0$, $i=+1$. A diagram of the positions of these levels is shown in Fig. 1. In these calculations we used the following values for the effective masses: $m_\parallel/m_0 = 0.04$, $m_\perp/m_0 = 0.13$ (for the light-hole subband), $m_\parallel/m_0 = 0.5$, $m_\perp/m_0 = 0.05$ (for the heavy-hole subband). We also used the following values for η^l and η^h: $\eta^l = 3.25$, $\eta^h = 0.1$. These values correspond to the high-strain limit for Ge.[5] In these calculations we used the variational functions listed in Table I.

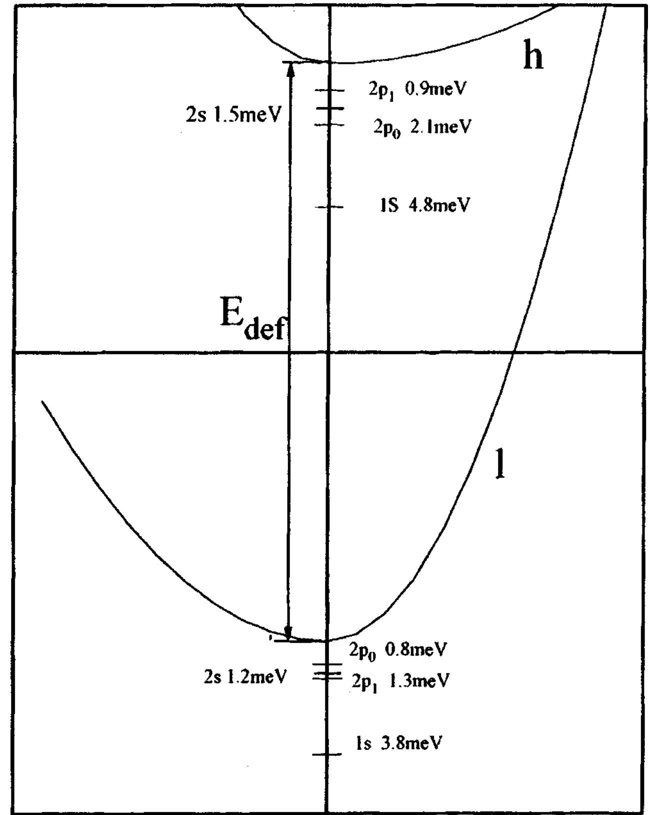

FIG. 1. Diagram of the energy levels of a shallow acceptor impurity in uniaxially compressed germanium. The classification of the levels corresponds to the high-strain limit.

3. RESULTS

By calculating the shallow-acceptor spectrum for Ge in the high-strain limit, we obtained the energy levels listed in Table II. In the second column we list the energies of states localized below the bottom of the light-hole subband, and in the third column the energies of resonant states below the bottom of the heavy-hole subband. The energies of the states are measured from the top of the respective subband. Bearing in mind that the states below the bottom of the h subband are resonant states, we calculated the energetic positions of the resonant levels. When the interaction between the subbands is taken into account, the states that are localized within our approximation become embedded in the continuous spectrum of the l subband, and we should introduce the interaction of these states with states of the continuous spectrum, i.e., the possibility of decay. Localized states then become quasilocal. Furthermore, there is an interaction with localized

TABLE I.

State	Trial function: f^l, f^h $F(\rho,z)=\exp\left(-\left(\frac{\rho^2}{a^2}+\frac{z^2}{b^2}\right)^{1/2}\right)$
$1s$	$CY_{00}(\theta,\varphi)F(\rho,z)=\tilde{C}\exp\left(-\left(\frac{\rho^2}{a^2}+\frac{z^2}{b^2}\right)^{1/2}\right)$
$2p_0$	$CY_{10}(\theta,\varphi)rF(\rho,z)=\tilde{C}z\exp\left(-\left(\frac{\rho^2}{a^2}+\frac{z^2}{b^2}\right)^{1/2}\right)$
$2s$	$(C_1Y_{00}(\theta,\varphi)+C_2Y_{20}(\theta,\varphi)r^2)F(\rho,z)$ $=(\tilde{C}_1+\tilde{C}_2\rho^2+\tilde{C}_3z^2)\exp\left(-\left(\frac{\rho^2}{a^2}+\frac{z^2}{b^2}\right)^{1/2}\right)$
$2p_{\pm1}$	$CY_{1\pm1}(\theta,\varphi)rF(\theta,\varphi)$ $=\tilde{C}(x\pm iy)\exp\left(-\left(\frac{\rho^2}{a^2}+\frac{z^2}{b^2}\right)^{1/2}\right)$

states in the band gap, which leads to a shift in the positions of the resonant levels. Figure 2 shows the dependence of the positions of the localized and resonant states on the pressure.

With spin taken into account, each state is characterized by the projection of the total angular momentum (orbital and internal: $M=L_z+J_z$) onto the z axis. For a hole in the l subband, the projection of the internal angular momentum onto the z axis equals $\pm1/2$, while in the h subband it is $\pm3/2$, and the energy levels found correspond to the following states within this classification:

l subband	h subband
$1s\rightarrow M=\pm1/2$,	$1s\rightarrow M=\pm3/2$,
$2p_{\pm1}\rightarrow M=\pm1/2,\ \pm3/2$,	$2p_{\pm1}\rightarrow M=\pm1/2,\ \pm5/2$,
$2s\rightarrow M=\pm1/2$,	$2s\rightarrow M=\pm3/2$,
$2p_0\rightarrow M=\pm1/2$,	$2p_0\rightarrow M=\pm3/2$.

TABLE II.

State	Energy of localized states above the bottom of the l subband, meV	Energy of resonant states above the bottom of the h subband, meV
$1s$	3.8	4.76
$2p_{\pm1}$	1.3	0.9
$2s$	1.2	1.53
$2p_0$	0.8	2

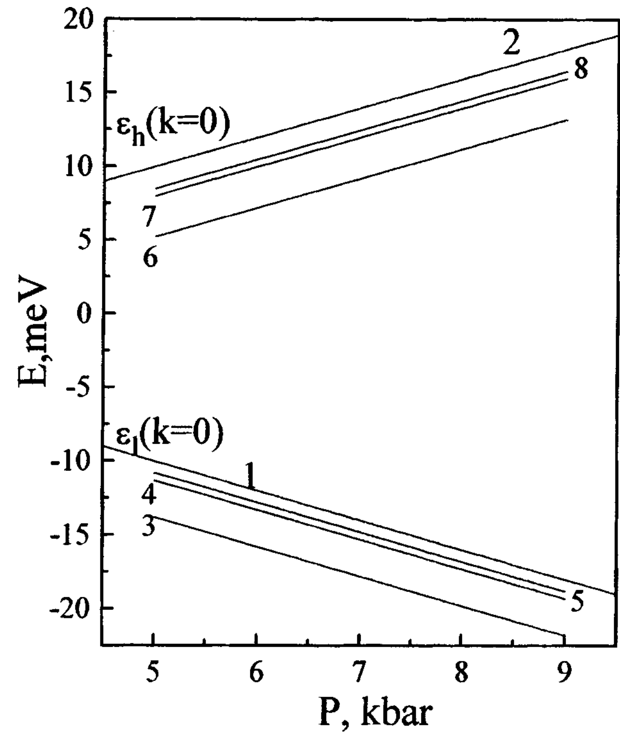

FIG. 2. Pressure dependence of the positions of shallow acceptor impurity levels in uniaxially compressed germanium: positions of the tops of the subbands for light (*1*) and heavy (*2*) holes; the series of localized states (*3* — $1s$, *4* — $2p_1$, *5* — $2p_0$), and the series of resonant states (*6* — $1s_{\rm res}$, *7* — $2p_{0\rm res}$, *8* — $2s_{\rm res}$). The position of the top of the valence band in the unstressed semiconductor is taken as the energy reference point.

The fourfold degeneracy with respect to the projection of the total angular momentum onto the z axis corresponding to the $2p_\pm$ level is lifted when we take into account the interaction between the h and l subbands.

Thus, in this paper we have described a simple calculation, which gives us information about the positions of resonant and localized levels in uniaxially strained Ge in the high-strain limit. In view of the lack of computational data regarding the positions of the resonant levels, even calculations as crude as these can be useful for analyzing experimental data on the spectra of shallow acceptor impurities in strained semiconductors.

This work was carried out with the partial support of Grants Nos. 97-02-16820 and 96-15-96392 from the Russian Fund for Fundamental Research and Grant No. (072) 97-1055 from the Ministry of Science.

[1] I. V. Altukhov, M. S. Kagan, K. A. Korolev, V. P. Sinis, and F. A. Smirnov, Zh. Éksp. Teor. Fiz. **101**, 756 (1992) [Sov. Phys. JETP **74**, 404 (1992)].

[2] M. A. Odnoblyudov, V. A. Chistyakov, and I. N. Yassievich, Fiz. Tekh. Poluprovodn. **31**, 1180 (1997) [Semiconductors **31**, 1014 (1997)].

[3] R. Buczko, Nuovo Cimento **9**, 669 (1987).

[4] J. M. Luttinger and W. Kohn, Phys. Rev. **97**, 869 (1955).

[5] G. L. Bir and G. E. Pikus, *Symmetry and Strain-Induced Effects in Semiconductors* (Wiley, New York, 1975) [Russian original, Nauka, Moscow, 1972].

[6] J. M. Luttinger and W. Kohn, Phys. Rev. **98**, 915 (1955).

Translated by Frank J. Crowne

Effect of metal impurities on the drift mobility of charge carriers in glassy chalcogenide semiconductors

L. P. Kazakova and É. A. Lebedev

A. I. Ioffe Physicotechnical Institute, Russian Academy of Sciences, 194021 St. Petersburg, Russia

(Submitted December 29, 1997; accepted for publication December 31, 1997)
Fiz. Tekh. Poluprovodn. **32**, 803–805 (July 1998)

The drift mobility of charge carriers in glassy semiconductors of the Se–As system doped with Ag, Au, and Tl is investigated. A considerable increase in the electron drift mobility is established in samples doped with Ag. These results are explained within a model of charged defects. © *1998 American Institute of Physics.* [S1063-7826(98)00807-2]

Studies of the optical and electrical properties of glassy chalcogenide semiconductors of the Se–As system indicate that the origin of the localized states that control the drift mobility of charge carriers in these systems is connected with charged defects.[1,2] The concentration of intrinsic charged defects can be controlled by doping with impurities capable of forming charged states.[2,3] We previously found[4,5] that the introduction of halogens, which appear as electrically negative impurities, into glassy chalcogenide semiconductors can lead to a considerable increase in the hole drift mobility.

In this paper we investigate the drift mobility of charge carriers in glassy chalcogenide semiconductors of the Se–As system doped with the metals Ag, Au, and Tl. We shall assume that these metals, in contrast to halogens, can behave as electrically positive impurities. Silver as an impurity is of special interest, since it is associated with phenomena such as negative photoconductivity,[6] memory effects, and switching.[7]

Impurities were introduced during synthesis in concentrations in the range 0.1–5.7 at. %. Measurements were made on samples of the ''sandwich'' type consisting of both layers prepared by mechanical methods from an ingot of the synthesized material and thin films obtained by thermal evaporation in vacuum. Al, In_2O_3, and Aquadag served as electrode materials. One of the electrodes was semitransparent. The concentration of impurities in the films was taken to equal its weighed content.

The drift mobility was investigated by time-of-flight measurements.[8,9] Since the shape of the time dependence of the photocurrent in glassy chalcogenide semiconductors of the Se–As system with metal impurities is typical of dispersive transport, the time of flight t_T was determined from the break on the $I(t)$ curve plotted in log-log coordinates.[10] The drift mobility was calculated from the expression $\mu = L/t_T F$, where L is the sample thickness and F is the electric field intensity.

Figure 1 shows the measured time dependence of the photocurrent for layers of $Se_{0.95}As_{0.05}$ containing 5.7 at. % Ag. The time of flight is marked by the arrows. It is clear that the introduction of silver as an impurity changes the time of flight of the charge carriers. For holes t_T increases, while for electrons it decreases. Accordingly, the hole mobility decreases from 2×10^{-4} to $2\times10^{-5}\,\mathrm{cm^2/V\cdot s}$, while the electron mobility increases from 6×10^{-5} to $1.1\times10^{-3}\,\mathrm{cm^2/V\cdot s}$.

A similar change in the hole mobility is observed in As_2Se_3 when Ag and Tl were introduced as impurities (Fig. 2). Electrons are practically immobile in this material. Doping decreases the hole drift mobility from $1.5\times10^{-5}\,\mathrm{cm^2/V\cdot s}$ in the pure material to $3\times10^{-6}\,\mathrm{cm^2/V\cdot s}$ and $6\times10^{-7}\,\mathrm{cm^2/V\cdot s}$ for As_2Se_3 with 2 at. % Ag and 0.1 at. % Tl, respectively. Moreover, the introduction of Au as an impurity also led to a decrease in the hole mobility. For a gold concentration of 0.2 at. % the value of the mobility was $5\times10^{-6}\,\mathrm{cm^2/V\cdot s}$.

Temperature measurements showed that the activation energy for conduction changes considerably (by 0.2 eV) when silver is introduced. At the same time, the activation energy for carrier drift mobility scarcely varied. In layers of $Se_{0.95}As_{0.05}$ with Ag as an impurity, the activation energy for electron and hole drift mobility lies in the range 0.45 − 0.48 eV, whereas the activation energy for drift mobility in bulk samples of As_2Se_3 with Ag as an impurity is $E\simeq0.6$ eV for holes. The higher values of the activation energy in the latter case are probably due to the dispersive character of transport in As_2Se_3, for which the drift mobility is found to depend on the sample thickness.[9]

A change in drift mobility upon doping can arise from a change in the concentration of the localized states that control its value. Assuming that the drift mobility is controlled by a discrete energy level of localized states, we expect its value to be given by the following expression:[11] $\mu=\mu_0(N_c/N_t)\exp(-\varepsilon/kT)$, where μ_0 is the charge-carrier mobility in the band of delocalized states, N_c and N_t are the effective densities of delocalized and localized states, respectively, and ε is the distance between the level of the localized-states and the edge of the band of the delocalized states. If the nature of the localized states is connected with charged defects similar to D^+ and D^- centers, then the value of the electron drift mobility is inversely proportional to the concentration of D^+ centers, and the hole mobility is inversely proportional to that of D^- centers.

If we assume that metals act as charged impurities,[2,3]

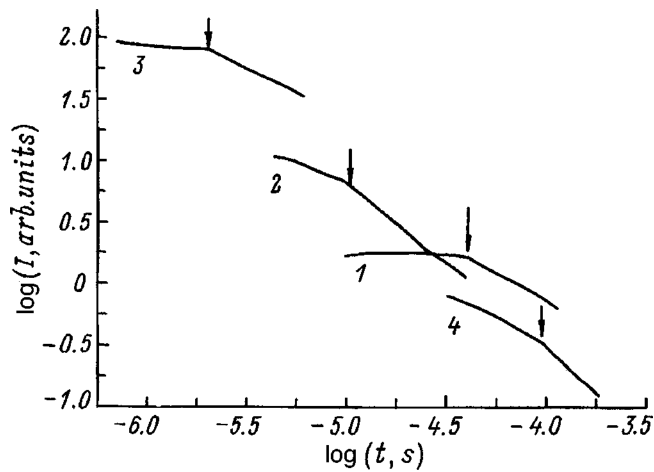

FIG. 1. Plots of $I(t)$ for electrons (*1*, *3*) and holes (*2*, *4*) measured in films of $Se_{0.95}As_{0.05}$ (*1*, *2*) and $Se_{0.95}As_{0.05}$ containing 5.7 at. % Ag (*3*, *4*). $F=10^5$ V/cm, L, μm: *1*, *2* — 2.3; *3*, *4* — 2.2.

when a positively charged impurity A^+ is added, the law of electroneutrality should be obeyed, which we write in terms of the concentrations of charged impurities and defects in the following form: $[A^+]+[D^+]=[D^-]$. The quantitative relation between the concentrations of the charged defects that form from the originally neutral defects D^0 in the reaction $2D^0 \rightarrow D^+ + D^-$ can be written in the form $[D^+][D^-] = [D^0]^2 =$ const according to the law of mass action. The latter equation combined with the electroneutrality equation implies that the introduction of an electrically positive impurity increases the concentration of negatively charged intrinsic defects $[D^-]$ and decreases the concentration of positively charged defects $[D^+]$. Consequently, the hole drift mobility decreases and the electron mobility increases. A similar behavior of the drift mobilities of charge carriers is observed in experiments when the impurity metals Ag, Au, Tl are introduced into glassy chalcogenide semiconductors.

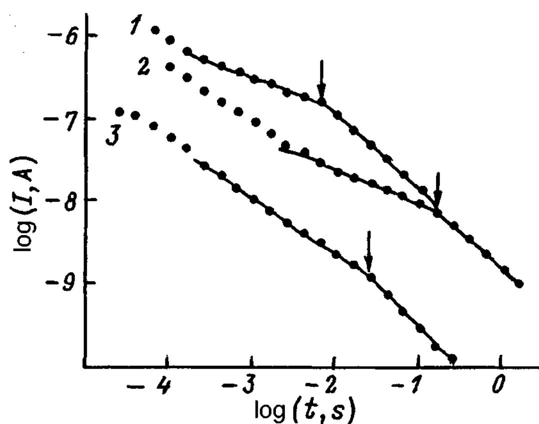

FIG. 2. Plots of $I(t)$ for holes obtained for bulk samples of As_2Se_3 (*1*), As_2Se_3 containing 0.1 at. % Tl (*2*), and As_2Se_3 containing 2 at. % Ag (*3*). $F=1.4\times10^5$ V/cm; L, μm: *1* — 120, *2* — 115, *3* — 100.

A comparison of these data with the results of Refs. 4 and 5 reveals that metals influence the drift mobility less effectively than do halogens. Thus, a considerable increase in the hole mobility is observed when halogen impurities are introduced in amounts of $10^{-4}-10^{-2}$ at. %, while the change in the electron mobility induced by silver concentrations even as large as $1-6$ at. % is considerably smaller.

To summarize, this work indicates that the introduction of metal impurities into glassy chalcogenide semiconductors of the Se–As system produces a considerable increase in the electron drift mobility. This result, like the considerable increase in the hole mobility previously established in Refs. 4 and 5 when halogen impurities were introduced, is in agreement with the model of charged defects. Our analysis allows us to conclude that metal impurities in glassy chalcogenide semiconductors can act as positively charged centers.

We are grateful to K. D. Tsendin for valuable comments offered during a discussion of the work.

This work was carried out with the support of the Russian Fund for Fundamental Research (Grant 97-02-18079).

[1] R. A. Street and N. F. Mott, Phys. Rev. Lett. **35**, 1293 (1975).
[2] M. Kastner, D. Adler, and H. Fritzsche, Phys. Rev. Lett. **37**, 1504 (1976).
[3] H. Fritzsche and M. Kastner, Philos. Mag. B **37**, 285 (1978).
[4] L. P. Kazakova, É. A. Lebedev, A. I. Isaev, S. I. Mekhtieva, N. B. Zakharova, and I. I. Yatlinko, Fiz. Tekh. Poluprovodn. **27**, 959 (1993) [Semiconductors **27**, 520 (1993)].
[5] L. P. Kazakova, E. A. Lebedev, N. B. Zakharova, I. I. Yatlinko, A. I. Isaev, and S. I. Mekhtieva, J. Non-Cryst. Solids **167**, 65 (1994).
[6] B. T. Kolomiets, É. A. Lebedev, L. P. Kazakova, and N. A. Rogachev, Fiz. Tekh. Poluprovodn. **7**, 187 (1973) [Sov. Phys. Semicond. **7**, 132 (1973)].
[7] B. T. Kolomiets, G. A. Andreeva, É. A. Lebedev, I. A. Taksami, and V. Kh. Shpunt, Prib. Sist. Upr. **4**, 27 (1980).
[8] W. E. Spear, J. Non-Cryst. Solids **1**, 197 (1969).
[9] L. P. Kazakova, B. T. Kolomiets, É. A. Lebedev, and S. A. Tauraĭtene, Fiz. Tekh. Poluprovodn. **21**, 274 (1987) [Sov. Phys. Semicond. **21**, 166 (1987)].
[10] G. Pfister and H. Scher, Phys. Rev. B **15**, 2062 (1977).
[11] A. Rose, *Concepts in Photoconductivity and Allied Problems* (Interscience, New York, 1963) [Mir, Moscow, 1969].

Translated by Frank J. Crowne

Donorlike behavior of rare-earth impurities in PbTe

G. T. Alekseeva, M. V. Vedernikov, E. A. Gurieva, P. P. Konstantinov, and L. V. Prokof'eva

A. I. Ioffe Physicotechnical Institute, Russian Academy of Sciences, 194021 St. Petersburg, Russia

Yu. I. Ravich

St. Petersburg State Technical University, 195251 St. Petersburg, Russia

(Submitted December 29, 1997; accepted for publication December 31, 1997)
Fiz. Tekh. Poluprovodn. **32**, 806–810 (July 1998)

The Hall coefficient, thermoelectric power, and electrical conductivity in PbTe doped with La, Pr, Sm, and Gd are investigated in the temperature range (77–700) K. The impurity atoms act as donors with an electrical activity that increases with temperature until the fraction of electrically active lanthanide atoms (Ln) reaches values close to or slightly more than half of their total number. A decrease in the electron mobility and a change in the thermoelectric power relative to their values in PbTe⟨I⟩ are also noted. At low temperatures, the Seebeck coefficient in PbTe⟨Ln⟩ is found to be higher than in PbTe⟨I⟩, while at high temperatures it is lower. The data are interpreted by invoking a band of impurity resonant states, whose energetic position and number are functions of composition and temperature. The experimental data imply that when La and Pr dope PbTe, the electrical activity of the compound is dominated by intrinsic donorlike defects that form when Ln is incorporated in the ratio LnTe.
© *1998 American Institute of Physics.* [S1063-7826(98)00907-7]

A review of data on the doping of lead chalcogenides shows that the majority of impurities (the halogens I, Cl, Br, Na, Tl, In, and Ti) exhibit a maximum in electrical activity at temperatures $T \simeq 0$ K; as the temperature T rises their electrical activity either remains unchanged[1] (for halogens) or decreases.[2–5] Possible exceptions to this general rule are the rare-earth metals with a primary valence +3. Analyzing the temperature behavior of the thermoelectric power in PbTe doped with Sm, Erofeev and Solomatnikova[6] showed that the electron concentration in Sm-doped samples increases with increasing temperature. In this paper, by measuring the concentration of charge carriers using the Hall effect we not only confirm and further explore this result for Sm, but also extend it to La, Pr and Gd, which, like Sm, incorporate into PbTe in the ratio LnTe (where Ln is a lanthanide).

We investigated the transport properties of polycrystalline samples in the temperature range 77–600 K; the maximum concentrations were 1 at. % for La and Pr, 2 at. % for Gd, and 5 at. % for Sm. According to the data from Ref. 6, the solubility of Sm in PbTe is 10 at. %. The composition of the samples, the electron concentration n, and the values of the mobility and the Seebeck coefficient S at 77 and 300 K are listed in Table I. A comparison of the data at 77 K shows that the electron concentration depends on the type of impurity and its concentration N and that it increases with increasing doping level, but remains considerably below the concentration of impurity ions. The donor activity of gadolinium is weaker than that of the other impurities at the same concentration; it is also small for Sm at a concentration of 0.5 at. %. Despite the considerable differences between the properties of La and Pr, their electrical activity in PbTe may be treated as the same.

A general property of all the samples we investigated was increasing electron concentration with increasing temperature T (Figs. 1 and 2). Hall measurements at 4.2 K show that the decrease in concentration with decreasing T continues for $T < 77$ K as well; in this case complete carrier freeze-out does not occur as $T \to 0$ K, and the Hall coefficient increases by no more than a factor of 2 as T decreases from 77 to 4.2 K. The rate of increase in the concentration and the corresponding temperature interval are also determined by the type and concentration of the impurity. The relative increase in concentration is greatest in the samples doped with Gd: in PbTe doped with 1 at. % Gd it reaches a factor of 5 over the range 77–600 K, so that the maximum electron concentration ($\sim 8 \times 10^{19}$ cm^{-3} at 600 K) approaches the values observed for La and Pr at $T < 400$ K, where more than

TABLE I.

		77 K			300 K		
Ln	N, at. %	S, μV/K	μ, cm^2/V·s	n, cm^{-3}	S, μV/K	μ, cm^2/V·s	n, cm^{-3}
La	0.5	20	3400	2.5×10^{19}	58	520	4.2×10^{19}
La	1.0	13	2100	4.0×10^{19}	38	330	8.7×10^{19}
Pr	0.5	–	3800	2.3×10^{19}	59	450	5.4×10^{19}
Pr	1.0	17	1900	4.5×10^{19}	40	320	1.0×10^{20}
Sm	0.5	–	–	1.3×10^{19}	100	340	1.5×10^{19}
Sm	1.0	24	3500	2.1×10^{19}	44	530	5.8×10^{19}
Sm	3.0	12	1200	5.3×10^{19}	23	140	1.9×10^{20}
Sm	5.0	13	300	1.3×10^{20}	24	80	2.8×10^{20}
Gd	0.5	33	6300	5.5×10^{18}	68	540	2.4×10^{19}
Gd	1.0	27	6600	9.3×10^{18}	54	320	5.1×10^{19}
Gd	2.0	13	1500	4.3×10^{19}	29	200	1.5×10^{20}

 © 1998 American Institute of Physics

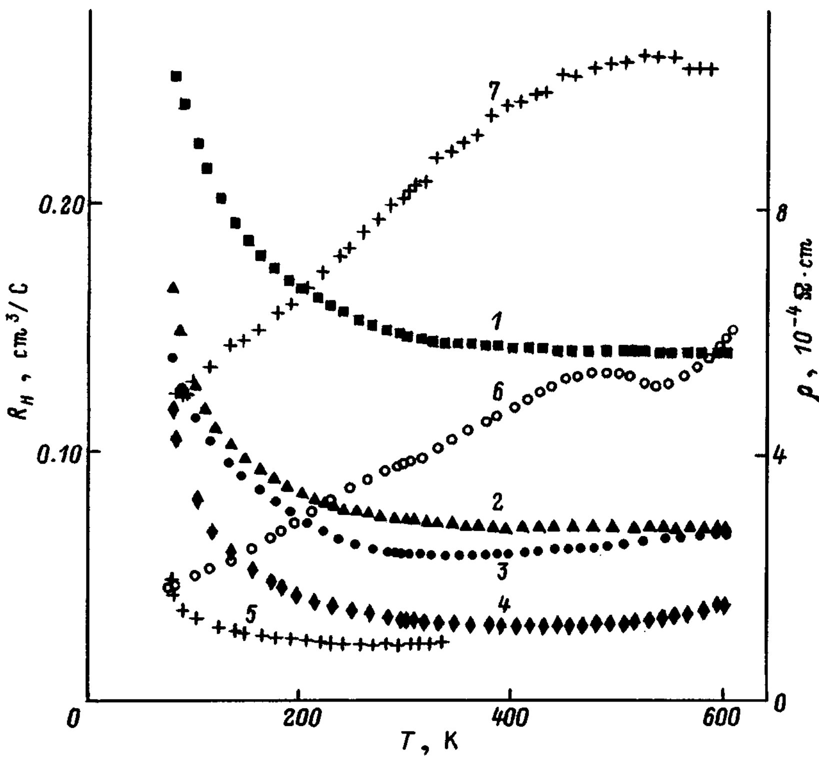

FIG. 1. Temperature dependences of the Hall coefficient R_H (*1–5*) and resistivity ρ (6,7) for PbTe doped with La, Pr, and Sm; type and concentration (N) of the impurity, at. %: *1* — La, 0.5;*2* — La, 1.0; *3* — Pr, 1.0; *4, 6* — Sm, 3.0; *5, 7* — Sm, 5.0.

half the impurity atoms are electrically active. In all the samples the temperature dependence of the Hall effect is strongest at temperatures below 400 K, and then saturation is achieved in the majority of samples. However, in PbTe doped with Pr (1 at. %) and Sm (1 at. % or more) the temperature curves may even increase again slightly at high T (Fig. 1): it turns out that in PbTe with 3 at. % Sm the temperature dependence of the Hall coefficient starts to increase once more at $T \simeq 480$ K, and at 5 at. % Sm the increase starts at $T \simeq 320$ K. In the latter sample, the electron concentration reaches the maximum for the samples of PbTe⟨Sm⟩, which match the data of Ref. 6 (2.8×10^{20} cm^{-3} at 300 K). According to these data, further increases in the impurity concentration lower the room temperature value of the Hall concentration.

The Seebeck coefficient depends only slightly on temperature in the range 77–300 K. This further confirms that the electron concentration increases with temperature in Ln-doped samples, since the increase in thermoelectric power with temperature due to the explicit function $S(T)$ is compensated by a decrease due to the increase in n. We compared our values of the Seebeck coefficient with values of S for halogen-doped PbTe with the same electron concentration. The following general rule was observed: at sufficiently high electron concentrations the value of S in PbTe doped with rare-earth elements was found to be higher at low T, and lower at high T, than in halogen-doped PbTe. The corresponding curves that illustrate this behavior for samples with various dopings are shown in Fig. 3a, where we compare results for PbTe with 1 at. % Pr and PbTe with a variable concentration of iodine, which ensures equality of the electron concentrations in both materials at any temperature within the range chosen. Figure 3b shows the relative change in the Seebeck coefficient ($S_{\mathrm{Ln}}/S_{\mathrm{I}}$) as a function of T for samples of PbTe with different compositions. It is clear that the quantitative characteristics of the relative change in thermoelectric power for PbTe⟨Ln⟩ are determined by the type and concentration of the impurity. The effect behaves non-

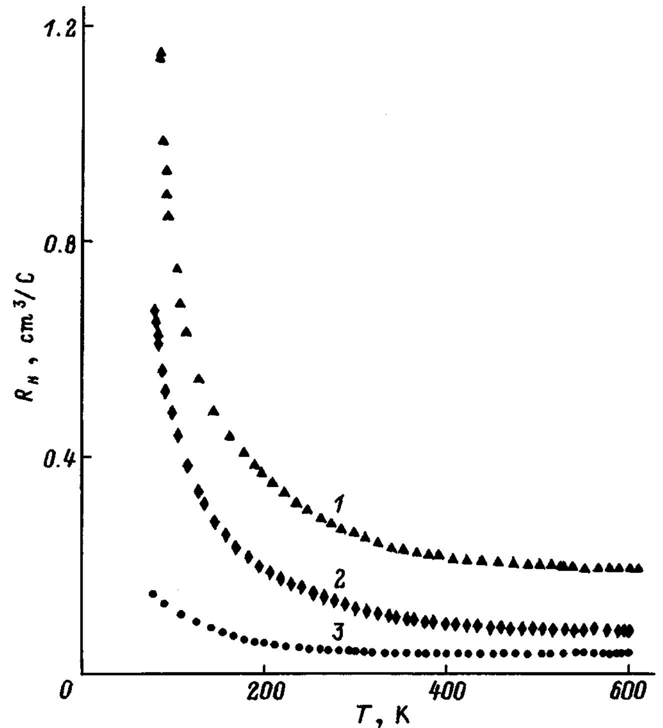

FIG. 2. Temperature dependence of the Hall coefficient R_H for PbTe doped with Gd. Gadolinium concentration N, at. %: *1* — 0.5, *2* — 1.0, *3* — 2.0.

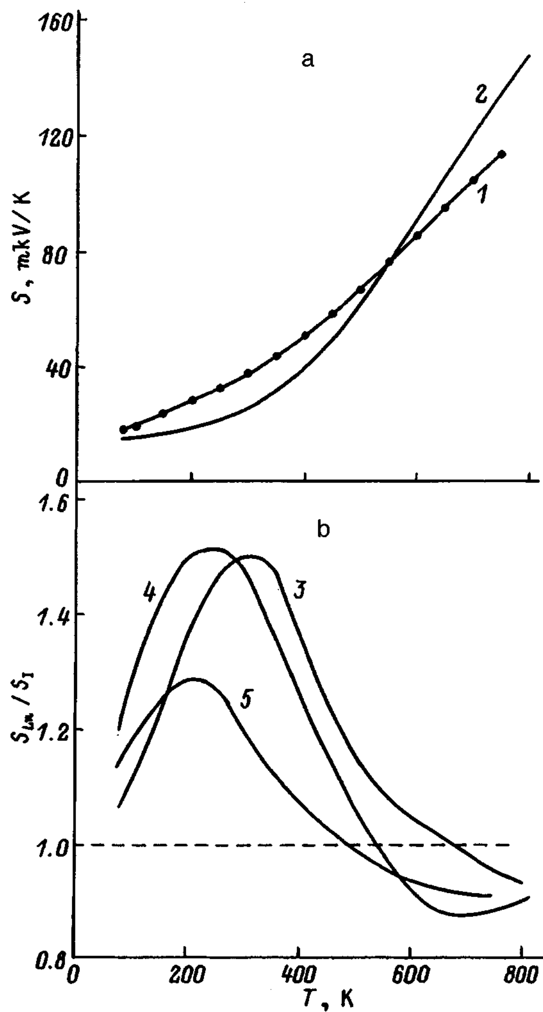

FIG. 3. Temperature dependences of the Seebeck coefficient S (a) and the ratio $S_{\mathrm{Ln}}/S_{\mathrm{I}}$ of the Seebeck coefficients for PbTe doped with rare-earth metals and iodine (b). Type and concentration (N) of the impurity, at. %: *1* — Pr, 1.0; *2* — I, 1.0–0.8; *3* — Gd, 1.0; *4* — Pr, 1.0; *5* — La, 5.0.

monotonically with temperature, the maximum increase in S being observed for T close to room temperature in all the samples. At high T the dependence reaches or approaches a minimum; in this case, the deviation from 1 is very small. At 85 K the relative change in thermoelectric power in PbTe with Gd is smaller than it is for other samples. This effect probably reflects the weaker donor activity of this element at low temperatures.

Our experimental data as a whole can be interpreted within a model of impurity resonant states whose energetic position relative to the bottom of the conduction band depends on the type and concentration of the impurity and on temperature. The first two factors determine the position of the impurity band at 0 K: the fact that the initial concentration of electrons is considerably smaller than the concentration of rare-earth metal atoms indicates that the Fermi level is stabilized by the impurity band and that the filling of the latter with electrons corresponds to $0<(1-n/N)<1$. Increasing N shifts the impurity band upward, so that the initial concentration of electrons in the conduction band, which equals the number of holes in the impurity band, increases.

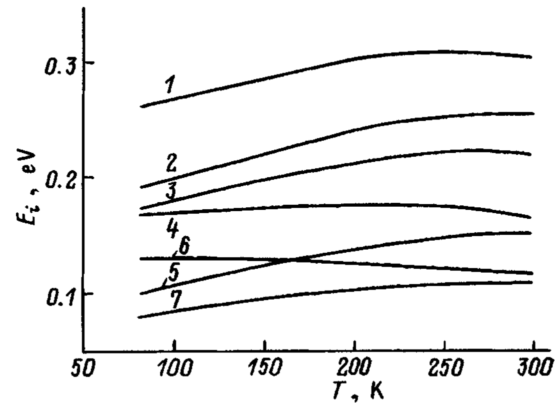

FIG. 4. Energy of impurity states versus temperature in PbTe doped with rare-earth metals. Type and concentration (N) of the impurity, at. %: *1* — Sm, 5.0, *2* — Sm, 3.0, *3* — Gd, 2.0, *4* — Pr, 1.0, *5* — Gd, 1.0, *6* — La, 0.5, *7* — Gd, 0.5.

However, the occupancy of the impurity states can remain at its original level in this case: thus, in samples with 0.5 and 1.0 at. % Gd the occupancies of the impurity states even at 77 K are close to 1 and practically the same (0.93).

As the temperature increases, the distance between the impurity band and the bottom of the conduction band increases, leading to an increase in the Fermi energy E_F and the electron concentration. We calculated the position of the impurity band E_i (without taking into account its broadening) using the neutrality equation:

$$n=\frac{N}{\exp[(E_F-E_i)/kT]+1}. \tag{1}$$

We calculated the dependence of E_F on n within the two-band (Kane) model of nonparabolicity under the assumption that its parameters are doping-independent. After substituting E_F into Eq. (1), we obtained the temperature dependence of E_i shown in Fig. 4. This dependence departs from linearity when T is close to room temperature, because the concentration of free electrons ceases to increase in strongly doped samples, perhaps due to a decrease in the capacity of the impurity band caused by the passage of some of the impurity atoms to different structural positions as T increases. The rate of temperature variation of E_i corresponding to the linear portions of the curves lies in the range $(1-4.5)\times 10^{-4}$ eV/K, depending on the composition of the samples, i.e., it is of the same order of magnitude as the rate of temperature variation of the gap width E_g. An exception is PbTe⟨La⟩; possible reasons for the decrease of E_i with T in this sample will be discussed later. The scatter of the data for dE_i/dT could be due, first, to doping-induced changes in the nonparabolicity parameters that were not included in the calculations, and, second, to the assumption that all the impurity atoms make up the impurity band.

The presence of quasilocal impurity states in the electronic spectrum of samples doped with rare-earth metals, which stabilize the Fermi level, gives rise to additional resonant electron scattering. At 77 K the electron mobility turns out to be 2–4 times smaller than the mobility in the corresponding PbTe samples with halogens;[7] at room temperature

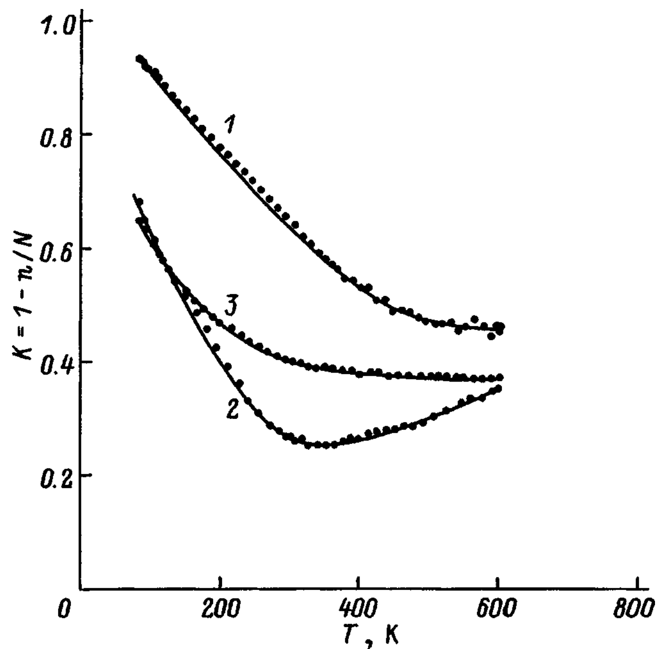

FIG. 5. Temperature-induced change in the electron occupancy (K) of the impurity band in PbTe doped with rare-earth metals. Type and concentration (N) of the impurity, at. %: *1* — Gd, 1.0; *2* — Pr, 1.0; *3* — La, 0.5.

this difference does not exceed a factor of 2.5 (an exception is the sample with 0.5 at. % Sm), but an appreciable difference in mobility is maintained even at $T \simeq 800$ K.

As we mentioned above in connection with our discussion of the experimental data on the Hall concentration, the capacity of the impurity band may decrease at high temperatures. This would lead to a decrease in the resonant scattering. In fact, the temperature dependences of the resistivity shown in Fig. 1 for PbTe strongly doped with Sm display saturation regions and even decreases in the resistivity at $T \simeq 500-600$ K.

The appearance of resonant scattering when samples are doped with rare-earth metals is also clearly evident from the thermoelectric power data. If the electron occupancy of the impurity band $K = 1 - n/N$ is greater than 0.5, the Fermi level is located above the center of the band and electrons with energies $E < E_F$ scatter more strongly than electrons with relatively high energies. In this case resonant scattering leads to an increase in the absolute value of the thermoelectric power S.[8] For values of the occupancy $K < 0.5$ it is primarily electrons with $E > E_F$ that scatter, and S decreases due to resonant scattering. The influence of resonant scattering on the thermoelectric power is maximal for values of K in the ranges 0.7−0.8 and 0.2−0.3. It is clear from Fig. 5 that at low temperatures $K > 0.5$, and the thermoelectric power in samples doped with rare-earth metals is larger in absolute value than in samples with halogens due to resonant scattering. When the band is almost completely filled by electrons (0.5 and 1.0 at. % Gd at 77 K) S increases more strongly than it does in PbTe⟨I⟩ or PbTe⟨Pr⟩ (where the occupancy is considerably lower). Increasing T to 200−300 K causes intense ionization of the impurities, which maximizes the effect of resonant scattering on the thermoelectric power. At still higher T the contribution of resonant scattering to the thermoelectric power gradually decreases, changes sign, and then increases once more, but only up to a far smaller value due to the considerable increase in the contribution from phonon scattering. Thus, although we were unable to achieve exact quantitative agreement between experiment and theory, we can make the qualitative assertion that the nonmonotonic temperature dependence of relative values of S shown in Fig. 3b correlates closely with the behavior of $K(T)$.

In PbTe with 1 at. % Gd the equality $S_{\mathrm{Gd}} = S_{\mathrm{I}}$ is obeyed for occupancies close to 1/2, whereas in PbTe with La and Pr this equation is violated, and the occupancy turns out to be less than 1/2. In addition, the initial electron concentration in samples with these impurities turns out to be considerably higher than in PbTe with Gd, and the temperature increase in n is weaker, producing a weakly increasing or even decreasing plot of $E_i(T)$ for the case of PbTe with La. In light of these facts, we may assume that when PbTe is doped by high concentrations of these elements, intrinsic donor defects form, whose influence increases with particular rapidity with decreasing T and rare-earth metal concentration. Their presence can also explain the observed decrease in the slope of the $E_i(T)$ lines as the concentration of Gd decreases from 2 to 0.5 at. % (curves *3*, *5*, and *7* in Fig. 4).

This work was supported by the ''Integration'' program, Project No. 75.

[1] G. T. Alekseeva, L. V. Prokof'eva, and T. S. Stavitskaya, Fiz. Tverd. Tela (Leningrad) **8**, 2819 (1966) [Sov. Phys. Solid State **8**, 2258 (1966)].
[2] G. T. Alekseeva, E. A. Gurieva, P. P. Konstantinov, L. V. Prokof'eva, and Yu. I. Ravich, Fiz. Tekh. Poluprovodn. **31**, 528 (1997) [Semiconductors **31**, 444 (1997)].
[3] A. N. Veĭs, V. I. Kaĭdanov, S. A. Nemov, S. N. Emelin, A. Ya. Ksendzov, and Yu. K. Shalabutov, Fiz. Tekh. Poluprovodn. **13**, 185 (1979) [Sov. Phys. Semicond. **13**, 106 (1979)].
[4] L. V. Prokof'eva, E. A. Gurieva, Sh. I. Zhumaksanov, P. P. Konstantinov, Kh. R. Maĭlina, Yu. I. Ravich, and L. S. Stil'bans, Fiz. Tekh. Poluprovodn. **21**, 1778 (1987) [Sov. Phys. Semicond. **21**, 1078 (1987)].
[5] T. N. Vinogradova, E. A. Gurieva, V. I. Zharskiĭ, S. V. Zarubo, L. V. Prokof'eva, T. T. Dedegkaev, and I. I. Kryukov, Fiz. Tekh. Poluprovodn. **12**, 663 (1978) [Sov. Phys. Semicond. **12**, 387 (1978)].
[6] R. S. Erofeev and O. V. Solomatnikova, Neorg. Mater. **10**, 423 (1974).
[7] Yu. I. Ravich, B. A. Efimova, L. V. Prokof'eva, and I. N. Dubrovskaya, Fiz. Tekh. Poluprovodn. **4**, 230 (1970) [Sov. Phys. Semicond. **4**, 183 (1970)] (Abstract); Paper deposited in the All-Union Institute of Scientific and Technical Information of the Academy of Sciences of the USSR (VINITI), No. 930/69.
[8] V. I. Kaĭdanov, S. A. Nemov, and Yu. I. Ravich, Fiz. Tekh. Poluprovodn. **26**, 201 (1992) [Sov. Phys. Semicond. **26**, 113 (1992)].

Translated by F. Crowne

Contribution of light holes to the Hall effect for the complex valence band in germanium and its dependence on doping level

M. V. Alekseenko, A. G. Zabrodskiĭ, and L. M. Shterengas

A. I. Ioffe Physicotechnical Institute, Russian Academy of Sciences, 194021 St. Petersburg, Russia
(Submitted December 15, 1997; accepted for publication January 20, 1998)
Fiz. Tekh. Poluprovodn. **32**, 811–820 (July 1998)

A method is proposed and implemented for experimentally isolating the influence of light holes on the classical Hall effect for the complex valence band in p-Ge. In this method the contribution from light holes is successively eliminated by an applied magnetic field, and then the absolute values of the hole concentrations are calibrated in pairs of samples specially prepared using neutron transmutation doping. The increase in electron concentration as a result of neutron transmutation doping is measured for one of the samples (the reference), while the hole concentration is measured for the other sample. This gives calibration curves for the effective Hall factor in p-Ge, which can be used to precisely measure the hole concentration over the entire range of doping levels. The use of this method for investigating the hopping transport of charge carriers and metal-insulator transitions is illustrated. © *1998 American Institute of Physics.* [S1063-7826(98)01007-2]

1. INTRODUCTION

The peculiarities of the galvanomagnetic properties of p-Ge are known to arise from its complex band structure (see, e.g., Refs. 1–3), in particular from the degeneracy of the valence band, which gives rise to light and heavy hole bands, and the nonspherical properties of the latter. The rather small number of high-mobility light holes present in p-Ge makes a rather small contribution to the electrical conductivity; however, in sufficiently weak magnetic fields they determine the values of the Hall coefficient R measured in experiments and its field dependence to a considerable degree. It is known, for example, that at $T \approx 100$ K applying a magnetic field of a few hundred oersteds to weakly doped p-Ge is enough to initiate a decrease in the magnitude of the Hall coefficient R by eliminating the contribution from light holes.[4] In strong fields, in which the effect of light holes is eliminated, the magnetic-field dependence of the Hall coefficient for the heavy-hole band is complicated by the appearance of a so-called ''fine structure'' (a minimum followed by a maximum).

Thus, the magnetic-field dependence of the Hall coefficient $R(H)$ in p-Ge is determined by the relative contributions of light and heavy holes in the region where the two-band model applies and exhibits one-band behavior in sufficiently strong fields. In this case both the features of the band structure and the carrier scattering mechanism are important. Incorporating these factors into a theory is very complicated, which is probably why it has not been done in any generality, and the theoretical calculations which have been performed[1–3] are limited to extremely weak doping levels. In order to illustrate the effect of two-band behavior, let us use the simplest expression for the magnetic-field dependence of the Hall coefficient, without taking into account the anisotropy of the heavy-hole band or the nonparabolicity of the light-hole band, as well as the energy dispersion of the carrier lifetime:[1)]

$$R = \frac{1}{eH} \frac{Y}{(X^2 + Y^2)}. \tag{1}$$

Here

$$X = \sigma_{xx}^{(1)}(H) + \sigma_{xx}^{(2)}(H) = e\left(\frac{p_1\mu_1}{1+\gamma_1^2} + \frac{p_2\mu_2}{1+\gamma_2^2}\right),$$

$$Y = \sigma_{xy}^{(1)}(H) + \sigma_{xy}^{(2)}(H) = e\left(\frac{\gamma_1 p_1\mu_1}{1+\gamma_1^2} + \frac{\gamma_2 p_2\mu_2}{1+\gamma_2^2}\right)$$

$$= \frac{eH}{c}\left(\frac{p_1\mu_1^2}{1+\gamma_1^2} + \frac{p_2\mu_2^2}{1+\gamma_2^2}\right),$$

for definiteness we assign the label $i=1$ to light holes, while $i=2$ applies to heavy holes, and the coefficient γ_i is defined by the product of the drift mobility μ_i and the magnetic field H:

$$\gamma_i = \frac{\mu_i H}{c}, \quad i = 1, 2, \tag{2}$$

where c is the velocity of light and $|e|$ is the absolute value of the electron charge.

In order to use Eq. (1), it is necessary to know the concentration p_i and the mobility μ_i of light and heavy holes. In the early theoretical calculations by Willardson *et al.*,[6] which dealt with weakly doped p-Ge, a more rigorous approach was used, and a concentration ratio $a = p_1/p_2 = 0.02$ and a mobility ratio $b = \mu_1/\mu_2 = 8$ ($T = 200-300$ K) were chosen for comparisons with experiment. Subsequently, they and other authors used the larger value $a = 0.04$. The mobility ratio was subsequently refined and re-estimated as well. We can probably assume that ratios $a = 0.04$ and $b = 8$ are cor-

 © 1998 American Institute of Physics

rect to a factor of 2. In the weak-field limit $H \to 0$ the use of these ratios of the concentrations and mobilities of light and heavy holes in Eq. (1) gives a value of R that is twice as large as the value for only one heavy-hole band.[2)]

For fields that satisfy the condition $H \gg H_1 = c/\mu_1$ (the so-called classical strong-field limit[3)] for high-mobility holes), the effect of the light holes is practically eliminated, and only the heavy-hole band "functions;" hence, we can write the following expression for the Hall coefficient:

$$R(H) = \frac{r_2(H)}{p_2 ec}, \tag{3}$$

where $r_2(H)$ is the Hall factor for heavy holes. When the magnetic field is increased further[4)] to $H \gg H_2 = c/\mu_2$, the following relation holds:[2]

$$R(H \to \infty) \equiv R_\infty \frac{1}{ec(p_1 + p_2)}. \tag{4}$$

The task of the experimentalist is to distinguish between the contributions of light and heavy holes to the Hall effect in p-Ge. For this it is sufficient to measure the magnetic-field dependence $R(H)$. Such measurements were also reported in Ref. 1 cited above, as well as in other papers, but only for weakly doped samples.

A more complicated experimental problem involves the use of Hall measurements to exactly calibrate the hole concentration in p-Ge.[5)] As a rule, the limiting expression (4) is used for this. In practice, to extract the hole concentration[6)] using Eq. (4), the value of R is usually measured in fields of order 10 kOe. However, as we shall show below, the Hall factor $r_p(H)$ does not yet reach unity at these fields, first, because we are at the limit of applicability of formula (4) and, second, because the function $R(H)$ has a fine structure, whose existence is not predicted by formula (1). In principle, the Hall factor can also be estimated by measuring the ratio between the Hall and drift mobilities. Unfortunately, the error in determining the latter is usually large.

Thus, despite its long history, the use of the Hall effect to precisely characterize the hole concentration in p-Ge over the entire range of doping levels and to separate the contributions of light and heavy holes (if the doping level is not small) is still problematic. This paper describes an attempt to experimentally resolve this problem. The idea is to conduct magnetic-field studies on pairs of samples prepared in a special way (using neutron transmutation doping). In one of the samples (the reference), we measure the increase in electron concentration caused by neutron transmutation doping, while in the other we measure the hole concentration.

2. EFFECTIVE HALL FACTOR AND METHOD OF DETERMINING IT

When the contribution from light holes is completely eliminated, the concentration of heavy holes is determined from the measured Hall coefficient within a simple one-band model using Eq. (3). It is convenient to use a similar formula for the case when the effect of the light-hole band is not negligibly small:

$$R(H) = \frac{r_p(H)}{epc}, \tag{5}$$

where $r_p(H)$ is some "effective Hall factor" and $p = p_1 + p_2$. Since the magnetic-field-induced change in the total hole concentration contributing to the Hall effect is small, we may say that $r_p(H)$ determines the relation between the measured Hall coefficient in a given magnetic field and the total hole concentration. Once we have investigated the behavior of the Hall coefficient in p-Ge at various magnetic fields and for various temperatures, we can determine the effective Hall factor for p-Ge over a wide range of doping levels and magnetic fields.

The idea of our approach is based on the induction of closely coupled changes in the concentrations of the majority carriers Δn and Δp in Ge with n- and p-type conductivity at similar doping levels and low degrees of compensation, which can be determined from Hall measurements. These "concerted changes" can be effected by the neutron transmutation doping of pairs of samples, in one of which we record the change in the electron concentration, while in the other we record the change in the hole concentration. As was shown in Ref. 8, when germanium with the natural isotopic composition is irradiated with strongly slowed neutrons, material is obtained with p-type conductivity and a degree of compensation close to 0.3.[7)] Thus, initially pure Ge, in which we measure Δp, is irradiated along with either n-Ge or germanium that is strongly enriched with ^{74}Ge, in which the change in the electron concentration Δn is recorded. Let us systematically discuss these experimental situations.

Experiment 1. Parallel irradiation of samples of pure Ge and n-type Ge by relatively small thermal neutron fluences (in the second sample neutron transmutation doping does not cause an $n \to p$ conversion, and, in addition, the degree of compensation is not high). In n-type Ge transmutation doping decreases the original electron concentration by $n_n - n_{nn}$, in which case

$$\frac{r_n}{eR_n c} - \frac{r_{nn}}{eR_{nn} c} = r_n n_n - r_{nn} n_{nn} = \bar{r}_n (n_n - n_{nn}). \tag{6}$$

Taking into account the closeness of the values of r_n and r_{nn}, here we introduce the value of the Hall factor

$$\bar{r}_n = \frac{r_n n_n - r_{nn} n_{nn}}{n_n - n_{nn}}, \tag{7}$$

where $n_n = (ecR_n)^{-1}$ and $n_{nn} = (ecR_{nn})^{-1}$ are the corresponding Hall concentrations; the label "n" corresponds to n-Ge before neutron transmutation doping, while "nn" refers to the material after doping.

In the parallel irradiated control sample of originally pure Ge we introduce a concentration of holes equal to

$$\frac{r_p}{eR_p c} = r_p p_p, \tag{8}$$

where $p_p = (ecR_p)^{-1}$ is the Hall concentration. From the conditions of the experiment it follows that the reason for the change in the concentration of majority carriers in both samples is the identical number of uncompensated trans-

muted gallium impurities. These changes are equal in magnitude and opposite in sign, i.e., the decrease in the electron concentration equals the increase in hole concentration:

$$\frac{r_n}{|R_n|}-\frac{r_{nn}}{|R_{nn}|}=\frac{r_p}{|R_p|}. \tag{9}$$

From this we find that

$$r_p=\bar{r}_n R_p\left(\frac{1}{R_n}-\frac{1}{R_{nn}}\right), \tag{10}$$

where $\bar{r}_n$ is defined by formula (7).

Experiment 2. Parallel irradiation of pure Ge and n-type Ge by large thermal neutron fluences, in which n-Ge with an electron concentration r_n/ecR_n is converted to a p-type material with a hole concentration r_{np}/ecR_{np} and a low degree of compensation. This is equivalent to a change in the concentration of charge carriers in both samples by an amount

$$\bar{r}_p=\frac{1}{ec}\left(\frac{1}{R_{np}}-\frac{1}{R_p}\right)=\frac{r_n}{ecR_n}. \tag{11}$$

By analogy with experiment *1* and in light of the closeness of the values of r_p and r_{np}, we can introduce the quantity $\bar{r}_p$ into the discussion:

$$\bar{r}_p=\frac{r_n R_p R_{np}}{R_n(R_p-R_{np})}. \tag{12}$$

Experiment 3. Combined irradiation of pure Ge and germanium strongly enriched with ^{74}Ge. The stationary free-hole concentration in the region of complete ionization of the acceptors in neutron-transmutation-doped, originally pure p-type Ge is

$$p_p=\frac{r_p}{eR_p c}=Np_{^{70}\mathrm{Ge}}\,\sigma_{^{70}\mathrm{Ge}}\,F(1-K), \tag{13}$$

and the corresponding electron concentration in monoisotopic ^{74}Ge subjected to neutron transmutation doping is

$$n_{on}=\frac{r_{on}}{eR_{on}c}=Np_{^{74}\mathrm{Ge}}\sigma_{^{74}\mathrm{Ge}}\,F(1-K'), \tag{14}$$

where $N=4.42\times10^{22}\ \mathrm{cm}^{-1}$ is the concentration of Ge atoms, R_{on} is the Hall coefficient in a weak field for originally pure irradiated monoisotopic n-Ge, r_{on} is the corresponding Hall factor, $p_{^{70}\mathrm{Ge}}$ is the abundance of ^{70}Ge in the natural mixture; $p_{^{74}\mathrm{Ge}}$ is the abundance of ^{74}Ge in the enriched mixture; $\sigma_{^{70}\mathrm{Ge}}$ and $\sigma_{^{74}\mathrm{Ge}}$ are the average cross sections for neutron capture by ^{70}Ge and ^{74}Ge in the real spectrum; K is the degree of compensation of neutron-transmutation-doped, originally pure Ge, K' is the degree of compensation of neutron-transmutation-doped monoisotopic ^{74}Ge, and F is the neutron fluence. Using Eqs. (13) and (14), we find that

$$r_p=r_{on}\frac{R_p p_{^{70}\mathrm{Ge}}\sigma_{^{70}\mathrm{Ge}}(1-K)}{R_{on}p_{^{74}\mathrm{Ge}}\sigma_{^{74}Ge}(1-K)}\equiv Ar_{on}\frac{R_p}{R_{on}}, \tag{15}$$

where $A=\sigma_{^{70}\mathrm{Ge}}\,p_{^{70}\mathrm{Ge}}(1-K)/\sigma_{^{74}\mathrm{Ge}}\,p_{^{74}\mathrm{Ge}}(1-K')$.

Thus, in all three experiments, once the radioactive decay reactions have ended, the stationary values of the Hall factor in p-Ge can be expressed in terms of the value of the Hall factor in n-type Ge based on Eqs. (10), (12), and (15). The latter, in turn, is calculated within the theory of anisotropic scattering.[10]

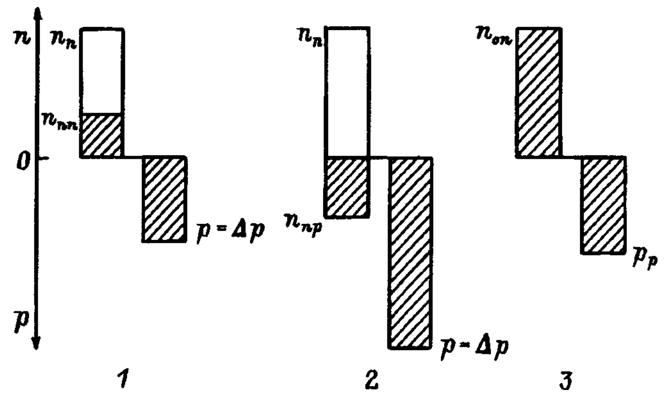

FIG. 1. Schematic representation of the changes in carrier concentration for pairs of samples subjected to neutron transmutation doping as part of experiments *1–3* to determine the effective Hall factor in p-Ge. In each pair, the originally pure sample of Ge with the natural isotopic composition is shown on the right. The notations for the concentration are explained in the text. Hatching indicates the concentrations after neutron transmutation doping.

3. OBTAINING PAIRS OF SAMPLES OF NEUTRON-TRANSMUTATION-DOPED Ge : Ga AND Ge : As WITH CONCERTED VARIATION OF THE CONCENTRATIONS OF MAJORITY CARRIERS. MAGNETIC-FIELD DEPENDENCE OF THE HALL COEFFICIENT IN NEUTRON-TRANSMUTATION-DOPED Ge : Ga

Following Sec. 2, we set up three versions of the experiments based on combined neutron-transmutation-doped pairs of Ge samples cut in a (111) plane perpendicular to the growth axis.[8)] In all the experiments, one of the irradiated samples consists of Ge with a purity high enough to neglect the concentrations of initial impurities in comparison to those introduced by transmutation.

Experiment 1. The original material is specially uncompensated n-Ge : As. The fluence of irradiating neutrons is chosen so as to produce in moderately compensated n-Ge : As (see Fig. 1a). Samples with various levels of initial doping with arsenic were used.

Experiment 2. The initial material is the same as in experiment 1, but the neutron fluence is considerably larger, so that after irradiation we obtain a moderately compensated p-type material (see Fig. 1b).

Experiment 3. The original material is strongly enriched with ^{74}Ge ($p_{^{74}\mathrm{Ge}}=0.988$) and has an initial concentration of ''background'' impurities negligibly small compared to the concentration of transmutation impurities. The ratio between the doping isotopes is such that the degree of compensation of neutron-irradiated monoisotopic Ge is $K'\approx2\%$ (Fig. 1c).

The samples were irradiated in channels V15 and V1 of the VVR-M reactor (in Gatchina) with flux ratios of thermal to fast neutron of 30–50 and 8–10, respectively. Based on the overall concentration of transmutation impurities in neutron-irradiated Ge, we covered the range $10^{14}-10^{18}\ \mathrm{cm}^{-3}$. Accompanying radiation defects were an-

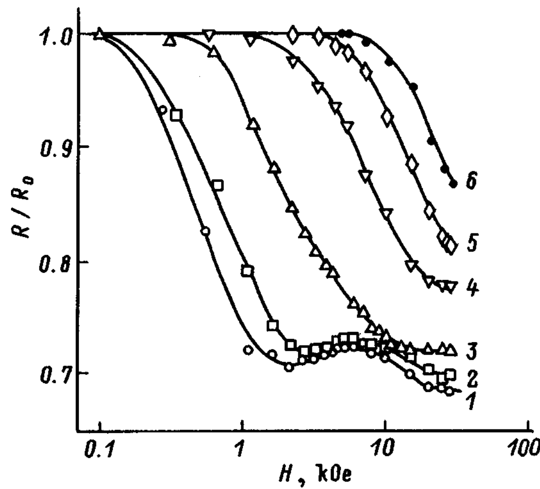

FIG. 2. Magnetic-field dependence of the ratio of Hall coefficients R/R_0 ($R_0 \equiv R(H \to 0)$) in neutron-transmutation-doped Ge : Ga at $T = 77.4$ K. Hall hole concentration $1/ecR_0$, cm^{-3}: *1* — 2.27×10^{13}, *2* — 1.80×10^{14}, *3* — 1.45×10^{15}, *4* — 1.09×10^{16}, *5* — 5.51×10^{16}, *6* — 6.91×10^{17}.

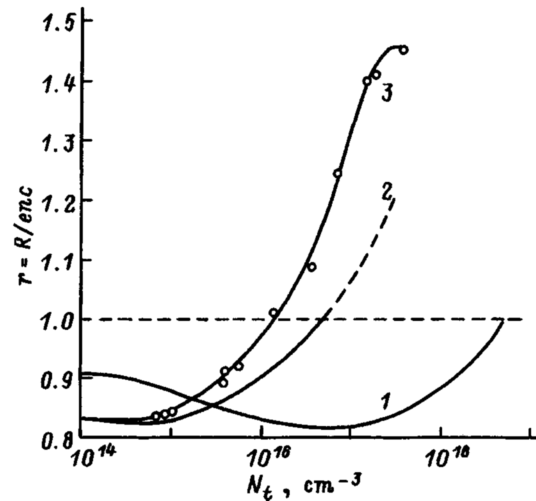

FIG. 3. Dependence of the Hall factor $r_n = 1/ecR_0$ in n-Ge on the concentration of ionized impurities N_t. T, K: *1* — 300, *2, 3* — 77.4. *1, 2* — calculations from Ref. 10, *3* — our data, obtained by dividing the computed values of r_n at $T = 300$ K (curve *1*) by experimental values of $r_n(300)/r_n(77)$.

nealed out in the standard way. The technology for depositing contacts differed somewhat, depending on the type of conductivity.

There was interest in first ascertaining to what extent neutron-irradiated Ge : Ga ($K \cong 0.3$) exhibits the features of the behavior of the Hall coefficient in a magnetic field described in the Introduction for weakly compensated p-Ge obtained by metallurgical means. The reason for this interest is that the work of Fritzsche and Cuevas,[12] where magnetic-field dependences of the Hall coefficient were studied in neutron-irradiated Ge, did not include data on either very weak or very strong magnetic fields. We were interested in the presence of a fine structure in the Hall coefficient, as well as a plateau in the low-field region, which is characteristic of specially uncompensated, weakly doped p-Ge.[1,6,13]

The magnetic-field dependence of the Hall coefficient was recorded up to $H \cong 28$ kOe, both at room temperature and at nitrogen temperature. Our experimental values of $R(H)$, calculated relative to $R(H \to 0)$, are shown in Fig. 2. A region of ''two-band'' saturation of $R(H)$ in weak fields is clearly visible along with a transition to ''one-band'' saturation in strong fields at low doping levels. Moreover, a fine structure in the Hall coefficient can be seen for weakly doped samples.

Thus, the magnetic-field dependences of the Hall coefficient in p-Ge with $K \cong 0$ (Ref. 4) and neutron-irradiated Ge with $K \cong 0.3$ are qualitatively identical, i.e., at low degrees of compensation they are independent of K.

4. EXPERIMENTAL ISOLATION OF THE CONTRIBUTION OF LIGHT HOLES TO THE HALL EFFECT FOR THE COMPLEX VALENCE BAND OF GERMANIUM

We now turn to the problem of isolating the contribution of light holes to the Hall effect in p-type germanium. As is clear from the previous section, we can reduce this problem to studying the behavior of the effective Hall factor in p-Ge.

Our first concern is with the value of the Hall factor r_n for n-Ge. As a basis, we took values of r_n calculated within the theory of anisotropic scattering[10] at $T = 300$ K in the approximation $H \to 0$ (Fig. 3, curve *1*).[9)]

At concentrations of order 3×10^{17} cm^{-3} it is no longer correct to use these data because of the influence of the impurity band at large concentrations. At nitrogen temperature the influence of this band is felt at even lower concentrations, of order 10^{16} cm^{-3} (Fig. 3, curve *2*). However, our experiments (Fig. 3, curve *3*) show that the influence of the impurity band is detectable (i.e., features are observed in the behavior of the Hall factor) at concentrations roughly an order of magnitude larger. Therefore, we can assume that our room-temperature calculations are also correct at higher concentrations than in Ref. 10. The value of r_n at 77.4 K [hereinafter $r_n(77)$] is found using calculations for $T = 300$ K and the ratio $r_n(300)/r_n(77)$ measured experimentally by us in the limit $H \to 0$. In Fig. 4 we compare the experimental and computed (using the theory of Ref. 10) values of $r_n(300)/r_n(77)$. It is clear that they are in good agreement only at small doping levels. For strong doping there are absolutely no calculated data on $r_n(77)$. However, even if such data were available they would scarcely be useful, because under these conditions impurity-band conduction already plays an important role, and in order to interpret the Hall data for strongly doped n-Ge at $T = 77$ K the two-band model should be used. This would sharply increase the error, and the n-Ge would cease to play its role as a reference in our experiments. It is for this reason that we use experimentally measured values of $r_n(300)/r_n(77)$ in our analysis (see Fig. 4, curve *1*).

The values of $r_p(300)$ and $r_p(77)$ sought were determined in the following way. In experiments *1* and *2* values of $r_p(300)$ were obtained from Eqs. (10) and (12), respectively. In this case we used computed values of $r_n(300)$ and $r_{nn}(300)$ from Ref. 10. The value of $r_n(77)$ was determined from the experimental ratio $r_n(300)/r_n(77)$

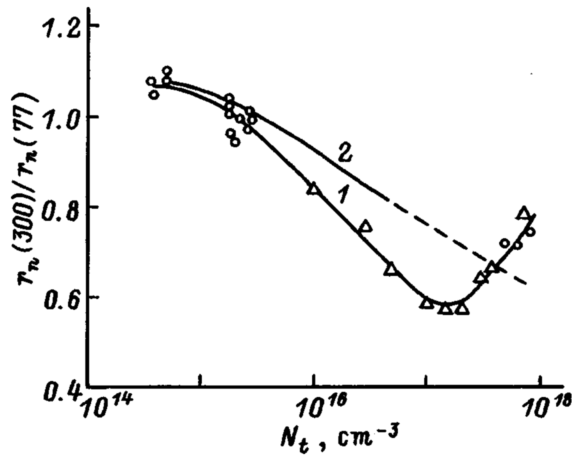

FIG. 4. Hall factor ratio $r_n(300)/r_n(77)$ in n-Ge at $T=300$ and 77.4 K in the limit $H\rightarrow 0$ as a function of the concentration of ionized impurities N_t: *1* — experiment, *2* — calculations based on the theory of Ref. 10.

$=R_n(300)/R_n(77)$. Then the value of $r_p(77)$ was found using the same expressions as for $r_p(300)$.

In experiment *3* we first determined the ratio $r_p/r_n \equiv r_p/r_{on}$ from Eq. (15) for $T=300$ and 77 K. In calculating the constant A appearing in this expression, we used the following values of the parameters from Ref. 8: $\sigma_{^{70}\mathrm{Ge}}\, p_{^{70}\mathrm{Ge}}/\sigma_{^{74}\mathrm{Ge}}\, p_{^{74}\mathrm{Ge}}=1.31$ and $K=0.31$ (channel V15), $K=0.35$ (channel V1). As a result, the values of A calculated for channels V15 and V1 were 0.921 and 0.868, respectively. Then, using the theory of Ref. 10, we found the value of $r_p(300)$, while the value of $r_p(77)$ was determined using the experimental ratio that we obtained, as in experiments *1* and *2*.

The results of our experimental determination of the Hall factor in p-Ge for $T=300$ and 77 K in a field of $H=5.2$ kOe are shown in Fig. 5. The smooth curve through our set of experimental points was plotted with consideration of weights that correspond to measurement errors. The curves (for more clarity, they are plotted without experimental points) for the three magnetic fields $H\rightarrow 0$, $H=5.2$ kOe, and $H=28.6$ kOe are shown in Fig. 6. The approximation of a weak field $H\rightarrow 0$ was chosen, because the effect of the light holes is maximal in this limit. We note that the Hall factor in n-Ge was calculated for just this field. The moderate magnetic field $H=5.2$ kOe was chosen, because it was most convenient for the practical determination of the concentration based on the results of standard laboratory Hall measurements, since, on the one hand, such fields already provide considerable suppression of the contribution of light holes, while, on the other hand, they are easy to create in the laboratory. The strong-field limit $H=28.6$ kOe was chosen to completely exclude (as much as possible) the effect of light holes on the value of the Hall factor in p-Ge and to make the transition to the one-band (heavy-hole) model.

Let us turn to the concentration dependence of the Hall factor r_p for various magnetic fields shown in Fig. 6. Since the measured Hall coefficient is proportional to $r_p(H)$, a qualitative measure of the contribution of light holes to the Hall effect is given by the vertical displacement of curves *2*

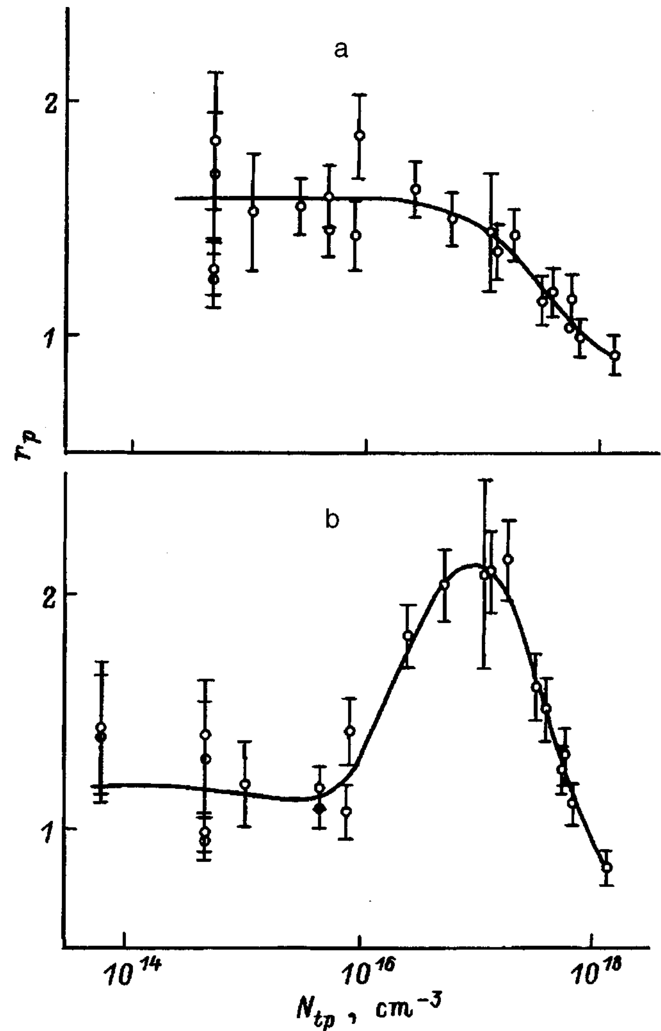

FIG. 5. Dependence of the effective Hall factor in p-Ge for $H=5.2$ kOe on the concentration of ionized impurities N_{tp}. T, K: a — 300, b — 77.4.

and *3* relative to curve *1* (the zero-field limit). As can be seen, this contribution is greatest at the weak doping levels $N_t \leqslant N_1=3\times 10^{15}$ cm^{-3}. At $N_t \geqslant N_1$ it decreases monotonically with increasing N_t and at $N_t \geqslant N_2=5\times 10^{17}$ cm^{-3} it becomes immeasurably small. The quantitative aspect of the question regarding the role of light holes and the absolute value of the Hall factor will be discussed in the next sections.

5. INFLUENCE OF THE LIGHT-HOLE BAND ON THE HALL EFFECT IN *p*-Ge

The values of the Hall factor determined above and the experimental values of the Hall coefficient in the weak-field limit allow us to describe the magnetic-field dependence $R(H)$ using Eq. (1), which takes into account only the two-band nature of the problem. In this case it is convenient to isolate two factors, one of which is the Hall coefficient for the heavy-hole band in a strong field $R_2=(ecp_2)^{-1}$, while the other, $f(H)$, is an "influence function" which describes the effect of the light holes on the Hall coefficient:

$$R=\frac{f(H)}{ecp_2}, \tag{16}$$

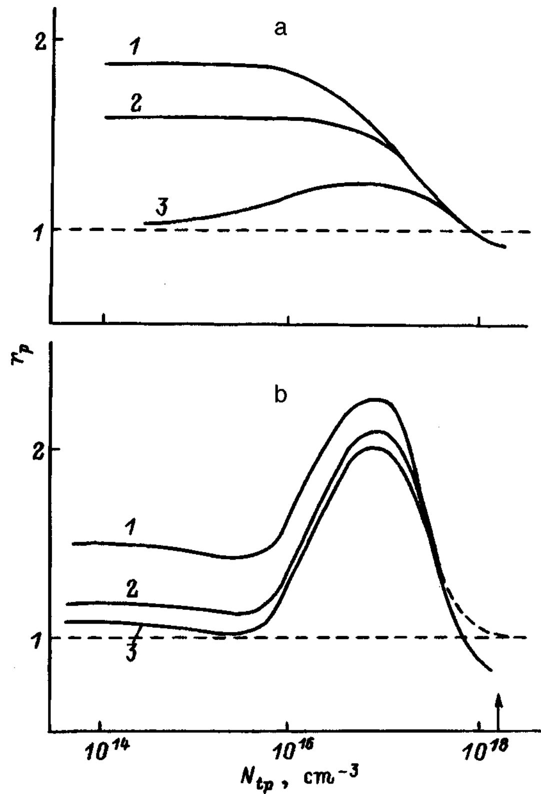

FIG. 6. Dependence of the effective Hall factor on the concentration of ionized impurities N_{tp} in p-Ge for $H\to 0$ (*1*), $H=5.2$ (*2*), and $H=28.6$ kOe (*3*). T, K: a — 300, b — 77.4.

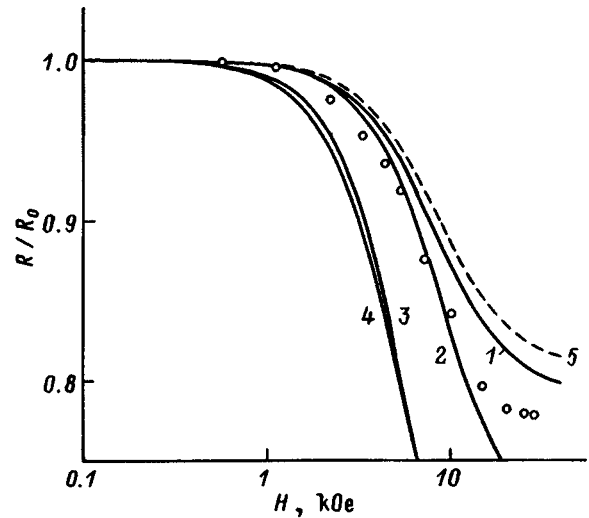

FIG. 7. Magnetic-field dependence of the ratio $R(H)/R_0$ at $T=77.4$ K for a sample with $1/ecR_0=1.09\times 10^{16}$ cm^{-3}: points — experiment (Fig. 2, curve *4*); dependences *1–4* — calculations based on Eqs. (16)–(18) for the following values of a and b, respectively: *1* — 0.02 and 5, *2* — 0.04 and 5, *3* — 0.04 and 8, *4* — 0.02 and 8; *5* — calculation based on Eq. (22) with the parameters indicated on curve *1*.

$$f(H)=\frac{A}{B^2+C^2}, \tag{17}$$

where

$$A=\frac{ab^2}{1+\gamma_1^2}+\frac{1}{1+\gamma_2^2},$$

$$B=\frac{ab}{1+\gamma_1^2}+\frac{1}{1+\gamma_2^2},$$

$$C=\frac{ab\gamma_1}{1+\gamma_1^2}+\frac{\gamma_2}{1+\gamma_2^2}.$$

The function $f(H)$ introduced in this way decreases monotonically with field from its largest value $f(0)$.

Equations (1), (16), and (17) do not include the energy dependence $\tau(\varepsilon)$. Hence, in order to correctly compare the simplified model used to derive these expressions with experiment, with the ultimate goal of isolating the contribution of the light-hole band, we first discuss the ratio of the magnetic field-induced change in the Hall coefficient to its largest, i.e., weak-field, value:

$$\frac{R(H)}{R(0)}=\frac{f(H)}{f(0)}, \tag{18}$$

where

$$f(0)=\frac{ab^2+1}{(ab+1)^2}. \tag{19}$$

Construction of the magnetic-field dependence of $R(H)/R(0)$ requires knowledge of the ratios a and b and one of the quantities μ_1 or μ_2. As a first approximation, we assign the ranges of values of these ratios known from the literature: $a\in[0.02;0.04]$ and $b\in[5,8]$. We next calculate μ_2 from our experimentally measured value of the conductivity σ in the samples under study:[10)]

$$\mu_2=\frac{\sigma}{ep_2(ab+1)}. \tag{20}$$

The heavy-hole concentration p_2 appearing in Eq. (20) is found from the experimental values of the Hall coefficient in the weak-field limit $R_{\exp}(0)$ and the Hall factor determined at these fields for p-Ge:

$$p_2=\frac{r_p(0)}{ecR_{\exp}(0)(1+a)}. \tag{21}$$

Figure 7 shows the magnetic-field dependence of the Hall coefficient calculated from Eqs. (17) and (18) for a sample with a Hall concentration of 1.09×10^{16} cm^{-3} (see Fig. 2, curve *4*) for several values of a and b together with our experimental data.

It should be noted that, strictly speaking, Eq. (17) is suitable for describing the magnetic-field dependence of the Hall coefficient (18) only over a limited range of magnetic fields. There are two reasons for this. First, the influence of hole scattering on the Hall coefficient changes as the field increases.[11)] Second, as we already noted, Eqs. (1), (17), and (18) cannot describe the fine structure in the Hall effect in strong magnetic fields that can be observed in weakly doped samples (Fig. 2), and therefore the corresponding range of fields should be excluded from the analysis. In light of what

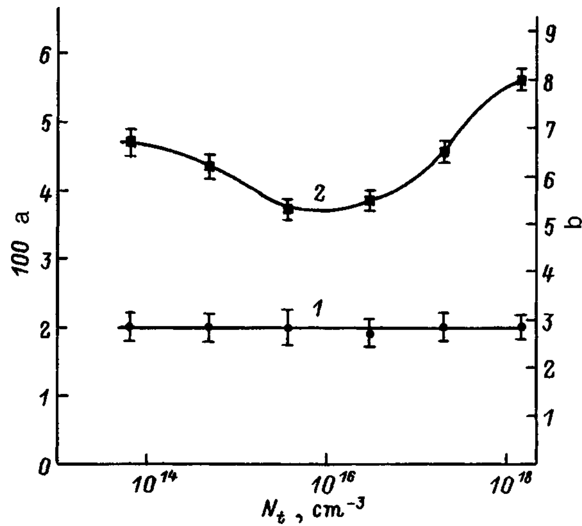

FIG. 8. Dependence of the experimental values of a (*1*) and b (*2*) at $T=77$ K on the concentration of ionized impurities N_t.

was said above, we limit ourselves to the range of fields corresponding to the inequality $\gamma \leqslant 1$ in comparing the experiment with calculations. The boundary defined by this inequality is located roughly in the middle of the region in Fig. 2 where the Hall coefficient falls off due to suppression of the influence of light holes. By some simple transformations based on the fact that $ab \ll 1$ and $\gamma_2 \ll \gamma_1$ in this range of fields, we obtain the asymptotic expression for the influence function $f(H)$ in fields that are not strong for light holes:

$$f(H)=\frac{a_{\text{eff}} b^2+1}{(a_{\text{eff}}+1)^2}, \tag{22}$$

where $a_{\text{eff}}=a/(1+\gamma_1^2)$ is the effective ratio between the light- and heavy-hole concentrations in a magnetic field. Equation (22) clearly shows the effect of the exclusion of light holes. In particular, at the limiting value $\gamma_1=1$ their influence factor is halved. It is clear from Fig. 7 (curves *2* and *5*) that in the range of magnetic fields of interest to us from the point of view of fitting, the asymptotic expression (22) is in good agreement with the original, more complicated function (17).

Let us now turn to the procedure for fitting the ratio $R(H)/R(0)$ calculated from Eqs. (17) and (18) to the corresponding experimental dependences. The values of a and b found from this procedure for the samples of p-Ge under investigation are shown in Fig. 8. In this case it turns out that the ratio between the light- and heavy-hole concentrations is constant to good accuracy:

$$a=0.02\pm 0.003. \tag{23}$$

However, the mobility ratio $b=\mu_1/\mu_2$ equals 6 in the weak-doping limit (phonon scattering) and then decreases to roughly 5 in the region of intermediate doping (mixed scattering), after which it increases to 8 as high doping levels are reached (scattering by ionized impurities and a transition to degeneracy). For weak doping levels the value $b\approx 6$ is in agreement with calculations that take into account the anisotropy of the heavy-hole band.[1,14]

6. INFLUENCE OF THE DOPING LEVEL ON THE EFFECTIVE HALL FACTOR IN *p*-Ge

Let us consider the concentration dependence of the effective Hall factor $r_p(N_{tp})$ in p-Ge in the limit $H\to 0$ at nitrogen temperature (Fig. 6b, curve *1*). Here we observe a gradual transition from the limit of pure lattice scattering (acoustic phonons) to scattering by ionized impurities and then to degeneracy as the doping level increases. In this case, the region of mixed scattering is characterized by equality of the relaxation rates for both scattering mechanisms, which is realized at a concentration $N_{tp}=4.4\times 10^{15}$ cm^{-3}. The experimental value for the effective Hall factor in this case is $r_p=1.4\pm 0.1$. It is known (see, e.g., Refs. 1–4) that this is the minimum value of the Hall factor for scattering with the participation of phonons and impurities. In the plateau region for lattice scattering by acoustic phonons, averaging over a data set bounded by a concentration of 10^{15} cm^{-3} gives $r_p=1.5\pm 0.3$. In the vicinity of the maximum of the $r_p(N_{tp})$ curve, which corresponds to scattering by ionized impurities, we have $r_p=2.3\pm 0.2$. Finally, for the case of hole degeneracy in p-Ge (at nitrogen temperatures it corresponds to an acceptor concentration $N_{\text{deg}}=10^{18}$ cm^{-3}, while for neutron-irradiated Ge : Ga with $K=0.3$ the total concentration of ionized impurities $N_{tp}\approx 2\times 10^{18}$ cm^{-3}) the value of r_p should tend to 1. However, in our case the value of r_p continues to decrease even when $N\approx N_{tp}$. A comparative analysis of the temperature dependences of the Hall coefficient and the resistivity shows that this is associated with the inadequacy of using the one-band model for conduction within the valence band, because at these concentrations conduction within the impurity band already has a strong influence. Values of the effective Hall factor corrected to take this fact into account are shown in Fig. 6b by dots.

Let us now discuss the function $r_p(N_{tp})$ at $T=300$ K. As in the case of nitrogen temperature, our interest is in certain characteristic points, viz., the point where the lattice scattering is comparable to impurity scattering (mixed scattering) and the point where degeneracy begins. In this case, for mixed scattering we should take into account scattering by optical vibrations as well (see, for example, Ref. 15). The corresponding values of N_{tp} are 1.4×10^{18} cm^{-3} and 1.6×10^{19} cm^{-3}. As we see, only the first of these appears in our data set. Thus, all of our samples at $T=300$ K are far from degeneracy. The plateau in the concentration range up to 10^{16} cm^{-3}, by analogy with $T=77$ K, corresponds to pure lattice scattering (''acoustics'' + ''optics'');[2,6] here $r_p=1.9\pm 0.2$. As the concentration of impurities increases further and impurity scattering becomes stronger, the Hall factor falls to values close to 1 for the most strongly doped samples. However, although r_p attains values somewhat less than 1, this anomaly is simply a consequence of mixed scattering (see Ref. 15) and differs in character from the anomalous decrease in r_p at the same concentrations at 77 K, which is caused by the two-band nature of the conductivity, as we have shown above.

We can explain the plots of $r_p(N_{tp})$ for $H=5.2$ and 28.6 kOe analogously (see Fig. 6). For these fields, however, a small decrease in r_p as the magnetic field increases is char-

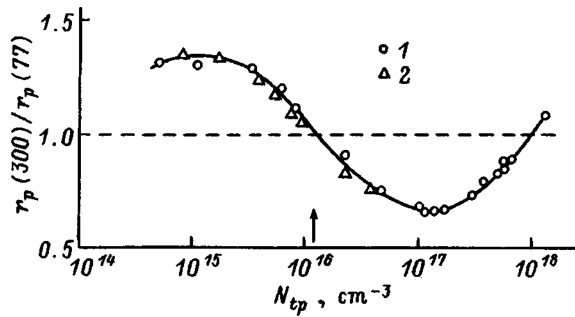

FIG. 9. Dependence of the experimental Hall factor ratio in p-Ge at $T=300$ and 77.4 K in a field $H=5.2$ kOe on the concentration of ionized impurities N_{tp}: *1* — data from the present work, *2* — data from Ref. 12 corrected by us using the value of K.

acteristic when $N_{tp}\leqslant 10^{17}$ cm^{-3}. The effect is strongest for lattice scattering and weak doping. Thus, at 77.4 K in the weak-doping limit, r_p equals 1.2 ± 0.2 ($H=5.2$ kOe) and 1.1 ± 0.2 ($H=28.6$ kOe). At $T=300$ K, in the limit of scattering by lattice vibrations only, r_p equals 1.6 ± 0.2 for 5.2 kOe and 1.0 ± 0.2 for 28.6 kOe.

In conclusion, we have described how the ratio $r_p(300)/r_p(77)$ depends on concentration in a field $H=5.2$ kOe (Fig. 9). This figure also shows data which we took from the paper by Fritzsche and Cuevas[12] and corrected for compensation. It is clear that these data are in good agreement with our own. From Fig. 9 we obtain a cutoff value of 1.3×10^{16} cm^{-3} for the concentration of ionized impurities in p-Ge, which is important for metrological reasons: below it we should use data from Hall measurements at 77.4 K for precision measurements of the hole concentration in p-Ge, while above it we should use data at 300 K.

7. SEVERAL APPLICATIONS OF OUR RESULTS

An important consequence of our results is the idea that the limiting value of the Hall factor $r_p=1$ in p-Ge is practically never achieved. The error arising from the use of the approximation $r_p=1$ can be very significant in determining the hole concentration. As an example, let us briefly consider the use of these results to investigate hopping conduction and the metal-insulator phase transition in neutron-irradiated p-Ge. As is well known, the pre-exponential factor σ_3 for nearest-neighbor hopping conduction is an exponential function of the distance $N^{-1/3}$ between impurities and is determined by the overlap integral of the corresponding localized wave functions of the nearest neighbors. If the latter can be characterized by the Bohr radius a, then in the region of weak overlap ($N^{1/3}a\ll 1$) we have the known result

$$\sigma_3^{-1}\propto \exp[\alpha/(N^{1/3}a)], \tag{24}$$

where α is a numerical coefficient, which depends weakly on the degree of compensation and can be calculated from percolation theory.[16]

For neutron-irradiated Ge : Ga with a degree of compensation $K\approx 0.3$, the theoretically calculated value is $\alpha=1.79\pm 0.03$. The experimental data of Fritzsche and Cuevas,[12] however, lead to a considerably different value: $\alpha=2.11\pm 0.10$. This disagreement between experiment and theory has stimulated efforts to include increasingly finer effects in the theory, which, however, have not lead to satisfactory agreement. As it turns out,[17] when the samples of neutron-irradiated Ge : Ga are correctly characterized with consideration of the effective Hall coefficient defined here and the degree of compensation, experiment does coincide with theory within the limits of error and gives

$$\alpha=1.81\pm 0.11. \tag{25}$$

In investigating metal-insulator transitions, the first problem is to precisely determine the critical point for the metal-insulator transition (in the case of the ''K-series'' of Ge : Ga samples, it is the concentration of primary impurities N_c). To this end we determine the transition point from both sides of the metal-insulator transition and then average the results, after which we use a self-consistent procedure to refine the critical point on the basis of the two-sided symmetry of the metal-insulator transition. In determining N_c from the insulator side, we use the fact that $T_0^{1/2}$ goes to zero approximately linearly with the concentration N for variable-range-hopping conduction in the Coulomb gap:

$$\sigma(T)\propto \exp(T_0/T)^{1/2},$$

while from the metal side we use the ''zero-temperature'' value $\sigma(0)$ for the low-temperature metallic conductivity. In both cases, a linear approximation is made using the least-squares method. Determining the critical point from both sides of the transition gives similar results with an average value $N_c=(1.81\pm 0.04)\times 10^{17}$ cm^{-3} for real values of r_p. Using the power-law dependence of the localization radius a and the quantity $\sigma(0)$ on the correlation length $\xi\propto(1-N/N_c)^{\nu}$ postulated in scaling theory and the value of N_c found above, we obtain the following values of the critical indices: $\nu_a=-0.85$, $\nu_\sigma=0.97$.

Our next step is to refine these indices from the symmetry of the metal-insulator transition within scaling theory:

$$\nu_\sigma=|\nu_a|=\nu. \tag{26}$$

This procedure reduces to weakly varying N_c up to the value $(N_c)_{\text{corr}}$, at which Eq. (26) is precisely satisfied:

$$(N_c)_{\text{corr}}=(1.85\pm 0.04)\times 10^{17}\text{cm}^{-3}. \tag{27}$$

In this case the critical index for the correlation length is

$$\nu=|\nu_a|=\nu_\sigma=0.93\pm 0.04. \tag{28}$$

We note that if the crude approximation $r_p=1$ is used, values that are underestimated by roughly 30% are obtained for N_c. The indices in this case differ less noticeably from the true indices by virtue of the relatively weak concentration dependence of the Hall factor in the critical region of the transition.

8. CONCLUSION

We have proposed and implemented a way to experimentally resolve the problem of determining the contribution of light holes to the Hall effect in p-Ge over the entire range of doping levels. It involves making closely coupled changes in the concentrations of free carriers Δp and Δn in germanium with p- and n-type conductivity that can be determined

from Hall measurements. These ''coupled changes'' are effected by the neutron transmutation doping of pairs of samples, in one of which the change in electron concentration is recorded (the reference sample), while in the other the hole concentration is recorded. The unambiguous connection between changes in the carrier concentrations in the sample under study and the reference sample, as determined by the schemes used in our three types of experiments, allows us to express the effective Hall factor in p-Ge in terms of the Hall factor for n-Ge calculated within the theory of anisotropic scattering.[10] The influence of light holes was investigated by eliminating it with the help of a magnetic field. By introducing the concept of an ''effective'' Hall factor $r_p(H)$ in p-Ge, we were able to establish a simple link between the measured Hall coefficient and the total concentration of holes in the one-band approximation. Isolating the contribution of light holes to the Hall effect for p-Ge in this case reduces to studying the behavior of its effective Hall factor in a magnetic field.

As the magnetic field increases, the contribution of light holes to the Hall effect is gradually eliminated; in this case the value of the Hall coefficient falls as the cyclotron frequency of the light holes approaches the collision frequency determined by their scattering mechanism.

The ratio between the light- and heavy-hole concentrations, which is optimally fitted to the magnetic-field dependence of the Hall coefficient turns out to equal 0.02. However, the ratio between their mobilities in the weak-doping limit is approximately equal to 6, which corresponds to calculations for the case of phonon scattering. As the doping level increases, the anisotropy of the heavy-hole band becomes less important due to the transition to impurity scattering, and the ratio subsequently approaches the calculated value for the case of an isotropic band, which equals 8. We have obtained the concentration dependences of the effective Hall factor for three magnetic fields, viz., $H\rightarrow 0$, $H\simeq 5$, and $H=30$ kOe, which show that the contribution of light holes to the Hall effect is greatest in the case of weak doping (the region of phonon scattering) and weak fields. It decreases with increasing magnetic field and vanishes as we approach the strong- field criterion for high-mobility holes. Determining the dependence of the effective Hall factor for p-Ge solves the problem of exactly characterizing the hole concentration in p-Ge from Hall measurements over the entire range of doping levels.

By applying these results to the precision determination of the hole concentration and degree of compensation, we have resolved the long-standing discrepancy between theory and experiment in describing the concentration dependence of the pre-exponential factor for hopping conduction among nearest neighbors in neutron-irradiated Ge : Ga. Our results also facilitate a considerably more correct study of the metal-insulator phase transition in neutron-irradiated Ge : Ga.

We are grateful to V. A. Evseev for working with us on irradiating the samples, as well as the participants in the ''Nonequilibrium Processes in Semiconductors'' laboratory seminar at the A. I. Ioffe Physicotechnical Institute of the Russian Academy of Sciences for discussing the results.

This work was partially supported by the Russian Fund for Fundamental Research (Grant 96-02-17936).

[1)] The derivation of this expression can be found, for example, in the book by Blatt.[5]

[2)] Consideration of the anisotropy effects increases this ratio (see, e.g., Ref. 7).

[3)] For scattering by acoustic phonons, the field H_1 at liquid-nitrogen temperatures amounts to several hundred oersteds.

[4)] At liquid-nitrogen temperature the value of the field H_2 for phonon scattering comes to a few kOe.

[5)] Higher accuracy is needed, for example, in analyzing hopping conduction, which depends exponentially on the concentration of majority carriers, and also in investigating whether or not metal-insulator transitions are type-II phase transitions.

[6)] Weakly doped samples are measured in liquid nitrogen in order to eliminate the effect of intrinsic carriers.

[7)] The degree of compensation of neutron- transmutation-doped Ge increases slightly with hardening of the spectrum of reactor neutrons.[9]

[8)] Some of our preliminary results were briefly reported in Ref. 11.

[9)] In Fig. 3 and subsequent figures, the total concentration of ionized impurities $N_t=N(1+K)$, where K is the degree of compensation and $N=n/(1-K)$ or $p/(1-K)$ in n- or p-type material, respectively.

[10)] Conductivity measurements were made simultaneously with the Hall measurements.

[11)] In the one-band model, for instance, the corresponding change in the Hall factor due to scattering by ionized impurities can be as large as a factor of 2 as the field varies from weak to strong. In the two-band model this effect is weaker, but does not disappear entirely.

[1] A. C. Beer and R. K. Willardson, Phys. Rev. **110**, 1286 (1958).
[2] A. C. Beer, *Galvanomagnetic Effects in Semiconductors* (New York–London, Academic Press, 1963).
[3] G. L. Bir, É. Normantas, and G. E. Pikus, Fiz. Tverd. Tela (Leningrad) **4**, 1180 (1962) [Sov. Phys. Solid State **4**, 867 (1962)].
[4] A. C. Beer, J. Phys. Chem. Solids **8**, 507 (1959).
[5] F. J. Blatt, *Physics of Electronic Conduction in Solids* (McGraw-Hill, New York, 1968) [Mir, Moscow, 1971].
[6] R. K. Willardson, T. C. Harman, and A. C. Beer, Phys. Rev. **96**, 1512 (1954).
[7] P. Lawaetz, Phys. Rev. **174**, 867 (1968).
[8] A. G. Zabrodskiĭ and M. V. Alekseenko, Fiz. Tekh. Poluprovodn. **27**, 2033 (1993) [Semiconductors **27**, 1116 (1993)].
[9] A. G. Zabrodskiĭ and M. V. Alekseenko, Fiz. Tekh. Poluprovodn. **28**, 168 (1994) [Semiconductors **28**, 101 (1994)].
[10] P. I. Baranskiĭ, I. S. Buda, I. V. Dakhovskiĭ, and V. V. Kolomoets, *Electrical and Galvanomagnetic Phenomena in Semiconductors* [in Russian] (Naukova Dumka, Kiev, 1977).
[11] M. V. Alekseenko, A. G. Andreev, A. G. Zabrodskiĭ, and V. V. Popov, Fiz. Tekh. Poluprovodn. **22**, 140 (1988) [Sov. Phys. Semicond. **22**, 86 (1988)].
[12] H. Fritzsche and M. Cuevas, Phys. Rev. **119**, 1238 (1960).
[13] P. I. Baranskiĭ and R. M. Vinetskiĭ, Fiz. Tverd. Tela (Leningrad) **4**, 289 (1962) [Sov. Phys. Solid State **4**, 208 (1962)].
[14] M. Tiersten, J. Phys. Chem. Solids **25**, 1151 (1964).
[15] J. S. Johannessen, Phys. Status Solidi A **12**, 251 (1972).
[16] N. Lien, B. I. Shklovskiĭ, and A. L. Éfros, Fiz. Tekh. Poluprovodn. **13**, 2192 (1979) [Sov. Phys. Semicond. **13**, 1281 (1979)].
[17] A. G. Zabrodskiĭ, A. G. Andreev, and M. V. Alekseenko, Fiz. Tekh. Poluprovodn. **26**, 431 (1992) [Sov. Phys. Semicond. **26**, 244 (1992)].

Translated by Frank J. Crowne

Computer-simulation investigation of nonlinear transport dynamics in a compensated semiconductor during low-temperature electric breakdown

K. M. Jandieri and V. S. Kachlishvili

Physics Department, Tbilisi State University, 380028 Tbilisi, Georgia
(Submitted May 12, 1996; accepted for publication February 7, 1998)
Fiz. Tekh. Poluprovodn. **32**, 821–826 (July 1998)

The possibility of chaotic behavior of the current in a partially compensated semiconductor during low-temperature electrical breakdown is explored by computer simulation. The influence of random fluctuations in the parameters or the variables of the mathematical model, as well as the effect of some weak periodic disturbances of the current density in the semiconductor, are discussed. As a result, various pictures of chaotic oscillations of the current are obtained, including a transition to a chaotic regime through period doubling, which is characteristic of the Feigenbaum scenario. © *1998 American Institute of Physics.* [S1063-7826(98)01107-7]

1. It is well known that the instability of electron transport in semiconductors manifests itself in the form of periodic, quasiperiodic, or chaotic oscillations in the current. The study this area of semiconductor physics has been pursued with special intensity in the last 15 years. Experiments have been done on various materials: Si, InSb, GaAs, Ge (see the review in Ref. 1), CdS,[2] etc. In order to observe chaotic oscillations it is necessary in some cases to impose additional conditions on the experiment, such as to switch on a magnetic field, to illuminate the sample, etc. A special place among these studies is occupied by the study of spontaneous oscillations in the neighborhood of electrical breakdown, where a precipitous increase in the free-carrier concentration leads to an abrupt change in the sample conductivity. In this case there have been discussions of both low-temperature and band-to-band breakdown. For these cases there are theoretical papers that predict nonlinear and, in particular, chaotic behavior of the current in the semiconductors (see, e.g., Refs. 3–5).

In Ref. 6 we investigated the question of how undamped current oscillations arise in a partially compensated, spatially homogeneous semiconductor during low-temperature electric breakdown. Based on a mathematical model including equations that describe generation-recombination processes, dielectric relaxation of the electric field, and the delay in the variation of the electron temperature relative to the variation of the electric field, we obtained a necessary and sufficient condition for the appearance of undamped oscillations due to Hopf bifurcation. By analyzing this condition, we obtained criteria from which it was clear which scattering mechanism and which values of the system parameters (such as the concentration of majority carriers, degree of compensation, delay time of the electron temperature, load resistance, etc.) favor the appearance of regular or even chaotic oscillations in a system (for chaotic behavior our condition is necessary but not sufficient).

In this work we use computer simulation based on the results of Ref. 6 to investigate the possibility of chaotic behavior in a system as a function of its parameters. In the computer calculations we use the Runge–Kutta method to solve the system of differential equations for the mathematical model described above:

$$\frac{dn}{dt}=-n^*a(z)x^2+[b(z)-2a(z)n^*]x + \frac{d}{n^*}+b(z)-a(z)n^*, \quad (1)$$

$$\frac{dy}{dt}=BL\left[\frac{\zeta}{E^*}-1-y-\frac{e\mu(z)SR}{L}n^*(1+x)(1+y)\right], \quad (2)$$

$$\frac{dz}{dt}=-\frac{1}{\tau}\left[1+z-\frac{\vartheta_0(y)}{\vartheta^*}\right], \quad (3)$$

where

$$x=\frac{n-n^*}{n^*},\quad y=\frac{E-E^*}{E^*},\quad z=\frac{\vartheta-\vartheta^*}{\vartheta^*}.$$

Here n is the concentration of free electrons; E is the electric field intensity along the sample; μ is the mobility of the free electrons $\mu=\mu_0\vartheta^{-1/2}$, where $\mu_0\approx 8\times 10^8\ \mathrm{cm^2/V\cdot s}$; $\vartheta=T_e/T$, where T_e is the electron temperature and T is the lattice temperature; and ϑ_0 is the stationary value of ϑ. According to Refs. 4 and 6, the appearance of undamped oscillations facilitates saturation of the drift velocity. Starting from this, we use the following expressions for ϑ_0:

$$\vartheta_0(E)=\alpha E^2,$$

where $\alpha\approx 1.4\times 10^4\ \mathrm{cm^2/V^2}$ (for $\vartheta\sim E^2$, $\mu\sim E^{-1}$, and $v=\mu E=\mathrm{const}$). The parameters n^*, E^*, and ϑ^* are the equilibrium values of the respective quantities; $a=A_I+B_T$; $b=-\gamma-B_TN_dc+A_IN_d(1-c)$; $\gamma=j\sigma+A_T$; $d=\gamma N_d(1-x)$; $j\sigma$ and A_T are the rates of optical and thermal generation from donor levels; $c=N_A/N_d$ is the degree of compensation of the sample; N_d and N_A are the concentrations of donors and acceptors, respectively; and A_I and B_T are the impact-ionization and thermal-recombination coefficients.

 © 1998 American Institute of Physics

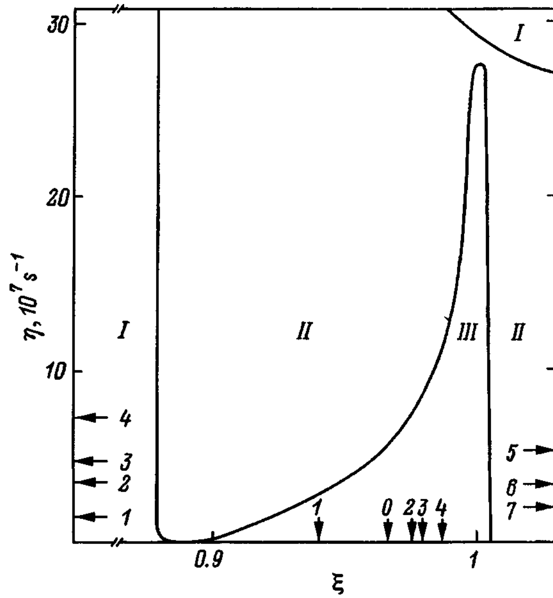

FIG. 1. Bifurcation diagram in the (ξ, η) plane for the following values of the system parameters: $c=0.9$; $N_d=10^{14}$ cm^{-3}; $\tau=4\times10^{-8}$ s; $\gamma=10^3$ s^{-1}. The breakdown value of the electric field $E_B\approx11.92$ V/cm. The arrows with numbers on the horizontal axis indicate the values of ξ_i, $0\leq i\leq4$; the arrows on the vertical axis indicate the values of η_i, $1\leq i\leq7$. See the text for the physical meaning of ξ_i and η_i.

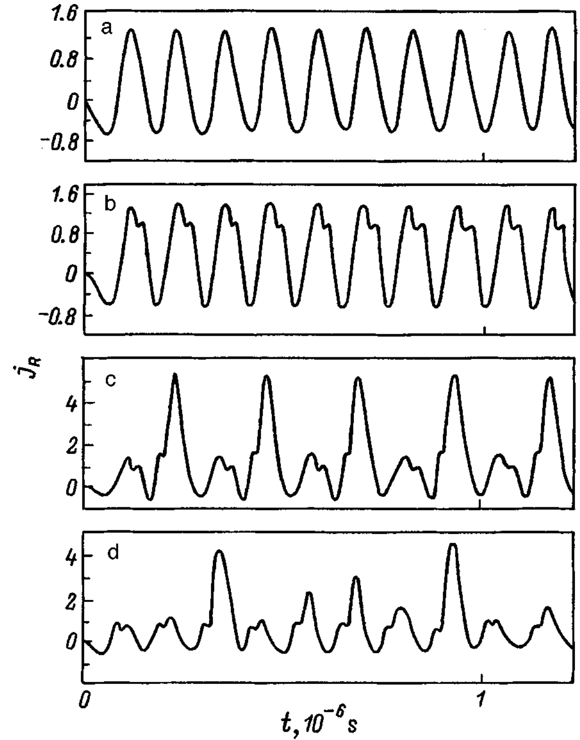

FIG. 2. Dependence of $j_R=(j-j^*)/j^*$ on the time t (where j^* is the equilibrium value of the current density). The nonbifurcation parameters are the same as in Fig. 1. The values of the bifurcation parameters are given in the text.

For the impact-ionization coefficient we use the results of Ref. 7, where A_I was calculated in the electron-temperature approximation using the Dravin cross section. For the thermal-recombination coefficient we use the results of Ref. 8, where B_T was calculated with the help of the corrected cascade theory of Lax. In order to minimize the expenditure of machine time, we used the approximate expressions

$$A_I=C_1\vartheta\exp(-C_2/\vartheta^2)\quad\text{and}\quad B_T=C_3/\vartheta^2.$$

Here $C_1\approx3.4\times10^{-7}$ cm^3/s, $C_2\approx250$, and $C_3\approx2.6\times10^{-4}$ cm^3/s (numbers chosen to match n-Ge), which give a good description of the real functions in the neighborhood of the breakdown point. The parameter $\zeta=\mathcal{E}/L$, where $\mathcal{E}$ is the emf of the dc power source, and L is the sample length along the current; S is the transverse cross-sectional area of the sample; R is the resistance of the load connected in series with the sample; and $B=4\pi/\varepsilon SR$, where ε is the dielectric constant of the sample.

The computer simulation consisted of two stages. In the first stage we established the bifurcation diagram (Fig. 1) using $\xi=E^*/E_B$, where E_B is the breakdown value of the electric field intensity, and the quantity $\eta=4\pi L/\varepsilon SR$ as the bifurcation parameters. On this diagram we demarcated a region of saddle-focus points (region III), which corresponds to the appearance of undamped oscillations. In the second stage we solved the system of Eqs. (1)–(3) and used the time dependences $x(t)$, $y(t)$, and $z(t)$ to obtain the temporal evolution of the behavior of the current density.

In the second stage we consider the nonlinear behavior of the semiconductor at low temperatures when illumination is present. As we established in Ref. 6, switching on illumination greatly broadens the region of undamped oscillations with respect to the electric field. The values of the nonbifurcation parameters are listed in Fig. 1, where region I corresponds to the stable nodal points and region II to the stable focal points (i.e., damped oscillations in the system).

The bifurcation parameters were varied in such a way that ζ remained unchanged. The parameters η, E^* and ζ obey the following dependence:

$$\eta\sim\mu(\vartheta^*)n^*E^*/(\zeta-E^*).$$

In particular, variations in η are connected with changes in the load resistance for fixed values of the external emf. Under these conditions, as ξ gradually increases, the following sequence of changes occurs in the behavior of the system: at the beginning (at $\xi=\xi_1\approx0.94$, see Fig. 1, which corresponds to $\eta=\eta_1\approx1.48\times10^7$ s^{-1} for the constant value $\zeta=86$ V/cm) we observe periodic current oscillations in the system (Fig. 2a). Increasing ξ to $\xi=\xi_2\approx0.975$ (which corresponds to $\eta=\eta_2\approx3.73\times10^7$ s^{-1}) initiates period doubling (Fig. 2b). When ξ is increased further to $\xi=\xi_3\approx0.978$ (which corresponds to $\eta=\eta_3\approx4.71\times10^7$ s^{-1}), the picture we observe is characteristic of period quadrupling (Fig. 2c), etc. Finally, at $\xi=\xi_4\approx0.987$ (which corresponds to $\eta=\eta_4\approx7.38\times10^7$ s^{-1}) chaotic undamped oscillations begin. Thus, we have reproduced the traditional picture of a transition to chaos via period doubling, i.e., the Feigenbaum scenario. The values of ζ_i and η_i mentioned here are marked by arrows with numerical labels in Fig. 1.

Next, we investigated the influence of small random variations in the system parameters or the variables x, y, and z themselves on the system dynamics in each step of the iterative calculations. Moreover, with the goal of studying

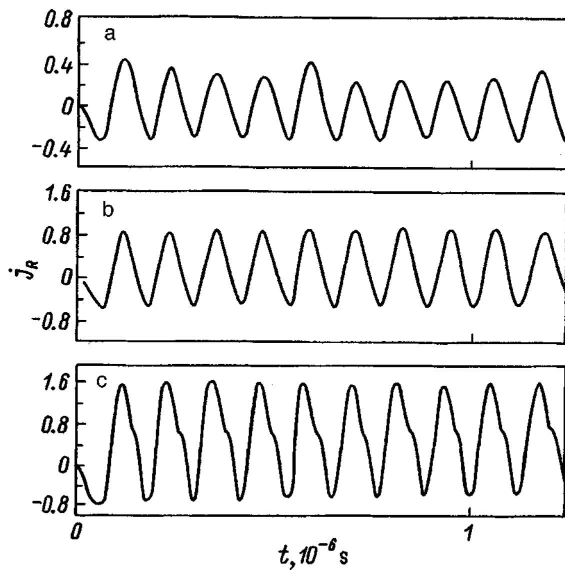

FIG. 3. Plots of $j_R(t)$ when the parameters R, ζ, and γ are subjected to a 4% random fluctuation for the following values of the bifurcation parameters: $\xi=\xi_0\approx 0.965$; a — $\eta=\eta_5\approx 5.43\times 10^7$ s^{-1}, b — $\eta=\eta_6\approx 3.41\times 10^7$ s^{-1}, c — $\eta=\eta_7\approx 2.05\times 10^7$ s^{-1}.

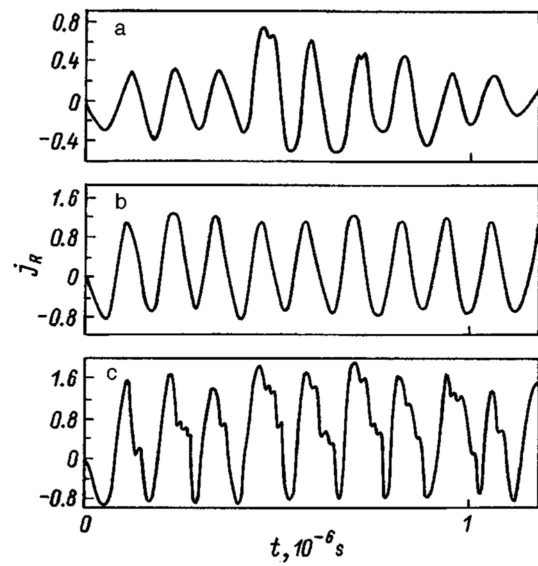

FIG. 4. Plots of $j_R(t)$ when the variables x, y, and z are subjected to a 4% random fluctuation. The values of the parameters are the same as in Fig. 3.

the influence of some periodic weak disturbances of the parameters of the system, we added periodic components with small amplitudes. The corresponding results are shown in Figs. 3–5.

(I). A 4% random fluctuation was imposed on the parameters R, ζ, and γ. The results obtained for this case (as in the two other cases) correspond to the variation of η at a fixed value of $\xi=\xi_0\approx 0.965$ within region III shown in the bifurcation diagram. (Of course, when R fluctuates, η fluctuates as well. However, because of the smallness of this fluctuation, the values of η we investigated do not overlap one another.) Plots of the corresponding temporal behavior of the relative magnitude of the current density are shown in Fig. 3. In contrast to the results shown in Fig. 2, the behavior of the system becomes more markedly chaotic, the closer η is to its bifurcation value. As η decreases, the amplitude of the oscillations increases, and, at the same time, the chaotic behavior becomes less and less noticeable. Below the value $\eta=\eta_6\approx 3.41\times 10^7$ s^{-1} it practically disappears completely, i.e., only regular oscillations are observed. As η is decreased further, a tendency towards period doubling is observed at $\eta=\eta_7\approx 2.05\times 10^7$ s^{-1}.

(II). A random 4% fluctuation was imposed on the variables x, y, and z. Here the chaotic behavior is much more apparent (Fig. 4). For the values of η where period doubling was observed in the previous case, chaos is clearly expressed here (Fig. 4c).

(III). We added a sinusoidal component to the parameter ζ, whose amplitude amounted to 4% of the value of ζ. Here also the chaotic behavior becomes more pronounced, the closer η is to the bifurcation value. As η decreases, the amplitude of the oscillations increases, and the chaotic behavior becomes less and less noticeable (Fig. 5b). As η is decreased further, we observe a tendency towards period doubling (Fig. 5c). It is noteworthy that the character of the chaotic behavior depends to a considerable degree on the frequency of the periodic component. When this frequency coincides with an eigenfrequency of the system, we observe a picture similar to beating. This finding may suggest that a simple superposition of regular oscillations occurs, but in reality this is not so, since exact repetition of the amplitude values would not occur within such a picture.

Thus, the cases just described gave different pictures of the appearance of chaotic oscillations in partially compensated semiconductors during low-temperature electrical breakdown, including a transition to a chaotic regime by way of period doubling, which is characteristic of the Feigenbaum scenario. In our view, this latter case is especially interesting, since it occurs only when the iteration step is no smaller than a specific value $\Delta t_0=5\times 10^{-9}$ s.

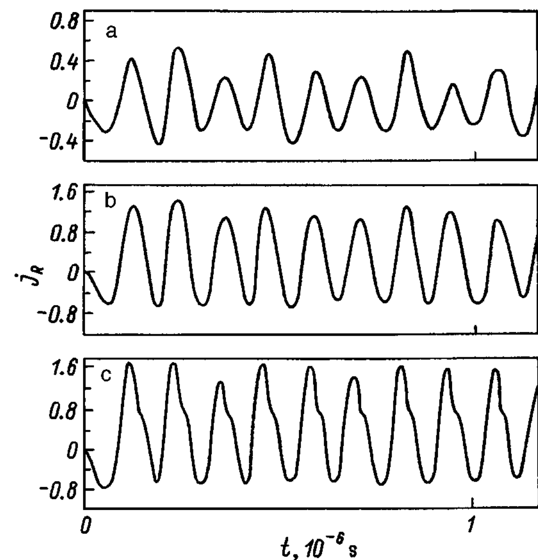

FIG. 5. Plots of $j_R(t)$ when a sinusoidal component is added to the parameter ζ. The amplitude of this component equals 4% of the value of ζ. The values of the parameters are the same as in Fig. 3.

Our calculations were performed with two different accuracy levels for representing numbers in the computer (with retention of 7 and 17 decimal places, respectively). A change in accuracy did not lead to qualitative changes in the behavior of the system, and the numerical changes were also insignificant. From this it follows that changes in the behavior of the system due to a decrease in the iteration step are associated not with accuracy of numerical representations in the computer, but simply with the size of the step. Despite the fact that the value $\Delta t_0 = 5\times 10^{-9}$ s is much smaller than the characteristic times of the equations in our mathematical model, the calculation results obtained with this step size do not correspond to reality (more precisely, these results are not solutions to our system of differential equations), since we observe a qualitatively different picture of the behavior of the system when we halve the step size, while further decreases in the step size leave the picture practically unchanged (i.e., we can assume that the results of the calculations with the step size $\Delta t_1 = 2.5\times 10^{-9}$ s correspond to an exact solution of our mathematical model). For this reason, it would be interesting to explore in what way and under what circumstances we can obtain a picture similar to Fig. 2 with the step size $\Delta t_1 = 2.5\times 10^{-9}$ s, i.e., a picture corresponding to a true solution to our differential equations.

Figures 6a and 6b show phase portraits of the system in the (x,z) and (x,y) planes obtained for the same values of parameters as in Fig. 2, but with an iteration step of size $\Delta t_1 = 2.5\times 10^{-9}$ s. Figure 6c shows the most interesting fragment of the phase portrait on the (x,y) plane obtained with the step size $\Delta t_0 = 5\times 10^{-9}$ s (curve *2*). In contrast, curve *1* is qualitatively the same as the curve in Fig. 6b. (For comparison, curve *1* in Fig. 6c represents the projection of the stationary trajectory corresponding to Δt_1.) The phase portraits in the (x,z) plane obtained for Δt_0 and Δt_1 scarcely differ from one another on every portion of the phase trajectory.

As we see from Fig. 6, the phase trajectories extend along positive values of x, i.e., the concentration oscillations are strongly anharmonic (due to the very rapid growth in the free-carrier concentration near the breakdown point). In the neighborhood of point A (Fig. 6b) the trajectories are extremely close to one another, and small deviations of the variables from their values can cause hops to a neighboring nonstationary quasicyclic trajectory. As a result, depending on the sign of the deviations, the point B, which corresponds to a maximum of x, can shift strongly to the right or to the left with a simultaneous downward or upward displacement, respectively. Therefore, fluctuations and random external disturbances can cause chaotic oscillations in the free-carrier concentration and the electric field with marked changes in amplitude. This is especially noticeable in the concentration oscillations (for example, a single 0.5% deviation in n from its value in the neighborhood of point A changes the oscillation amplitude by 3%, a 1% deviation by 5%, a 5% deviation by 25%, etc.). The oscillation amplitude ϑ remains practically unchanged, and the relative change in the oscillation amplitude for E is of the same order of magnitude as the change in the oscillation amplitude for n due to the smallness of the value of E itself (in the neighborhood of the point B the value of y is close to -1).

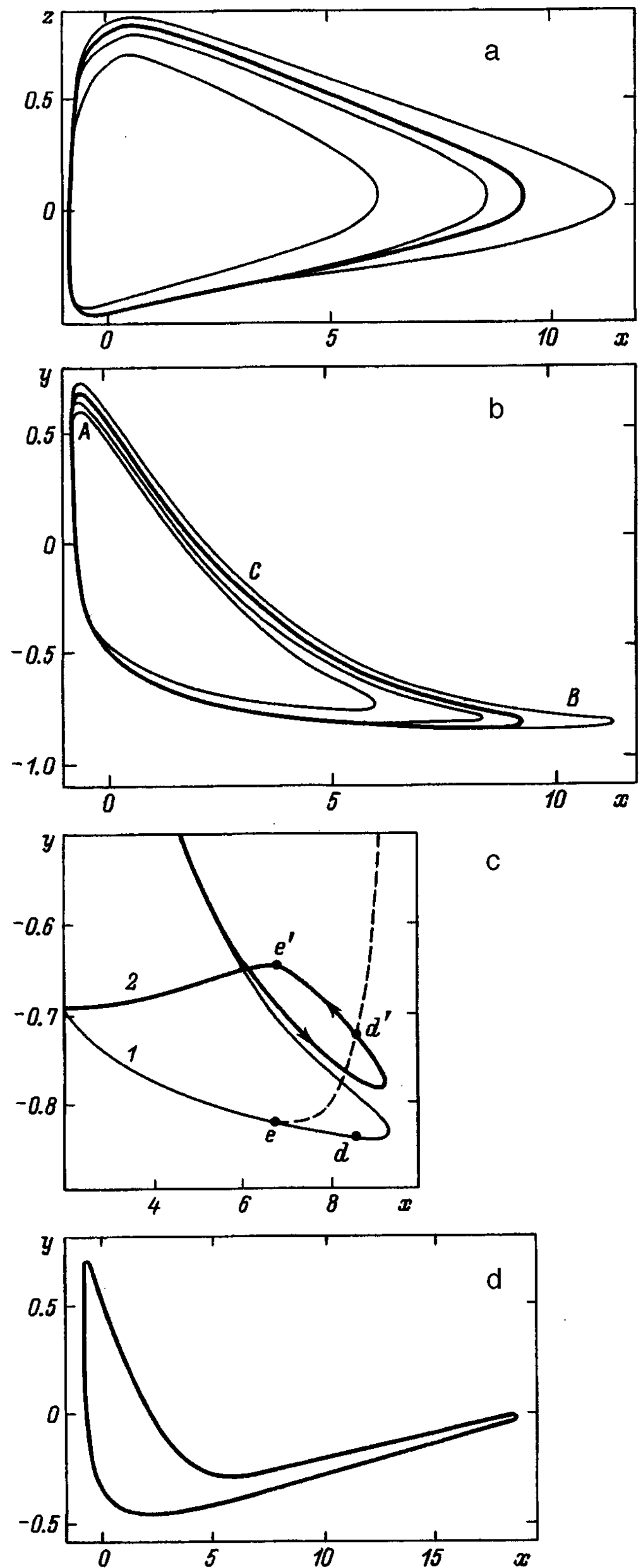

FIG. 6. Phase portraits in the (x,y) and (x,z) planes. In Figs. a and b the thick curve corresponds to a stationary cyclic trajectory, while the thinner curves correspond to nonstationary quasicyclic trajectories (further explanations are given in the text).

Oscillations of the current density do not display a similar picture. This is primarily because the minimum and maxi-

mum of each oscillation in j_R on the phase portrait correspond to neighborhoods of points A and C (Fig. 6b), which do not undergo significant changes in response to random deviations. The value of j_R does not change appreciably in the neighborhood of point B either, since, according to what was said above, the value of z does not change, while the change in n is partially compensated by the change in E. Thus, under the conditions of this problem, oscillations in the current density should be more stable toward random external disturbances and fluctuations than oscillations in n and E.

Let us now turn to Fig. 6c, where we show a loop-shaped projection of the phase trajectory onto the (x,y) plane obtained with the step size $\Delta t_0 = 5\times10^{-9}$ s (curve *2*). It is associated with computational errors in the neighborhood of point B and consequently cannot correspond to reality, but such a trajectory can be obtained from the exact solution as well (with the step size $\Delta t_1 = 2.5\times10^{-9}$ s) with the help of a properly tailored external disturbance of the system, more precisely a guided variation of y. A comparison of curves *1* and *2* clearly demonstrates what we have just said. In fact, the phase trajectories that correspond to curves *1* and *2* in the (x,y) plane differ from one another mainly with respect to the values of y [we recall that the projection of the phase trajectories onto the (x,z) plane obtained using the step sizes Δt_0 and Δt_1 are practically identical], and these differences have the same sign (positive). Moreover, if, for example, at point d we add an increment to the value of y corresponding to a transition from point d to point d', then in the course of roughly two iteration steps of size $\Delta t_1 = 2.5\times10^{-9}$ s the phase point, which moves along a nonstandard trajectory (the dashed curve), returns once more to curve *1* at point e (close to point d), which is characterized by the same values of x and z as point e' on curve *2*, which in turn is close to point d', i.e., it is obtained from d' after one iteration step of size $\Delta t_0 = 5\times10^{-9}$ s. Therefore, for a transition from point e to point e' it is sufficient to add an increment only to the value of y at point e, etc. Adding the corresponding increments to y in each iteration step in the region corresponding to the formation of the loop, we can obtain a phase trajectory similar to trajectory *2* with an iteration step of size $\Delta t_1 = 2.5\times10^{-9}$ s. Physically, this corresponds to a complex modulation of the external emf, but it turns out that the use of such a complicated modulation is not necessary. It is sufficient to impart constant positive deviations to the value of y. This is equivalent to adding a step function, which equals a certain constant ($\approx 3\times10^7$) in this region and zero in the remaining region, to the right-hand side of the equation for y. Physically, this corresponds to adding rectangular pulses to the external emf, whose value is roughly 10% of the value of the latter. Under these conditions, small random deviations are capable of causing chaotic oscillations in the value of j_R similar to the oscillations shown in Fig. 2.

We can obtain chaotic oscillations in j_R with still more marked variation of the amplitude due to fluctuations by choosing a disturbance of the system which would ensure motion of the maximum of j_R in the vicinity of point B with simultaneous motion of these two points in the direction of positive values of y, so that they come as close to zero as possible. The calculations show that for this it is sufficient to increase the right-hand side of the relaxation equation for y by a term proportional to $(x+1)^2/(y+1)$. The corresponding picture of the phase portrait is given in Fig. 6d for a value of the proportionality factor of order 2.5×10^6. Physically, this can come about if for positive values of j_R we add a bell-shaped pulse to the external emf whose height is 3–4 times larger than the value of the emf and whose width is approximately equal to half the oscillation period (5×10^{-8} s). Moreover, when we replace the bell-shaped pulse by a corresponding triangular pulse, we obtain a qualitatively similar picture of the phase portrait, i.e., a picture which is similar to the picture of chaotic oscillations in a semiconductor.

[1] R. P. Huebener, J. Parisi, and J. Feinke, Appl. Phys. A **48**, 107 (1989).
[2] L. L. Golik, M. M. Gutman, and V. E. Paskeev, Phys. Status Solidi B **162**, 199 (1990).
[3] E. Echoll, Appl. Phys. **48**, 95 (1989).
[4] É. S. Kachlishvili and I. D. Kezerashvili, Fiz. Tekh. Poluprovodn. **24**, 1106 (1990) [Sov. Phys. Semicond. **24**, 697 (1990)].
[5] V. V. Vladimirov and V. N. Gorshkov, Fiz. Tekh. Poluprovodn. **14**, 417 (1980) [Sov. Phys. Semicond. **14**, 247 (1980)]; V. V. Vladimirov, P. M. Golovinskiĭ, and V. N. Gorshkov, Fiz. Tekh. Poluprovodn. **15**, 40 (1981) [Sov. Phys. Semicond. **15**, 23 (1981)]; V. V. Vladimirov, V. N. Gorshkov, and V. K. Malyutenko, Fiz. Tekh. Poluprovodn. **26**, 1580 (1992) [Sov. Phys. Semicond. **26**, 887 (1992)].
[6] K. M. Jandieri and Z. S. Kachlishvili, Bull. Georgian Acad. Sci. **154** (1), 61 (1996); **154** (2), 208 (1996).
[7] Z. S. Kachlishvili, Phys. Status Solidi B **48**, 65 (1971).
[8] T. O. Gegechkori and V. Dzhakeli, Soobshch. Akad. Nauk Gruz. SSR **3**, 565 (1981).

Translated by Frank J. Crowne

Preparation and properties of GeS_2 single crystals

A. V. Golubkov,*) G. B. Dubrovskiĭ, and A. I. Shelykh

A. F. Ioffe Physicotechnical Institute, Russian Academy of Sciences, 194021 St. Petersburg, Russia

(Submitted February 2, 1998; accepted for publication February 10, 1998)
Fiz. Tekh. Poluprovodn. **32**, 827–828 (July 1998)

Single crystals of GeS_2 are grown by two methods: crystallization from a melt and chemical vapor transport. All crystals are found to have a monoclinic structure with the unit-cell parameters $a = 11.45$ Å, $b = 16.09$ Å, $c = 6.7$ Å, and $\beta = 91°$. The reflection and transmission spectra are measured in the region of the absorption edge. The gap width is found to be equal to 3.2 eV. © *1998 American Institute of Physics.* [S1063-7826(98)01207-1]

Germanium disulfide occupies a special place among metal dichalcogenides because of the structure of its crystal lattice. The unit cell of crystals of this compound contains 16 formula units and belongs to the monoclinic system.[1] The physical properties of GeS_2 single crystals have not yet been studied; therefore the present work is a first attempt to examine them.

The GeS_2 single crystals investigated in the present work were grown by two methods: crystallization from a melt and chemical vapor transport in a two-zone furnace with iodine as the transporting agent. In both cases germanium disulfide obtained by fusing a stoichiometric mixture of composites in an evacuated quartz ampoule at a temperature somewhat above the melting point served as the starting material. High-purity ingredients were used—germanium single crystals with impurity content no greater than $10^{14} cm^{-3}$ and OSCh 15-3 sulfur. When crystals were grown by the first method, germanium disulfide was melted in an evacuated and sealed quartz crucible with a conical bottom to reduce the number of nuclei. Then the temperature of the melt was set 40 °C above the melting point (830 °C), and the crucible was lowered through the temperature-gradient zone. The rate of lowering of the crucible was 0.5 cm/h for a temperature gradient of 180 °C/cm. In this way a boule 1 cm in diameter and 2.5 cm in length was obtained. In the lower (conical) part of the boule it was possible to split off plane-parallel wafers of the required thickness, suitable for physical investigations.

X-ray structural and powder diffraction analysis showed that these crystals had the composition GeS_2 and a monoclinic structure with the unit-cell parameters $a = 11.45$ Å, $b = 16.09$ Å, $c = 6.7$ Å, and $\beta = 91°$, in agreement with the data of Ref. 1.

When crystals were grown using chemical vapor transport, a few grams of GeS_2 and iodine were placed in quartz ampoules 20 mm in diameter and 25 cm in length to achieve a quantity of 4.5 mg per cubic centimeter of the ampoule volume. After evacuation and sealing of the ampoule, it was placed in a furnace, in which the temperature of the hot zone was maintained at a level of 600 °C, and the cold zone was maintained at 500 °C. Material passed into the cold zone. The GeS_2 single crystals obtained in this way were shiny, transparent, and often well-faceted wafers of thickness up to 100 μm and area up to 0.5 cm^2. Their crystal structure and properties did not differ from those of the samples obtained from a melt.

Optical measurements were performed on the samples. Figure 1 displays the spectral dependence of the transmittance (T) and reflectance (R) of the samples. In the region of the edge of the fundamental absorption band the transmittance was measured at temperatures from 20 to 100 °C. The temperature coefficient of the gap width in this range is about -1×10^{-3} eV/°C. The dependence of the absorption coefficient α on the photon energy $h\nu$ at room temperature, calculated from the data of Fig. 1, is plotted in Fig. 2 in $(\alpha h\nu)^{1/2}$ versus $h\nu$ coordinates. As can be seen from this figure, the spectral dependence of the absorption coefficient has the form of two intersecting straight lines in these coor-

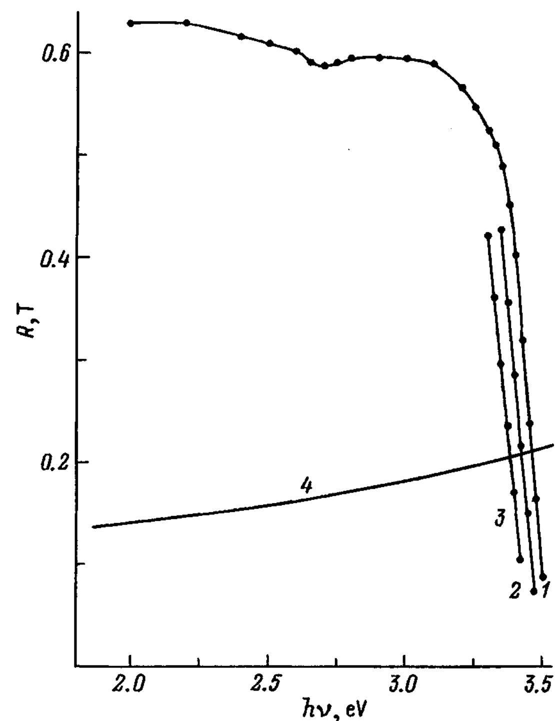

FIG. 1. Spectral dependence of the optical reflectance R (*4*) and transmittance T (*1–3*) for samples of GeS_2 of thickness 14 μm. Temperature, °C: *1* — 20, *2* — 70, *3* — 120.

 © 1998 American Institute of Physics

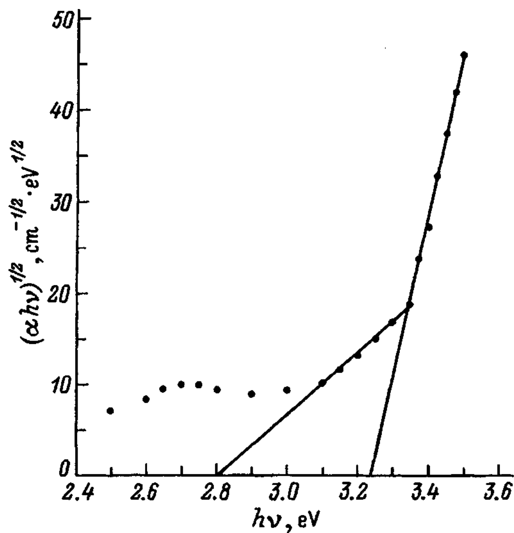

FIG. 2. Dependence of $(\alpha h\nu)^{1/2}$ on $h\nu$ in the region of fundamental absorption for a sample of GeS_2 of thickness 14 μm at room temperature.

dinates, which is characteristic for indirect optical transitions from the valence band to the conduction band with the participation of phonons. The value of the gap width obtained from this plot is 3.2 eV.

On the long-wavelength side of the edge there is a weak, but distinct absorption maximum at 2.7 eV, which coincides with the optical gap width of glassy germanium disulfide.[2] This is probably evidence of the presence of a moderate degree of amorphization of the sample, most likely in the form of inclusions of microscopic regions with violation of the long-range order.

Measurements of the photoconductivity gave a somewhat unexpected result: this effect could not be detected in the region of the fundamental absorption edge; however, an isolated wide photoconductivity peak was observed near 1.7 eV. Additional study is needed to determine the nature of this peak.

We are grateful to N. F. Kartenko and N. V. Sharenkova for carrying out the x-ray structural analysis of the GeS_2 crystals.

This work was carried out with the financial support of the Russian Fund for Fundamental Research (Grant No. 97-02-18300).

*)lev.vasiliev@shuvpop.ioffe.rssi.ru

[1] M. Rubenstein and G. Roland, Acta Crystallogr. **27**, 505 (1971).

[2] A. Feltz, *Amorphe und glasartige anorganische Festk<F6>rper (Amorphous and Glassy Inorganic Solids)* (Akademie-Verlag, Berlin, 1983) [Moscow, 1986].

Translated by Paul F. Schippnick

Photovoltaic effect in In/I–III–VI_2-thin-film surface-barrier structures

V. Yu. Rud'

St. Petersburg State Technical University, 195251 St. Petersburg, Russia

Yu. V. Rud'

A. F. Ioffe Physicotechnical Institute, Russian Academy of Sciences, 194021 St. Petersburg, Russia

I. V. Bodnar', V. F. Gremenok, O. S. Obraztsova, and S. L. Sergeev-Nekrasov

Belorussian State University of Information Science and Radio Engineering, 220027 Minsk, Belarus
(Submitted November 19, 1997; accepted for publication December 23, 1997)
Fiz. Tekh. Poluprovodn. **32**, 829–831 (July 1998)

Surface-barrier structures have been prepared on films of the ternary compounds $CuInTe_2$, $AgGaTe_2$, and $AgInTe_2$ and the solid solution $Cu_{0.5}Ag_{0.5}InSe_2$. When these structures are illuminated, the photovoltaic effect is observed. It has been established that structures based on the ternary compound p-$AgGaTe_2$ possess the highest photovoltaic sensitivity. It has been shown that films of I–III–VI_2 compounds and the solid solution $Cu_{0.5}Ag_{0.5}InSe_2$ obtained by laser deposition can be used to create wideband photoconverters of natural radiation. © *1998 American Institute of Physics.* [S1063-7826(98)01307-6]

1. INTRODUCTION

In recent years ternary I–III–VI_2-semiconductor compounds have attracted attention as one of the most promising groups of materials for fabricating highly efficient solar converters. They possess a high optical absorption coefficient ($10^4-10^5\ cm^{-1}$) in the region of the solar spectrum and direct optical transitions. Thin-film elements with efficiency greater than 16% have been fabricated on the basis of the ternary compound $CuInSe_2$, as well as the solid solutions $CuGaIn_{1-x}Se_2$.[1,2] Numerous experimental studies have shown that the electrical and optical properties of I–III–VI_2 semiconductors are determined in large measure by the type of intrinsic defects associated with deviations from stoichiometry.[3,4] In this regard, further improvement of the characteristics of solar cells based on these compounds will be possible after we achieve a better understanding of the physical properties of such materials and devices based on them. The present paper reports results of a study of In/I–III–VI_2-thin-film surface-barrier structures.

2. PREPARATION OF CRYSTALS AND FILMS

Crystals of the ternary compounds (Cu,Ag)(Ga,In)Te_2 and the solid solutions $Cu_xAg_{1-x}InSe_2$ were grown by the Bridgman–Stockbarger method. The boules of $CuGaTe_2$, $CuInTe_2$, $AgGaTe_2$ prepared in this way were monocrystalline, and the boules of $AgInTe_2$ and the solid solutions had the form of large blocks and were used as targets for sputtering films.

Film deposition was carried out in a vacuum with a residual pressure of $\sim 10^{-5}$ Pa using a laser operating in the free-lasing regime ($\lambda = 1.06\ \mu m$, $\tau_p = 10^{-3}$ s, $E_p = 130-150$ J).

The composition of the crystals and films was determined by energy-dispersive x-ray analysis on a JEOL6400 scanning electron microscope. The data so obtained are displayed in Table I. It can be seen that the experimental and calculated quantities are in satisfactory agreement.

The structure and parameters of the crystals and films were determined by x-ray diffraction analysis. The diffraction patterns were recorded on a DRON-3M diffractometer. These studies showed that the diffraction patterns of the films, as well as the crystals, always contain a system of lines corresponding to a chalcopyrite structure. The unit-cell parameters for the crystals and films agree.

3. FABRICATION OF STRUCTURES

Surface-barrier structures were fabricated by the vacuum thermal sputtering of thin films of metallic indium ($d_c \approx 1-2\ \mu m$) onto the outer surface of I–III–VI_2-film samples prepared by pulsed laser deposition. The surfaces of the films were not subjected to any kind of processing before deposition of the indium layers, and the films themselves were not subjected to any heating above room temperature during deposition or afterwards. The indium films exhibited high adhesion to the surface of the I–III–VI_2-thin-film substrates. The use of indium as a barrier contact was shown to be possible by our own preliminary studies of contact phenomena on I–III–VI_2-film samples.

4. PHOTOSENSITIVITY OF STRUCTURES

When the structures fabricated from the compounds indicated and the solid solution $Cu_{0.5}Ag_{0.5}InSe_2$ were illuminated, a photovoltaic effect was observed (Table II). The sign of the photovoltage does not depend on the point of incidence of the light probe on the surface of the structures and corresponds to positive polarity of the photovoltage on the chalcogenide films. The maximum photosensitivity is usually manifested when the structures are illuminated from

 © 1998 American Institute of Physics

TABLE I. Results of energy-dispersive x-ray analysis of the ternary compounds (Cu,Ag)(Ga,In)Te_2 and the solid solutions $Cu_xAg_{1-x}InSe_2$.

Film composition	Cu, at. %		Ag, at. %		Ga, at. %		In, at. %		Se, at. %		Te, at. %	
	calc.	experiment	calc.	experiment	calc.	experiment	calc.	experiment	calc.	experiment	calc.	experiment
$AgGaTe_2$	–	–	25.00	26.20	25.00	24.56	–	–	–	–	50.00	49.24
$CuGaTe_2$	25.00	26.60	–	–	25.00	24.20	–	–	–	–	50.00	49.22
$AgInTe_2$	–	–	25.00	25.12	–	–	25.00	24.32	–	–	50.00	50.56
$CuInTe_2$	25.00	26.18	–	–	–	–	25.00	24.51	–	–	50.00	49.08
$Cu_{0.5}Ag_{0.5}InSe_2$	12.50	11.86	12.50	13.49	–	–	25.00	25.48	50.00	49.17	–	–
$Cu_{0.7}Ag_{0.3}InSe_2$	17.50	18.10	7.50	9.35	–	–	25.00	23.60	50.00	48.95	–	–

the side of the barrier contact; its values are listed in Table II. It can be seen from Table II that the maximum photovoltaic sensitivity $S_U \approx 0.8$ V/W is reached when structures of $AgGaTe_2$ films are used.

The spectral dependence of the relative photoconversion quantum efficiency η is plotted in Figs. 1 and 2 for typical structures at $T=300$ K, and some of their characteristics are given in Table II. The main trends in the behavior of the thin-film structures fabricated are the following.

All the structures exhibit a wideband photovoltaic effect. The full width at half-maximum (FWHM, $\delta_{1/2}$) of the η spectra in all the structures turned out to be approximately the same and equal to ≈ 1.2 eV. The long-wavelength photosensitivity edge of all the structures is exponential and localized in the vicinity of the energy of the incident photons at ~ 1 eV. The values of the slope $S=(\delta(\ln \eta)/\delta(\hbar\omega))$ of the long-wavelength photosensitivity edge lie within the range $20-50\ \mathrm{eV}^{-1}$, giving grounds to assume that the interband optical transitions in these materials are direct. This deduction agrees with the data from direct optical measurements in bulk crystals of some of the semiconductors,[5,6] whereas for the solid solution $Cu_{0.5}Ag_{0.5}InSe_2$ this supposition is formulated here for the first time. This means that the energy spectra of the component compounds do not undergo significant changes as a result of the formation of the solid solution.

The exponential growth of the quantum efficiency η observed as the energy of the incident photons is increased for all the structures (Figs. 1 and 2) ends in the vicinity of practically the same energy, 1.08 eV. With further increases in the photon energy, the photoconversion quantum efficiency in the structures investigated that include indium as one of their components achieves a nearly constant level. From Fig. 2 it can be seen that for the structure based on a film in whose makeup indium is replaced by gallium, η continues to grow over a very wide range of energies. This growth, as follows from Fig. 3 (curve *1*), obeys the law $\sqrt{\eta\hbar\omega} \sim \hbar\omega$. It is very important to note that in an analogous structure based on a bulk single crystal of p-$AgGaTe_2$, which was used as a source for film deposition, the spectral dependence of the long-wavelength boundary of the photoconversion quantum efficiency follows an analogous law. In this case it turns out that the conventional extrapolation for such cases $\sqrt{\eta\hbar\omega} \to 0$ gives the same energy value $\hbar\omega \approx 1.06$ eV. This circumstance is probably a consequence of the fact that the current technology for converting a target into a thin film

TABLE II. Photoelectric properties of In/I–III–VI_2-thin-film structures prepared by laser deposition.

Film composition	T_s, °C	d_c, μm	ρ, $\Omega \cdot$cm	S_u V/W	$\delta_{1/2}$ eV	S, eV^{-1}
$AgGaTe_2$	380	0.50	3×10^3	0.8	1.25	16
$CuGaTe_2$	400	0.30	0.5	–	–	–
$AgInTe_2$	460	0.60	10^5	0.4	1.16	45
$CuInTe_2$	480	0.38	1	0.5	1.16	40
$Cu_{0.5}Ag_{0.5}InSe_2$	460	0.55	5×10^3	0.2	$\sim$1.2	20
$Cu_{0.7}Ag_{0.3}InSe_2$	460	0.45	10^4	–	–	–

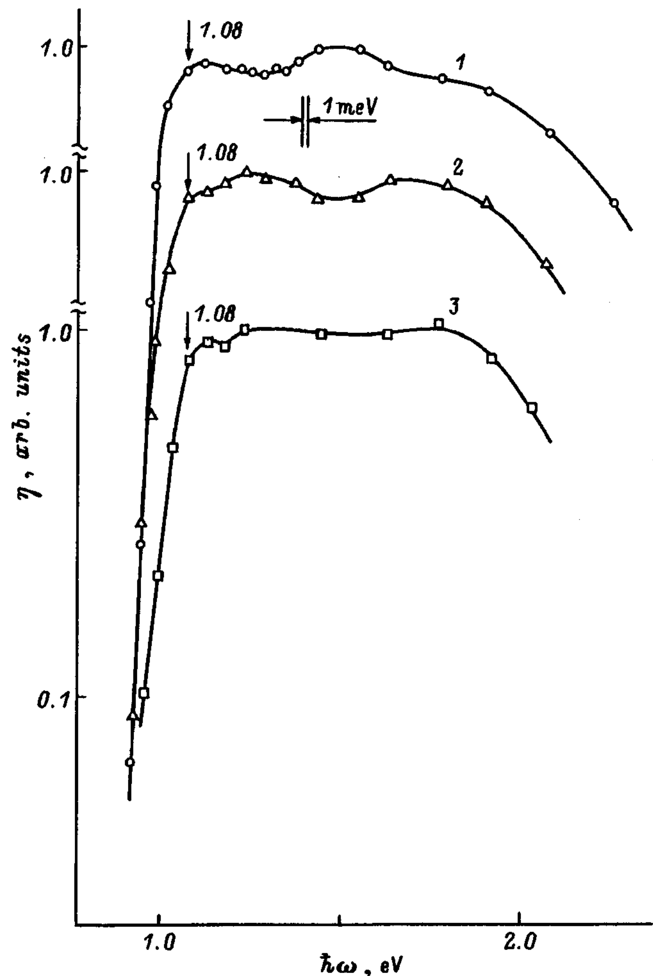

FIG. 1. Spectral dependence of the relative photoconversion quantum efficiency of surface-barrier structures based on thin films of I–III–VI_2 materials and layers of indium at $T=300$ K. Composition of the films: *1* — $AgInTe_2$, *2* — $CuInTe_2$, *3* —$Cu_{0.5}Ag_{0.5}InSe_2$. Illumination from the indium layer side.

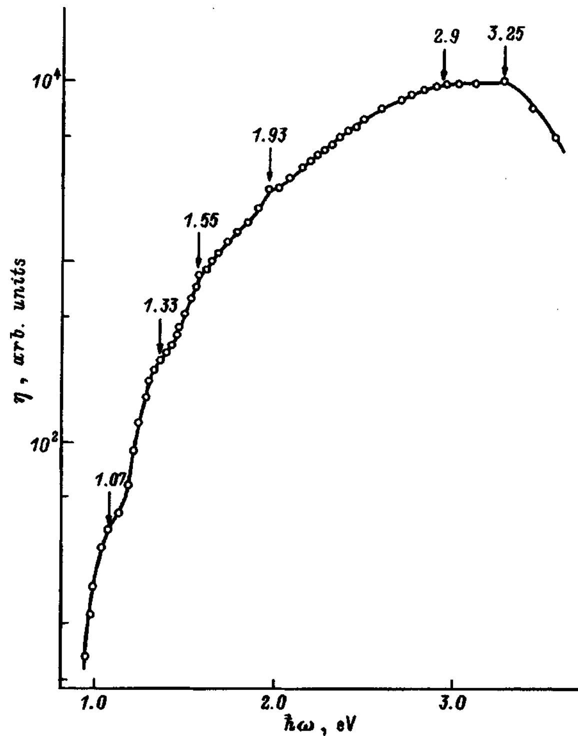

FIG. 2. Spectral dependence of η for the In/AgGaTe$_2$ thin-film structure at 300 K.

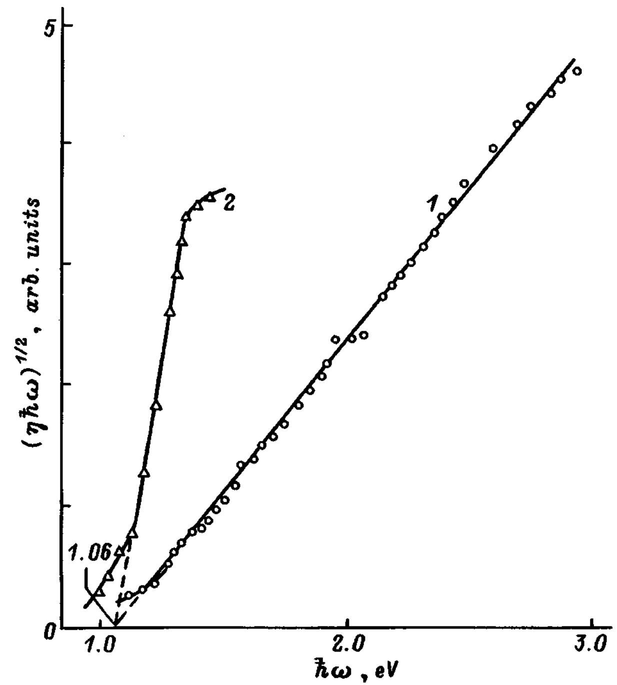

FIG. 3. Dependence of $(\eta\hbar\omega)^{1/2}$ on $\hbar\omega$ for In/AgGaTe$_2$ structures at 300 K: *1* — thin film of AgGaTe$_2$, *2* — AgGaTe$_2$ single crystal.

proceeds without disturbing the composition or crystal structure of the target before sputtering.

Thus, the physical and technological study reported here allows us to conclude that laser-deposited films of I–III–VI$_2$ compounds and their solid solutions can be used to fabricate wideband thin-film photoconverters of natural radiation.

[1] H. W. Schock, Sol. Energy Mater. Sol. Cells **34**, 19 (1994).
[2] H. W. Schock, Appl. Surf. Sci. **92**, 606 (1996).
[3] H. Neumann and R. D. Tomlinson, Sol. Cells **28**, 301 (1990).
[4] A. Rockett and R. W. Birkmire, J. Appl. Phys. **70**, R81 (1991).
[5] J. L. Shay and J. H. Wernick, *Ternary Chalcopyrite Semiconductors: Growth, Electronic Properties and Applications* (Pergamon Press, New York, 1975).
[6] G. A. Medvedkin, V. D. Prochukhan, Yu. V. Rud', and M. A. Tairov, Phys. Status Solidi B **151**, 711 (1989).

Translated by Paul F. Schippnick

SEMICONDUCTOR STRUCTURES, INTERFACES AND SURFACES

Allowing for current spreading in semiconductors during measurements of the contact resistivity of ohmic contacts

A. N. Andreev, M. G. Rastegaeva, V. P. Rastegaev, and S. A. Reshanov

A. F. Ioffe Physicotechnical Institute, Russian Academy of Sciences, 194021 St. Petersburg, Russia
(Submitted December 17, 1997; accepted for publication December 23, 1997)
Fiz. Tekh. Poluprovodn. **32**, 832–837 (July 1998)

A modification of the contact-area pattern with radial geometry, which has certain advantages in determining the contact resistivity of ohmic contacts (ρ_c) fabricated on substrates and low-resistance semiconductor layers, is proposed. Different variants of its application for both the transmission line method (TLM) and methods based on a numerical calculation of the resistance of the semiconductor with allowance for current spreading are considered. It is shown that the transmission line method makes it possible to obtain an upper estimate of the contact resistivity on substrates. The errors of such estimates are also calculated as a function of the parameters of the semiconductor and the contact. The TLM estimate is a good first approximation for determining the exact value of ρ_c by numerically calculating the resistance of the semiconductor. The results obtained are used to study the contact resistivity of Ni-based ohmic contacts on n-6H-SiC substrates. © *1998 American Institute of Physics.*
[S1063-7826(98)01407-0]

1. INTRODUCTION

The development of accurate procedures for measuring the contact resistivity of ohmic contacts (ρ_c) has played an important role in the technology of semiconductor devices. Usually, to determine the value of ρ_c probe methods are used to measure the total resistance R_t between coplanar contact areas, which depends on the resistances of both the contact and the semiconductor. Therefore, one of the main problems in the calculation of the contact resistivity of ohmic contacts is to determine the contribution from the semiconductor material to the value of R_t. This contribution depends in a major way on the contact-area pattern chosen and is governed by the processes of current spreading between them. Consideration of the current spreading processes is generally quite complicated, and most methods for determining ρ_c are based on a simplification of the pattern of the system in which the measurements are performed.

The most common technique is to measure the contact resistivity in the limiting case of thin semiconductor layers electrically isolated from the substrate, e.g., a $p-n$ junction. Under these conditions, the problem of determining the resistance of the semiconductor and, accordingly, ρ_c is solved within the one-dimensional model of current flow. One of these methods is the transmission line method (TLM).[1–4] The most suitable versions of the transmission line method employ a radial contact-area geometry[3,4] since it eliminates the necessity of additional profiling of the structures with the aim of eliminating undesirable effects associated with current flow on the edges of the contact areas.[4] Factors causing errors in measurements of the contact resistance have been revealed and estimated for these methods. They include the effect of the size of the contact areas and the distance between them[5] and the effect of a finite spreading resistance in the material of the contact coating.[5,6] When these factors are taken into account, use of the transmission line method permits accurate determination of fairly low contact resistivities ($\rho_c \sim 10^{-6}-10^{-5}\ \Omega\cdot\mathrm{cm}^2$). We note that in the case of low-resistance ohmic contacts on semiconductors with high conductivity, R_t can be quite small. In view of the small size of the contact areas, the measurement of such quantities is a complex task. For example, when current and potential probes are placed on a contact area of small radius, special approaches are necessary (see, e.g., Ref. 3). As a consequence, the procedure for measuring the contact resistivity is substantially complicated. In addition, in this case the necessity of measuring small voltage drops at high current densities arises. These factors lead to an increase in the error in the determination of ρ_c.[7,8]

Analysis of the current flow is significantly complicated for semiconductor layers whose thickness is comparable with or exceeds the characteristic dimensions of the contact areas, since the lack of analytical expressions for this case requires the use of numerical methods. Examples of such numerical calculations, which are based on various models and allow for the nonuniform propagation of current through the volume of the semiconductor, are described in Refs. 9 and 10. It is noteworthy that the procedure for measuring the contact resistance on substrates imposes more rigid requirements on the geometric dimensions of the system of contact areas than in the case of thin semiconductor layers because of the lower values of R_t.

Along with the necessity of determining the value of ρ_c as accurately as possible, in many cases of practical impor-

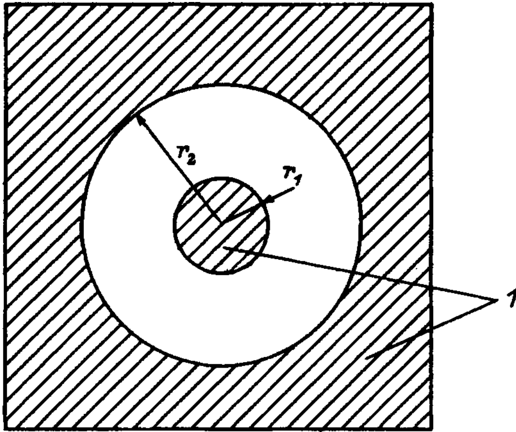

FIG. 1. Fragment of a pattern with radial symmetry for measuring the contact resistance of ohmic contacts. *1* — con tact covering, r_1 and r_2 — radii of the contact areas.

tance it is sufficient simply to determine that the contact resistivity does not exceed a certain acceptable level (i.e., an upper estimate), which can be done using a simpler technique.

To solve such problems, this paper proposes a modification of the radial contact-area geometry and considers different variants of its application in the transmission line method and in a method based on numerical calculation of the resistance of the semiconductor with allowance for current spreading. The results obtained are used to study the contact resistivity of nickel-based ohmic contacts on n-6H-SiC substrates.

2. CONTACT-AREA GEOMETRY

To determine the value of ρ_c, Boberg *et al.*[3] proposed a pattern consisting of concentrically arranged contact areas, the smaller of which has a radius r_1, while the larger has an inner radius r_2 (Fig. 1). Several such contact areas are fabricated on one sample, where the inner areas have a fixed radius $r_1=$const, and the outer radius r_2 varies. In the case of thin layers considered in Ref. 3, a set of values of resistances R_t measured between these contact areas was used to determine the contact resistivity and the sheet resistance of the semiconductor layer R_s by the transmission line method. Such a geometry requires a high degree of uniformity of the contact resistivity over the area of the sample; nevertheless, it is quite convenient in comparison with the system of concentric rings proposed in Ref. 4, since for a small value of R_s the value of R_t will be higher than the resistance measured between the two outer rings in the scheme proposed in Ref. 4 due to the larger contribution to R_t from the contact resistance of the area of the smaller radius r_1.

As an alternative, let us consider a geometry analogous to that proposed in Ref. 3, but where the radii of the contact areas r_1 and r_2 are chosen so as to fulfill the condition $\ln(r_2/r_1)=C$, where C is a constant. We shall perform a comparative analysis of techniques for determining the contact resistivity based on these two geometries for ohmic contacts on thin semiconductor layers and on substrates. For the calculations we choose the values of r_1 and r_2 as follows: in the first case the range of variation of r_2 is 50−250 μm for the fixed value of $r_1=20$ μm; in the second the range of variation of r_1 is 10−30 μm for $\ln(r_2/r_1)=2$. These values are quite typical, since decreasing r_1 substantially complicates the measurement procedure, while it is undesirable to increase r_1 for small values of ρ_c because of the decrease in the contribution of the contact resistance of the contacts to R_t.

3. BASIC RELATIONS FOR THE CASE OF THIN SEMICONDUCTOR LAYERS

Within the transmission line model the resistance between the contact areas is given by the expression (Ref. 3 and 4)[1)]

$$R_t=\frac{R_s}{2\pi}\ln\frac{r_1}{r_2}+\frac{R_s}{2\pi}\frac{1}{\alpha r_1}\frac{I_0(\alpha r_1)}{I_1(\alpha r_1)}, \tag{1}$$

where R_t is the total resistance measured between the contact areas, R_s is the sheet resistance of the semiconductor layer, r_1 and r_2 are the outer and inner radii of the respective contact areas (Fig. 1); $I_0(\alpha r_1)$ and $I_1(\alpha r_1)$ are the modified Bessel functions of orders 0 and 1, $\alpha=(R_s/\rho_c)^{1/2}$, ρ_c is the contact resistivity of the ohmic contacts. An obvious way of determining ρ_c using expression (1), which was employed in Ref. 3, is to construct the dependence of the measured resistance R_t on $\ln(r_2/r_1)$ for a fixed value of r_1. The slope of the straight line so obtained determines the value of R_s, and the y intercept (together with R_s) determines the value of ρ_c.

We note that the variation of R_t is due in this case only to the variation of r_2 and, as a consequence, for small values of R_s the range of variation of R_t is not large. This state of affairs increases the error in the determination of ρ_c and requires good measurement statistics. In addition, even for test measurements it is necessary to use current and potential probes. In the opposite case the value of ρ_c will be overestimated due to the probe/contact-coating resistance, since it is determined from the y intercept of the approximating linear dependence of R_t on $\ln(r_2/r_1)$.

These drawbacks can be easily avoided if the pattern for forming the contact areas is designed so as to decrease r_1 while keeping $\ln(r_2/r_1)$ constant. If $\ln(r_2/r_1)=C=$const, then the dependence of R_t on r_1 takes the form

$$R_t=\frac{CR_s}{2\pi}+\frac{R_s}{2\pi}\frac{1}{\alpha r_1}\frac{I_0(\alpha r_1)}{I_1(\alpha r_1)}. \tag{2}$$

When r_1 is sufficiently small, the main contribution to R_t will come from the contact resistance and the relative variation of R_t in the measurements will grow. Figure 2 plots calculated dependences of R_t on $\ln(r_2/r_1)$ and of R_t on r_1^{-2} for the pattern parameters indicated above. It can be seen from Fig. 2 that the range of variation of R_t is substantially expanded (by several-fold) in the second case. The values of ρ_c and R_s can be easily determined from a set of experimental points (R_{ti},r_{1i}) $(i=1,\ldots,N$; N is the number of measurements), for example, by minimizing the discrepancy function $\phi(\rho_c,R_s)$ based on the Gauss equalization criterion[11]

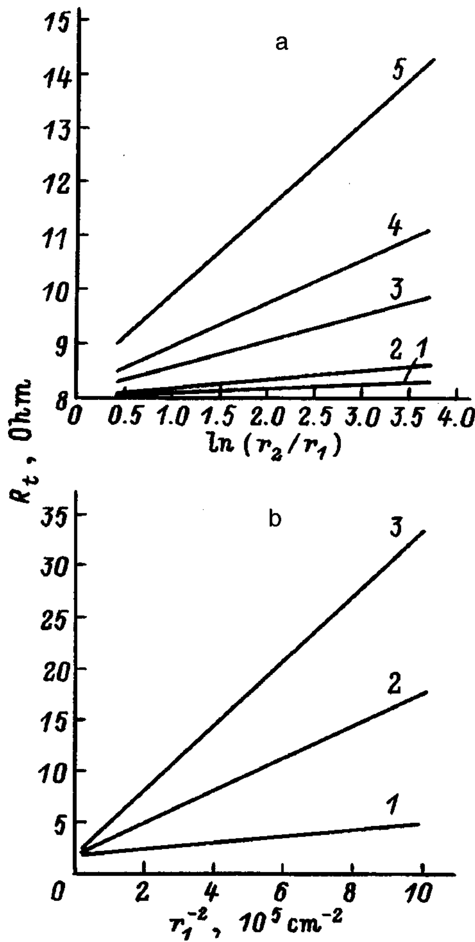

FIG. 2. a — Calculated dependences of R_t on $\ln(r_2/r_1)$ for the case of epitaxial layers with $\rho_c = 1\times10^{-4}$ $\Omega\cdot$cm^2. The curves correspond to the following values of R_s ($\Omega/\Box$): *1* — 0.5, *2* — 1, *3* — 3, *4* — 5, *5* — 10. b — Calculated dependences of R_t on r_1^{-2} for the case of epitaxial layers with $R_s = 5$ $\Omega/\Box$. The curves correspond to the following values of ρ_c, $\Omega\cdot$cm^2: *1* — 1×10^{-5}, *2* — 5×10^{-5}, *3* — 1×10^{-4}.

$$\phi(\rho_c, R_s) = \sum_{i=1}^{N} [R_t(\rho_c, R_s) - R_{ti}]^2. \quad (3)$$

If the condition

$$\alpha r_1 \ll 1 \quad (4)$$

is fulfilled, then the asymptotic limit $I_0(\alpha r_1)/I_1(\alpha r_1) \rightarrow 2/(\alpha r_1)$ holds, and expression (2) can be written in the form

$$R_t = \frac{CR_s}{2\pi} + \frac{r_c}{\pi r^2}. \quad (5)$$

Thus, if condition (4) is fulfilled, the function $R_t = R_t(r_1^{-2})$ is linear. The slope of the approximating straight line determines ρ_c, and if the resistance of the measuring probes is constant, their resistance does not distort the measured value of ρ_c. For $\alpha r_1 \geqslant 1$ expression (5) gives an upper estimate (ρ_c') for the contact resistivity (ρ_c) (Fig. 3).

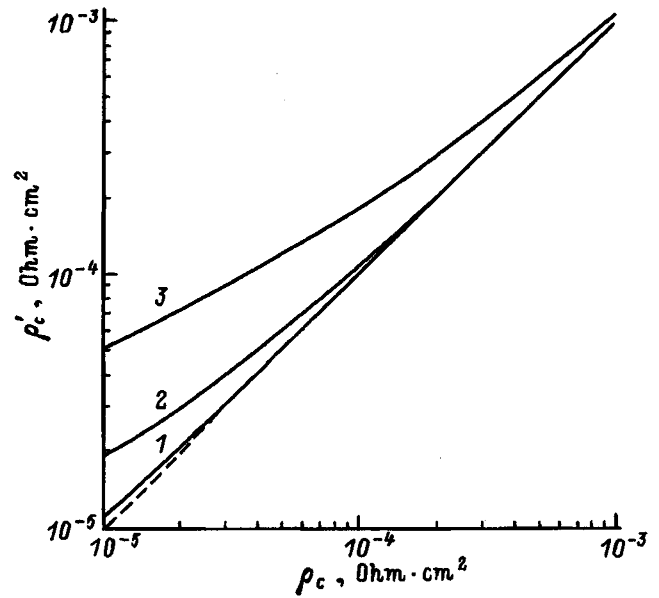

FIG. 3. Deviation of the value of the contact resistivity of ohmic contacts obtained using approximation (5) (ρ_c'), from the value of ρ_c given by formula (2) for $\alpha r_1 \geqslant 1$ and the pattern considered. Curves *1*, *2* and *3* correspond to the following values of R_s ($\Omega/\Box$): 10, 100, and 1000.

4. APPLICATION OF NUMERICAL CALCULATIONS OF THE RESISTANCE OF THE SEMICONDUCTOR IN DETERMINING THE CONTACT RESISTIVITY

To calculate the contact resistivity of ohmic contacts on layers (or substrates) of arbitrary thickness using the geometry considered above, we can use the method developed in Ref. 10. This method is based on calculation of the current distribution in the structure under investigation by discretizing the semiconductor into a finite number of elementary volumes, within each of which the electric field can be taken to be uniform. Each elementary volume is matched to one of a set of resistances, which, with consideration of the radial symmetry of the contact areas, form the equivalent circuit of the structure under investigation (Fig. 4). Thus, the determination of the total resistance R_t reduces to solving the problem of current flow in an electric circuit consisting of discrete resistors. For semiconductor crystals of intermediate crystal systems (e.g., hexagonal modifications of silicon carbide) the calculation can be carried out with allowance for the conductivity anisotropy factor. This model was used earlier to determine the contact resistivity of ohmic contacts on thin epitaxial layers. The results obtained coincided with the results obtained by the transmission line method.[10]

As for the contact-area patterns considered, the contact resistivity ρ_c and the resistivity of the semiconductor ρ can be determined using expression (3) with the one difference that there is no analytical expression for the function $R_t(\rho_c, \rho)$ and it must be calculated numerically. We note that the search for the minimum of the discrepancy function can be quite laborious in the absence of a good initial approximation.

Let us consider how the resistance between the contact areas varies as the thickness of the epitaxial layer (or substrate) is increased. Obviously, for a constant value of the

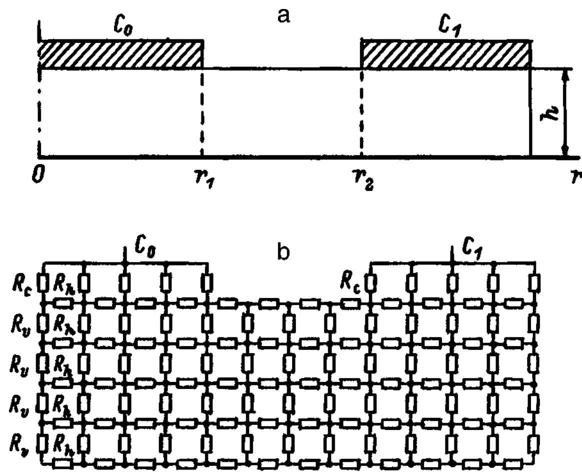

FIG. 4. Structure investigated (a) and the equivalent circuit used for numerical calculations of the resistance of the semiconductor (b). C_0 and C_1 are the contact areas; r_1 and r_2 are their radii; h is the thickness of the substrate; R_h, R_v, and R_c are the resistances corresponding to elementary volumes of the semiconductor and contact covering. For an isotropic semiconductor $R_h = R_v$.

contact resistivity, the variation of R_t is due to the variation of the spreading resistance in the semiconductor. The nature of this variation will depend substantially on the relative values of R_h and R_v (Fig. 4). Results of a numerical calculation of the dependence of R_t on h for an isotropic ($R_h = R_v$) crystal are plotted in Fig. 5 (curve *1*).

5. USE OF TRANSMISSION LINE METHODS TO ESTIMATE THE CONTACT RESISTIVITY OF OHMIC CONTACTS ON SUBSTRATES

The determination of the resistance of the substrate on the basis of the transmission line model is, generally speaking, not an accurate procedure, as indicated by the difference between curves *1* and *2* in Fig. 5. Curve *2* was calculated in the transmission line approximation for the same structure

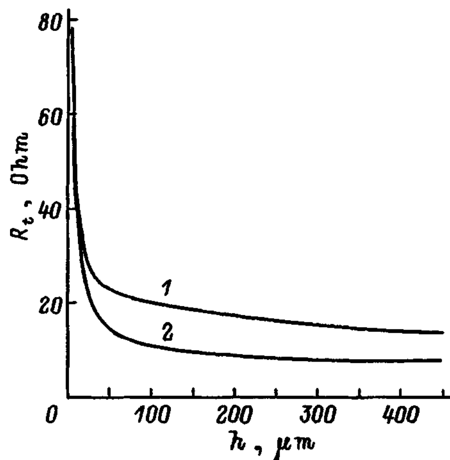

FIG. 5. Calculated plots of the total resistance R_t as a function of the substrate thickness for $\rho_c = 5\times10^{-5}\ \Omega\cdot\mathrm{cm}^2$; $\rho = 0.1\ \Omega\cdot\mathrm{cm}$; $r_1 = 15\ \mu\mathrm{m}$; $\ln(r_2/r_1) = 2$ for an isotropic semiconductor. Curve *1* was obtained using numerical calculations, curve *2* was obtained by the transmission line method ($R_s = \rho/h$).

parameters as was curve *1* with consideration of the relation $R_s = \rho/h$. These differences are due to the fact that any circular cylindrical surface described about the axis which passes through the origin and is perpendicular to the surface is not equipotential due to the nonuniform distribution of the current across the thickness of the semiconductor under the contact areas. Consequently, the value of the contact resistivity determined by the transmission line method is overestimated. However, the influence of this factor decreases if the flow of current to the semiconductor is determined mainly by the contact resistance of the contacts. In the transmission line model this approximation corresponds to the condition $\alpha r_1 \ll 1$.

To estimate the error due to using the transmission line approximation in the cases under consideration, we carried out a comparative calculation. The dependences of R_t on $\ln(r_2/r_1)$ and on $1/r_1^2$ were calculated using the technique described in Sec. 4 for assigned values of ρ_c and ρ; these dependences were then fitted to the analytical expressions (1), (2), and (5), which follow from the transmission line model for the respective cases. On the basis of these expressions we determined the values of the contact resistivity ρ_c'. The dependences so obtained are plotted in Fig. 6.

It can be seen from Fig. 6 that the differences between the values of ρ_c and ρ_c' depend substantially on the choice of the contact-area pattern and its dimensions, as well as on the resistivity of the semiconductor. For the patterns considered the use of the dependence of R_t on r_1^{-2} gives a more accurate estimate of the contact resistivity. For contacts on substrates with a resistivity of $0.1-0.2\ \Omega\cdot\mathrm{cm}$, measurements can be performed by this method all the way down to $\rho_c = 5\times10^{-5}\ \Omega\cdot\mathrm{cm}^2$. For such values of ρ_c the error does not exceed 15–20% and drops substantially as ρ_c increases. In contrast, the determination of ρ_c from the dependence of R_t on $\ln(r_2/r_1)$ introduces substantial errors starting at $\rho_c = (1-5)\times10^{-3}\ \Omega\cdot\mathrm{cm}^2$, and such a contact-area pattern can be used only to obtain a very rough estimate. The error decreases as the resistivity of semiconductor decreases.

Thus, using expressions obtained in the transmission line approximation, it is easy to obtain an upper estimate for the contact resistivity. The magnitude of the deviation in this case depends substantially on the contact-area geometry chosen and on the parameters of the semiconductor.

6. MEASUREMENT OF THE CONTACT RESISTIVITY OF NICKEL OHMIC CONTACTS ON *n*-6*H*-SiC SUBSTRATES

Ohmic contacts were formed on 6*H*-SiC substrates of *n*-type conductivity grown by the Lely method with uncompensated donor concentration $3-5\times10^{18}\ \mathrm{cm}^{-3}$, resistivity $0.1-0.3\ \Omega\cdot\mathrm{cm}$, and thickness 450 μm. In the first stage of this method, nickel was deposited by electron-beam evaporation in vacuum onto the substrate surface, which was preheated to 300 °C. Then the structures were subjected to high-temperature annealing at 900–1300 °C. Contact areas of the required geometry were formed by photolithography. The technology for forming the ohmic contacts and the results of studies of the structure and composition of the contact coating are described in detail in Refs. 12 and 13.

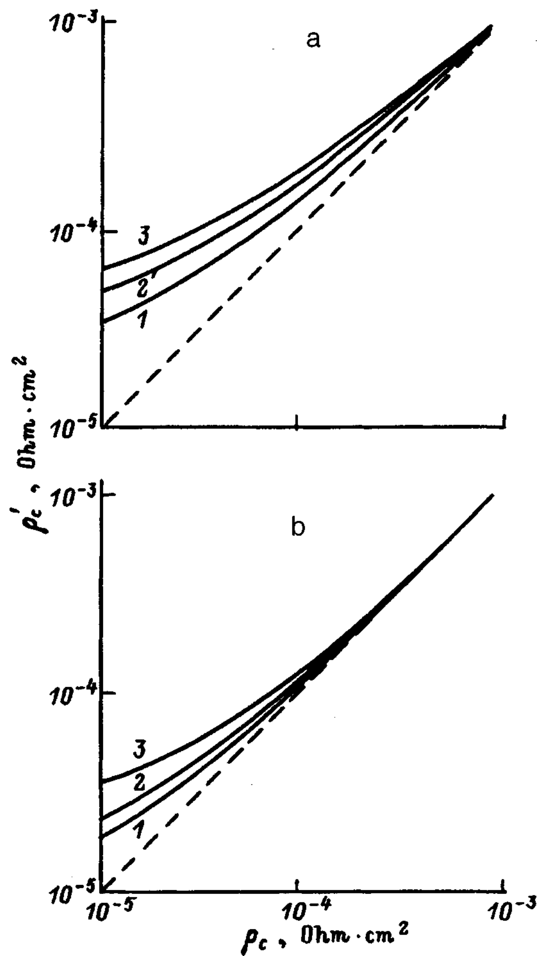

FIG. 6. Comparison of the results of calculations of the contact resistivity of ohmic contacts based on the two-dimensional model (Fig. 4) (ρ_c) and the transmission line model (ρ_c') using different expressions: a) the dependence of R_t on $\ln(r_2/r_1)$; b) the dependence of R_t on r_1^{-2}. Curves *1*, *2*, and *3* correspond to the following values of ρ, $\Omega\cdot$cm: 0.1, 0.2, and 0.3.

Results of a study of the contact resistivity using various techniques are summarized in Table I. It should be noted that crystals of silicon carbide of the 6*H* polytype have substantial conductivity anisotropy: the ratio between the resistivities in the direction of the hexagonal *C* axis and in the plane perpendicular to it (the anisotropy factor) is equal to $\rho_v/\rho_h=3.7$ (Refs. 14 and 15). Results of calculations of the contact resistivity of the ohmic contacts with and without allowance for the anisotropy factor are given in the last two rows of the table. We note that the determination of ρ_c in the transmission line approximation using the geometry with a constant ratio between the outer and inner radii of the contact areas gives an upper estimate (rows 2 and 3) that essentially coincides with the values obtained by numerical calculation (row 5) with allowance for the anisotropy factor. Significantly greater differences are observed when the dependence of R_t on $\ln(r_2/r_1)$ is used for the case where $\rho_c=3.6\times10^{-5}$ $\Omega\cdot\text{cm}^2$; the results differ by a factor of 2.5.

7. CONCLUSION

Transmission line methods provide an upper estimate of the contact resistivity of ohmic contacts on substrates. The error depends substantially on the contact-area geometry chosen and on the parameters of the semiconductor. The proposed geometry, which is based on fitting the dependence of R_t on r_1^{-2} to (3) or (5), makes it possible to determine the contact resistivity or to obtain an upper estimate for it, depending on the parameters of the structure being measured. In the case of measurements of the contact resistivity on substrates, this method gives a more accurate estimate in comparison with the traditional technique. The estimate for silicon-carbide substrates with resistivity $0.1-0.3\ \Omega\cdot$cm shows that down to contact resistivities $\sim10^{-4}\ \Omega\cdot\text{cm}^2$ the error of the method does not exceed 15−20%. For lower contact resistivities the estimate obtained is a good initial approximation for determining ρ_c by means of numerical calculations of the resistance of the semiconductor. Advantages of the technique also include extending the range of measurable resistance values by increasing the contribution of the contact resistance, which increases the confidence level in the determination of ρ_c.

This work was carried out with the partial support of the University of Arizona and the Schneider Electric Group.

TABLE I. Values of the contact resistivity of nickel-based ohmic contacts on the *C* face of *n*-6*H*-SiC substrates determined by various methods.

Method for calculating the contact resistivity ρ_c		Values of ρ_c ($\Omega\cdot\text{cm}^2$), for the annealing temperature T_a		
		$T_a=800$ °C	$T_a=1000$ °C	$T_a=1200$ °C
Transmission	1[a]	1.6×10^{-4}	9.0×10^{-5}	1.2×10^{-4}
line	2	1.1×10^{-4}	4.0×10^{-5}	1.1×10^{-4}
methods	3	1.1×10^{-4}	3.9×10^{-5}	1.1×10^{-4}
Numerical	4	8.3×10^{-4}	2.5×10^{-5}	8.6×10^{-5}
calculation	5	1.0×10^{-4}	3.6×10^{-5}	9.5×10^{-5}

Note: [a]The numerals denote the following methods for determining the value of ρ_c:

1—from a linear approximation of the dependence of R_t on $\ln(r_2/r_1)$ for $r_1=\text{const}$ [expression (1)];

2—from a linear approximation of the dependence of R_t on r_1^{-2} for $\ln(r_2/r_1)=\text{const}$ [expression (5)];

3—from the dependence of R_t on r_1^{-2} given by expression (2) using minimization of the discrepancy function (3);

4—from the results of a numerical calculation of R_t without allowance for the anisotropy of the substrate resistivity followed by minimization of the discrepancy function (3);

5—from the results of a numerical calculation of R_t with allowance for the anisotropy of the substrate resistivity [the anisotropy factor is 3.7 (Ref. 15) followed by minimization of the discrepancy function (3).

The values of the error of ρ_c determined from the spread of the experimental data over the area of the substrate did not exceed 15−20%.

[1)]Expression (1) does not include terms whose influence can be neglected when the geometric dimensions of the system of contact areas are appropriately chosen.[4,5]

[1]V. Ya. Niskov, Prib. Tekh. Éksp. **1**, 235 (1971).
[2]H. H. Berger, Solid-State Electron. **15**, 145 (1972).
[3]G. Boberg, L. Stolt, P. A. Tove, and H. Norde, Physica Scripta **24**, 405 (1981).
[4]G. K. Reeves, Solid-State Electron. **23**, 487 (1980).
[5]G. S. Martow, M. B. Das, Solid-State Electron. **25**, 91 (1982).
[6]J. S. Chen, A. Bashli, M.-A. Nicolet, L. Baud, C. Jaussaud, and R. Madar, Mater. Sci. Eng., B **29**, 185 (1995).
[7]L. K. Mak, C. M. Rogers, and D. C. Northrop, J. Phys. E **22**, 317 (1989).

[8] Yu. D. Chistyakov, V. V. Baranov, and A. P. Dostanko, *Reviews of Electronics Technology. Series: Semiconductor Devices* [in Russian] (TsNII ''Élektronika'' Press, Moscow, 1973), No. 7 (143).
[9] A. M. Strel'chuk and B. N. Gresserov, Pis'ma Zh. Tekh. Fiz. **22** (8), 1 (1996) [Tech. Phys. Lett. **22** (4), 304 (1996)].
[10] V. Rastegaev, S. Reshanov, A. Andreev, and M. Rastegaeva, in *Transactions of the 3rd International High Temperature Conference* (USA, 1996), p. 149.
[11] I. N. Bronshteĭn and K. A. Semendyaev, *Handbook of Mathematics* [in Russian] (Nauka, Moscow, 1980).
[12] M. G. Rastegaeva, A. N. Andreev, V. V. Zelenin, A. I. Babanin, I. P. Nikitina, V. E. Chelnokov, and V. P. Rastegaev, in *Proceedings of the 6th Conference on Silicon Carbide and Related Materials, 1995 (ICSCRM-95) 18-21 September 1995, Kyoto, Japan (Institute of Physics Conference Series, No. 142)*, edited by S. Nakashima *et al.* (Institute of Physics, Bristol–Philadelphia, 1996), p. 581.
[13] M. G. Rastegaeva, A. B. Andreev, A. A. Petrov, A. I. Babanin, M. A. Yagovkina, and I. P. Nikitina, in *Abstracts of E-MRS, Spring Meeting* (France, 1996), A–VII.3.
[14] Yu. M. Tairov and Yu. A. Vodakov, in *Luminescence (Topics in Applied Physics, Vol. 17)*, edited by J. I. Pankove (Springer, Berlin–New York, 1977), p. 31.
[15] Yu. A. Vodakov, G. A. Lomakina, E. N. Mokhov, V. G. Oding, V. V. Semenov, and V. I. Sokolov, in *Problems of the Physics and Technology of Wideband Semiconductors* [in Russian] (Leningrad, 1980), p. 164.

Translated by Paul F. Schippnick

Donor-acceptor recombination in short-period silicon-doped GaAs/AlAs superlattices

I. I. Reshina

A. F. Ioffe Physicotechnical Institute, Russian Academy of Sciences, 194021 St. Petersburg, Russia

R. Planel'

Centre National de la Recherche Scientifique, 92225 Bagneux Cedex, France

(Submitted December 23, 1997; accepted for publication December 24, 1997)
Fiz. Tekh. Poluprovodn. **32**, 839–842 (July 1998)

A low-frequency band is observed along with an exciton band in photoluminescence spectra of short-period GaAs/AlAs superlattices doped with Si in the barriers or in the barriers and wells. This band is ascribed to donor-acceptor recombination on the basis of the dependence of its frequency on the excitation intensity under cw excitation and on the time delay under pulsed excitation. Mainly type-II superlattices are investigated. The estimate $E_A + E_D \approx 120$ meV can be obtained from the peak energy of the donor-acceptor band with a very weak excitation intensity. The estimates $E_A \approx 23$ meV and $E_D \approx 90$ meV are obtained from the temperature dependence of the band intensity. It is suggested that the deep donor level is associated with a *DX* center in the AlAs layers. © *1998 American Institute of Physics.*
[S1063-7826(98)01507-5]

In narrow type-II silicon-doped GaAs/AlAs superlattices, we have observed a lower-frequency luminescence band along with the luminescence bands of direct and indirect excitons. The specific properties of this band suggest that it is associated with donor-acceptor recombination involving deep centers.

On the other hand, it is known that in such superlattices silicon doping leads to the formation of so-called *DX* centers—deep donor centers which are associated with strong lattice relaxation and the phenomenon of persistent photoconductivity at low temperatures.[1,2] It is tempting to associate the observed luminescence with *DX* centers, and it is also of interest to compare the donor-acceptor recombination properties in GaAs/AlAs structures of types I and II.

SAMPLES AND EXPERIMENTAL TECHNIQUE

GaAs/AlAs superlattices (35J22) with a nominal well width of 2 nm, a nominal barrier width of 1.1 nm, and a number of periods equal to 290 were fabricated by molecular-beam epitaxy. Growth took place without rotation; therefore, in the larger samples grown the well thickness and barrier thickness varied over the area of the sample. This made it possible to obtain a set of samples with somewhat different well and barrier thicknesses. Most of the samples were assigned to type II, in which the lowest electron band with X_z symmetry is located in the AlAs layers, and the valence band with Γ symmetry is located in the GaAs layers. The energy gap between the Γ and X_z minima varied over the area of the original sample. Sample 35J22 was uniformly doped with silicon to an electron concentration of 3.3×10^{10} cm^{-2} per period at room temperature. We also obtained a set of samples (JA-15) with 100 periods, which were selectively doped with silicon in the barriers (however, the diffusion of silicon into the GaAs layers during growth cannot be ruled out). The layer electron concentration at room temperature was 3.9×10^{10} cm^{-2} per period. The sample cleaved from the edge of the original JA-15 sample was assigned to type I, but was close to type II.

Luminescence spectra were recorded at temperatures from 4.2 to 250 K on DFS-24 and U-1000 (Jobin–Yvon) diffraction spectrometers with a double monochromator. Excitation was effected by cw Ar^+ (2.41 eV) and He-Ne (1.96 eV) lasers. Time-resolved measurements were also performed using nitrogen laser excitation (3.69 eV) with pulse duration 10 ns.

EXPERIMENTAL RESULTS AND DISCUSSION

Most of the measurements reported below were carried out on one of the type-II 35J22 samples. Figure 1 displays its luminescence spectrum at $T = 77$ K and different excitation intensities. The peak intensity corresponds to an indirect X_z exciton. The small hump on the high-frequency side of the peak corresponds to a direct Γ exciton. The low-frequency band (designated below as the $D-A$ band) is associated presumably with donor-acceptor recombination. Grounds for such an interpretation are given below.

The peak frequency of the $D-A$ band, as can be seen from Fig. 1, depends strongly on the excitation intensity. When the intensity of the exciting light is decreased by roughly four orders of magnitude, the band shifts by 49 meV toward lower energies (Fig. 2) and is strongly broadened. Such behavior is characteristic of $D-A$ luminescence. The energy of the $D-A$ band is given by the well-known expression[3]

$$E = E_G - (E_A + E_D) + \frac{e^2}{\varepsilon r}, \tag{1}$$

 © 1998 American Institute of Physics

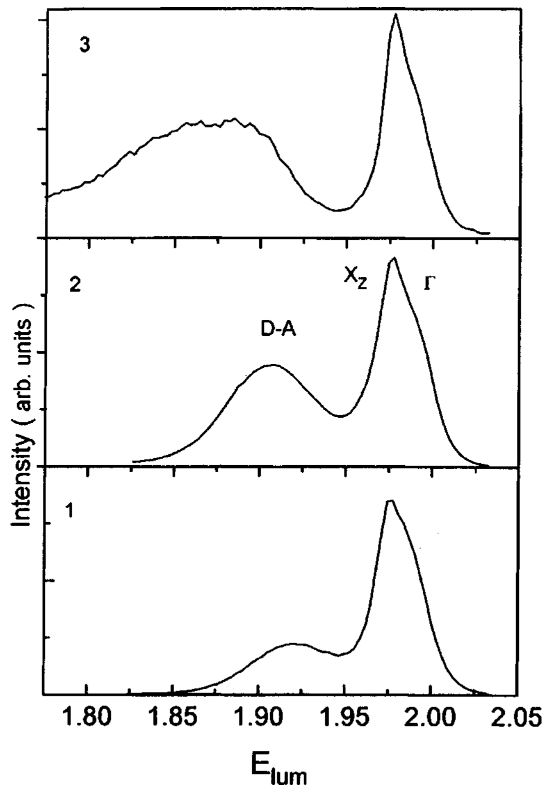

FIG. 1. Luminescence spectra of type-II silicon-doped GaAs/AlAs structures for various excitation intensities P, W/cm^2: *1* — 8.5×10^2, *2* — 1.5, *3* — 4.5×10^{-2}. Sample 35J22, $E_{\rm exc}=2.41$ eV, $T=77$ K.

where E_A and E_D are the ionization energies of the acceptors and donors, r is the distance between the donor and acceptor in a pair, and ε is the dielectric constant. When the excitation intensity is increased, the luminescence of distant pairs saturates since these pairs are characterized by a lower probability of recombination than close pairs, and the $D-A$ band correspondingly shifts toward higher energies.[4] Such a large shift in our case in comparison with the 4-meV shift observed for the $D-A$ band in GaAs (Ref. 5) may be linked with the fact that here we are dealing with an indirect material (a type-II superlattice). A significantly larger shift of the $D-A$ band was observed in the indirect semiconductor GaP than in GaAs (roughly 15 meV with an intensity change amounting to four orders of magnitude[4]). The lower transition probability in indirect semiconductors promotes saturation of distant pairs, which also leads to the greater magnitude of the shift (Ref. 3).[1)]

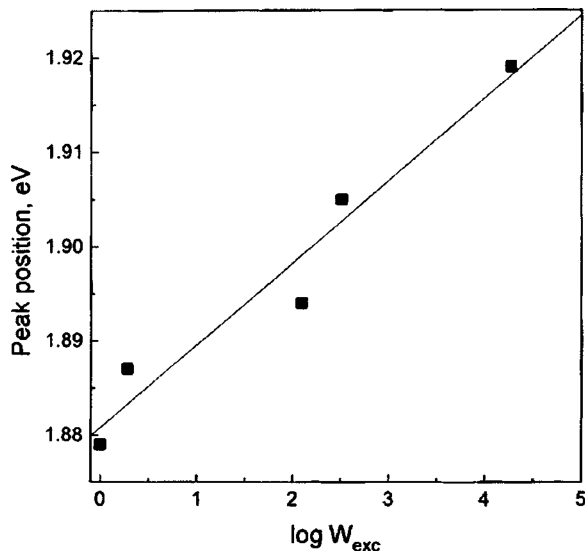

FIG. 2. Peak position of the $D-A$ band as a function of the logarithm of the excitation intensity. Sample 35J22, $E_{\rm exc}=2.41$ eV, $T=77$ K.

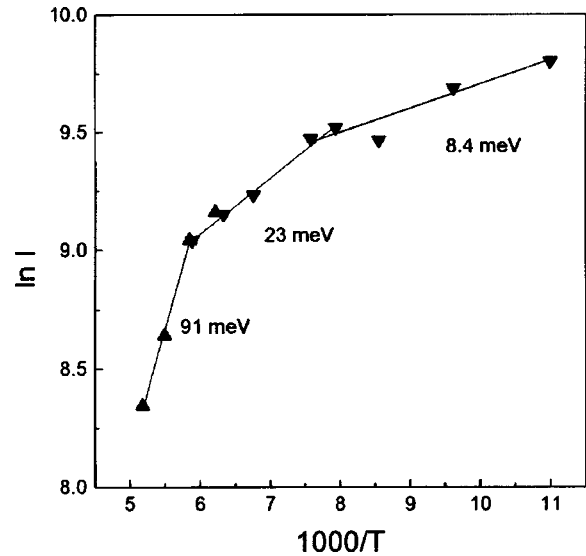

FIG. 3. Temperature dependence of the peak intensity of the $D-A$ band. Sample 35J22, $E_{\rm exc}=1.96$ eV, $P=50$ W/cm^2.

The estimate $E_A+E_D\approx120$ meV can be obtained from the peak energy of the $D-A$ band for very low excitation intensity with neglect of the Coulomb term in expression (1).

Measurements of the dependence of the peak intensity and frequency of the $D-A$ band on the temperature were also performed. Figure 3 plots the dependence of the logarithm of the peak intensity on the reciprocal temperature. The temperature dependence can be approximated by three linear segments, whose slopes give the activation energy in the respective temperature region. In the highest-temperature region the slope is equal to 90 meV, in the intermediate region it is ≈23 meV, and in the low-temperature region it is ≈8 meV. We link the 23-meV slope with the ionization energy of the acceptors, the 90-meV slope with the activation energy of the deep donor, and the 8-meV slope with the ionization energy of the shallow donor. The sum 90 meV $+23$ meV$=113$ meV is in line with the sum $E_A+E_D\approx120$ meV found from the peak frequency of the band at minimal excitation intensity. The decrease in the band intensity with increasing temperature can probably be explained by ionization of the acceptors and donors in a pair followed by nonradiative recombination.

Figure 4 plots the temperature dependence of the peak energy. It shows both measured values and values corrected for the temperature dependence of the X extremum in AlAs using of the Varshni formula:[6]

$$E_z(T)=E_z(0)-\alpha_z T^2/(T+\beta_z), \tag{2}$$

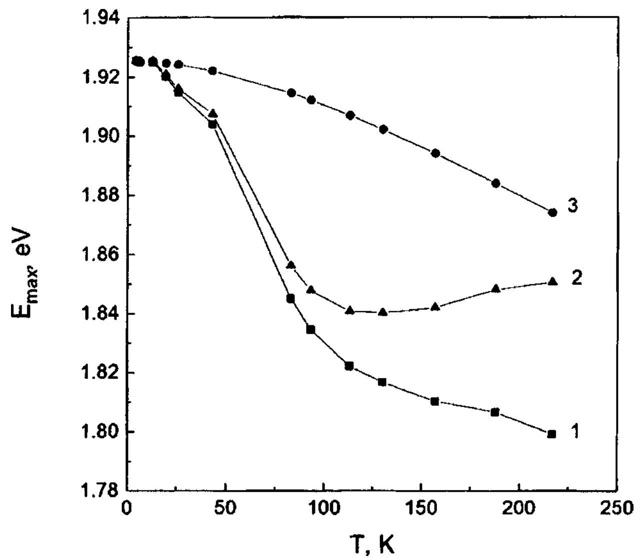

FIG. 4. Temperature dependence of the peak position of the $D-A$ band: *1* — measured values, *2* — values corrected for the temperature dependence of the width of the X_z band, *3* — calculated temperature dependence of the width of the X_z band. Sample 35J22, $E_{exc}=1.96$ eV, $P=17$ W/eV^2.

where $\alpha_z=4.60\times10^{-4}$ eV/K and $\beta_z=204$ K.[7]

The strong shift toward lower energies in the range from 40 to 80 K is noteworthy. It then ceases and is replaced in the range 110−220 K by a weak shift toward higher energies. The shift of the maximum of the $D-A$ band toward lower energies may be attributed to more rapid ionization of close pairs as the temperature rises since their ionization energies are lower due to the Coulomb interaction.

The spectrum with a discrete structure which is characteristic of close pairs and has been observed in a number of bulk semiconductors, for example, in GaP,[7] was not observed in our case. In the absence of such a spectrum, time-resolved luminescence measurements can provide evidence of the donor-acceptor nature of the band investigated.[3] We carried out measurements of this kind with excitation by a pulsed nitrogen laser. Here, as a consequence of the high excitation intensity per pulse the $D-A$ band shifts toward higher energies and overlaps with the strong exciton band. The separation of the spectrum into a direct and an indirect exciton band and a $D-A$ band shows that for a time delay of 500 ns the maximum of the $D-A$ band is shifted by 12 meV toward lower energies in comparison with its position for zero delay. As was noted above, close pairs, to which a higher luminescence energy corresponds, have a higher probability of recombination; therefore, when there is a large delay, the spectrum is governed by the luminescence of distant pairs, and a shift toward lower energies takes place. The intensity of the $D-A$ band rises relative to the intensity of the indirect exciton with increasing delay times, as can happen if its lifetime is greater than that of the indirect exciton.

The results adduced regarding the dependence of the peak energy of the $D-A$ band on the intensity of the exciting light and the delay time in the pulsed measurements provide sufficient grounds for ascribing this band to donor-acceptor recombination in a type-II superlattice.

Let us turn to the question of the nature of the centers forming the donor-acceptor pair. As is well known, silicon is an amphoteric impurity and, depending on its concentration, can lead to the creation not only of donors, but also of hydrogenic acceptors.[8] However, the large value $E_A+E_D \approx 120$ meV found from both the spectrum and measurements of the temperature dependence of the intensity is an indication that one of the partners in the pair is an impurity with an ionization energy of roughly 90 meV.

As we know, in many semiconductors (e.g., AlGaAs) silicon doping leads to the formation of so-called DX centers—deep donor centers which cause strong lattice relaxation and are associated with the phenomenon of persistent photoconductivity at low temperatures.[9] Similar DX centers were also detected in narrow type-II GaAs/AlAs superlattices.[1,2] In these structures two types of such centers can exist: DX_0 centers in the GaAs layers (Si in a Ga environment) and DX_3 centers in the AlAs layers (Si in an Al environment). The positions of the DX_0 and DX_3 centers relative to the bottom of the X_z band were found in Ref. 1 from Hall measurements in a 2.3/1.4 nm GaAs/AlAs superlattice (i.e., with layer widths similar to those in the superlattice investigated here). The position of the DX_3 center was estimated as 86 meV, which is very close to the value we found (90 meV) from the temperature dependence of the intensity of the $D-A$ band. In this light it makes sense to assume that the role of the deep donor in the pair is played by a DX_3 center, i.e., the donor-acceptor recombination in narrow type-II superlattices is caused by the deep donor center located in the AlAs layers and the hydrogenic acceptor in the GaAs layers (which is most probably also associated with Si), i.e., the interaction takes place through the interface. It is therefore possible, despite the large ionization energies, that the spectrum observed was not the line spectrum characteristic of the $D-A$ recombination of very close pairs. We also note that this case provides support for the model of a DX center with two electrons and a negative correlation energy.[9] Indeed, since the spectra were recorded under constant illumination, it may be thought that a center with one electron remains under illumination conditions.

The same results were observed in type-II superlattices doped only in the AlAs layers (JA-15). We note that the type-I (but close to type-II) sample also displayed a $D-A$ band caused by a deep donor.

The donor-acceptor recombination in a type-I 4/10 nm GaAs/AlAs quantum-well structure doped with silicon in its wells to a concentration of $\sim2\times10^{11}$ cm^{-2} had an entirely different form.[10] At helium temperatures, a band shifted from the exciton band by 24.5 meV toward lower energies was observed. We ascribe this band to donor-acceptor recombination with E_A+E_D equal to 39 meV. As the pump power is increased from 5 to 80 mW, the band shifts toward higher energies by 5 meV. As the temperature is raised, the intensity of the donor-acceptor band falls rapidly and is no longer observed at 40 K. This indicates that the recombination is associated with shallow Si donors. The acceptors are probably also associated with Si since the band intensity increased strongly in the concentration range in which Si forms both acceptors and donors.

CONCLUSION

We have detected a low-frequency band in the luminescence spectra of silicon-doped short-period GaAs/AlAs superlattices, which we ascribe to donor-acceptor recombination based on the dependence of its frequency on the intensity of the exciting light for continuous excitation and on the delay time for pulsed excitation. This band is associated with a deep donor center, which is presumably a DX center in the AlAs layers.

We thank A. Gurevich for the pulsed laser measurements.

[1)] It is noteworthy, however, that in one of the JA-15 samples assigned to type I, the same rate of displacement of the $D-A$ band was observed, although over a smaller dynamic range of excitation intensities. Measurements were impossible at higher excitation intensities since the $D-A$ band was masked by the very intense direct exciton band.

[1] P. Sellitto, P. Jeanjean, J. Sicart, J. L. Robert, and R. Planel, J. Appl. Phys. **74**, 7166 (1993).
[2] P. Sellitto, J. Sicart, and J. L. Robert, J. Appl. Phys. **75**, 7356 (1994).
[3] E. W. Williams and H. Barry Bebb, in *Semiconductors and Semimetals*, edited by R. K. Willardson and A. C. Beer (Academic Press, New York), Vol. 8, p. 321.
[4] K. Maeda, J. Phys. Chem. Solids **26**, 595 (1965).
[5] R. C. C. Leite and A. E. Di Giovanni, Phys. Rev. **153**, 841 (1967).
[6] Y. P. Varshni, Physica (Amsterdam) **34**, 149 (1967).
[7] F. Williams, Phys. Status Solidi **25**, 493 (1968).
[8] J. E. Northrup and S. B. Zhang, Phys. Rev. B **47**, 6791 (1993).
[9] P. M. Mooney, J. Appl. Phys. **67**, R1 (1990).
[10] V. F. Sapega (private communication).

Translated by Paul F. Schippnick

LOW-DIMENSIONAL SYSTEMS

Theoretical study of the threshold characteristics of InGaN multiquantum well lasers

G. G. Zegrya*) and N. A. Gun'ko†)

A. F. Ioffe Physicotechnical Institute, Russian Academy of Sciences, 194021 St. Petersburg, Russia
(Submitted July 24, 1997; accepted for publication November 18, 1997)
Fiz. Tekh. Poluprovodn. **32**, 843–848 (July 1998)

The threshold characteristics of InGaN multiquantum well lasers are investigated. A detailed analysis of the dependence of the threshold current on the quantum-well parameters and the temperature is performed. It is shown that, in comparison with long-wavelength lasers, InGaN lasers have a qualitatively different dependence of the threshold current on the quantum-well parameters (well width and number of quantum wells). The possibility of optimizing a InGaN laser structure is analyzed with the aim of improving the threshold characteristics and increasing the peak radiated power. © *1998 American Institute of Physics.*
[S1063-7826(98)01607-X]

1. INTRODUCTION

In the last few years the interest in superconductor compounds based on GaN has grown apace.[1–4] This has been due, first of all, to the wide practical applications of nitrides in opto-electronics. Recently, Nakamura *et al.*[1] reported the construction of a laser employing InGaN quantum wells as its active medium. They analyzed the threshold characteristics of this laser and noted that a fundamental analysis of the physical processes governing the operation of devices based on nitrides is needed to build advanced opto-electronic devices based on them. A detailed theoretical analysis of the physical processes governing the threshold characteristics of GaN lasers is lacking in the literature.

The present paper presents a first-principles theoretical analysis of the threshold characteristics of an InGaN multiquantum well laser. The gain coefficient of such a laser is calculated as a function of temperature and carrier concentration. The dependence of the threshold carrier concentration on temperature and the number of quantum wells is investigated in detail.

A detailed analysis of the dependence of the threshold current density on temperature, quantum-well width, and the number of quantum wells is carried out. It is shown that in contrast to long-wavelength lasers, in which the threshold current density depends nonmonotonically on the number of quantum wells, in InGaN lasers the threshold current density is a linear function of the number of quantum wells. This means that the main contribution to the threshold current comes from radiative recombination processes. We also perform a qualitative analysis of the influence of heating of the charge carriers on the threshold characteristics of the laser. We show that insignificant heating of the electron gas leads to a substantial increase in the threshold current density at high lattice temperatures. Finally, we compare our theoretical results with experimental data.[1] Good qualitative agreement is obtained.

2. GAIN COEFFICIENT AND RADIATIVE RECOMBINATION RATE

References 2–4 investigated the charge-carrier spectrum in GaN quantum wells and proposed a model for calculating the gain coefficient. However, an analysis of the temperature dependence of the gain coefficient is lacking. Also lacking is an analysis of the temperature dependence of the radiative recombination rate.

We calculate the gain coefficients $g(\omega)$ using the density-matrix formalism.[5]

The polarization vector $\mathbf{P}(t)$ is related to the single-particle density matrix operator by the following expression ρ:[5,6]

$$\mathbf{P}(t)=eN\sum_{mm'}\int\int \mathbf{r}_{m'm}(\mathbf{P},\mathbf{P}')\rho_{mm'}(\mathbf{P},\mathbf{P}',t)d\mathbf{P}d\mathbf{P}'. \tag{1}$$

Here e is the charge of the electron, N is the three-dimensional electron concentration, $\mathbf{r}_{m'm}$ is the dipole matrix element of the interband transition, and the $\rho_{mm'}$ are the matrix elements of the density operator ρ.

In what follows we will be interested only in four components of the density matrix: ρ_{vv} describes the state of an electron in the valence band, ρ_{cc} describes the state of an electron in the conduction band, ρ_{vc} describes a transition from the conduction band (state c) to the valence band (state v), and ρ_{cv} describes a transition from v to c. We consider direct interband transitions, where $\mathbf{r}_{vv}=\mathbf{r}_{cc}=0$. The matrix element of an interband transition between electron and hole levels can be represented in the form

$$r_{vc}(\mathbf{q}_c,\mathbf{q}_v)=r_{cv}(\mathbf{q}_c,\mathbf{q}_v)=r_{vc}(\mathbf{q})\delta_{\mathbf{q}_c-\mathbf{q}_v,0}, \tag{2}$$

where $\mathbf{q}$ is the longitudinal momentum of the charge carriers [$\mathbf{q}=(q_y,q_z)$, the x axis is perpendicular to the plane of the quantum well]. Taking these remarks into account, we have the following expression for the polarization vector:

 © 1998 American Institute of Physics

$$\mathbf{P}(t)=\frac{en}{a}\sum_{n_c,n_h}\int \mathbf{r}_{vc}(\mathbf{q})[\rho_{vc}(\mathbf{q},t)+\rho_{cv}(\mathbf{q},t)]d\mathbf{q}. \quad (3)$$

Here the summation is carried out over the size-quantization levels of the electrons (n_c) and holes (n_h), n is the two-dimensional electron concentration, and a is the quantum-well width.

The off-diagonal components of the density matrix are defined by the system of equations

$$i\hbar\frac{\partial\rho_{vc}}{\partial t}=\hbar\omega_{vc}\rho_{vc}-\frac{i\hbar}{T_{vc}}\rho_{vc}-e\mathbf{E}[\mathbf{r},\rho]_{vc}, \quad (4)$$

$$i\hbar\frac{\partial\rho_{cv}}{\partial t}=\hbar\omega_{cv}\rho_{cv}-\frac{i\hbar}{T_{cv}}\rho_{cv}-e\mathbf{E}[\mathbf{r},\rho]_{cv}, \quad (5)$$

where $\omega_{cv}=(E_c-E_v)/\hbar$, E_c and E_v are the electron and hole energies, respectively, and $\mathbf{E}$ is the electric field vector of the wave. Since ρ is a Hermitian operator, it is necessary that $T_{vc}=T_{cv}=\tau$. The constant τ is called the transverse dipole relaxation time and is associated with the linewidth of the optical transition. In order to solve Eqs. (4) and (5) for ρ_{cv} and ρ_{vc}, we use the approximation of the first harmonic of the electromagnetic field. We ultimately obtain

$$\rho_{vc}(\mathbf{q},t)=-\frac{e}{\hbar}D(q)\frac{\mathbf{r}_{vc}(\mathbf{q})\cdot\mathbf{E}e^{i\omega t}}{\omega_{vc}-\omega+i/\tau}, \quad (6)$$

$$\rho_{cv}(\mathbf{q},t)=-\frac{e}{\hbar}D(q)\frac{\mathbf{r}_{cv}(\mathbf{q})\cdot\mathbf{E}e^{-i\omega t}}{\omega_{cv}-\omega+i/\tau}, \quad (7)$$

where $D(q)=\rho_{cc}-\rho_{vv}$ is the difference between the levels in the conduction band and in the valence band. We express D in terms of the electron distribution functions in the conduction band and in the valence band f_c and f_v:

$$D=\frac{2}{(2\pi)^2 n}[f_c(q)-f_v(q)]. \quad (8)$$

Ultimately, according to Eqs. (3), (6)–(8), for the polarization vector we obtain the following expression:

$$\mathbf{P}(t)=-\frac{4e^2}{\hbar a}\mathbf{E}\sum_{n_c,n_h}\int\frac{d^2q}{(2\pi)^2}(\mathbf{r}_{cv}\cdot\mathbf{e})^2[f_c(q)-f_v(q)] \times\frac{(\omega_{cv}-\omega)\cos\omega t+(1/\tau)\sin\omega t}{(\omega_{cv}-\omega)^2+1/\tau^2}, \quad (9)$$

where $\mathbf{e}$ is the unit vector in the direction of the electric field vector $\mathbf{E}$ of the light wave. Next, we invoke the definition of the dielectric susceptibility χ

$$\mathbf{P}(t)=\chi(\omega)\mathbf{E}. \quad (10)$$

The imaginary part of the dielectric susceptibility $\varepsilon''(\omega)=4\pi\,\mathrm{Im}\,\chi(\omega)$. The gain coefficient $g(\omega)$ is related to $\varepsilon''(\omega)$ by the expression[7]

$$g(\omega)=-\frac{\omega}{c}\frac{\varepsilon''}{\sqrt{\kappa_0}}, \quad (11)$$

where κ_0 is the static dielectric constant. Substituting the above expression for $\varepsilon''(\omega)$ into expression (11) and employing relations (9) and (10), we obtain the following expression for the gain coefficient $g(\omega)$:

$$g(\omega)=\frac{16\pi}{\sqrt{\kappa_0}}\frac{e^2}{\hbar c}\frac{\hbar\omega}{a}\sum_{n_c,n_h}\frac{d^2q}{(2\pi)^2}(\mathbf{r}_{cv}\cdot\mathbf{e})^2 \times[f_c(q)+f_h(q)-1]\frac{\delta_\tau}{(E_c-E_h-\hbar\omega)^2+\delta_\tau^2}, \quad (12)$$

where $\delta_\tau=\hbar/\tau$. In expression (12) we have taken into account that $f_v(q)=1-f_h(q)$, where $f_h(q)$ is the hole distribution function. It is convenient to represent the dipole matrix element $\mathbf{r}_{cv}$ in the form

$$\mathbf{r}_{cv}=\boldsymbol{\mathcal{P}}_{cv}/\hbar\omega, \quad (13)$$

$$\boldsymbol{\mathcal{P}}_{cv}=\int dx\,\mathbf{j}_{cv}. \quad (14)$$

Here $\mathbf{j}_{cv}$ is the probability flux density,

$$\mathbf{j}_{cv}=i\gamma(u_c^*\mathbf{v}_v+u_v\mathbf{v}_c^*), \quad (15)$$

where $u(\mathbf{r})$ and $\mathbf{v}(\mathbf{r})$ are the smooth envelopes of the Bloch functions of s and p type,[5] $\gamma^2\simeq(\hbar^2/2m_c)E_g$, m_c is the effective mass of the electron, and E_g is the band-gap width.

With the help of formulas (12) and (13) we obtain the final expression for the gain coefficient

$$g(\omega)=\frac{8\pi}{\sqrt{\kappa_0}}\frac{e^2}{\hbar c}\frac{1}{\hbar\omega}\frac{1}{a}\sum_{n_c,n_h}\int q\,dq|\boldsymbol{\mathcal{P}}_{cv}|^2 \times[f_c(q)+f_h(q)-1]\mathcal{L}(\omega,q), \quad (16)$$

where

$$\mathcal{L}(\omega,q)=\frac{1}{\pi}\frac{\delta_\tau}{(E_c-E_h-\hbar\omega)^2+\delta_\tau^2}, \quad (17)$$

$$\mathcal{L}(\omega,q)\rightarrow\delta(E_c-E_h-\hbar\omega)\quad\text{for }\delta_\tau\rightarrow 0,$$

$|\boldsymbol{\mathcal{P}}_{cv}|^2=|\boldsymbol{\mathcal{P}}_{cv}^{\parallel}|^2/2$ for the TE mode, and $|\boldsymbol{\mathcal{P}}_{cv}|^2=|\boldsymbol{\mathcal{P}}_{cv}^{x}|^2$ for the TM mode. We have taken into account that, according to relations (13) and (14), the radiative matrix element is equal to $\boldsymbol{\mathcal{P}}_{cv}=(\mathcal{P}^x_{cv},\mathcal{P}^{\parallel}_{cv})$.

The spectral radiated intensity $\Phi(\omega)$ per unit area due to the recombination of nonequilibrium electrons and holes is related to the absorption coefficient $\alpha(\omega)$ as follows:[7,8]

$$\frac{\Phi(\omega)}{\alpha(\omega)}=\frac{\hbar\omega^3}{\pi^2 v^2}\frac{1}{e^{(\hbar\omega-\Delta F)/T}-1}, \quad (18)$$

where $v=c/\sqrt{\varepsilon_\infty}$, $\Delta F=F_e-F_h$ is the difference between the Fermi quasilevels for electrons and holes, respectively, and ε_∞ is the high-frequency dielectric constant.

In thermodynamic equilibrium the spectral radiated intensity $\Phi(\omega)$ is equal to the spectral radiated intensity of an ideal blackbody. Thus, relation (18) yields Kirchhoff's law.[7]

On the basis of Eq. (18), the frequency-integrated radiative recombination rate can be represented by the following integral:

$$R_{\mathrm{ph}}=\int_0^\infty \frac{1}{\hbar\omega}\Phi(\omega)d\omega$$

$$=\frac{\varepsilon_\infty}{\pi^2 c^2}\int_0^\infty \frac{\alpha(\omega)\omega^2 d\omega}{\exp[(\hbar\omega-\Delta F)/T]-1}. \quad (19)$$

In the particular case when $\Delta F=0$ expression (19) goes over to the formula of Roosbroeck and Schockley.[9] The absorption coefficient can be found using expression (16). Substituting the expression for $\alpha(\omega)$ into expression (19) and integrating over ω with allowance for the relation $\mathcal{L}(\omega,q)=\delta[E_c(q)-E_h(q)-\hbar\omega]$, for the two-dimensional radiative recombination rate we obtain

$$R_{\mathrm{ph}}=\frac{8\varepsilon_\infty}{\pi\sqrt{\kappa_0}}\frac{e^2}{\hbar c}\frac{1}{\hbar^3 c^2}$$

$$\times\sum_{n_c,n_h}\int q dq\left[|\mathcal{P}_{cv}^x|^2+\frac{1}{2}|\mathcal{P}_{cv}^{\parallel}|^2\right]$$

$$\times f_c(E_c)f_h(E_h)(E_c-E_h). \quad (20)$$

We shall make use of the above expression for R_{ph} below to calculate the threshold current density of the laser.

3. THRESHOLD CHARACTERISTICS OF AN InGaN MULTIQUANTUM WELL LASER

To calculate the threshold current, it is necessary to calculate the threshold concentration of nonequilibrium carriers. The threshold concentration is found from the condition

$$\tilde{g}_{\mathrm{th}}\equiv\Gamma g_{\mathrm{th}}=\alpha_i+\alpha^*, \quad (21)$$

where $\alpha^*=(1/L)\ln(1/R)$. Here the modal gain coefficient $\tilde{g}_{\mathrm{th}}$ is expressed in terms of the local gain coefficient g [see Eq. (16)] and the optical confinement factor Γ; α_i denotes the internal optical losses, L is the resonator length, and R is the reflection coefficient of the laser mirrors.

Below, in the analysis of the laser threshold characteristics we shall take into account the internal losses associated with absorption at the interface.[5] The internal losses influence the dependence of the gain coefficient on temperature and concentration. Figure 1 plots the dependence of the maximum value of the modal gain coefficient $\tilde{g}_{\mathrm{th}}^{\max}$ on the carrier concentration at different temperatures for a laser structure consisting of twenty quantum wells with well width 25 Å. In the temperature interval from 300 to 400 K the concentration dependence of the gain coefficient is practically linear. One consequence of the linear dependence of the gain coefficient on the concentration is temperature stability of the threshold characteristics of the InGaN laser at high temperatures ($T>400$ K). Here we can expect an increase in the maximum radiated power of such lasers in comparison with long-wavelength lasers by more than an order of magnitude.[1] Figure 2 plots the dependence of the maximum value of the gain coefficient $\tilde{g}_{\mathrm{th}}^{\max}$ on the temperature for three carrier concentrations in laser structures with quantum-well thickness 25 Å (as before, the number of quantum wells equals 20). As in the case of long-wavelength lasers, $\tilde{g}_{\mathrm{th}}^{\max}$ falls with rising temperature. For a fixed concentration the gain coefficient

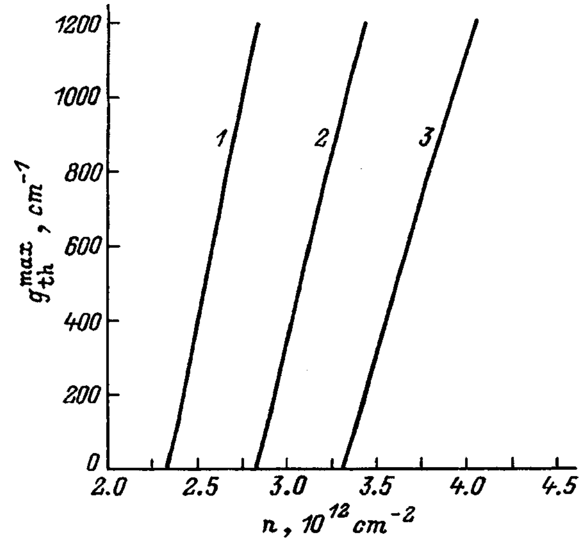

FIG. 1. Maximum value of the modal gain coefficient $\tilde{g}_{\mathrm{th}}^{\max}$ as a function of carrier concentration at different temperatures. $N=20$, $a=25$ Å. T, K: *1* — 300, *2* — 350, *3* — 400. The parameters used in the calculation were for the $In_{0.2}Ga_{0.8}N/In_{0.05}Ga_{0.95}N$ laser structure in Ref. 1.

decreases with increasing well width (e.g., when the well width increases from 25 to 50 Å, the gain coefficient falls by approximately a factor of two).

The threshold carrier concentration n_{th} found from Eq. (21) depends on the quantum-well parameters: on the heights of the heterobarriers for electrons and holes V_c and V_v, on the quantum-well width a and on the number of quantum wells N. It follows from an analysis of the temperature dependence of the gain coefficient (Fig. 2) that the threshold concentration depends on T nearly linearly. Allowance for the internal radiation losses leads to a nonlinear dependence of n_{th} on T. As was noted above, the threshold concentration also depends on the number of quantum wells N. It follows

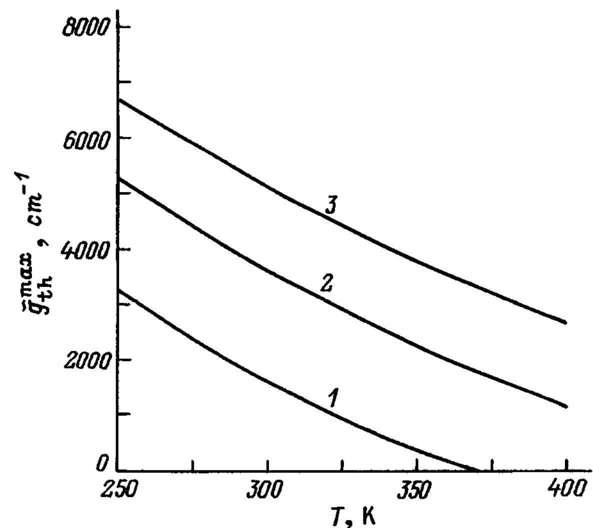

FIG. 2. Maximum value of the gain coefficient $\tilde{g}_{\mathrm{th}}^{\max}$ as a function of the temperature for different carrier concentrations in an InGaN laser structure. $N=20$, $a=25$ Å. n, 10^{12} cm^{-2}: *1* — 3, *2* — 4, *3* — 5. The parameters used in the calculation were for the $In_{0.2}Ga_{0.8}N/In_{0.05}Ga_{0.95}N$ laser structure in Ref. 1.

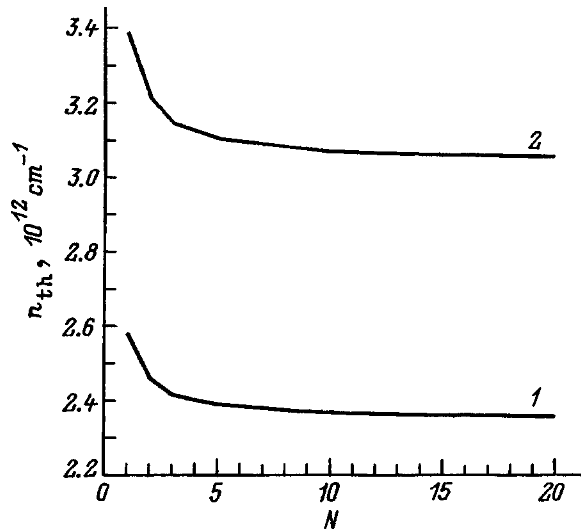

FIG. 3. Threshold carrier concentration $n_{\rm th}$ versus number of quantum wells N for $T=300$ K, $a=25$ (*1*) and 50 (*2*) Å. $\alpha^*=30$ cm^{-1}. The parameters used in the calculation were for the $In_{0.2}Ga_{0.8}N/In_{0.05}Ga_{0.95}N$ laser structure in Ref. 1.

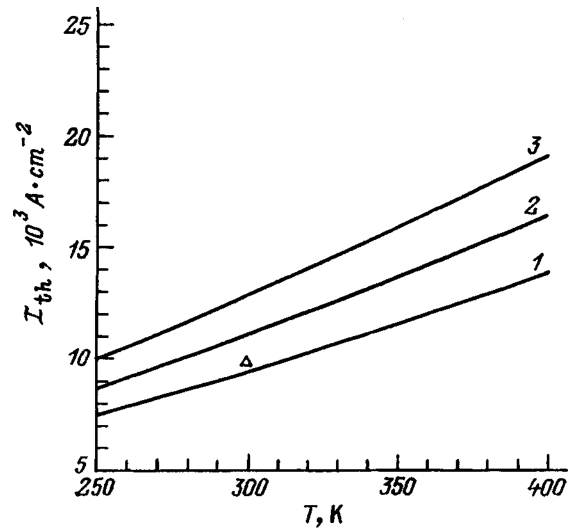

FIG. 4. Threshold current density $\mathcal{I}_{\rm th}$ versus temperature for different degrees of carrier heating $\alpha=(T_e-T_0)/T_0$: *1* — 0, *2* — 0.1, *3* —0.2. $a=25$ Å, $N=20$. $\alpha^*=30$ cm^{-1}. The parameters used in the calculation were for the $In_{0.2}Ga_{0.8}N/In_{0.05}Ga_{0.95}N$ laser structure in Ref. 1. The triangle marks the experimental value of $\mathcal{I}_{\rm th}$ from Ref. 1.

from Fig. 3 that the threshold concentration depends on the number of quantum wells N in a nonlinear fashion and tends to saturate at large values of N. For $N>5$ the threshold concentration is essentially independent of the number of quantum wells. Note that the threshold concentration is a more abrupt function of the number of quantum wells N for long-wavelength lasers than for an InGaN laser.[10]

As our analysis has shown, the main contribution to the threshold current density of InGaN lasers comes from radiative recombination processes. Consequently, the threshold current is equal to

$$\mathcal{I}_{\rm th}\simeq eR_{\rm ph}(n_{\rm th}), \tag{22}$$

where the radiative recombination rate $R_{\rm ph}$ is calculated according to formula (20).

Figure 4 plots the temperature dependence of the threshold current density $\mathcal{I}_{\rm th}$ for a laser with quantum-well thickness $a=25$ Å. Qualitative and quantitative analysis show that the radiative recombination rate $R_{\rm ph}$ depends on the temperature according to a power law. Here the main contribution to the temperature dependence of $\mathcal{I}_{\rm th}$ comes from the temperature dependence of the concentrations of the nonequilibrium electrons (n) and holes (p). It was noted above that the temperature dependence of the threshold concentration is practically linear, $n_{\rm th}\sim T$. Consequently, the threshold current density $\mathcal{I}_{\rm th}$ is a weakly nonlinear function of temperature: $\mathcal{I}_{th}\sim T^{1+\beta}$, where $\beta\ll 1$ (see Fig. 4). An analysis of the temperature dependence of $\mathcal{I}_{\rm th}$ was performed for various degrees of carriers heating: $\alpha=(T_e-T_0)/T_0$, where T_e is the carrier temperature and T_0 is the lattice temperature. Note that regardless of the degree of carrier heating, the dependence of the threshold current on temperature remains nearly linear since $\beta\ll 1$ up to $T=400$ K and even at higher temperatures. The linear dependence of $\mathcal{I}_{\rm th}$ on T signifies a high temperature stability of nitride lasers at high temperatures. For long-wavelength lasers ($\lambda>1$ μm) $\beta>1$. Therefore, the nonlinear temperature dependence of $\mathcal{I}_{\rm th}$, in turn, has a strong effect on the temperature stability of long-wavelength lasers at high temperatures.[10]

The triangle in Fig. 4 corresponds to the experimental value of the threshold current density for an InGaN laser with 20 quantum wells.[1]

Let us turn now to an analysis of the dependence of the threshold current density $\mathcal{I}_{\rm th}$ on the number of quantum wells N. Figure 5 plots the dependence of $\mathcal{I}_{\rm th}$ on N at $T=300$ K. For actual laser structures the threshold current $\mathcal{I}_{\rm th}$ grows linearly as the number of quantum wells is increased (Fig. 5). The threshold current, according to expression (22), is proportional to the radiative recombination rate: $R_{\rm ph,th}\simeq\gamma n_{\rm th}^2$, where γ is the bimolecular recombination coefficient. There-

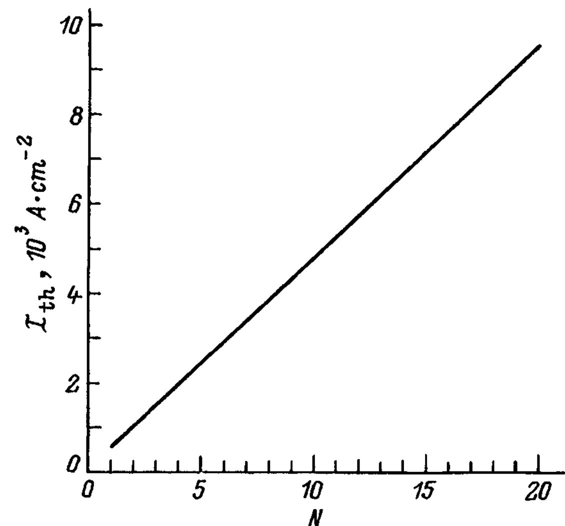

FIG. 5. Threshold current density $\mathcal{I}_{\rm th}$ versus number of quantum wells for $T=300$ K. $a=25$ Å. $\alpha^*=30$ cm^{-1}. The parameters used in the calculation were for the $In_{0.2}Ga_{0.8}N/In_{0.05}Ga_{0.95}N$ laser structure in Ref. 1.

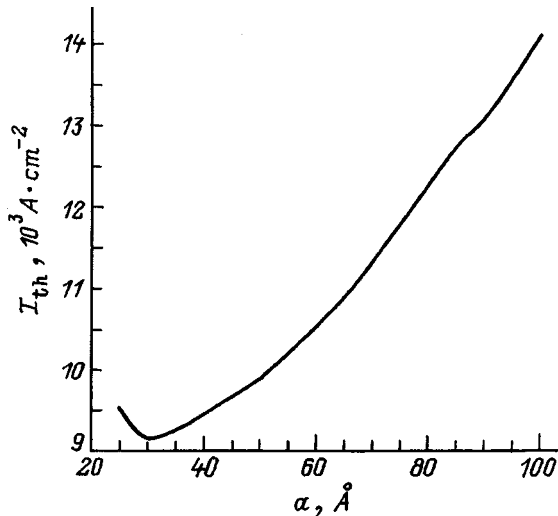

FIG. 6. Threshold current density $\mathcal{I}_{th}$ versus quantum-well width a for $T=300$ K. $N=20$. $\alpha^*=30$ cm^{-1}. The parameters used in the calculation were for the $In_{0.2}Ga_{0.8}N/In_{0.05}Ga_{0.95}N$ laser structure in Ref. 1.

fore, the dependence of $\mathcal{I}_{th}$ on N is governed by the dependence of both the threshold concentration and γ on N. The threshold concentration n_{th} falls nonmonotonically as N rises (Fig. 3). Consequently, the main contribution to the dependence of $\mathcal{I}_{th}$ on N comes from the bimolecular recombination coefficient γ, which increases linearly with N.

In long-wavelength lasers the dependence of $\mathcal{I}_{th}$ on N is fundamentally different: as the number of quantum wells N rises, the threshold current $\mathcal{I}_{th}$ at first falls and reaches a minimum at a certain value of N; then $\mathcal{I}_{th}$ begins to increase practically linearly with N (Ref. 10).

Figure 6 plots the dependence of the threshold current density $\mathcal{I}_{th}$ on the quantum-well width a. The dependence of $\mathcal{I}_{th}$ on the quantum-well width a is nonmonotonic. At a certain value of a, $\mathcal{I}_{th}$ has a minimum. The nonmonotonic dependence of $\mathcal{I}_{th}$ on a is connected with the dependence of the threshold concentration, as well as the bimolecular recombination coefficient γ, on the quantum-well width. The coefficient γ is proportional to the electron-hole overlap integral I_{ch}: $\gamma \sim |I_{ch}|^2$ [see Eq. (20)]. With decrease in the quantum-well width, the overlap integral falls and, at a certain thickness, saturates since only one bound state remains in the quantum well. For a fixed value of the Fermi quasilevel, the threshold concentration n_{th} grows as a is decreased. As a result, $\mathcal{I}_{th}$ falls with decrease in the quantum-well width a. At the value of a at which $I_{ch}=$const, $\mathcal{I}_{th}$ reaches a minimum, and further reduction of the quantum-well width leads to an increase in $\mathcal{I}_{th}$ due to the growth of n_{th}.

Thus, an analysis of the dependence of the threshold current on the number of quantum wells and their width shows that optimal parameters exist, for which the value of $\mathcal{I}_{th}$ is minimized. For InGaN lasers the optimum number of quantum wells is $5 \leqslant N \leqslant 10$ since for $N>10$ the threshold concentration n_{th} is essentially independent of N, and $\mathcal{I}_{th}$ increases linearly with N. Therefore, a decrease in the number of quantum wells by a factor of 2 leads to a decrease in $\mathcal{I}_{th}$ by a factor of 2, and a decrease in $\mathcal{I}_{th}$ leads to a weakening of the carrier heating processes and to a suppression of leakage currents.

4. CONCLUSION

In this paper we have carried out a microscopic analysis of the threshold characteristics of an InGaN multiquantum well laser. We have shown that the threshold characteristics of such a laser depend substantially on the parameters of the laser structure and on the temperature (see Figs. 2–6). We have demonstrated that the threshold current of nitride lasers has a qualitatively different dependence on the quantum-well parameters in comparison with long-wavelength lasers. This analysis makes it possible to optimize the laser structures, which is very important for building high-power GaN lasers operating at high temperatures.

This work was partially supported by the Russian Fund for Fundamental Research (Grants No. 96-02-17952 and No. 97-02-18151) and by the Russian State Program ''Physics of Solid-State Nanostructures'' (Grants No. 97-0003, 97-1035, and 97-2014).

*)E-mail: zegrya@theory.ioffe.rssi.ru
†)E-mail: gunko@ammp.ioffe.rssi.ru

[1] S. Nakamura, M. Senoh, S. Nagahama, N. Iwasa, T. Yamada, T. Matsushita, H. Kiyoku, and Y. Sugimoto, Jpn. J. Appl. Phys. **35**, L217 (1996).
[2] S. L. Chuang and C. S. Chang, Appl. Phys. Lett. **68**, 1657 (1996).
[3] A. T. Meney, E. P. O'Reilly, and A. R. Adams, Semicond. Sci. Technol. **11**, 897 (1996).
[4] W. J. Fan, M. F. Li, T. C. Chong, and J. B. Xia, J. Appl. Phys. **80**, 3471 (1996).
[5] G. G. Zegrya, in *Antimonide Related Strained Layer Heterostructures*, edited by M. O. Manasreh (Gordon and Breach, Newark, N.J., 1997).
[6] R. H. Pantell and H. E. Puthoff, *Fundamentals of Quantum Electronics* (Wiley, New York, 1969).
[7] L. L. Landau and E. M. Lifshitz, *Electrodynamics of Continuous Media* (Pergamon Press, Oxford, 1984).
[8] V. P. Gribkovskiĭ, *Theory of Absorption and Emission of Light in Semiconductors* (Minsk, Nauka i Tekhnika, 1975).
[9] W. van Roosbroeck and W. Shockley, Phys. Rev. **94**, 1558 (1954).
[10] Peter S. Zory, Jr. (Ed.), *Quantum Well Lasers* (Academic Press, San Diego, 1993).

Translated by Paul F. Schippnick

Modulation of optical absorption of GaAs/AlGaAs quantum wells in a transverse electric field

L. E. Vorob'ev, E. A. Zibik, D. A. Firsov, and V. A. Shalygin*)

St. Petersburg State Technical University, 195251 St. Petersburg, Russia

O. N. Nashchekina and I. I. Saĭdashev

A. F. Ioffe Physicotechnical Institute, Russian Academy of Sciences, 194021 St. Petersburg, Russia

(Submitted December 23, 1997; accepted for publication December 23, 1997)
Fiz. Tekh. Poluprovodn. **32**, 849–851 (July 1998)

Results of experimental investigations of the transformation of intraband light absorption spectra by the quantum-well electrons in a transverse electric field are presented. In addition to the familiar Stark effect, absorption oscillations in the photoionization band are detected. These oscillations are caused by electron transitions from the ground state in a quantum well to quasidiscrete levels arising in the continuum of states above the well due to the linear potential of the external electric field. © *1998 American Institute of Physics.* [S1063-7826(98)01707-4]

Processes of intraband optical absorption in quantum wells govern the operation of a new class of infrared detectors based on nanostructures.[1] The most efficient are photodetectors on near-resonant quantum wells, in which one of the discrete levels is located near the top of the well. Numerous papers have been dedicated to a theoretical analysis of the intraband optical absorption spectrum of such wells both under equilibrium conditions and in a strong transverse electric field (see, e.g., Refs. 2–4). Experimental studies of nanostructures have revealed that the intersubband absorption line undergoes a Stark shift and broadening in strong electric fields.[1,5,6] At the same time, quasiperiodic oscillations of the absorption coefficient in the photoionization spectrum of a quantum-well, which, as was theoretically predicted in Ref. 2, should arise in strong transverse electric fields, have not yet been observed experimentally. The aim of the present work was to experimentally detect these oscillations.

The structure investigated includes fifty GaAs quantum wells of width $L_W = 5.1$ nm separated by $Al_{0.33}Ga_{0.67}As$ barriers of width $L_B = 25.4$ nm, which were grown on a semi-insulating GaAs substrate. A simple calculation by the effective-mass method in the single-electron approximation (without allowance for nonparabolicity and collective effects) gives two discrete levels for such wells: $E_1 = -174$ meV and $E_2 = -4$ meV (the energies are measured from the top of the well; the depth of the well is $|V| = 247$ meV). Since the E_2 level is shallow, the quantum well is near-resonant. The electron concentration in the wells is $n_s = 3 \times 10^{11}$ cm^{-2}. Between the substrate and the quantum-size layers there was a doped layer of thickness 0.5 μm with an electron concentration of 10^{18} cm^{-3}, on which, after local etching of the quantum-size layers, four ohmic point contacts were created at the corners of the sample (the total area of the sample was 6×4 mm^2). There was an analogous doped layer on the free surface of the structure, in the central part of which two point contacts were created. The point contacts on each of the conducting layers were joined together, and the resistance of the sample in a weak field was 150 Ω at $T = 77$ K. The optical and electro-optical measurements were all performed at this same temperature. The comparatively small magnitude of the resistance of the structure in a transverse field indicates the presence of shorting channels in the quantum-size layers. Consequently, the transverse field in the structure is not uniform. How the effective intensity of this field was determined will be indicated below.

Optical radiation was introduced into the structure through a 45° bevelled end face of the substrate. Thanks to multiple total internal reflections, the total length of the optical path of the light beam through the quantum-size layers was 17 μm.

A polarizer was placed in front of the sample. By rotating it, it was possible to excite either an s wave (i.e., an ordinary wave, for which the electric field vector is perpendicular to the optical axis of the structure and, consequently, parallel to the plane of the quantum well) or a p wave (i.e., an extraordinary wave, linearly polarized in the orthogonal direction) in the quantum-size layers.

The equilibrium spectra of the optical absorption coefficient α (in the absence of an external electric field) were investigated for both polarizations (α_p and α_s) in the range $h\nu = 130 - 280$ meV. Figure 1 displays the spectral dependence of the difference $\alpha_p - \alpha_s$ which exhibits an intense absorption peak corresponding to interlevel transitions $E_1 \rightarrow E_2$ at $h\nu \approx 170$ meV. The absorption peak is noticeably asymmetric, its short-wavelength wing being more intense thanks to the contribution to the absorption from photoionization, i.e., electron transitions under the action of light from the E_1 level to the continuum of states above the well. In the absence of an external field, photoionization has a threshold at $h\nu_i = 174$ meV.

The electrical measurements were performed in a pulsed electric field in order to avoid heating the sample. To enhance the sensitivity of the measuring circuit, we used a

 © 1998 American Institute of Physics

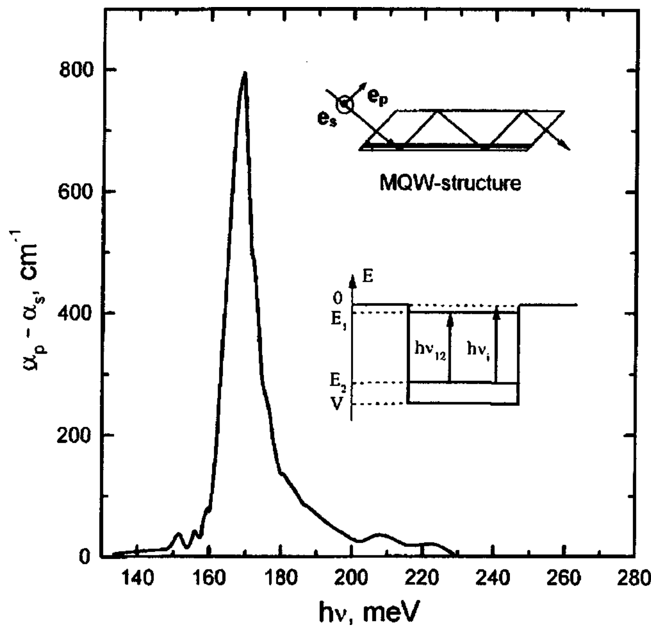

FIG. 1. Equilibrium optical absorption spectrum of a quantum-well structure. The upper inset shows the ray path in the sample and the direction of the electric field of light waves with s and p polarization, and the lower inset shows an energy level diagram of the optical transitions for a quantum well in the absence of an external electric field.

synchronous detector. For an s wave electro-optical modulation was absent over the entire spectral range investigated. The measured spectral dependence of absorption modulation for a p wave is shown in Fig. 2.

In the spectral region $h\nu<200$ meV the nature of the observed modulation spectra corresponds to a Stark shift of the $E_1 \rightarrow E_2$ interlevel absorption line in an electric field, as well as its broadening. Line broadening is indicated by the fact that an increase in the intensity of the external electric field F leads to optical bleaching of the sample $[\alpha_p(F) < \alpha_p(0)]$ in the central part of the equilibrium absorption peak ($h\nu \approx 170$ meV), while on either side of the bleaching

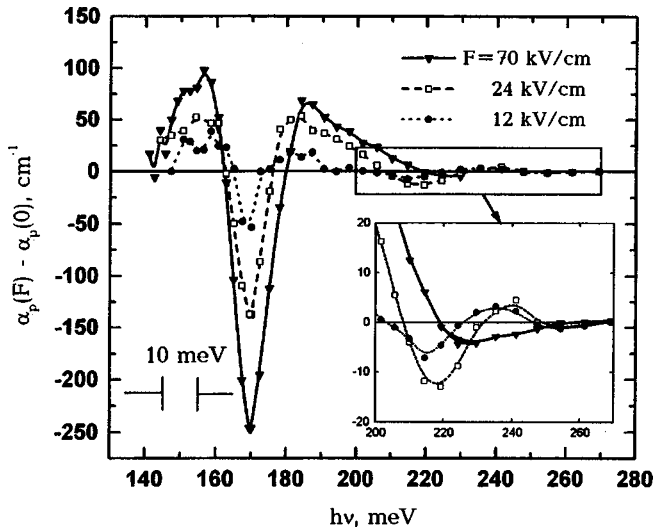

FIG. 2. Spectral curves of the absorption coefficient for p-polarized light in a transverse electric field.

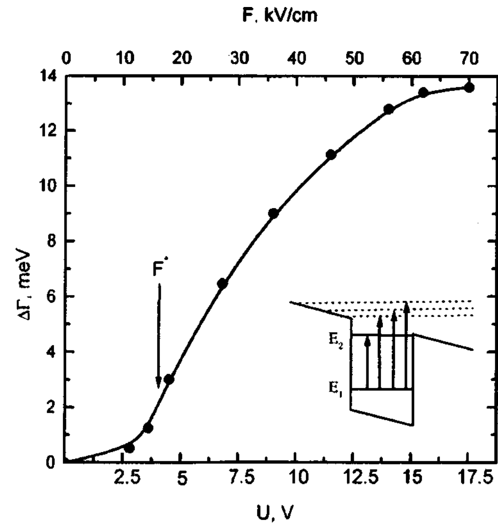

FIG. 3. Width of the interlevel absorption line ($E_1 \rightarrow E_2$) as a function of the transverse potential difference U. The transverse field strength in the quantum wells is plotted along the upper horizontal axis. The inset presents a diagram of the optical transitions for a quantum well located in an external electric field.

band there are adjoining regions of increased absorption, in which $\alpha_p(F) > \alpha_p(0)$. This broadening occurs because the transverse electric field enables electron tunneling from the E_2 level to the above-barrier space. Figure 3 shows how the width of the interlevel absorption line increases as the transverse potential difference is increased to $U=17.5$ V. The course of the observed dependence is in qualitative agreement with the calculation in Ref. 2. Referring to the point of inflection on this curve, which corresponds to a field $F^* = |E_2|/(eL_W)$, we can establish the relationship between the magnitude of the effective transverse electric field strength F in the structure and the experimentally measured potential difference U. The corresponding values of F are indicated in Fig. 3 along the upper horizontal axis of the graph.

From the equilibrium absorption spectrum $\alpha_p(0)$ and the modulation curves $\alpha_p(F) - \alpha_p(0)$ it is possible to reconstruct the nonequilibrium absorption spectra in a transverse field $\alpha_p(F)$. An analysis of the latter demonstrates that the maximum electric field reached in the experiment ($F=70$ kV/cm) corresponds to a Stark shift of the interlevel absorption line of $+3$ meV. This result is in good agreement with the experimental data of Ref. 6.

The most important result of the present work, in our opinion, is the experimental detection of oscillations in the absorption modulation spectra for a transverse field at photon energies $h\nu>200$ meV. In the absence of an electric field, weak optical absorption is observed in this spectral region due to optical transitions from the E_1 level to the continuum of states above the well. According to the calculation in Ref. 4 for near-resonant wells, for $h\nu > |E_1| + |E_2|$ absorption should decrease monotonically with increasing photon energy, as was observed in experiment (Fig. 1). The presence of a transverse electric field leads to a transformation of the energy spectrum of the electrons in the well. Due to the linear potential of the external field, a series of quasidiscrete

levels appears against the background of the continuum of states above the well in addition to the sparsely arranged levels of the rectangular well. As a result, peaks corresponding to electron transitions from the E_1 level to these quasi-discrete levels appear in the optical absorption spectrum. The distance between these peaks grows as the transverse field strength is increased.[2]

The inset to Fig. 2 displays the electronic absorption spectra in the photoionization band far from the interlevel absorption line. For a fixed field the electronic absorption changes sign quasiperiodically. As the external field strength F is increased, the energy interval between the zeros on the modulation curve increases monotonically, in qualitative agreement with the calculation in Ref. 2.

Varying the model parameters in the calculation and fitting it to the experiment, we can, in principle, independently determine the quantum-well parameters: the width L_W and depth V. Thus, electronic absorption measurements in a transverse field are quite informative from the point of view of the metrics of quantum wells.

We are grateful to A. G. Petrov and A. Ya. Shik for discussing the results of these studies.

This work was partially supported by the Russian Fund for Fundamental Research (Grants No. 96-02-17404 and No. 96-02-17961), the Russian Fund for Fundamental Research together with INTAS (Grant No. 00615i96), the Ministry of Science and Technology of the Russian Federation (Grant No. 96-1029), Ministry of General and Professional Education of Russia (Grant No. 95-0-7.2-159 and a grant within the scope of the ''Russian Universities'' Program), and by the State Directed Program ''Integration'' (Project No. 75).

*)E-mail:vadim@phsc8.stu.neva.ru

[1] B. F. Levine, J. Appl. Phys. **74**, R1 (1993).
[2] A. G. Petrov and A. Ya. Shik, Fiz. Tekh. Poluprovodn. **24**, 1431 (1990) [Sov. Phys. Semicond. **24**, 846 (1990)].
[3] F. L. Serzhenko and V. D. Shadrin, Fiz. Tekh. Poluprovodn. **25**, 1579 (1991) [Sov. Phys. Semicond. **25**, 953 (1991)].
[4] A. G. Petrov and A. Ya. Shik, Fiz. Tekh. Poluprovodn. **31**, 666 (1997) [Semiconductors **31**, 567 (1997)].
[5] A. Harwit, Jr. and J. C. Harris, Appl. Phys. Lett. **50**, 685 (1987).
[6] E. Rosencher, E. Martinet, F. Luc, Ph. Bois, and E. Böckenhoff, Appl. Phys. Lett. **59**, 3255 (1991).

Translated by Paul F. Schippnick

Light absorption and refraction due to intersubband transitions of hot electrons in coupled GaAs/AlGaAs quantum wells

L. E. Vorob'ev, I. E. Titkov, D. A. Firsov,*) and V. A. Shalygin

St. Petersburg State Technical University, 195251 St. Petersburg, Russia

A. A. Toropov and T. V. Shubina

A. F. Ioffe Physicotechnical Institute, Russian Academy of Sciences, 194021 St. Petersburg, Russia

V. N. Tulupenko

Donbass State Mechanical Engineering Academy, 343913 Kramatorsk, Ukraine

E. Towe

Laboratory for Optics and Quantum Electronics, Thornton Hall, University of Virginia, Charlottesville, Virginia 22903-2442, USA

(Submitted December 23, 1997; accepted for publication December 23, 1997)
Fiz. Tekh. Poluprovodn. **32**, 852–856 (July 1998)

Variation of the absorption coefficient and refractive index of a system of tunnel-coupled GaAs/AlGaAs quantum wells in a longitudinal electric field is discovered and investigated in the spectral region corresponding to intersubband electron transitions. The phenomena observed are explained by electron heating in the electric field and electron transfer in physical space. The equilibrium absorption spectra at lattice temperatures of 80 and 295 K are presented.
© *1998 American Institute of Physics.* [S1063-7826(98)01807-9]

INTRODUCTION

The wavelengths corresponding to intersubband (i.e., taking place within the valence band or conduction band) transitions in quantum wells of semiconductor heterostructures usually lie in the middle and far infrared (IR) regions ($\lambda > 5\ \mu$m). Changes in the design of the quantum wells lead to changes in the energy spectrum, making it possible to study new phenomena and build opto-electronic devices on intersubband transitions that operate in a prescribed spectral range. A classical example of the application of intersubband transitions in optics is photodetectors in the middle infrared region.[1] One of the significant advances in the optics of intersubband transitions is the development of the quantum-cascade laser,[2] which has made it possible to substantially advance the wavelength of semiconductor lasers into the long-wavelength region. The latest development in the technology of intersubband lasers is the ''fountain'' laser with optical pumping.[3] Intersubband transitions of electrons in quantum wells are also used to modulate the intensity of radiation transmitted through the structure. Modulators based on a pair of tunnel-coupled quantum wells operating on the effects of spatial electron transfer between wells in a transverse (directed along the growth axis of the structure) electric field are well known.[4] The modulation of light on intersubband transitions in simple rectangular quantum wells by electron heating in a longitudinal electric field applied in the plane of the nanolayers has also been investigated.[5–7] The present work examines the modulation of the absorption coefficient and refractive index by electron heating in a longitudinal electric field in a specially designed system of tunnel-coupled GaAs/AlGaAs quantum wells.

SAMPLES

For these studies, we developed and grew a structure containing 150 pairs of tunnel-coupled GaAs/$Al_xGa_{1-x}As$ quantum wells (QW's) separated by tunnel-opaque barriers 20 nm in width. The potential profile and energy levels in the quantum wells are shown in Fig. 1. The structure parameters were chosen so that the distance between the ε_2 and ε_3 levels would correspond to the energy of a CO_2-laser photon and the distance $\varepsilon_2-\varepsilon_1$ would be less than the energy of an optical phonon $\hbar\omega_0 = 37$ meV. Part of the barrier was doped with silicon, which reduced the effect of impurity scattering on the electron mobility in the quantum wells, and the surface electron concentration was $N_s = 5\times10^{11}\ \mathrm{cm}^{-2}$.

We note the following features of the structure. The states with energies ε_1 and ε_4 are genetically linked to the first, deeper quantum well, while the states with energies ε_2 and ε_3 are due to the presence of the second, wider quantum well. This causes, in particular, the wave function of the first state to be localized mainly within the first well and the wave function of the second state to be localized in the second well (see Fig. 1). In addition, the values of the optical matrix elements $|M_{ik}|^2 = |\int\Psi_k^*\hat{p}_z\Psi_i dz|^2$, which specify the probabilities of optical transitions between the ith and kth levels, differ strongly. The largest contribution to the intersubband absorption comes from transitions between neighboring

 © 1998 American Institute of Physics

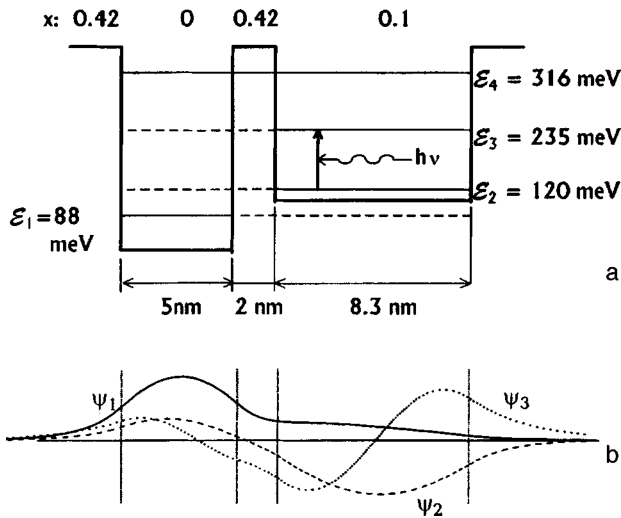

FIG. 1. a — Potential profile of the structure investigated and calculated energy levels in that structure; b — electron wave functions at the first three energy levels.

levels genetically linked with the same quantum well: $|M_{13}|^2=0.16$, $|M_{23}|^2=1$, $|M_{14}|^2=0.89$, $|M_{24}|^2=0.0062$ (in arbitrary units).

The physics of the modulation of the absorption coefficient in a longitudinal electric field in such a structure can be described as follows. At the lattice temperature $T_0=77$ K all the electrons are concentrated at the first energy level ε_1. The longitudinal electric field heats the electrons and thereby fills higher-lying states of this level (subband). As a result, electron transitions to the second subband ε_2 become possible as a consequence of phonon or impurity scattering. The resulting increase in the electron concentration in the second subband leads to the appearance of (or a substantial increase in) absorption on $\varepsilon_2 \rightarrow \varepsilon_3$ transitions. Increase in the absorption coefficient α_{23} is also facilitated by satisfaction of the condition $\varepsilon_2-\varepsilon_1<\hbar\omega_0$, which lowers the probability of electrons scattering from the second subband back to the first with emission of an optical phonon. The space charge arising upon selective doping modifies the above picture somewhat. More will be said about this below.

EXPERIMENTAL TECHNIQUE

Electro-optical measurements were performed at $T_0=80$ K. The electric field was applied in the plane of the layers of the quantum-size structure with the help of gold ohmic contacts deposited on the end faces of the wafer. The duration of the electric field pulse was 200 ns. Optical radiation was introduced into the structure through the bevelled lateral edges of the wafer and underwent a series of internal reflections in it. Such a geometry made it possible to study absorption and refraction of both s- and p-polarized light (see Fig. 2). A diagram of the electro-optical measurements is shown in Fig. 2. The changes in the absorption of CO_2-laser radiation at $\lambda=10.6$ μm were investigated. The polarization vector of the incident radiation $\mathbf{e}_\omega$ formed an angle $\alpha=45°$ with the x axis so that the incident wave contained both s ($\mathbf{e}_\omega \| OX$) and p ($\mathbf{e}_\omega \perp OX$) polarizations. The changes in the absorption of light by the quantum-size structure in a longitudinal electric field were recorded by a Ge⟨Hg⟩ photodetector at analyzer azimuthal angles $\beta=0°$ (s-polarization) and 90° (p-polarization). Along with the amplitude modulation, we also measured the phase modulation due to anisotropic changes in the refractive index of the structure in an electric field. Information about the phase shift between the s and p components of the light wave could be obtained by measuring the output signal at other values of β: $0<\beta<90°$.

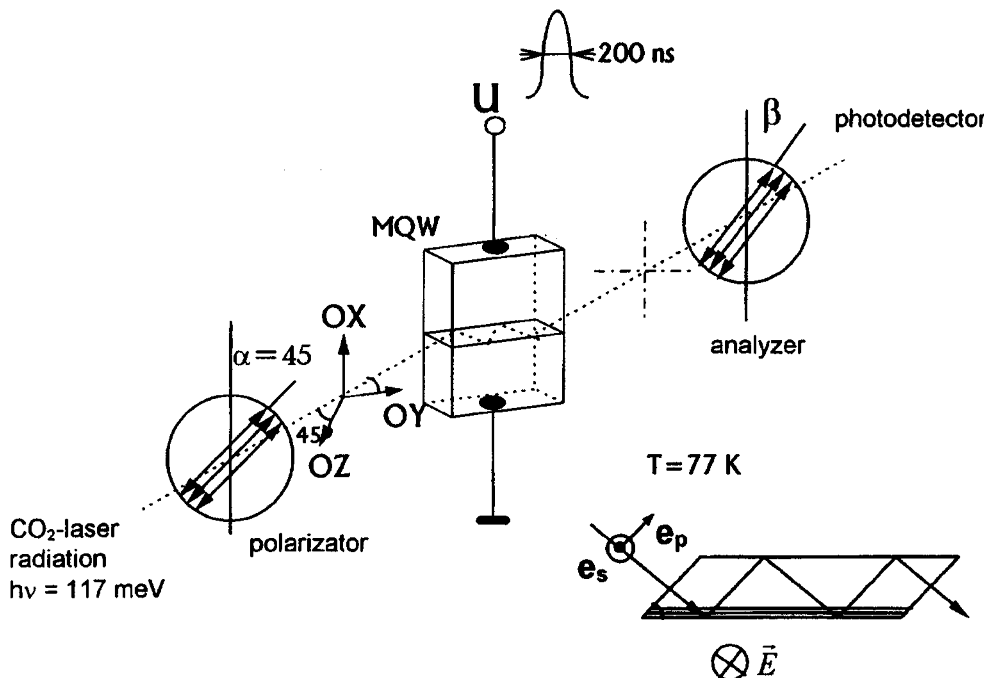

FIG. 2. Diagram of the electro-optical measurements, polarization directions, and ray path in the sample.

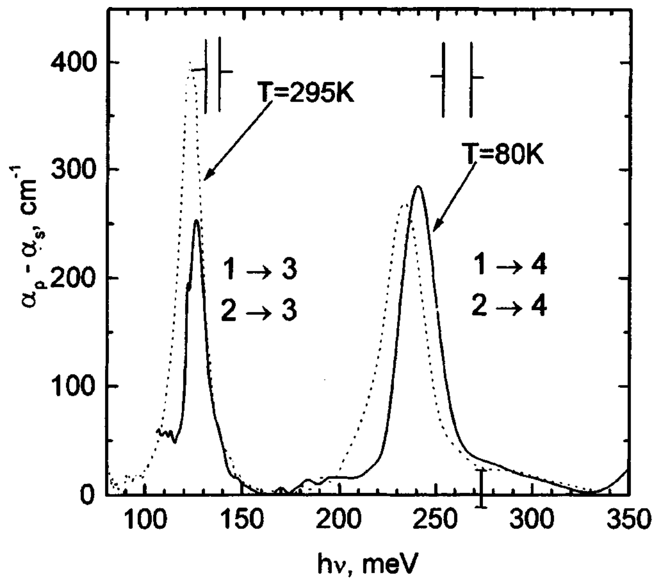

FIG. 3. Equilibrium absorption spectra.

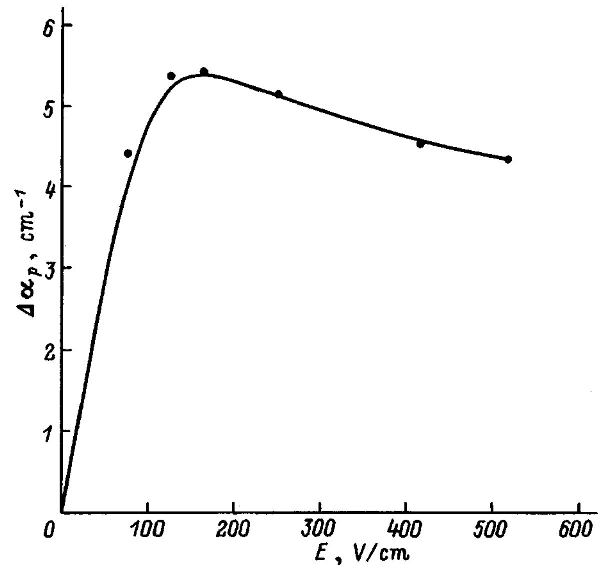

FIG. 4. Absorption coefficient of p-polarized light as a function of the longitudinal electric field strength. $T=80$ K. $\lambda=10.6$ μm.

EXPERIMENTAL RESULTS AND DISCUSSION

With the aim of refining the structure parameters and positions of the energy levels, we investigated the equilibrium spectra of the absorption coefficient. The results for two lattice temperatures are shown in Fig. 3. The spectra consist of two pronounced absorption bands. The spectral positions of the bands allows us to link the long-wavelength band with the *1→3* and *2→3* transitions and the short-wavelength band with the *1→4* and *2→4* transitions, the peaks corresponding to the transitions from levels *1* and *2* having coalesced. We explain the temperature dependence of the band intensities as follows. At 80 K the electrons are concentrated mainly at the first size-quantization level ε_1. As the temperature rises, filling of the second level ε_2 takes place. However, because $M_{23} \gg M_{12}$ even an insignificant increase in the electron concentration at the second level with increasing temperature leads to a considerable increase in absorption. Since absorption in the second band is governed almost entirely by electrons of the first level ($M_{14} \gg M_{24}$), a small decrease in the electron concentration at this level in response to an increase in the temperature has only a weak effect on the absorption intensity in the second band.

Figure 4 plots the dependence of the absorption coefficient of the structure on the longitudinal electric field strength. As expected, changes in absorption are observed only for the p-polarized radiation, which is active for optical intersubband transitions. The modulation curve consists of two parts: growth in relatively weak electric fields and an insignificant falloff in the high-field region.

By virtue of the selection rules for the polarization of the incident radiation, the quantum wells have a strong optical anisotropy in the spectral region corresponding to intersubband transitions. As a consequence, even in the absence of an electric field the refractive indices for the s and p waves differ. In an electric field this difference in the refractive indices varies. This phenomenon can be explained, for example, with the help of the Kramers–Kronig relation

$$\Delta n = |\Delta(n_p - n_s)| = \frac{c}{\pi} \int \frac{\Delta\alpha(\omega')d\omega'}{\omega'^2 - \omega^2}. \tag{1}$$

Figure 5 plots the experimentally determined dependence of Δn on the electric field strength. The behavior of this curve is similar to that of $\Delta\alpha_p(E)$.

Let us discuss the nature of the dependences observed. The structures investigated were selectively doped. The quantum-well potential is distorted as a consequence of the appearance of a space charge field due to electrons localized in the quantum wells and impurity ions found in the barrier. The exact potential distribution in space can be obtained from the self-consistent solution of the Schrödinger and Poisson equations. In this paper we confine ourselves to a qualitative discussion. The general form of the quantum-well potential allowing for space-charge effects is shown in Fig.

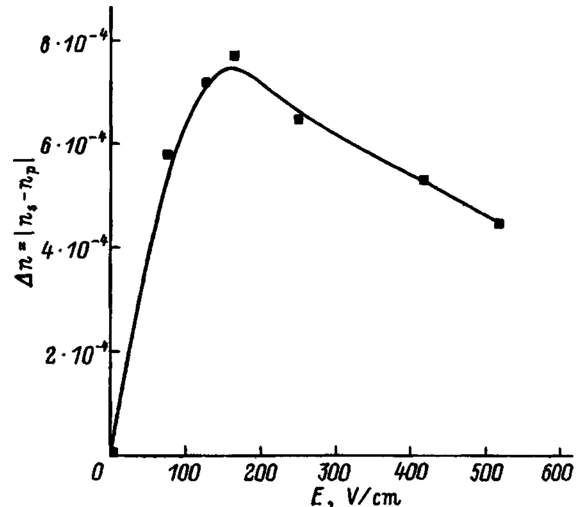

FIG. 5. Difference between the refractive indices of s- and p-polarized light as a function of the longitudinal electric field strength. $T=80$ K. $\lambda=10.6$ μm.

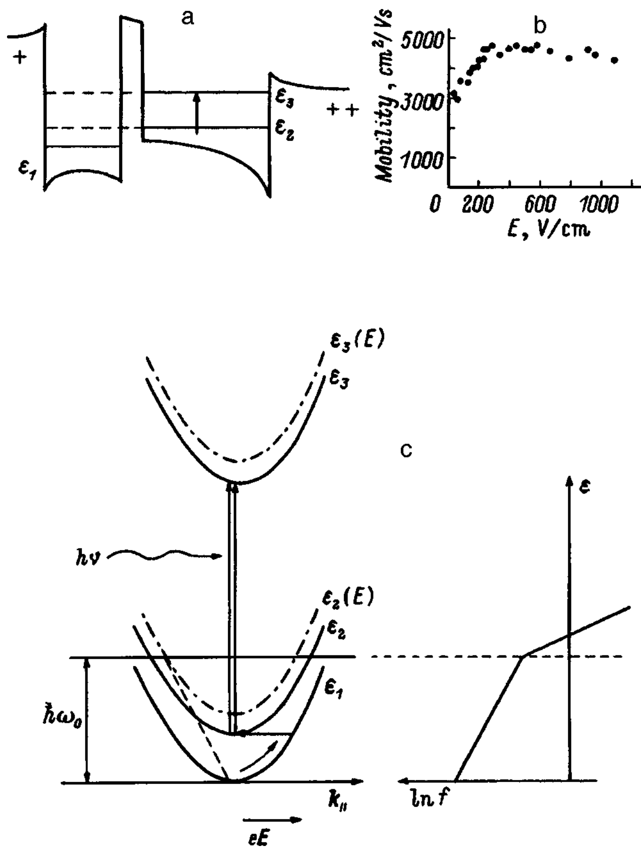

FIG. 6. Illustration of the proposed model of the observed phenomena: a — dependence of the potential with allowance for the space charge ; b — plot of the mobility as a function of the electric field strength; c — heating and redistribution of electrons between subbands 1 and 2 in an electric field E.

6. The distortion of the potential relief lowers the energies of the ε_2 and ε_3 levels and narrows the energy distance between the ε_1 and ε_2 levels. The convergence of these levels to energies of the order of 10 meV can possibly explain the coalescence of the *1→3* peak with the *2→3* peak and of the *1→4* peak with the *2→4* peak in the equilibrium absorption spectra (see Fig. 3).

Let us consider the phenomena arising in a heating electric field. In the absence of a field the electrons are found in the first level ε_1 and are spatially localized in the first quantum well. Heating of the electrons by the electric field leads to an increase in their mean energy. As a consequence of scattering by acoustic phonons, impurities, and bumps on the interfaces, electrons pass from the first size-quantization subband to the second size-quantization subband, causing an increase in the absorption coefficient on the $\varepsilon_2 \rightarrow \varepsilon_3$ transitions. This process is depicted schematically in Fig. 6. Filling of the second subband in an electric field explains the growth segment of the absorption coefficient in Fig. 4. But along with the mechanism providing for an increase in the absorption coefficient, competing factors also begin to be manifested in strong fields. As was already mentioned, electrons occupying the second energy level are localized to a significant degree in the second quantum well, whereas electrons with energy ε_1 are found in the first quantum well. Thus, as the electrons undergo transitions from the first to the second level in an electric field, they redistribute in physical space, and this redistribution corresponds to a decrease in space charge. The distortion of the potential decreases, causing levels *2* and *3* to begin to return to the positions dictated by the square-well potential. The positions of subbands *2* and *3* in an electric field are depicted in Fig. 6 by the dot-dashed line. Such a shift of the ε_2 level in an electric field lowers the fraction of active electrons of this level contributing to absorption. Indeed, contributions to the $\varepsilon_2 \rightarrow \varepsilon_3$ absorption are made almost entirely by electrons with energies less than the energy level of an optical phonon $\hbar\omega_0$. Because of strong scattering with emission of an optical phonon and transition of an electron back to the first band, the number of electrons with energy $\varepsilon > \hbar\omega_0$ is small. As an illustration, Fig. 6 shows the qualitative form of the nonequilibrium distribution function $f(\varepsilon)$, which falls abruptly at energies $\varepsilon > \hbar\omega_0$.[1)] The decrease of the fraction of light-absorbing electrons leads to a diminution of the increase in the absorption coefficient with the field. In addition, in strong fields stronger heating of the electrons in the second subband in comparison with the first is manifested. This is due to a relative weakening of the role of scattering on imperfections of the interfaces in the second, wider well. An increase in the mean energy in the second subband leads to intense scattering with emission of optical phonons upon the transition of electrons back to the first subband, which in turn leads to saturation and even a small falloff of absorption in a strong electric field (see Fig. 4). Confirmation of the role of electron transfer in physical space in the phenomena considered here is provided by the behavior of the electron mobility in a strong field shown in Fig. 6. The small value of the mobility in weak fields is explained by significant scattering by interface imperfections when the electrons are localized in the first, relatively narrow quantum well. As the field is increased, filling of the states of subband *2* takes place, electrons are partially localized in the second, wider well, in which scattering at the interface is relatively weak, and the mobility begins to grow. In strong fields the above-described mechanisms for the reflux of electrons into the first subband step into action, and the mobility begins to fall.

We note that electron–electron scattering between the ε_1 and ε_2 subbands is greatly weakened as a result of the spatial separation of the electrons in these subbands. Therefore, the mean energies and distribution functions of the electrons in these levels (subbands) can be different.

CONCLUSION

We have examined the optical properties of tunnel-coupled quantum wells governed by intersubband transitions of electrons in a longitudinal electric field. Modulation of the absorption coefficient and refractive index in an electric field has been detected and explained on the basis of a model of heating and spatial electron transfer.

This work was partially supported by the Russian Fund for Fundamental Research (Grant No. 96-02-17404), the Russian Fund for Fundamental Research in conjunction with INTAS (Grant No. 00615i96), the Ministry of Science and Technology of the Russian Federation (Grant No. 96-1029), the State Directed Program ''Integration'' (Project No. 75),

and NATO (Grant No. HTECH LG 960931).

*)E-mail: dmfir@phsc2.stu.neva.ru

1)Under conditions of strong scattering on optical phonons the nonequilibrium distribution function can be represented in the form of two segments of Boltzmann functions with different temperatures joined together at the optical phonon energy $\hbar\omega_0$.

[1] B. F. Levine, J. Appl. Phys. **74**, R1 (1993).

[2] J. Faist, F. Capasso, D. L. Sivco, C. Sirtori, A. L. Hutchinson, and A. Y. Cho, Science **264**, 533 (1994).

[3] O. Gauthier-Lafaye, S. Sauvage, P. Boucaud, F. H. Julien, R. Prazeres, F. Glotin, J.-M. Ortega, V. Thierry-Mieg, R. Planel, J.-P. Leburton, and V. Berger, Appl. Phys. Lett. **70**, 3197 (1997).

[4] E. Dupont, D. Delacourt, V. Berger, N. Vodjdani, and M. Papuchon, Appl. Phys. Lett. **62**, 1907 (1993).

[5] L. E. Vorob'ev, E. A. Zibik, Yu. V. Kochegarov, S. N. Danilov, D. A. Firsov, E. Towe, D. Sun, A. A. Toropov, and T. V. Shibina, Fiz. Tekh. Poluprovodn. **29**, 1136 (1995) [Semiconductors **29**, 588 (1995)].

[6] E. Towe, D. Sun, L. E. Vorobjev, S. N. Danilov, D. A. Firsov, and E. A. Zibik, Superlattices Microstruct. **17** (2), 129 (1995).

[7] L. E. Vorob'ev, I. I. Saĭdashev, D. A. Firsov, and V. A. Shalygin, [JETP Lett. **65**, 544 (1997)].

Translated by Paul F. Schippnick

Light absorption in aperiodic PbS/C superlattices in an electric field

S. F. Musikhin,*) V. I. Il'in, O. V. Rabizo, and L. G. Bakueva

St. Petersburg State Technical University, 195251 St. Petersburg, Russia

L. V. Sharonova

A. F. Ioffe Physicotechnical Institute, Russian Academy of Sciences, 194021 St. Petersburg, Russia

(Submitted January 12, 1998; accepted for publication January 19, 1998)
Fiz. Tekh. Poluprovodn. **32**, 857–859 (July 1998)

Light absorption is investigated in aperiodic PbS/C Fibonacci and Thue–Morse superlattices at room temperature for two orientations of the light wave electric field. In the first case the electric field vector is directed parallel to the plane of the superlattice. In the second case there is a component perpendicular to the plane of the superlattice. Light absorption is investigated in an external electric field directed along the axis of the superlattice. © *1998 American Institute of Physics.* [S1063-7826(98)01907-3]

A characteristic feature of aperiodic superlattices is the form of the energy spectrum of electrons, holes, phonons, and other collective excitations. Superlattices based on hierarchical structures continue to attract the attention of researchers[1,2] as objects which have an energy spectrum constructed using the principles of Cantor sets. The formation of the energy spectrum in aperiodic superlattices is governed by of the choice of alternation of layers of different thickness or of different composition.

Thus it is possible to assign the required form of the energy spectrum during fabrication of the lattice. Among the various forms of superlattices, structures in which the alternation of layers obeys definite laws, viz., Fibonacci lattices, Thue–Morse lattices, Rudin–Shapiro lattices, and their generalizations, have been the focus of special attention. Fibonacci superlattices are a one-dimensional analog of a quasicrystal and, in this regard, can serve as a model object for studying the electron and phonon energy spectra.[3] However, aperiodic lattices, in their own right, exhibit interesting optical and electrical properties, which can be studied both theoretically[4,5] and experimentally.[6–8] From the practical point of view, they can be used to design materials with an energy spectrum of prescribed structure, in particular for optoelectronic applications. In this context, a study of the optical properties of aperiodic superlattices and the influence of an electric field on them is of interest. The present study explores the transmission of polarized and unpolarized light by Fibonacci and Thue–Morse superlattices. The effect of an electric field applied along the growth axis of the superlattice is also examined.

The structures were prepared by pulsed laser deposition on glass, quartz, and silicon substrates in vacuum. A semitransparent layer of silver was deposited on the insulating substrate before preparation of the superlattice and on the surface of the superlattice after its deposition.

These silver layers served as electrical contacts to the superlattice. The lattices contained 20 pairs of layers, each pair consisting of a layer of diamondlike carbon about 5 Å in thickness and a layer of lead sulfide 114 or 57 Å thick. The PbS layers had n-type conductivity.

The optical properties of the superlattices were investigated at room temperature. As ellipsometric measurements showed, the extinction coefficient for $\lambda = 0.6328\ \mu$m had a value of 1.2 for a periodic PbS/C lattice and 1.3 for Fibonacci and Thue–Morse lattices with similar values of the layer thickness. This indicates different absorption in periodic and aperiodic superlattices and, consequently, energy spectra of different structure. We also investigated the transmission spectra of the superlattices in the region of photon energies $1-3$ eV. Steps associated with transitions between spatial-quantization levels, which are typical for superlattices, are clearly visible in the transmission spectra as a function of photon energy. Thanks to the nonparabolicity of the electron and hole bands in PbS, light absorption associated with transitions between quantization levels is also possible for normal incidence of light on the surface of the lattices, where the electric field vector is parallel to the superlattice layer. The nature of light absorption is different for the components of the electric field vector of the light wave that are parallel and perpendicular to the superlattice layers. To study the effect of the parallel and perpendicular components of the electric field vector, we investigated the transmission of normally incident light and of polarized light incident at a 45° angle. In the latter case the electric field vector has a component perpendicular to the superlattice plane. As revealed by measurements of the polarized-light transmission spectra, the absorption increases with the perpendicular component of the electric field vector.

Figure 1a shows the spectrum of the difference between the incident and transmitted light fluxes $(1-T)$ (T is the optical transmittance) as a function of the photon energy E for a Fibonacci lattice with normal incidence of unpolarized light (curve *1*) and polarized light having a component of the electric field vector perpendicular to the superlattice plane (curve *2*). Figure 1b shows the analogous spectra for a Thue–Morse lattice. As can be seen from Fig. 1a, for the absorption of light having a perpendicular component of the

 © 1998 American Institute of Physics

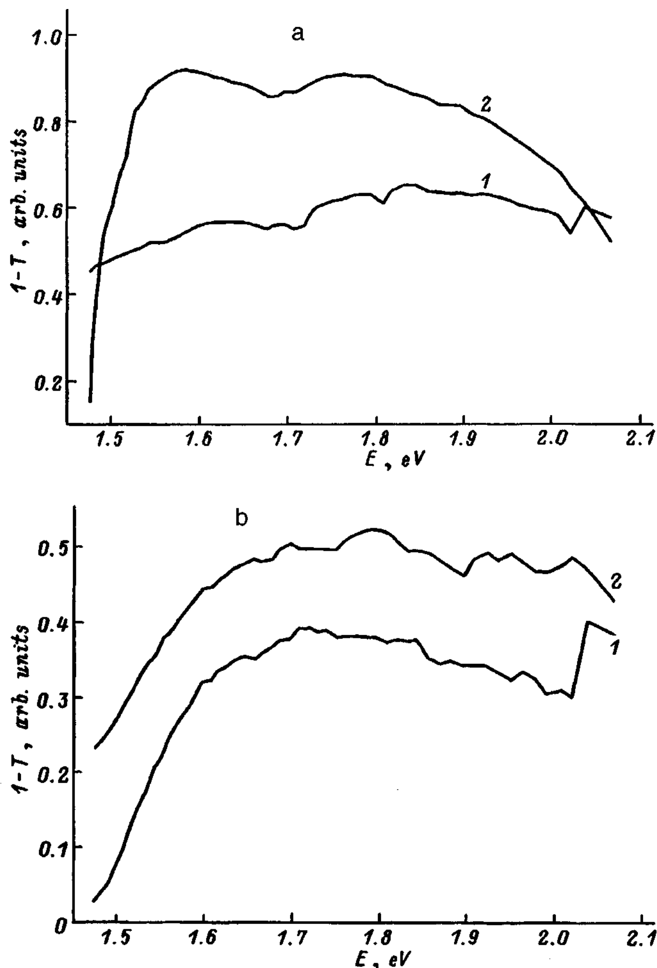

FIG. 1. Difference between the incident and transmitted light fluxes $(1-T)$ in relative units as a function of photon energy E for a Fibonacci lattice (a) and a Thue–Morse lattice (b): *1* — normal incidence of unpolarized light (the electric field vector of the light wave is parallel to the superlattice plane), *2* — linearly polarized light incident at a 45° angle to the superlattice plane (the electric field vector of the light wave has a component perpendicular to the superlattice plane).

electric field vector an absorption region appears in the interval 1.52–1.68 eV. The second feature is associated with a decrease in absorption in the region of photon energies greater than 1.8 eV. In the Thue–Morse lattices regions of absorption appear in the intervals 1.67–1.69, 1.75–1.82, and 1.88–1.97 eV when the electric field vector of the light wave has a perpendicular component.

Electron transitions associated with light absorption in superlattices are possible between hole and electron size-quantization levels. In our superlattices

all the valence-band levels are occupied by electrons. As a calculation of the levels in a PbS/C Fibonacci superlattice shows,[9] segments of forbidden states and segments with a dense array of levels are present in the energy spectrum. Transitions between regions with a dense array of levels produce wide absorption regions. It can be seen from the experimental spectra that the locations of these regions are different for the Fibonacci and Thue–Morse lattices. This is evidence of a difference in the energy spectra of these two types of superlattices.

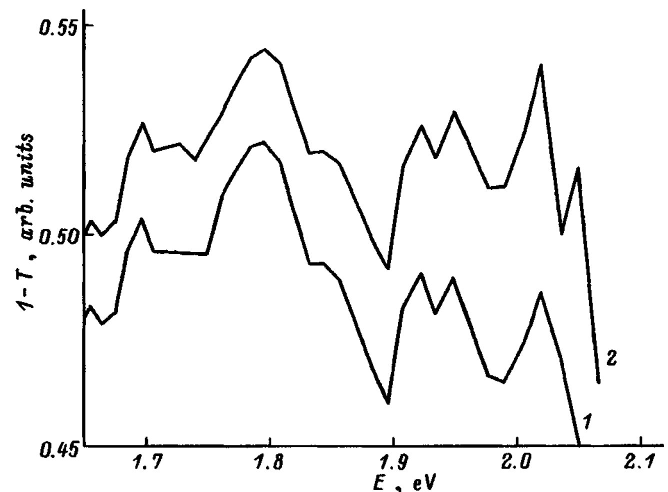

FIG. 2. Difference between the incident and transmitted light fluxes $(1-T)$ in relative units as a function of photon energy E for a Thue–Morse lattice. External voltage applied perpendicular to the superlattice layers: $U=0$ (*1*) and 3 V (*2*).

Application of an electric field parallel to the superlattice axis induces changes in the energy spectrum. As was shown in Ref. 9, application of an electric field breaks down the strict hierarchy of levels and, if the bias is large enough (greater than 0.4 V), causes the gap between the levels of the higher hierarchy to disappear. Our measurements show that in Fibonacci lattices absorption grows in an electric field. In Thue–Morse lattices absorption in the region 1.55–2.06 eV causes an increase or a decrease in transparency, depending on the polarity of the applied voltage (Fig. 2), and in the region 1.075–1.13 eV bleaching is observed for normal incidence, while the absorption grows for any polarity when the electric field vector of the light wave has a perpendicular component. Hysteresis of the optical transmittance in an electric field was observed earlier in Fibonacci superlattices.[10]

Thus, aperiodic superlattices possess a variety of optical and electro-optical properties that can be used in optoelectronic devices.

This work was supported by the State Directed Program ''Integration'' (Project No. 75) and the Russian Foundation for Basic Research (Grant No. 96-02-17200).

*)E-mail: smus@twonet.stu.neva.ru

[1] E. Diez, F. Dominguez-Adame, E. Maciá, and A. Sánchez, Phys. Rev. B **54**, 16 792 (1996).
[2] P. Carpena, V. Gasparian, and M. Ortuño, Phys. Rev. B **51**, 12 813 (1995).
[3] M. Quilichini and T. Janssen, Rev. Mod. Phys. **69**, 277 (1997).
[4] A. Rodriguez and F. Dominguez-Adame, Phys. Rev. B **56**, 10 737 (1997).
[5] P. E. de Brito, C. A. A. da Silva, and H. N. Nazareno, Phys. Rev. B **51**, 6096 (1995).
[6] S. F. Musikhin, L. G. Bakueva, V. I. Il'in, O. V. Rabizo, and L. V. Sharonova, Fiz. Tekh. Poluprovodn. **29**, 474 (1995) [Semiconductors **29**, 245 (1995)].
[7] S. F. Musikhin, V. I. Il'in, O. V. Rabizo, L. G. Bakueva, and T. V.

Yudintseva, Fiz. Tekh. Poluprovodn. **31**, 56 (1997) [Semiconductors **31**, 46 (1997)].

[8] V. I. Il'in, S. F. Musikhin, L. G. Bakueva, O. V. Rabizo, and S. A. Rykov, Mater. Sci. Eng., B **35**, 120 (1995).

[9] E. Ya. Glushko and V. N. Evteev, Fiz. Tekh. Poluprovodn. **31**, 889 (1997) [Semiconductors **31**, 756 (1997)].

[10] V. I. Il'in, S. F. Musikhin, L. G. Bakueva, and O. V. Rabizo, in *Proceedings of the International Symposium ''Nanostructures: Physics and Technology''* (St. Petersburg, Russia, June 26–30, 1995), p. 111.

Translated by Paul F. Schippnick

Growth of InAs quantum dots on vicinal GaAs(001) surfaces misoriented in the [010] direction

V. P. Evtikhiev,*) V. E. Tokranov, A. K. Kryzhanovskiĭ, A. M. Boĭko, R. A. Suris, and A. N. Titkov

A. F. Ioffe Physicotechnical Institute, Russian Academy of Sciences, 194021 St. Petersburg, Russia

A. Nakamura and M. Ichida

CIRSE, Nagoya University, 464-01 Nagoya, Japan

(Submitted January 15, 1998; accepted for publication January 19, 1998)
Fiz. Tekh. Poluprovodn. **32**, 860–865 (July 1998)

Atomic-force microscopy (AFM) is used to study InAs quantum-dot structures grown by molecular-beam epitaxy (MBE) on vicinal GaAs(001) surfaces misoriented in the [010] direction by 1, 2, 4, and 6°. It is shown for a chosen misorientation direction that a vicinal GaAs(010) surface is covered with a network of stepped terraces. The thickening of the network of terraces with increasing misorientation angle leads to the suppression of adatom surface diffusion and makes it possible to achieve higher densities and more uniform ensembles of quantum dots, while simultaneously decreasing the probability of their coalescence. © *1998 American Institute of Physics.* [S1063-7826(98)02007-9]

Realization of the unique electronic properties of semiconductor quantum dots (QD) due to the δ-like energy dependence of the density of electron states for quantum dots requires the creation of dense arrays of uniform quantum dots.[1] Traditional methods for preparing semiconductor nanostructures based on lithography followed by etching, unfortunately, do not provide sufficiently uniform ensembles of quantum dots. The use of such methods also produces defects on the interfaces in the structures. For this reason, a method for obtaining quantum dots directly during heteroepitaxial growth of lattice-mismatched semiconductors via the Stranski–Krastanow mechanism has attracted wide attention.[2] The stresses arising due to lattice mismatch lead to a shift in the growth mode from two-dimensional to three-dimensional. The increase in the energy of the system caused by the mechanical stresses is partially compensated by the formation of dislocation-free nanometer-scale islands, i.e., quantum dots. For one of the most thoroughly studied systems, viz., InAs/GaAs(001), the critical InAs layer thickness for the transition to island growth is roughly 1.5 monolayers.[3]

A number of studies[4–6] have examined in detail the effect of the main growth parameters for molecular-beam epitaxy (MBE) on the density and size of InAs quantum dots. It has been shown that an increase in the thickness of the InAs coating deposited leads to increases in the size and density of the quantum dots. Varying the flux ratio of the III- and V-group elements, as well as the substrate temperature, also affects these parameters and permits control of the density of quantum-dot arrays in the concentration range $10^8-10^{11}\ \mathrm{cm}^{-2}$ (Refs. 4 and 5). The formation of InAs quantum-dot arrays with a density greater than $3\times10^{10}\ \mathrm{cm}^{-2}$ on a correctly oriented GaAs(001) surface is accompanied, as a rule, by coalescence of a noticeable number of quantum dots into large islands, which leads to a radical broadening of the quantum-dot size distribution function.[5] The data just considered are indicative of the decisive role of surface adatom diffusion in the process of quantum-dot formation. Increasing the substrate temperature increases the surface diffusion length and this leads to an increase in the size of the InAs quantum dots and a decrease in their density.[6]

Oshinowo *et al.*[7] examined the influence of the misorientation angle of the GaAs(001) substrate in the [111B] direction on the size distribution function of InGaAs quantum dots. They found that increasing the misorientation angle from 0° to 41° leads to a decrease in the size of the quantum dots and an increase in their density. They attributed these results to the fact that an increase in the misorientation angle leads to an increase in the density of growth steps on the misoriented surfaces and, as a consequence, to a decrease in the surface diffusion length.

Among the possible misorientation directions of a GaAs(001) surface, the [010] direction is of special interest. On a misoriented vicinal surface of this kind there should be steps distributed in two directions, viz., [110] and $[\bar{1}10]$ (Ref. 8). The intersection of these steps can form a network of terraces of specific configuration on the surface, as depicted in Fig. 1a. Ploog and Daweritz[9] have suggested that such vicinal surfaces be used to create an ordered distribution of dopant atoms or submonolayer InAs islands. They showed that an ordered distribution is possible thanks to the preferential incorporation of adatoms at corners of the terraces.

The present study addresses the effect of the misorientation of a GaAs(001) surface in the [010] direction on the dimensions, distribution, and density of InAs quantum wells grown by MBE. A study of the growth of quantum wells on such vicinal surfaces is of interest for the following reason.

 © 1998 American Institute of Physics

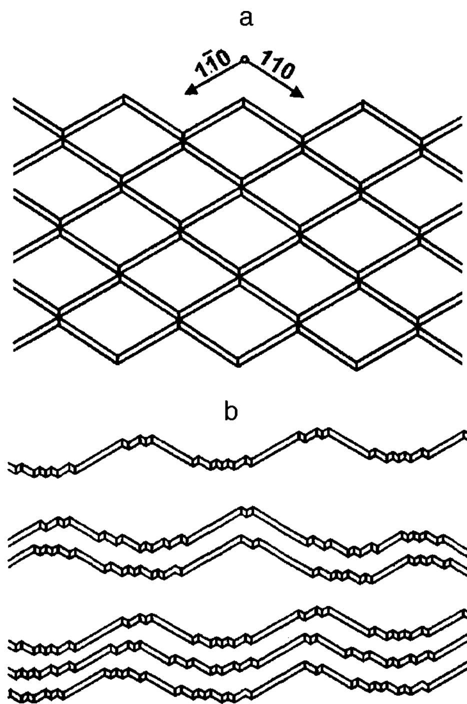

FIG. 1. Schematic representation of the structure of a vicinal GaAs(001) surface misoriented in the [001] direction: a — ideal, b — actually expected.

According to the model of Takura *et al.*[10], there are energy barriers in the surface potential to diffusing adatoms on the step boundaries. These barriers should inhibit the diffusion of adatoms from one terrace to another. The ideal form of a vicinal surface depicted in Fig. 1a, on which each terrace is bounded on four sides by [110] and [$\bar{1}$10] steps, is a limiting case and difficult to realize. In reality, the high probability of the escape of atoms from the external corners of the terraces should lead to rounding of the corners and, as a result, to a partial merging of the terraces, as depicted schematically in Fig. 1b. We presume that the diffusion of adatoms between terraces, even those joined by gateways, will, as in the previous case, be hindered. In this case, the growth of the quantum dot at each site will occur primarily because of material deposited on the same terrace. Obviously, such diffusion blocking should lead to changes in the density, dimensions, and uniformity of the ensemble of quantum dots.

We grew InAs layers 1.8 and 3 monolayers (ML) in thickness by MBE on GaAs(001) surfaces misoriented in the [010] direction by 0, 1, 2, 4, and 6°. The comparatively small range of variation of the misorientation angles was chosen so that the surfaces would differ from one another only in growth-step density without qualitative variation of the surface morphology caused by the approach to new singular faces. Each epitaxy process was performed simultaneously on all surfaces with the misorientation angles chosen. To create a uniform network of terraces, a GaAs buffer layer was grown in the ''step-flow'' regime before epitaxy of the InAs layer was begun. Growth was carried out on an MBE TsNA-4 system. The conditions of the transition to the step-flow growth regime were determined by high-energy electron diffraction (HEED). An InAs growth rate of order 0.15 ML/s was calibrated from the HEED oscillations. The errors in the determination of the InAs growth rate did not exceed 5%.

The surface structure of the samples was investigated by atomic-force microscopy (AFM). Surface images were obtained at room temperature by scanning in the constant-force regime (contact mode). The spatial resolution achieved using a Si_3N_4 tip of radius $R<300$ Å mounted on a V-shaped cantilever allowed reliable observation even of monoatomic surface steps and was consequently sufficient for detecting and characterizing much larger objects such as quantum dots.

Figure 2 shows AFM images of vicinal surfaces with a 1.8-ML thick InAs coating. As expected, the surfaces were broken up into atomically smooth terraces, some of which were joined by gateways. Increasing the misorientation angle led to an increase in the linear density of the terraces and a decrease in their width. The mean terrace widths were, respectively, 500 Å for 1°, 360 Å for 2°, and 250 Å for 6°. These values are considerably larger than the dimensions of the terraces calculated under the assumption that the step height is one monolayer. The observed differences are explained by the well-known phenomenon of step-bunching, which increases with increasing misorientation angle.[11] An analysis of the AFM image in Fig. 2 showed that in our case the mean terrace height rises with increasing misorientation angle from 2–3 ML for 1° to roughly 10 ML for 6°.

An InAs coating thickness of 1.8 ML corresponds to the very onset of island growth via the Stranski–Krastanow mechanism. Indeed, only isolated, sparse quantum dots are observed on the surface of samples with 0° and 1° misorientations. It is interesting to note here that a further increase in the misorientation angle leads to the disappearance of even these quantum dots. An examination of the AFM images and the height profile of the quantum dots in Fig. 2 shows that the quantum dots are located primarily on terrace edges adjoining higher-lying terraces. Such an arrangement of the quantum dots corresponds to the picture of favored incorporation of adsorbed atoms on breaks in higher-lying steps.[9,12]

Figure 3 shows AFM images of vicinal surfaces with a thickness of the InAs coating equal to 3 ML. A large number of InAs quantum dots are observed on the surfaces, whose density grows and whose size decreases with increase in the misorientation angle. Also present on the surfaces are large InAs islands, formed as a result of the coalescence of InAs quantum dots. However, their number falls dramatically with increase in the misorientation angle, and on the surface with 6° misorientation there are scarcely any large InAs islands. The histograms of the quantum-dot height distributions shown in Fig. 4 show that the mean height of the InAs quantum dots varies from 34 Å for 0° to 20 Å for 6°. The spread in the height drops from $\pm 15\%$ to $\pm 10\%$, respectively. Since it is not possible to make out steps under the quantum dots due to their dense coverage of the surface, the height of the quantum dots was measured relative to the mean surface height. Thus, the effective height of a quantum dot in an AFM image is equal to the sum of the actual height of the quantum dot plus the height of the terrace under it, which itself has a spread of values as a consequence of step bunch-

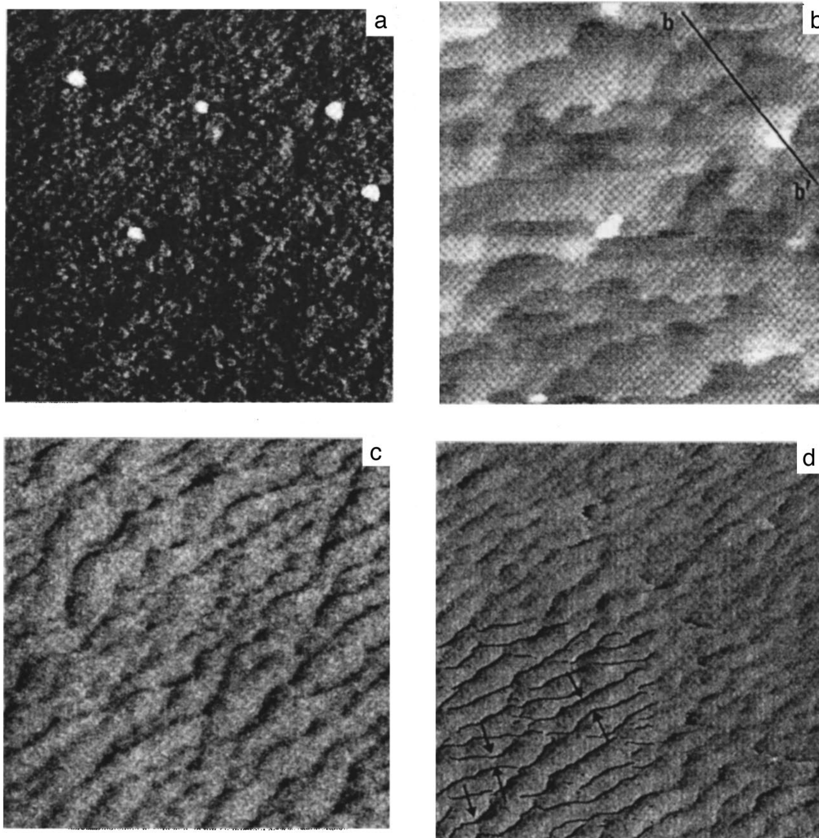

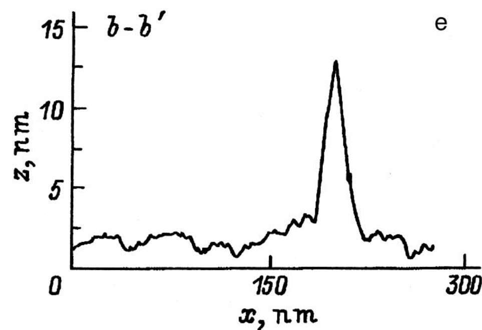

FIG. 2. AFM images (500×500 nm) of vicinal GaAs(001) surfaces. The surfaces are covered with a layer of InAs of thickness 1.8 ML. Misorientation angles of the GaAs surface, deg: a — 0, b — 1, c — 2, d — 6. Figure 2e shows a surface profile corresponding to the line segment $b-b'$ in Fig. 2b. The arrows in the retouched part of Fig. 2d point to individual constrictions between terraces.

ing. Therefore, the spread in the height of the InAs quantum dots actually achieved is less than $\pm 10\%$.

We attribute the observed variations in the density of the quantum dots and in their size distribution, as well as the absence of large islands on the vicinal surfaces, to the suppression of indium adatom diffusion as a result of the terraced structure of such surfaces. The large magnitude of the effect is noteworthy. A misorientation of the GaAs(001) surface in the [010] direction by only $2°$ essentially suppresses the coalescence of quantum dots and radically increases their density. The character of the breakup of the surface into terraces, as can be seen from Fig. 2, would seem to leave open the possibility of adatom diffusion along the steps through the gateways joining individual terraces.

In order to get an idea of the possible role of adatom diffusion along the steps, we estimate the coalescence rate of the quantum dots located on neighboring terraces. In general, the growth of a quantum dot is mediated by atoms adsorbed on an area of radius $R \leqslant L$, where L is the effective surface diffusion length of the adatoms. The adatom concentration near a quantum dot is a function of the incident flux, substrate temperature, and radius of the quantum dot.[13] If in the vicinity of a quantum dot of radius R there is a second quantum dot, then the competition between them can lead to absorption of the dot of smaller radius, i.e., to coalescence. Since the potential barriers on the terrace edges impede the jumping of adatoms from one terrace to another in our case, we considered the coalescence of neighboring quantum dots only as a result of the motion of atoms through the gateways joining the terraces (see Fig. 5). In this approximation we simulated the motion of the adatoms by the Monte-Carlo method and determined the number of adatoms υ which began to move on the edge of one quantum dot and reached the edge of a neighboring quantum dot per unit time. Obviously,

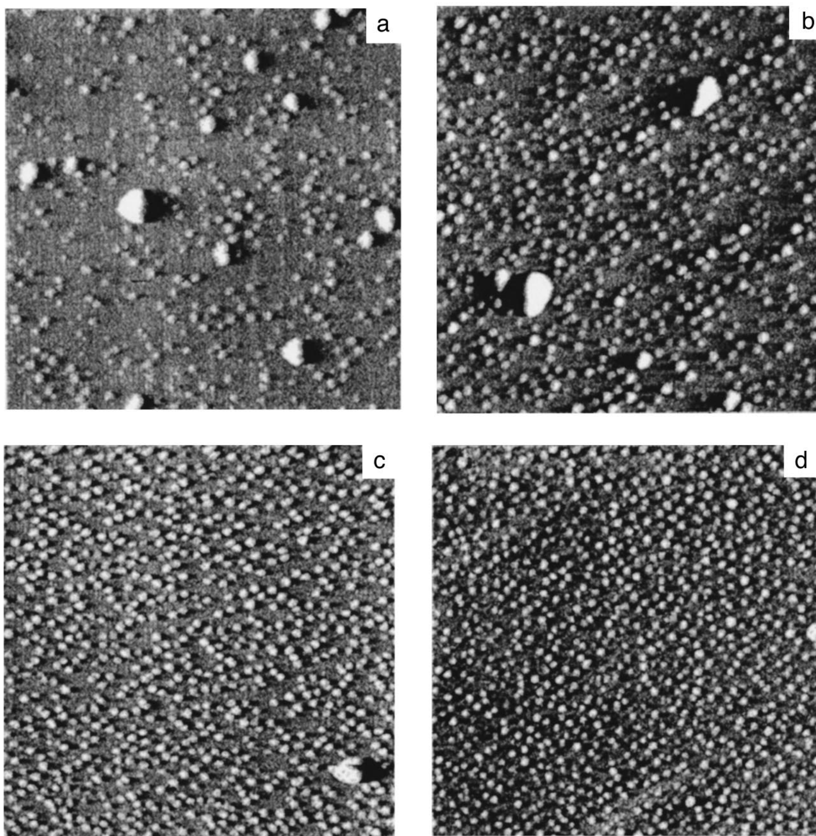

FIG. 3. AFM images of vicinal GaAs(001) surfaces covered with a layer of InAs of thickness 3 ML. Misorientation angles of the GaAs surface, deg.: a — 0, b — 1, c — 2, d — 6.

the value of v determined in this way is the maximum rate of material transfer from one quantum dot to another and, accordingly, the maximum rate of coalescence. Such a one-way type of transfer corresponds to the situation when the radius of the first quantum dot R_1 is much smaller than that of the second, R_2. Figure 6 plots the ratio of the maximum coalescence rate v_d (for terraces with the gateway width d) to the maximum coalescence rate v_{d_0} (for terraces without any constriction) as a function of the relative gateway width d/d_0 (d_0 is the diameter of the quantum dot). Increasing the constriction retards the coalescence process, and for $d/d_0=0.5$ the maximum coalescence rate is cut roughly in half. The linear nature of the dependence for this model in essence reflects the fact that the magnitude of the diffusion flux from dot to dot is directly proportional to the gateway width. Allowance for the reverse diffusion flux from the second quantum dot to the first, as well as the actual ratio of the

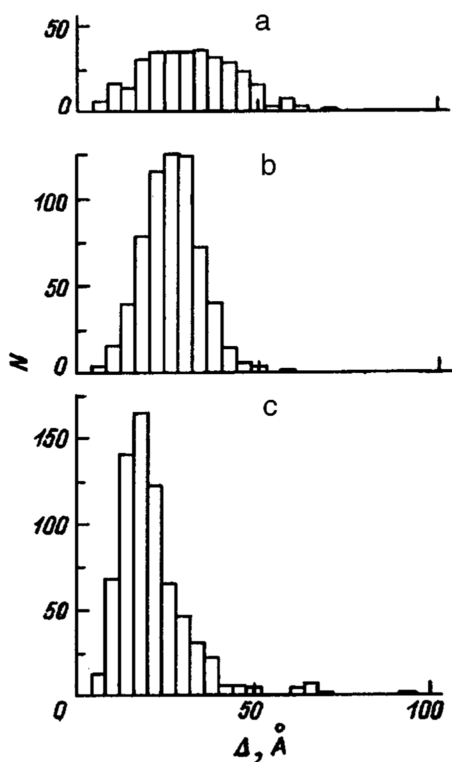

FIG. 4. Histograms of the height distribution of InAs quantum dots (Δ is the height) for vicinal GaAs surfaces with misorientation angles in degrees: a — 0, b — 2, c — 6. N — number of dots.

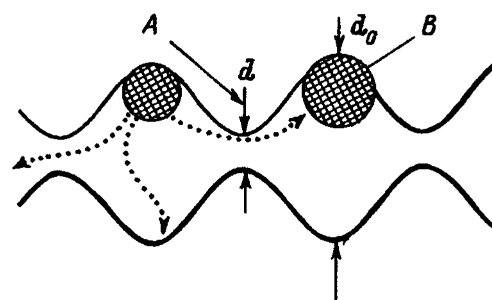

FIG. 5. Model of connecting terraces used in the calculation: B — quantum dot, A — gateway between terraces.

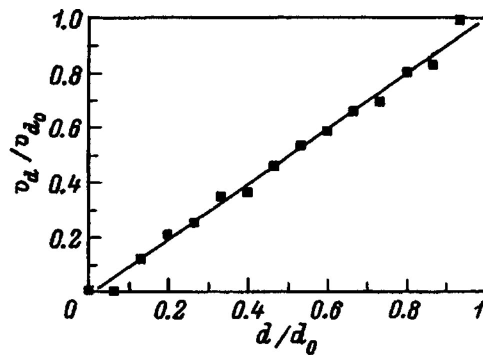

FIG. 6. Dependence of the ratio of maximum transfer rates (v_d/v_{d0}) on the relative width of the gateway joining the terraces (d/d_0).

dot radii R_1/R_2, can only decrease the coalescence rate. The above treatment shows that significant blocking of adatom diffusion between neighboring terraces makes the participation of quantum dots located on more distant terraces in coalescence improbable, as we sought to show.

Thus, the results of this study show that the creation of a network of terraces on vicinal GaAs(001) surfaces misoriented in the [010] direction opens up the interesting possibility of controlling the density, dimensions, and uniformity of InAs quantum dots, lowers the probability of their coalescence, and increases the critical thickness of the InAs coating.

We are grateful to A. B. Komissarov for assistance in preparing the samples.

This work was supported by the Russian Fund for Fundamental Research (Grants Nos. 95-02-06038, 96-02-17952, and 97-02-18291) and the State Program ''Physics of Solid-State Nanostructures'' (Grant No. 97-2014).

*)E-mail: evt@mbe.ioffe.rssi.ru

[1] L. V. Asryan and R. A. Suris, Semicond. Sci. Technol. **11**, 554 (1996).
[2] I. N. Stranski and L. Von Krastanow, Akad. Wiss. Lit. Mainz Abh. Math. Naturwiss. Kl. **146**, 797 (1939).
[3] D. Leonard, K. Pond, and P. M. Petroff, Phys. Rev. B **50**, 11 687 (1994).
[4] G. S. Solomon, J. A. Trezza, and J. S. Harris, Appl. Phys. Lett. **66**, 991 (1995).
[5] J. M. Moison, F. Houzay, F. Barthe, L. Leprince, E. André, and O. Vatel, Appl. Phys. Lett. **64**, 196 (1994).
[6] G. S. Solomon, J. A. Trezza, and J. S. Harris, Jr., Appl. Phys. Lett. **66**, 3161 (1995).
[7] J. Oshinowo, M. Nishioka, S. Ishida, and Y. Arakawa, Jpn. J. Appl. Phys. **33**, L1634 (1994).
[8] M. Kasu and N. Kobayashi, Jpn. J. Appl. Phys. **33**, 712 (1994).
[9] D. H. Ploog and L. Daweritz, Mater. Sci. Technol. **11**, 820 (1995).
[10] Y. Tokura, H. Saito, and T. Fukui, J. Cryst. Growth **94**, 46 (1989).
[11] T. Ide, A. Yamashita, and T. Mizutani, Phys. Rev. B **46**, 1905 (1992).
[12] N. Ikoma and S. Ohkouchi, Jpn. J. Appl. Phys. **34**, L724 (1995).
[13] A. Yu. Kaminski and R. A. Suris, Solid State Commun. **89**, 697 (1994).

Translated by Paul F. Schippnick

Scattering of hot electrons by neutral acceptors in GaAs/AlAs quantum well structures

D. N. Mirlin, V. I. Perel', and I. I. Reshina

A. F. Ioffe Physicotechnical Institute, Russian Academy of Sciences, 194021 St. Petersburg, Russia
(Submitted February 10, 1998; accepted for publication February 12, 1998)
Fiz. Tekh. Poluprovodn. **32**, 866–875 (July 1998)

The optical alignment of hot electrons and its destruction in a magnetic field under conditions when electron scattering by neutral acceptors plays a large role is investigated. This makes it possible to determine the probability of the scattering of hot electrons from an initial photoexcited state, as well as the times characterizing the energy and momentum relaxation of hot electrons on scattering by neutral acceptors. The experimental results are compared with calculations. © *1998 American Institute of Physics.* [S1063-7826(98)02107-3]

1. INTRODUCTION

The observation of the optical alignment of the momenta of hot photoexcited electrons and its variation in a magnetic field makes it possible to measure directly the times characterizing the relaxation of hot electrons with respect to the magnitude and direction of their quasimomentum. This method is based on the fact that under excitation by linearly polarized light the quasimomentum distribution of photoexcited electrons is anisotropic in a plane perpendicular to the exciting beam. In GaAs-type crystals, if the warping of the valence band is neglected, this anisotropy is characterized by the existence of a preferential axis associated with the polarization plane of the exciting light. In turn, this results in linear polarization of the hot photoluminescence (HPL). The degree of polarization of the HPL and its dependence on the magnetic field and luminescence photon energy directly reflect the relaxation of the momentum distribution of the photoexcited electrons.[1–4]

In lightly and moderately doped GaAs crystals with acceptor density less than 3×10^{17} cm^{-3} hot electrons are scattered predominantly by longitudinal optical phonons.[1] An additional mechanism arises in crystals with a higher acceptor density — scattering by neutral acceptors accompanied by their excitation and ionization.[1]

An extension of the optical alignment method to quantum well structures was first made in Ref. 5 (see the review in Ref. 6). In moderately doped GaAs/AlAs quantum well (QW) structures, the phonon scattering of hot two-dimensional electrons exhibits specific features which distinguish it from the bulk case.[7–9] Phonon scattering occurs mainly by quantized (confined) GaAs phonons and interface AlAs-type phonons.

The present paper explores the scattering of hot electrons by shallow acceptors in QW structures and compares the results with the bulk case. Some of these results were published earlier in Ref. 10. Here we present the results of investigations of the scattering of hot electrons with energies 0.16–0.3 eV in GaAs(50 Å)/AlAs(100 Å) QW structures doped with beryllium as an acceptor impurity in the range $3\times10^{17}-5\times10^{18}$ cm^{-3}. The experimental results are compared with a theoretical model.

The paper is organized as follows. A description of the samples and measurement method is given in Sec. 1. A theoretical analysis, which makes it possible to express the measured quantities in terms of the times characterizing the relaxation of the momentum distribution of hot electrons in a quantum well, is given in Sec. 2. The experimental results and their discussion are contained in Secs. 3 and 4, respectively. An approximate calculation of the cross sections for the relaxation of hot electrons on acceptors in a quantum well is given in the Appendix.

2. SAMPLES AND MEASUREMENT METHOD

The GaAs/AlAs quantum well structures were grown by molecular-beam epitaxy on (100) GaAs substrates. They consisted of 70 periods with 50 Å wide wells and 100 Å wide barriers. The wells were doped with beryllium as an acceptor impurity in the range $3\times10^{17}-5\times10^{18}$ cm^{-3} in a 20 Å wide region at the center. Bulk 1 μm thick GaAs:Be films were grown by the same method.

The free-hole density at room and higher temperatures right up to 430 K was found from Hall measurements. Since the density remained constant in the range 300–430 K, it could be assumed that all acceptors are ionized, and the free-hole density at 300 K could be taken as the density of neutral acceptors at liquid-helium temperatures. The measured values of the densities are presented in Table I.[1)]

The scattering probability was measured by a method based on an investigation of the photoluminescence of hot carriers (or hot photoluminescence, HPL) and its polarization characteristics in a magnetic field. We previously developed this method for the purpose of investigating the dynamics of hot electrons,[1] and it has been recently used successfully to investigate the electron-phonon interaction in quantum wells.[8,9] The essence of the method is as follows. Electrons are excited by a cw laser with low pump power into a high-energy state in the first size-quantization electronic subband. They recombine with holes localized on acceptors both from the initial excited state with energy ε_0 and during energy relaxation in the first electronic subband. The photoluminescence of hot electrons is partially linearly polarized as a re-

 © 1998 American Institute of Physics

TABLE I. Hole density in samples at $T=300$ K.

Samples	Sample No.	Hole density $p, 10^{18}$ cm^{-3}
GaAs/AlAs : Be 55 Å/100 Å	1-261	0.3
GaAs/AlAs : Be 50 Å/100 Å	424	0.8
–″–	452	1.4
–″–	812	4.6
GaAs : Be	598	0.9
–″–	626	1.6
GaAs : Cd	4020	0.05

sult of their anisotropic momentum distribution. A magnetic field applied in the Faraday geometry depolarizes the luminescence (the Hanle effect). In this case

$$\frac{\rho_B}{\rho_0}=\frac{1}{1+4\omega_c^2\tau_H^2}, \tag{1}$$

where ρ_B and ρ_0 are, respectively, the degrees of linear polarization in a field B and with $B=0$, $\omega_c=eB/m^*c$ is the cyclotron frequency, and τ_H is the ''Hanle time.'' If electrons recombine from the initial excited state, then $\tau_H\equiv\tau_0$ and can be expressed directly in terms of the scattering probability (see Sec. 2):

$$\frac{1}{\tau_0}=\frac{1}{\tau_{\text{esc}}^{\text{inel}}}+\frac{1}{\tau_2^{\text{el}}}, \tag{2}$$

where $\tau_{\text{esc}}^{\text{inel}}$ is the escape time from the initial photoexcited state as a result of inelastic collisions and τ_2^{el} is the momentum-alignment decay time due to elastic collisions.

In the special case where the electrons recombine after some energy relaxation from a state with energy ε and energy is lost in small portions $\Delta\varepsilon$ (where $\Delta\varepsilon<\varepsilon_0<\varepsilon$) over the course of relaxation, the formula (1) can be used, to a good approximation to measure τ_H, which in this case becomes the descent time τ_d and can be expressed in terms of a time $\tau_{\varepsilon 2}$, which takes into account the destruction of the alignment during energy relaxation (see Sec. 2 for the precise definition of $\tau_{\varepsilon 2}$):

$$\tau_d=\int_{\varepsilon}^{\varepsilon_0}\tau_{\varepsilon' 2}\frac{d\varepsilon'}{\varepsilon'}. \tag{3}$$

For $\varepsilon_0-\varepsilon\ll\varepsilon_0$ the formula (3) can be put into the form

$$\tau_d=\frac{\tau_{\varepsilon 2}}{\varepsilon_0}(\varepsilon_0-\varepsilon). \tag{4}$$

Therefore, once the descent time τ_d has been measured by the method described above, the relaxation time $\tau_{\varepsilon 2}$ can be found using Eq. (4).

In the bulk case scattering by acceptors is mainly by small angles.[11] Then the second term in Eq. (2) can be neglected, while the time $\tau_{\varepsilon 2}$ is virtually identical to the energy relaxation time τ_ε.[1] In the case of a quantum well this is not so, and $\tau_{\varepsilon 2}$ is substantially different from τ_ε (see the Appendix).

The spectral dependence of the linear polarization in the absence of a magnetic field is determined by the rate of destruction of the anisotropy of the momentum distribution in the course of energy relaxation (which occurs with time τ_2). Isotropization of the momentum distribution decreases the linear polarization of the HPL. This decrease can be approximated by the expression

$$\frac{\rho(\varepsilon)}{\rho(\varepsilon_0)}=\left(\frac{\varepsilon}{\varepsilon_0}\right)^{\gamma}. \tag{5}$$

The quantity γ can be expressed in terms of the relaxation time (in the bulk case $\gamma=\tau_\varepsilon/\tau_2$).

Therefore, the problem is to measure the times τ_0 and $\tau_{\varepsilon 2}$, on the basis of data on the depolarization of the HPL in a magnetic field as a function of the acceptor density, as well as the quantity γ, which characterizes the decrease in polarization as the energy of an electron participating in an emission event relaxes. The approximation

$$\frac{1}{\tau}=\frac{1}{\tau_{\text{ph}}}+N_A\sigma v \tag{6}$$

was used for both relaxation times τ_0 and $\tau_{\varepsilon 2}$. Here τ_{ph} is the corresponding time due to interactions with phonons, v is the electron velocity, σ is the scattering cross section, and N_A is the density of neutral acceptors. For comparison with the bulk case it is helpful to introduce an effective bulk density for the QW structure. It can be defined naturally as the density within the quantum well averaged with the weight $|\psi(z)|^2$, where

$$\psi(z)=\sqrt{\frac{2}{d}}\cos\frac{\pi z}{d}$$

is the electron wave function in the first size-quantization subband. In the presence of doping, N_A in a region of width l near the center of the well ($l\ll d$) is the two-dimensional density N_{2D} divided by $d/2$:

$$N_A=2\int_0^{l/2}\frac{N_{2D}}{l}|\psi|^2dz=\frac{2N_{2D}}{d}.$$

The ultimate aim of this work is to measure the cross sections σ_0 and $\sigma_{\varepsilon 2}$ and to compare the results for a bulk sample and a QW structure, as well as to compare the measured values with the results of an approximate calculation. The measurements were performed on a DFS-24 diffraction spectrometer with a double monochromator equipped with a cooled photomultiplier and a phonon counting system. The experiment was controlled by a computer. Continuous-wave lasers with energies 1.96 eV (He–Ne) and 1.916 and 1.833 eV (Kr^+) were used to excite the luminescence. The samples were immersed in helium vapor in a cryostat with a superconducting solenoid, which produced magnetic fields up to 7 T. The laser power at the cryostat entrance did not exceed 17 mW. The temperature of the samples did not exceed 6 K.

3. DEGREE OF MOMENTUM ALIGNMENT OF PHOTOEXCITED ELECTRONS IN A QUANTUM WELL WITH ALLOWANCE FOR COLLISIONS

The objective of the present section is to express the degree of alignment of photoexcited electrons and its magnetic-field dependence in terms of the collision characteristics. In what follows it is assumed that the electrons belong to the first size-quantization subband and that their state is characterized by a two-dimensional wave vector $\mathbf{k}$ in the plane of the well. The distribution function $f(\mathbf{k})$ satisfies the kinetic equation

$$\omega_c \frac{\partial f(\mathbf{k})}{\partial \psi} + f(\mathbf{k}) \int W(\mathbf{k},\mathbf{k}') \frac{d^2 k'}{(2\pi)^2} - \int f(\mathbf{k}') W(\mathbf{k}',\mathbf{k}) \frac{d^2 k'}{(2\pi)^2} = F(\mathbf{k}). \tag{7}$$

Here $F(\mathbf{k})$ characterizes the excitation. It is assumed that the magnetic field is directed along the Z axis perpendicular to the plane of the well; ψ is the angle between the vector $\mathbf{k}$ and the X axis, to which the alignment axis is parallel at the moment of excitation, and $W(\mathbf{k},\mathbf{k}')$ is the probability of an electron transition from the state $\mathbf{k}$ into the state $\mathbf{k}'$ per unit time. We characterize the state of an electron by its two-dimensional energy ε and the angle ψ, and we expand $f(\mathbf{k})$ and $F(\mathbf{k})$ in Fourier series:

$$f(\mathbf{k}) = \sum_m f_m(\varepsilon) e^{im\psi} \quad \text{and} \quad F(\mathbf{k}) = \sum_m F_m(\varepsilon) e^{im\psi}. \tag{8}$$

The probabilities $W(\mathbf{k},\mathbf{k}')$ depend on the energies ε and ε' and the angle $\varphi = \psi' - \psi$ between the vectors $\mathbf{k}$ and $\mathbf{k}'$. Taking this into account, from Eq. (7) equations we obtain for the Fourier components of the distribution function

$$im\omega_c f_m(\varepsilon) + f_m(\varepsilon) \int W_0(\varepsilon,\varepsilon') \rho d\varepsilon' - \int f_m(\varepsilon') W_m(\varepsilon',\varepsilon) \rho d\varepsilon' = F_m(\varepsilon), \tag{9}$$

$$W_m(\varepsilon',\varepsilon) = \int_{-\pi}^{\pi} W(\mathbf{k}',\mathbf{k}) e^{im\varphi} \frac{d\varphi}{2\pi} = \frac{1}{2\pi} \int_{-\pi}^{\pi} W(\mathbf{k}',\mathbf{k}) \cos(m\varphi) d\varphi. \tag{10}$$

Here the facts that $W(\mathbf{k}, \mathbf{k}')$ is an even function of the angle φ and ρ is the density of states (we recall that ρ does not depend on energy) were taken into account.

The degree of alignment α, which is proportional to the linear polarization of the luminescence, is defined by the formula

$$\alpha(\varepsilon) = \frac{f_2(\varepsilon) + f_{-2}(\varepsilon)}{f_0(\varepsilon)}, \tag{11}$$

so that of Eqs. (9) we need only the equations with $m = 0$, ± 2.

In what follows we shall confine our attention to low temperatures, where collisions cannot increase the electron energy: $W(\varepsilon,\varepsilon') = 0$ for $\varepsilon' > \varepsilon$. In collisions with impurity centers (specifically, acceptors) a distinction must be made between inelastic collisions, in which the energy of an electron is partially transferred to a carrier (hole) on an acceptor, and elastic collisions, in which the electron wave function only rotates with no change in magnitude. Accordingly, we set

$$W_m(\varepsilon',\varepsilon) = W_m^{\text{inel}}(\varepsilon',\varepsilon) + W_m^{\text{el}}(\varepsilon',\varepsilon), \tag{12}$$

where $W_m^{\text{el}}(\varepsilon',\varepsilon)$ contains the factor $\delta(\varepsilon - \varepsilon')$.

We shall assume below that electrons with the energy ε_0 are excited. Therefore, we neglect all mechanisms for broadening of the initial electron distribution (including warping of the valence band). Then $F_m(\varepsilon) \propto A_m \delta(\varepsilon - \varepsilon_0)$ (for linear polarization of the excitation $A_m = A_{-m}$), and the solution of Eq. (9) can be written in the form

$$f_m(\varepsilon) = a_m \delta(\varepsilon - \varepsilon_0) + b_m(\varepsilon), \tag{13}$$

where $b_m(\varepsilon)$ is a smooth function describing electrons undergoing energy relaxation. If broadening mechanisms are taken into account, then the δ function is replaced by a peak with a finite width. For what follows it is important only that the height of this peak at $\varepsilon = \varepsilon_0$ be much greater than the smooth part $b_m(\varepsilon)$. From Eq. (9) with allowance for Eq. (12), we have the following equations for a_0 and $a_{\pm 2}$:

$$\frac{a_0}{\tau_{\text{esc}}^{\text{inel}}} = A_0 \quad \text{and} \quad \pm 2i\omega_c a_{\pm 2} + \left(\frac{1}{\tau_{\text{esc}}^{\text{inel}}} + \frac{1}{\tau_2^{\text{el}}} \right) a_{\pm 2} = A_2, \tag{14}$$

where

$$\frac{1}{\tau_{\text{esc}}^{\text{inel}}} = \int W_0^{\text{inel}}(\varepsilon,\varepsilon') \rho d\varepsilon', \tag{15}$$

$$\frac{1}{\tau_2^{\text{el}}} = \int [W_0^{\text{el}}(\varepsilon,\varepsilon') - W_2^{\text{el}}(\varepsilon,\varepsilon')] \rho d\varepsilon'. \tag{16}$$

The time $\tau_{\text{esc}}^{\text{inel}}$ characterizes the escape time from a state with energy ε_0 as a result of inelastic collisions. The time τ_2^{el} is the decay time of the second harmonic f_2 of the distribution function as a result of elastic collisions. These times appear in Eqs. (15) and (16) with $\varepsilon = \varepsilon_0$.

Using Eqs. (11), (13), and (14), for the degree of alignment with energy ε_0 we find

$$\alpha_B = \frac{\alpha_0}{1 + (2\omega_c \tau_0)^2}, \tag{17}$$

$$\alpha_0 = \frac{2A_2}{A_0} \frac{\tau_0}{\tau_{\text{esc}}^{\text{inel}}}, \tag{18}$$

where τ_0 is the time in (2), which determines the relaxation of alignment in a magnetic field. The formula (18) gives the dependence of the degree of alignment at the point of creation in a zero magnetic field on the elastic collision rate. If there are no elastic collisions (for example, relaxation occurs only on optical phonons), then $\tau_0 = \tau_{\text{esc}}^{\text{inel}}$, and the value of α_0 is determined by excitation and does not depend on relaxation.

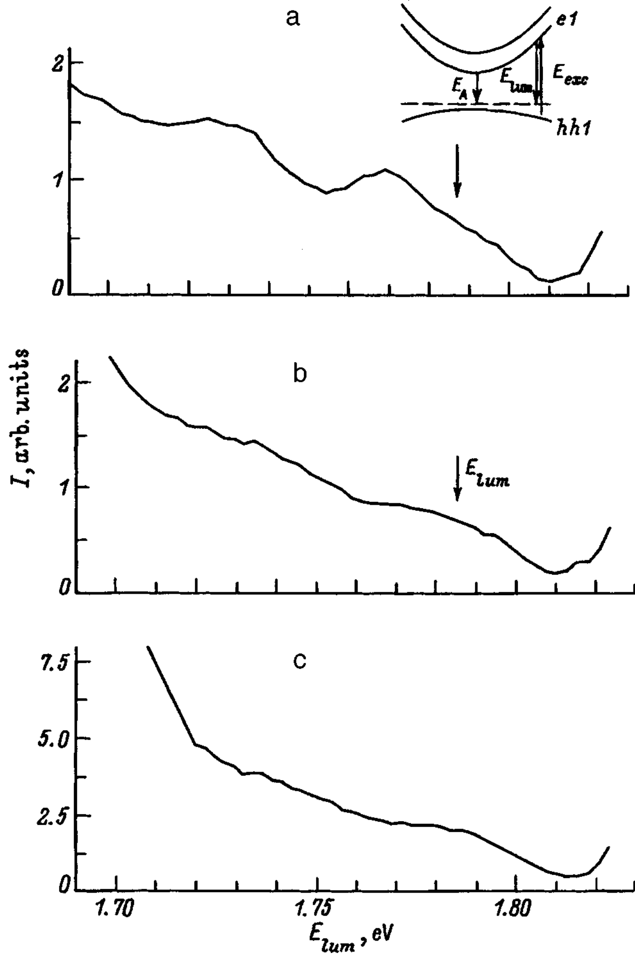

FIG. 1. Photoluminescence spectra of hot electrons for quantum well structures with density N_A, 10^{18} cm^{-3}: a — 0.8, b — 1.4, c — 4.6; $E_{exc} = 1.833$ eV, $\varepsilon_0 = 0.16$ eV, $T \approx 6$ K. The arrows mark the energy at which the depolarization curve corresponding to ε_0 was measured. Inset: transition schemes.

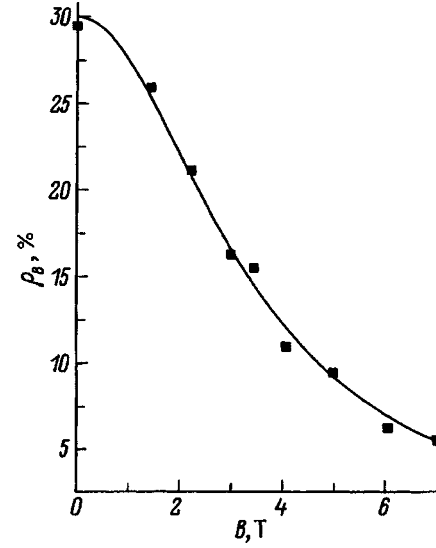

FIG. 2. Magnetic depolarization curve. $N_A \approx 1.4 \times 10^{18}$ cm^{-3}, $E_{exc} = 1.833$ eV, $E = 1.786$ eV, $T \approx 6$ K. The solid curve corresponds to the function $\rho_B/\rho_0 = 1/(1+4\omega_c^2\tau_0^2)$.

Let us now examine the alignment of electrons which have undergone energy relaxation, i.e., the case of $\varepsilon < \varepsilon_0$. The distribution of such electrons is characterized by the quantities $b_m(\varepsilon)$ [see Eq. (13)]. For them we obtain from Eqs. (9), (12), and (13)

$$b_0(\varepsilon)\int W_0(\varepsilon,\varepsilon')\rho d\varepsilon' - \int b_0(\varepsilon')W_0(\varepsilon',\varepsilon)\rho d\varepsilon' = a_0 W_0(\varepsilon_0,\varepsilon)\rho, \quad (19)$$

$$\pm 2i\omega_c b_{\pm 2}(\varepsilon) + b_{\pm 2}(\varepsilon)\frac{1}{\tau_2} + b_{\pm 2}(\varepsilon)\int W_2(\varepsilon,\varepsilon')\rho d\varepsilon' - \int b_{\pm 2}(\varepsilon')W_2(\varepsilon',\varepsilon)\rho d\varepsilon' = a_{\pm 2}W_2(\varepsilon_0,\varepsilon)\rho. \quad (20)$$

Here τ_2 is defined by a formula similar to Eq. (16) but which contains the total probabilities $W_m(\varepsilon,\varepsilon')$ [see Eq. (12)]. In Eq. (19) the left-hand side describes the gradual descent of an electron from ε_0 to ε, while the right-hand side describes a direct transition from ε_0 to ε. If $\varepsilon_0 - \varepsilon \gg \Delta\varepsilon$, where $\Delta\varepsilon$ is the characteristic energy loss, then the right-hand sides in Eqs. (19) and (20) can be neglected, while on the left-hand sides we can switch to the Fokker–Planck approximation, i.e., we can set (assuming, in addition, that $\varepsilon \gg \Delta\varepsilon$)

$$b_m(\varepsilon)\int W_m(\varepsilon,\varepsilon')\rho d\varepsilon' - \int b_m(\varepsilon')W_m(\varepsilon,\varepsilon')\rho d\varepsilon' \approx -\frac{\partial}{\partial\varepsilon}\frac{b_m(\varepsilon)\varepsilon}{\tau_{\varepsilon m}}, \quad (21)$$

where

$$\frac{1}{\tau_{\varepsilon m}} = \frac{1}{\varepsilon}\int W_m(\varepsilon,\varepsilon')\rho d\varepsilon'. \quad (22)$$

We note that $\tau_{\varepsilon 0}$ is simply the energy relaxation time $\tau_{\varepsilon 0} \equiv \tau_\varepsilon$.

Therefore, in the region $\varepsilon_0 - \varepsilon \gg \Delta\varepsilon$, $\varepsilon \gg \Delta\varepsilon$ Eqs. (19) and (20) become differential equations, whose solution gives

$$b_0(\varepsilon) \propto \tau_\varepsilon,$$

$$b_{\pm 2} \propto \tau_{\varepsilon 2}\exp\left[\int_\varepsilon^{\varepsilon_0}\left(\mp 2i\omega_c - \frac{1}{\tau_2}\right)\tau_{\varepsilon 2}\frac{d\varepsilon}{\varepsilon}\right]. \quad (23)$$

In the range of energies ε under consideration the formulas (23) give the dependence of the angle-integrated distribution function and its second harmonic on ε. The proportionality coefficients in these formulas can depend on ε_0. Finding them requires solving the integral equations (19) and (20) for ε close to ε_0. Replacing f_m in Eq. (11) by the expression for b_m from Eq. (23), for the degree of alignment when $\varepsilon_0 - \varepsilon \gg \Delta\varepsilon$, $\varepsilon \gg \Delta\varepsilon$ we obtain

$$\alpha_B(\varepsilon) \propto \alpha_0(\varepsilon)\cos 2\omega_c\tau_d, \quad (24)$$

where τ_d is the "descent time" (3), while $\alpha_0(\varepsilon)$ is the degree of alignment in a zero field

$$\alpha_0(\varepsilon) \propto \frac{\tau_{\varepsilon 2}}{\tau_\varepsilon}\exp\left(-\int_\varepsilon^{\varepsilon_0}\frac{\tau_{\varepsilon 2}}{\tau_2}\frac{d\varepsilon}{\varepsilon}\right). \quad (25)$$

TABLE II. Escape time τ_0 and the parameter γ for GaAs/AlAs (50/100Å) quantum well structures.

N_A, 10^{18} cm^{-3}	$\varepsilon_0=0.26$ eV		$\varepsilon_0=0.16$ eV	
	τ_0, fs	γ	τ_0, fs	γ
0.8	96	2.1	64	3
1.4	83	2.6	62	3.7
4.6	40	3.4	31	3.5

The formula (24) corresponds to the situation when the alignment axis rotates in a magnetic field, while the degree of alignment relative to this rotating axis remains constant. Indeed, the corrections to the Fokker–Planck equation will introduce a damping of the oscillations of α as a function of ω_c. However, in the range of magnetic fields where $\alpha(\varepsilon)/\alpha_0(\varepsilon)\leqslant 1/2$ (which is usually used in experiments) the function $\cos 2\omega_c\tau_d$ differs very little from a Lorentzian curve: $1/[1+(2\omega_c\tau_d)^2]$. For this reason, it can be assumed that the descent time τ_d plays the role of the Hanle time in the energy interval under consideration. Of course, here τ_d can be much greater than the escape time τ_{esc}^{inel} from a state with energy ε_0.

4. EXPERIMENTAL RESULTS

Figure 1 shows hot luminescence spectra for QW structures as an example. At an acceptor density equal to 0.8×10^{18} cm^{-3} phonon oscillations are still observed in the spectrum; they are obliterated as the acceptor density increases. This attests to the fact that the interaction with holes localized on acceptors becomes the main relaxation mechanism. Depolarization in a magnetic field was measured at the high-frequency edge of the spectra at E_{lum}, which is marked by the arrows in Fig. 1. This energy corresponds to the electron kinetic energy $\varepsilon_0=E_{lum}-E_A$, where E_A is the energy of a transition to an acceptor from the bottom of the first electronic subband. The value of E_A was determined from the edge luminescence spectrum, which was decomposed into two peaks corresponding to the transition to an acceptor and an excitonic transition.

Figure 2 shows an example of a depolarization curve for a QW structure. Similar measurements were performed for $\varepsilon_0=0.16, 0.23$, and 0.26 eV in QW structures and for $\varepsilon_0=0.28$ eV in bulk samples. The corresponding values of τ_0, which are presented in Table II for the QW structures and in Table III for the bulk samples, were determined for them.

Figure 3 shows the dependence of the scattering probability on the density of neutral acceptors in QW structures ($\varepsilon_0=0.26$ eV) and in bulk samples ($\varepsilon_0=0.28$ eV). These dependences can be approximated by a formula of the type (6)

TABLE III. Results of measurements for bulk samples ($T=6$ K).

Samples	Sample No.	N_A, 10^{18} cm^{-3}	ε_0, eV	τ_0, fs	$\tau_{\varepsilon 2}$, ps	γ
GaAs : Be	598	0.9	0.28	77	0.74	3.8
GaAs : Be	626	1.6	0.28	54	0.43	3.2
GaAs : Cd	4020	0.05		135		

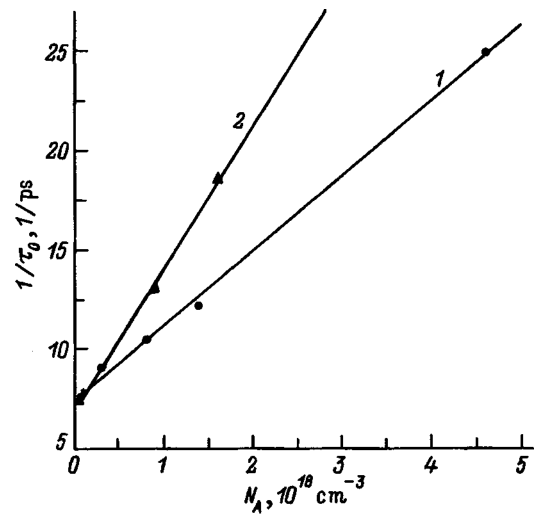

FIG. 3. Dependence of $1/\tau_0$ on the neutral acceptor density N_A for a quantum well structure (*1*) and bulk samples (*2*). Scattering cross section σ_0, 10^{-14} cm^2: *1* — 4.0, *2* — 7.2.

$$\frac{1}{\tau_0}=\frac{1}{\tau_{ph}}+N_A\sigma_0 v, \tag{26}$$

where $1/\tau_{ph}$ is the scattering probability for $N_A=0$ associated with the emission of optical phonons. From these results we find $\sigma_0=7.2\times 10^{-14}$ cm^2 for bulk samples, which is close to the value obtained earlier for bulk crystals,[1] and $\sigma_0=4.0\times 10^{-14}$ cm^2 for QW structures. Therefore, the scattering cross section for the bulk samples is approximately two times larger than for the QW structures. The interaction with neutral acceptors in a QW structure with $N_A=2\times 10^{18}$ cm^{-3} makes the same contribution to the scattering rate as does the phonon mechanism. At the same time, in bulk samples both scattering mechanisms make the same contribution even with $N_A=10^{18}$ cm^{-3}. In this connection, we observe traces of phonon oscillations in the hot luminescence spectra of the QW structures even with $N_A=1.4\times 10^{18}$ cm^{-3}.

The values of σ_0 in the QW structures as a function of $1/\varepsilon_0$ are presented in Fig. 4. The measurements were per-

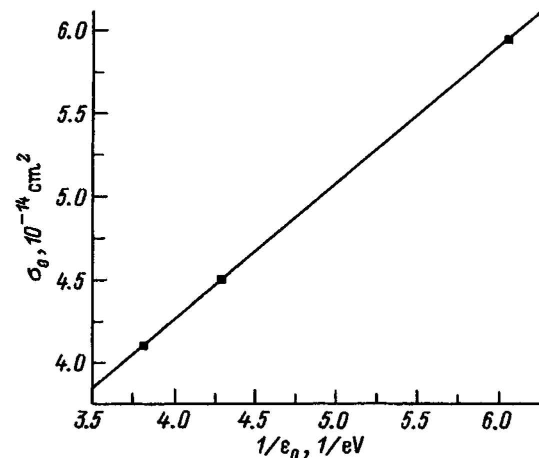

FIG. 4. σ_0 versus $1/\varepsilon_0$ for a quantum well structures.

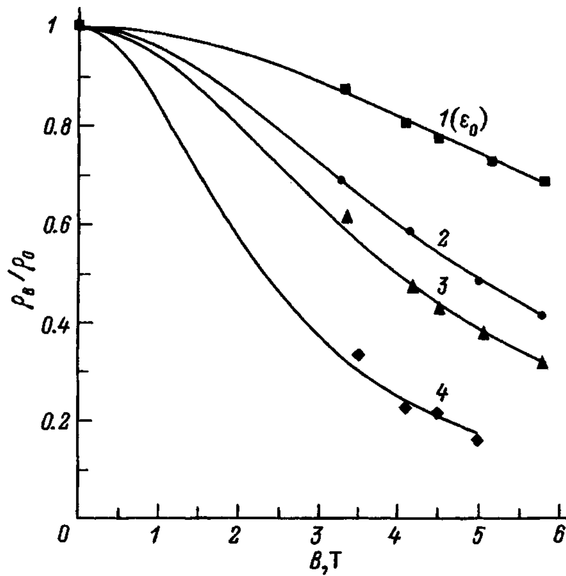

FIG. 5. Magnetic depolarization curves for $\varepsilon_0=0.26$ eV and $\varepsilon<\varepsilon_0$ for a structure with $N_A=4.6\times10^{18}$ cm^3. $E_{\rm exc}=1.96$ eV, $T\approx6$ K. $E_{\rm lum}$, eV: *1* — 1.907, *2* — 1.873, *3* — 1.823, *4* — 1.771.

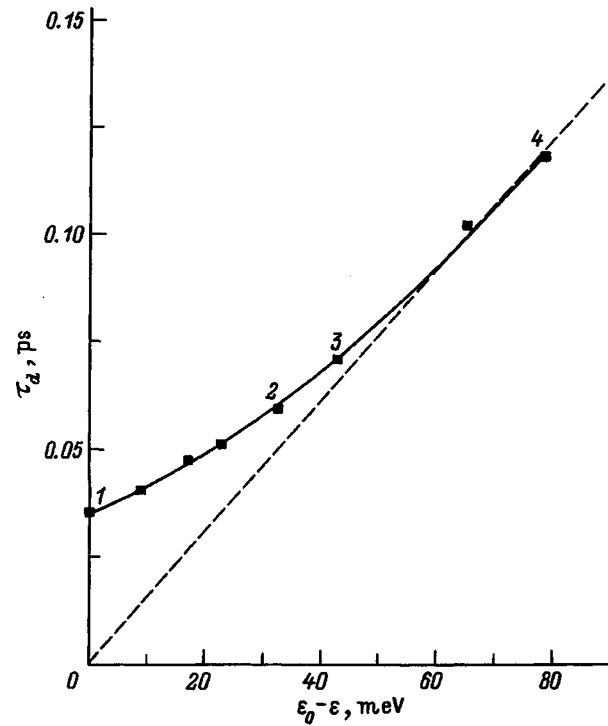

FIG. 6. Descent time τ_d versus $\varepsilon_0-\varepsilon$. The descent time was found from the magnetic depolarization curves, some of which are shown in Fig. 5. The numbers labeling the symbols correspond to the values of $E_{\rm lum}$ given in the caption to Fig. 5. The dashed straight line corresponds to Eq. (4), whence the relaxation time $\tau_{\varepsilon2}$ is determined.

formed with excitation by 1.96, 1.916, and 1.833-eV lasers. As we see, σ_0 is inversely proportional to the initial energy of the photoexcited electrons. Figure 5 shows examples of depolarization curves of QW structures in a magnetic field for $\varepsilon_0=0.26$ eV (curve *1*) and for lower energies. As already mentioned in Sec. 1, the depolarization curves for $\varepsilon<\varepsilon_0$ can be used to determine the descent time τ_d and to construct its dependence on $\varepsilon_0-\varepsilon$, as shown in Fig. 6. The relaxation time $\tau_{\varepsilon2}$ can be determined from these data. The values $\tau_{\varepsilon2}=500$, 390, and 330 fs were obtained for samples with acceptor density $N_A=(0.8, 1.4, 4.6)\times10^{18}$ cm^{-3}, respectively, for $\varepsilon_0=0.26$ eV. Hence, the cross section $\sigma_{\varepsilon2}=2.4\times10^{-15}$ cm^2 was found using Eqs. of the type (6).

Figure 7 shows an example of the energy dependence of the linear polarization approximated by the function (4) in the absence of a magnetic field. The measured values of γ at $T\approx6$ K are presented in Table II. The results of the measurements of τ_0, $\tau_{\varepsilon2}$, and γ for bulk samples are presented in Table III.

5. DISCUSSION

As one can see from Fig. 4, the measured cross section σ_0 for scattering by acceptors in QW structures, which determines the width of the Hanle curve with initial electron energy ε_0, is inversely proportional to ε_0. This agrees with Eq. (A8), since according to Table IV the quantity $P_0=P_{\rm esc}^{\rm inel}+P_2^{\rm el}$ is almost independent of the electron energy. The experimental values of the cross section for scattering from the initial state for $\varepsilon_0=0.26$ eV ($\sigma_0=4.0\times10^{-14}$ cm^2) and for $\varepsilon_0=0.16$ eV ($\sigma_0=5.9\times10^{-14}$ cm^2) are in agreement with the computed values for $d/a\approx1.3$, i.e., $a\approx40$ Å.[2)] Allowance for a Hall factor different from 1 in determining the density from Hall measurements decreases this value. In the bulk case,[10] in agreement with the experimental value σ_0 for $\varepsilon_0=0.28$ eV, $\tilde{a}\approx21$ Å was obtained for

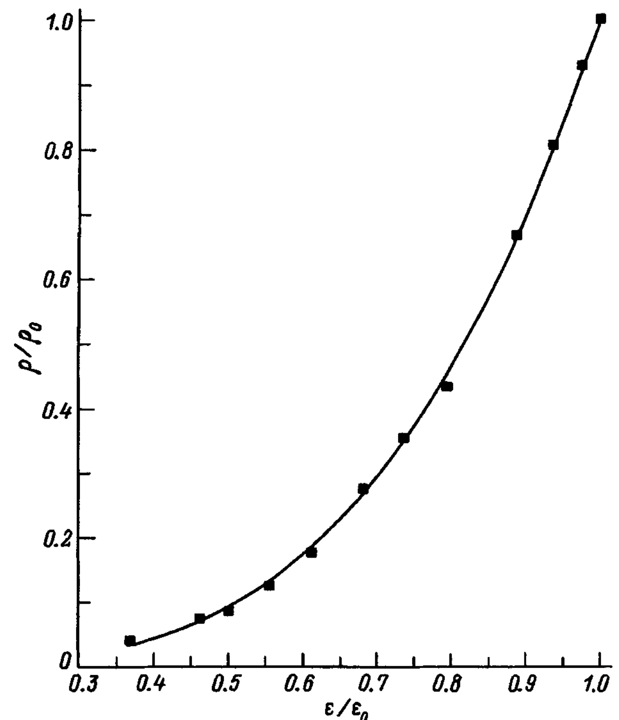

FIG. 7. Linear polarization versus the energy of hot electrons for structures with $N_A=4.6\times10^{18}$ cm^{-3}, $E_{\rm exc}=1.96$ eV, $T\approx6$ K, $\gamma=3.4$. Solid curves — approximation by Eq. (5).

TABLE IV. Computed values of the relaxation parameters.

Parameters	d/a	$2kd$ = 6	7	8	9
	0.5	1.051	1.048	1.046	1.044
	1.0	0.4415	0.4389	0.4369	0.4354
	1.5	0.2571	0.2552	0.2536	0.2523
$P_{\rm exc}^{\rm inel}$	2.0	0.172	0.171	0.170	0.169
	3.0	0.096	0.095	0.095	0.094
	4.0	0.062	0.062	0.062	0.061
	0.5	0.1752	0.1454	0.1224	0.1043
	1.0	0.1114	0.09703	0.08454	0.07393
	1.5	0.07309	0.06673	0.06019	0.05404
$P_2^{\rm el}$	2.0	0.050	0.047	0.044	0.040
	3.0	0.025	0.026	0.025	0.024
	4.0	0.015	0.016	0.016	0.016
	0.5	0.192	0.1536	0.1257	0.1048
	1.0	0.1511	0.1234	0.1024	0.08631
	1.5	0.1202	0.1002	0.08454	0.07207
$P_2^{\rm inel}$	2.0	0.097	0.082	0.070	0.061
	3.0	0.064	0.057	0.050	0.044
	4.0	0.045	0.041	0.037	0.033
A_ε		0.176	0.135	0.107	0.086
B_ε		0.037	0.027	0.021	0.016
$A_{\varepsilon 2}$		0.028	0.026	0.024	0.022
$B_{\varepsilon 2}$		0.012	0.011	0.009	0.008

the radius of a bulk acceptor. We note that the assumption of small-angle scattering is quite good for the bulk case. The fact that the QW-structure cross section σ_0 is half of the bulk value is due to the smaller number of the final electronic states that make the main contribution to σ_0 in the case of scattering in the first size-quantization subband.

The calculation of $\sigma_{\varepsilon 2}$ using Eqs. (A8), (A14), and (A15) (with A_ε and B_ε replaced by $A_{\varepsilon 2}$ and $B_{\varepsilon 2}$), as well as the data in Table IV, for $\varepsilon_0=0.26$ eV gives the value $\sigma_{\varepsilon 2}=0.25\times 10^{-14}$ cm^2, which is virtually identical to the experimental value $\sigma_{\varepsilon 2}=0.24\times 10^{-14}$ cm^2.

If the spectral depolarization in a zero magnetic field is approximated by the formula (5), then a calculation based on Eq. (25) gives $\gamma\approx 5.6$, which is appreciably greater than the experimental values (see Table II). In view of the quite rough approximation for the acceptor wave function adopted in the calculation [see Eq. (A17)], this discrepancy is not surprising.

6. CONCLUSIONS

We have investigated the mechanism of the scattering of hot electrons by neutral acceptors in structures with narrow GaAs/AlAs quantum wells doped with Be in the range $3\times 10^{17}-5\times 10^{18}$ cm^{-3}. Values have been obtained for the probabilities of scattering from the initial excited state and for the times characterizing energy and momentum relaxation. The rate of destruction of the anisotropy of the momentum distribution accompanying energy relaxation was determined.

Some results for QW structures and bulk samples have been compared. The QW-structure cross section for scattering from the initial state was found to be approximately half the bulk value. The experimental results are in satisfactory agreement with a calculation that takes into account the nonsmall-angle scattering in a quantum well.

This work was supported by the Russian Fund for Fundamental Research (Grants Nos. 96-02-16895 and 96-15-96392) and by Volkswagen Stiftung (Grant No. I/70958).

APPENDIX CALCULATION OF THE RELAXATION TIMES ON ACCEPTORS FOR QUANTUM WELL STRUCTURES

The relaxation times determining the degree of alignment and its magnetic-field dependence can be written in the form

$$\frac{1}{\tau}=N_A v\sigma, \tag{A1}$$

where N_A is the bulk acceptor density determined as a two-dimensional density divided by $d/2$, σ is the effective scattering cross section determined as the cross section for two-dimensional scattering multiplied by $d/2$, and v is the electron velocity. The effective cross section σ can be determined by the Born-approximation formula

$$\sigma=\frac{d}{2}\int W(k,k')Q\frac{d^2k'}{(2\pi)^2}, \tag{A2}$$

$$W(k,k')=\frac{2\pi}{\hbar v}\sum_n{}'|\langle 0|U_{kk'}|n\rangle|^2\delta(\varepsilon_k-\varepsilon_{k'}-E_n+E_0),$$

where the electron–hole interaction operator U for inelastic processes is

$$U=-\frac{e^2}{\chi|\mathbf{r}_e-\mathbf{r}_h|}, \tag{A3}$$

while the operator for interactions with a hole and a nucleus in elastic processes is

$$U=-\frac{e^2}{\chi|\mathbf{r}_e-\mathbf{r}_h|}+\frac{e^2}{\chi|\mathbf{r}_e-\mathbf{r}_0|}. \tag{A4}$$

Here χ is the permittivity, $\mathbf{r}_0$ is the coordinate of the nucleus, $\mathbf{r}_e$ and $\mathbf{r}_h$ are the coordinates of the electron and hole, and $U_{kk'}$ is the matrix element of U with respect to the electronic wave functions of the initial ($\mathbf{k}$) and final ($\mathbf{k}'$) states. The label n denotes the state of the hole after the collision, and it is assumed that before the collision the hole is in the ground state ($n=0$). In the case of inelastic processes the sum over n must not include the $n=0$ term, while for elastic processes, conversely, the sum (A2) contains only the $n=0$ term.

The quantity Q in Eq. (A2) depends on which cross section is being calculated. The value $Q=1$ is for the escape cross section $\sigma_{\rm esc}^{\rm inel}$. For the cross section σ_2, which describes the destruction of the second harmonic of the distribution function,

$$Q=Q_2=1-\cos 2\varphi,$$

where φ is the angle between the vectors $\mathbf{k}$ and $\mathbf{k}'$. For the cross section σ_ε, which determines the energy relaxation,

$$Q=Q_{\varepsilon}=(\varepsilon_k-\varepsilon_{k'})/\varepsilon=(E_n-E_0)/\varepsilon.$$

For the cross section determining the time $\tau_{\varepsilon 2}$ appearing in Eq. (23)

$$Q=Q_{\varepsilon 2}=[(E_n-E_0)\cos 2\varphi]/\varepsilon.$$

The calculation of the cross sections of inelastic processes using Eq. (A.2) requires knowledge of the energies and wave functions of the excited states of the acceptors, including the continuous spectrum. However, if the initial electron energy ε_k is much greater than the binding energy of an acceptor, then it can be assumed that the energy losses $\Delta\varepsilon=E_n-E_0$ on scattering will be small compared with ε_k, and the quantity E_n-E_0 in the argument of the δ function can be neglected. This approximation is similar to the approximation employed in the book by Landau and Lifshitz[12] in the calculation of the total inelastic ''escape cross section'' for the scattering of a fast electron by a hydrogen atom in the three-dimensional case. The further calculations of inelastic cross sections are performed as follows. Assuming that both the initial and final states of the electron belong to the first size-quantization subband, for the electron wave function we have

$$\Psi_{\mathbf{k}}(\mathbf{r}_e)=e^{i\mathbf{k}\cdot\boldsymbol{\rho}_e}\Psi(z_e),\quad \Psi(z_e)=\sqrt{\frac{2}{d}}\cos\left(\frac{\pi z_e}{d}\right) \tag{A5}$$

and similarly for $\Psi_{\mathbf{k}'}(\mathbf{r}_e)$. Using Eq. (A5) we calculate the matrix element of U [Eq. (A3)] with respect to the electronic functions

$$U_{kk'}=\frac{2\pi e^2}{\chi q}e^{i\mathbf{q}\cdot\boldsymbol{\rho}_h}G(z_h,q),$$

$$G(z_h,q)=\int dz e^{-q|z-z_h|}\Psi^2(z)dz, \tag{A6}$$

$$\mathbf{q}=\mathbf{k}'-\mathbf{k}.$$

We now utilize the fact that

$$\sum_n |\langle 0|U_{kk'}|n\rangle|^2=\overline{|U_{kk'}|^2}. \tag{A7}$$

The overbar denotes averaging over the ground state of the acceptor. In Eq. (A7) the summation is performed over all n, including $n=0$. As indicated above, before substituting the sum into Eq. (A2) for inelastic processes, the term with $n=0$ should be subtracted from it. Furthermore, replacing $\mathbf{k}'$ by the integration variable $\mathbf{q}$, integrating the δ function over the angle of the vector $\mathbf{q}$ (neglecting the difference E_n-E_0 in it) and performing some simple manipulations, we obtain formulas that can be written in the following form for all the cross sections:

$$\sigma=4\pi d^2\left(\frac{e^2}{\chi\hbar v}\right)^2 P, \tag{A8}$$

where

$$P_{\text{esc}}^{\text{inel}}=\frac{1}{2d}\int_0^{2k}\{\overline{G^2(z_h,q)}-[\overline{e^{i\mathbf{q}\cdot\boldsymbol{\rho}_h}G(z_h,q)}]^2\}\times\left(1-\frac{q^2}{4k^2}\right)^{-1/2}\frac{dq}{q^2}, \tag{A9}$$

$$P_2^{\text{inel}}=\frac{1}{k^2 d}\int_0^{2k}\{\overline{G^2(z_h,q)}-|\overline{e^{i\mathbf{q}\cdot\boldsymbol{\rho}_h}G(z_h,q)}|^2\}\times\left(1-\frac{q^2}{4k^2}\right)^{1/2}dq. \tag{A10}$$

For elastic collisions we have a formula similar to Eq. (A8), where

$$P_2^{\text{el}}=\frac{1}{k^2 d}\int_0^{2k}|[\overline{e^{i\mathbf{q}\cdot\boldsymbol{\rho}_h}G(z_h,q)}]-G(z_0,q)|^2\times\left(1-\frac{q^2}{4k^2}\right)^{1/2}dq. \tag{A11}$$

The calculation of $\sigma_{\varepsilon 2}$ and σ_{ε} requires a special analysis. Here we use the technique employed by Yu. T. Rebane,[11] which is based on the identity

$$\sum_n |\langle 0|U_{kk'}|n\rangle|^2(E_n-E_0)=\frac{1}{2}\overline{[U_{kk'}^*[\hat{H}U_{kk'}]]}, \tag{A12}$$

where the square brackets denote a commutator and $\hat{H}$ is the Hamiltonian for the hole on the acceptor in a quantum well. Since the potential energy of the interaction of the hole with the acceptor nucleus and with the well walls commutes with $U_{kk'}$, it can be assumed that $\hat{H}$ is the kinetic energy of the hole, i.e., the Luttinger Hamiltonian

$$\hat{H}=\frac{\hbar^2}{2m_0}\left(\gamma_1+\frac{5}{2}\gamma_2\right)\hat{\mathbf{k}}^2-\frac{\hbar^2}{m_0}\gamma_2(\hat{k}_x J_x^2+\hat{k}_y J_y^2+\hat{k}_z J_z^2)+\dots, \tag{A13}$$

where $\hat{\mathbf{k}}=-i\nabla$, γ_1 and γ_2 are Luttinger constants, and J_x, J_y, and J_z are the matrices for angular momentum 3/2. The omitted terms contain products of the type J_xJ_y and vanish on averaging over the ground state. We assume that the ground state corresponds to a projection of the angular momentum onto the z axis $J_z=\pm 3/2$. Then $\overline{J_z^2}=9/4$ and $\overline{J_x^2}=\overline{J_y^2}=(\overline{J^2}-\overline{J_z^2})/2=3/4$. Calculation of the commutator gives an expression similar to Eq. (A8) for σ_{ε} and $\sigma_{\varepsilon 2}$. In addition,

$$P_{\varepsilon}=\frac{m_c}{m_0}[(\gamma_1+\gamma_2)A_{\varepsilon}+(\gamma_1-2\gamma_2)B_{\varepsilon}], \tag{A14}$$

$$A_{\varepsilon}=\frac{1}{2k^2 d}\int_0^{2k}\overline{G^2(z_h q)}\left(1-\frac{q^2}{4k^2}\right)^{-1/2}dq, \tag{A15}$$

$$B_{\varepsilon}=\frac{1}{2k^2 d}\int_0^{2k}\overline{\left(\frac{dG}{dz}\right)^2}\left(1-\frac{q^2}{4k^2}\right)^{-1/2}\frac{dq}{q^2}. \tag{A16}$$

Finally, $P_{\varepsilon 2}$ is given by an expression similar to Eq. (A14), but $A_{\varepsilon 2}$ and $B_{\varepsilon 2}$ differ from the expressions (A15) and (A16) by the additional multiplier

$$\left[1-8\frac{q^2}{4k^2}\left(1-\frac{q^2}{4k^2}\right)\right]$$

in the integrand. The equations (A9)–(A11) and (A14)–(A16) make it possible to calculate all the required scattering cross sections, if the ground state wave function $\Phi(z_h,\rho_h)$ of the hole on the acceptor is known. To estimate the cross sections we used the function

$$\Phi(z_h,\rho_h)=\sqrt{\frac{2}{\pi d^2}}\exp\left(-\frac{\rho_h}{a}\right)\Phi(z_h), \tag{A17}$$

$$\Phi(z_h)=\sqrt{\frac{2}{d}}\cos\frac{\pi z}{d}.$$

Our approximation differs from that used in the book by Landau and Lifshitz (for the three-dimensional cross section $\sigma_{\rm esc}^{\rm inel}$) and in Ref. 10 (for the two-dimensional cross section $\sigma_{\rm esc}^{\rm inel}$) in that here it is not assumed that the scattering angles are small (though, once again, it is assumed that the energy losses are small). To go over to the case of small scattering angles, it is necessary to take the limit $k\to\infty$ in all integrals appearing in the different P. This does not change $\sigma_{\rm esc}^{\rm inel}$ much (because $P_{\rm esc}^{\rm inel}$ contains $1/q^2$ in the integrand, and the integral is determined by small values of q). However, for the rest of the cross sections σ the results obtained in the small-angle scattering approximation differ strongly from the values calculated here.

We underscore once again the deficiencies of our calculation. Apparently, for real experimental conditions the assumption of small energy losses is not very good. Moreover, the choice of the acceptor wave function in the form (A17) is a quite rough approximation. Nonetheless, it can be supposed that the calculation gives a reasonable estimate of the cross sections and their dependence on the electron energy. The quantities P were calculated numerically as functions of the two parameters d/a and $2kd$. The quantities A_ε, B_ε, $A_{\varepsilon 2}$, and $B_{\varepsilon 2}$ do not depend on d/a and were calculated as functions of $2kd$. The computational results are presented in Table IV. One can see that $P_{\rm esc}^{\rm inel}$ and $P_2^{\rm el}$ are virtually independent of $2kd$, i.e., independent of the electron energy in the interval from $2kd=6$ to $2kd=9$ studied here, which corresponds to the energy interval from 0.15 to 0.27 eV for $d=50$ Å.

Calculations were also performed for an acceptor wave function uniformly distributed as a function of z within the well $[\Phi(z_h)=1/\sqrt{d}$ instead of the second formula in Eq. (A17)]. The results were found to be virtually unchanged. The calculation in which the quantity $E_n-E_0\leqslant 60$ meV, which is independent of n and q, is substituted (instead of $E_n-E_0=0$) in the argument of the δ function in Eq. (A2) likewise did not significantly alter the results in the important electron energy range $\varepsilon\simeq 0.26$ eV.

[1)] In the preliminary results published in Ref. 10, the density of neutral acceptors was also measured by secondary-ion mass spectroscopy (SIMS). Both methods gave close results for bulk samples. However, for QW structures SIMS gave much higher densities than did the Hall measurements. In view of the inconclusiveness of the interpretation of the SIMS results for QW structures, we preferred to use the Hall results in the present work.

[2)] In Ref. 10 the value $a\approx 20$ Å was found for the acceptor radius in the plane of a quantum well under the assumption of small-angle scattering with the neglect of $\sigma_2^{\rm el}$. As already mentioned, this discrepancy is due to the fact that the densities used in the SIMS measurements in Ref. 10 were overestimated.

[1] B. P. Zakharchenya, D. N. Mirlin, V. I. Perel', and I. I. Reshina, Usp. Fiz. Nauk **136**, 459 (1982) [Sov. Phys. Usp. **25**, 143 (1982)].

[2] D. N. Mirlin, I. Ya. Karlik, L. P. Nikitin, I. I. Reshina, and V. F. Sapega, Solid State Commun. **37**, 757 (1981).

[3] S. A. Lyon, J. Lumin. **35**, 121 (1986).

[4] D. N. Mirlin and V. I. Perel', in *Spectroscopy of Nonequilibrium Electrons and Phonons*, edited by C. V. Shank and B. P. Zakharchenya, North-Holland, Amsterdam, 1992, p. 269.

[5] B. P. Zakharchenya, P. S. Kop'ev, D. N. Mirlin, D. G. Polakov, I. I. Reshina, V. F. Sapega, and A. A. Sirenko, Solid State Commun. **69**, 203 (1989).

[6] D. N. Mirlin and V. I. Perel', Semicond. Sci. Technol. **7**, 1221 (1992).

[7] H. Rücker, E. Molinari, and P. Lugli, Phys. Rev. B **45**, 6747 (1992).

[8] D. N. Mirlin, P. S. Kop'ev, I. I. Reshina, A. V. Rodina, V. F. Sapega, A. A. Sirenko, and V. M. Ustinov, in *Proceedings of the 22nd International Conference on the Physics of Semiconductors*, edited by D. J. Lockwood, World Scientific, 1994, Vol. 2, p. 1288.

[9] D. N. Mirlin and A. V. Rodina, Fiz. Tverd. Tela (St. Petersburg) **38**, 3201 (1996) [Phys. Solid State **38**, 1749 (1996)].

[10] I. I. Reshina, D. N. Mirlin, V. I. Perel', A. Yu. Dobin, A. G. Agranov, and B. Ya. Ber, Solid State Commun. **103**, 151 (1997).

[11] Yu. T. Rebane, Fiz. Tekh. Poluprovodn. **15**, 2179 (1981) [Sov. Phys. Semicond. **15**, 1265 (1981)].

[12] L. D. Landau and E. M. Lifshitz, *Quantum Mechanics: Non-Relativistic Theory*, 3rd. ed., Pergamon Press, Oxford, 1977 [Russian original, Nauka, Moscow, 1989, Vol. 3, Sec. 148].

Translated by M. E. Alferieff

Defects and short- and medium-range order in the structural network of hydrogenated amorphous silicon

O. A. Golikova and V. Kh. Kudoyarova

A. F. Ioffe Physicotechnical Institute, Russian Academy of Sciences, 194021 St. Petersburg, Russia

(Submitted November 4, 1997; accepted for publication November 10, 1997)
Fiz. Tekh. Poluprovodn. **32**, 876–878 (July 1998)

The effect of defects (dangling Si–Si bonds) produced during the deposition of *a*-Si:H films by the glow-discharge method and upon boron doping, as well as photoinduced defects, on changes in the short- and medium-range order in the structural network is investigated. It is shown for a constant defect density N_D=const that charged defects influence the *a*-Si:H structure much more strongly than do neutral defects. © *1998 American Institute of Physics.*
[S1063-7826(98)02207-8]

1. INTRODUCTION

Interest in studying the structural changes accompanying the formation of defects (dangling Si–Si bonds) in hydrogenated amorphous silicon (*a*-Si:H) has increased. These changes could be due to features of the local structure of the level of both the short-range order (for example, the spread of the angles between bonds) and the medium-range order (for example, the spread of the dihedral angles), as well as various statistical features of the rings composed of silicon tetrahedra. This applies mostly to the formation of photoinduced defects, which, according to the hypothesis of Fritzsche,[1] should be accompanied by rearrangement of the structure at the medium-range order level. Indeed, such changes in the structure of *a*-Si:H as a result of illumination have been observed by NMR.[2,3] Moreover, other photostructural changes in *a*-Si:H, specifically, a decrease of entropy,[4] a change in the angles between Si–Si bonds,[5] and a decrease in the compressive stresses,[6] have also been established, and it has also been found that films expand after intense illumination.[7] In Ref. 8 it was shown that the formation of defects during the growth of an undoped *a*-Si:H film, which can be controlled by the deposition conditions, is accompanied not only by changes in the position of the Fermi level (pseudodoping), but also by changes in the Urbach parameter E_U, the transverse-optical phonon frequency ω_{TO}, and the full width at half-maximum ($\Delta\omega_{\mathrm{TO}}$) of the optical phonon line in the Raman scattering spectrum, i.e., parameters characterizing the degree of ordering of the amorphous structure. The doping of *a*-Si:H with electrically active impurities is also known to lead to the formation of defects, but the character of the accompanying transformation of the structural network has not been established with the same certainty.

Our aim in the present paper is to compare the changes in the short- and medium-range order produced in the structural network of *a*-Si:H as a result of the formation of defects by different methods: during the deposition of films of undoped *a*-Si:H (deposition-induced or ‘‘native’’ defects), as a result of illumination (photoinduced defects), and by doping with boron.

2. EXPERIMENTAL PROCEDURES

The conditions for obtaining pseudodoped *a*-Si:H films by plasma-enhanced chemical vapor deposition (PECVD or the glow-discharge method) have been described in detail in Ref. 8, while the conditions for doping the films with boron from the gas phase and by ion implantation have been described in Ref. 9. The deposition temperature of all the films was constant: $T_s = 300\ ^\circ\mathrm{C}$. It has been reported[10] that light induces a photoconductivity σ_{ph} in *a*-Si:H, whose value decreases with the illumination time t as $\sigma_{\mathrm{th}} \sim t^{-\gamma}$.

We surmise that light not only produces defects (dangling Si–Si bonds), but also additional structural changes in the bulk of the material. To study the effect of illumination on structure, pseudodoped material with fast photoconductivity decay kinetics was chosen: under the action of light from an AM-1 source with specific power $100\ \mathrm{mW/cm^2}$ in the spectral range $\lambda < 0.9\ \mu\mathrm{m}$ the exponent $\gamma = 0.66$. After illumination for 5 h, the photoconductivity reaches a stationary level, and it can be expected that photostructural changes have occurred.

Information about the structure at the short- and medium-range order levels was obtained, just as in Ref. 11, by analyzing Raman spectra. The spectra were obtained on an U-1000 spectrometer (range 20–620 $\mathrm{cm^{-1}}$, step 1 $\mathrm{cm^{-1}}$, slit 5 $\mathrm{cm^{-1}}$, measurement accuracy $\pm 2.5\ \mathrm{cm^{-1}}$). The wavelength and power of the exciting radiation were equal to $\lambda = 488$ nm and 100 mW. The half-width $\Delta\omega_{\mathrm{TO}}$ of the transverse-optical phonon peak yields information about the spread of the angles between Si–Si bonds (short-range order), and the intensity of the transverse-acoustic (TA) phonon peak scaled to the intensity of the TO peak, $I_{\mathrm{TA}}/I_{\mathrm{TO}}$, yields information about the medium-range order. According to Ref. 11, an increase in the ratio $I_{\mathrm{TA}}/I_{\mathrm{TO}}$ indicates an increase in the degree of disorder in the arrangement of the Si tetrahedra.

3. EXPERIMENTAL RESULTS AND DISCUSSION

Let us see how $\Delta\omega_{\mathrm{TO}}$ and $I_{\mathrm{TA}}/I_{\mathrm{TO}}$ vary as functions of the position of the Fermi level ε_F in the mobility gap of *a*-Si:H relative to the conduction-band edge ε_c (Fig. 1). For

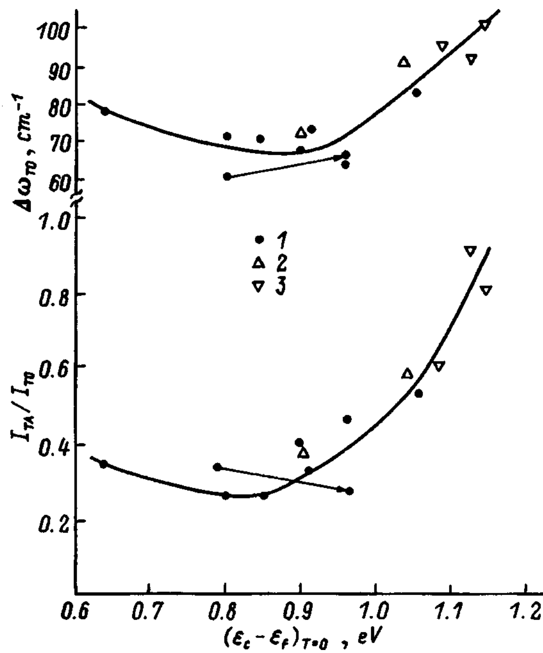

FIG. 1. Dependence of $\Delta\omega_{\mathrm{TO}}$ and $I_{\mathrm{TA}}/I_{\mathrm{TO}}$ on the position of the Fermi level relative to the conduction–band edge in a–Si:H. *1* — Pseudodoped a–Si:H (the arrows mark transitions into the postillumination state). *2* — a–Si:H doped with boron by ion implantation; *3* — a–Si:H doped with boron from the gas phase.

pseudodoped n-type a-Si:H $(\varepsilon_c-\varepsilon_F)_{T=0}=\Delta E$, where ΔE is the activation energy for dark conduction; for boron-doped p-type a-Si:H $(\varepsilon_c-\varepsilon_F)_{T=0}=E_g-\Delta E$ (E_g is the optical band gap with allowance for the known decrease in E_g with boron doping[9]). It follows from Fig. 1 that $\Delta\omega_{\mathrm{TO}}$ and $I_{\mathrm{TA}}/I_{\mathrm{TO}}$ as functions of $(\varepsilon_c-\varepsilon_F)_{T=0}$ approach a minimum corresponding to a-Si:H with $(\varepsilon_c-\varepsilon_F)_{T=0}=0.85$ eV. We note also that for shifts of ε_F away from the minimum, $\Delta\omega_{\mathrm{TO}}$ and $I_{\mathrm{TA}}/I_{\mathrm{TO}}$ increase simultaneously, and the relative change in $I_{\mathrm{TA}}/I_{\mathrm{TO}}$ for pseudodoped a-Si:H is greater when the Fermi level shifts in the direction of the valence-band edge, i.e., when $(\varepsilon_c-\varepsilon_F)_{T=0}>0.85$ eV. Moreover, it follows from Fig. 1 that both $\Delta\omega_{\mathrm{TO}}$ and $I_{\mathrm{TA}}/I_{\mathrm{TO}}$ increase rapidly for a-Si:H films when $(\varepsilon_c-\varepsilon_F)_{T=0}=1.05-1.15$ eV.

The defect density N_D produced in pseudodoped a-Si:H films is known to be at a minimum for $(\varepsilon_c-\varepsilon_F)_{T=0}=0.85$ eV.[8] On the basis of the data presented in Fig. 2, the same can also be said of a-Si:H films doped with boron both by ion implantation and from the gas phase.

The content C_{H} of hydrogen bound with silicon, as determined from the infrared spectra, is lowest in pseudodoped films when $(\varepsilon_c-\varepsilon_F)_{T=0}=0.85$ eV. At the same time, in films with boron impurities C_{H} decreases in the region $(\varepsilon_c-\varepsilon_F)_{T=0}=0.85-1.15$ eV (Fig. 2). However, $\Delta\omega_{\mathrm{TO}}$ and $I_{\mathrm{TA}}/I_{\mathrm{TO}}$ increase in this region for both pseudodoped and boron-doped a-Si:H (Fig. 1). Therefore, it can be concluded that changes in C_{H} do not have a decisive influence on $\Delta\omega_{\mathrm{TO}}$ and $I_{\mathrm{TA}}/I_{\mathrm{TO}}$. The results of Ref. 12 agree with this conclusion, at least with respect to $\Delta\omega_{\mathrm{TO}}$: $\Delta\omega_{\mathrm{TO}}=70-73$ cm^{-1} for $C_{\mathrm{H}}\simeq 5-25$ at.%. Data on $I_{\mathrm{TA}}/I_{\mathrm{TO}}$ are not given in Ref. 12; the films were obtained by the glow-discharge method.

Let us now consider $\Delta\omega_{\mathrm{TO}}$ and I_{TA}/I_{TO} as functions of

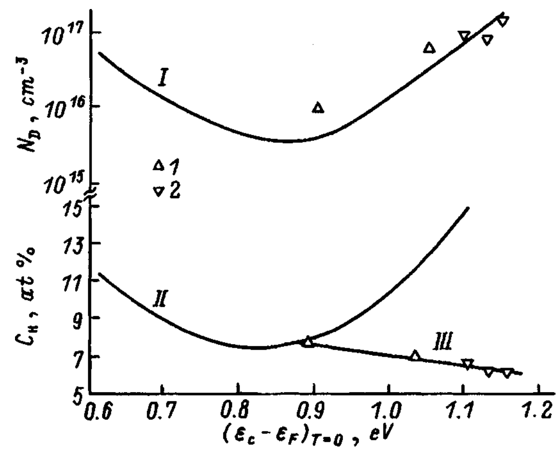

FIG. 2. Defect density N_D (*I*) and hydrogen content C_H (*II*,*III*) as functions of the position of the Fermi level. Curves *I*, *II* — data obtained in Ref. 8 for pseudodoped samples, curve *III* — data obtained in Ref. 9 for boron–doped samples; *1*, *2* — samples doped with boron by ion implantation and from the gas phase, respectively.

the defect density N_D determined by the constant photocurrent method (Fig. 3). In what follows we shall talk about N_D in the ranges $(\varepsilon_c-\varepsilon_F)_{T=0}=0.65-0.85$ and $0.85-1.15$ eV. As one can see from Fig. 3, the dependence of $\Delta\omega_{\mathrm{TO}}$ on N_D for both regions can be described by a single smooth curve on which the points for all films — pseudodoped and boron-doped — fall. At the same time, the $I_{\mathrm{TA}}/I_{\mathrm{TO}}$ versus N_D curves for pseudodoped films from the two regions indicated

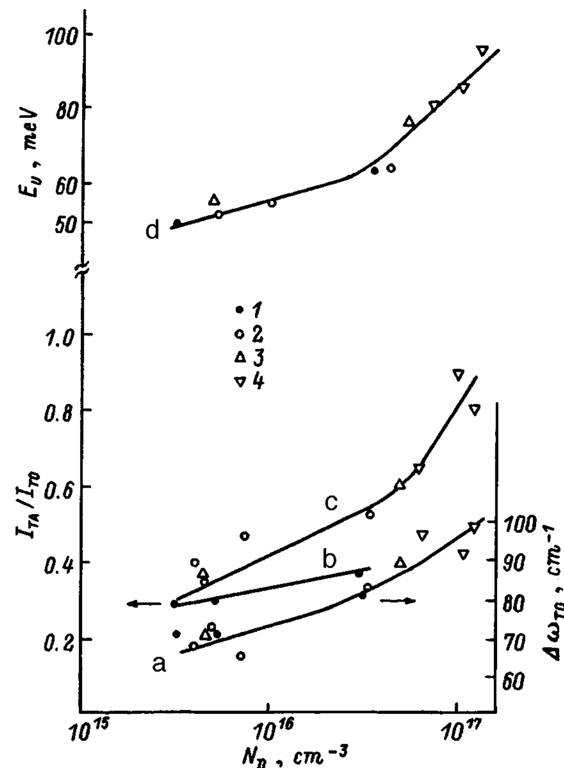

FIG. 3. $\Delta\omega_{\mathrm{TO}}$ (a), $I_{\mathrm{TA}}/I_{\mathrm{TO}}$ (b, c), and E_U (d) as functions of the defect density. *1* — Pseudodoped a–Si:H from the region $\varepsilon_c-\varepsilon_F=0.65-0.85$ eV, *2* — pseudodoped a–Si:H from the region $\varepsilon_c-\varepsilon_F=0.85-1.05$ eV, *3* — a–Si:H doped with boron by ion implantation, *4* — a–Si:H doped with boron from the gas phase.

above differ appreciably. This can apparently be attributed to different charge states for the defects (dangling bonds): D^- and D^+, respectively.[8] In doped *a*-Si:H, the boron atoms, which become incorporated into Si tetrahedra, produce an additional disordering of the structure. Indeed, sharper growth of both the ratio I_{TA}/I_{TO} and the Urbach parameter E_U (points *3* and *4* in Fig. 3) is observed for a defect density $N_D \geqslant 5\times10^{16}$ cm^{-3}. We note that no large differences in E_U are observed for pseudodoped films from the two regions indicated above.

Let us now consider the effect of illumination on $\Delta\omega_{TO}$ and I_{TA}/I_{TO}. The illumination−induced changes in $\Delta\omega_{TO}$ and I_{TA}/I_{TO} for one of the samples are marked by arrows in Fig. 1; the photoinduced defect density was equal to 10^{17} cm^{-3}. As a result of illumination, the activation energy ΔE for dark conduction in the sample increased from 0.8 to 0.96 eV. It follows from Fig. 1 that if $\Delta\omega_{TO}$ determined after illumination of a film equals $\Delta\omega_{TO}$ for another, unilluminated, film with $(\varepsilon_c-\varepsilon_F)_{T=0}$=const, then the values of I_{TA}/I_{TO} determined under the conditions indicated for these films are different: the value of I_{TA}/I_{TO} is much lower for the illuminated film. Moreover, the formation of photoinduced defects does not lead to simultaneous increases in $\Delta\omega_{TO}$ and I_{TA}/I_{TO}: only the former increases, while the latter decreases, i.e., the spread of the angles between Si–Si bonds increases, but the arrangement of the tetrahedra becomes more ordered.

The results of the present work once again raise the question, long discussed in the literature (see, for example, Refs. 13 and 14), of the difference between the defects formed in the structural network of *a*−Si:H by different methods.

Once again[8,14] we proceed from the fact that neutral dangling bonds (D^0) are formed during the deposition of ''native″ *a*−Si:H alone. Photoinduced defects are also in the same state (D^0).[14] The data which we have presented show that for N_D=const ($N_D \simeq 10^{17}$ cm^{-3}) photoinduced defects produce much smaller structural changes than do defects produced by pseudodoping and doping. Therefore, the rapid growth of structural disorder at all levels is due to the formation of charged defects. The changes in the charge states of the defects influence especially the medium−range order. This is indicated by the differences between the I_{TA}/I_{TO} versus N_D curves for the pseudodoped films from the two regions indicated above (Fig. 3), as well as by the difference between the values of I_{TA}/I_{TO} for two films with $(\varepsilon_c-\varepsilon_F)_{T=0}$=const: for the unilluminated film from the region 0.85−1.05 eV and the illuminated film from the region 0.65−0.85 eV (Fig. 1).

This work was supported by INTAS under Grant No. 931916.

[1] H. Fritzsche, Solid State Commun. **94**, 953 (1995).
[2] H. M. Branz and P. A. Fedders, Mater. Res. Soc. Symp. Proc. **338**, 129 (1994).
[3] M. J. Kernan, R. L. Corey, P. A. Fedders, D. J. Leopold, R. E. Norberg, W. A. Turner, and W. Paul, Mater. Res. Soc. Symp. Proc. **377**, 395 (1995).
[4] C. M. Formann, R. M. Dawson, H. Y. Liu, and C. R. Wronski, Appl. Phys. **76**, 768 (1994).
[5] K. Shimizu, T. Shiba, T. Tabuchi, and H. Okamoto, Jpn. J. Appl. Phys. **36**, 29 (1997).
[6] K. Shimizu, T. Tabuchi, M. Iida, and H. Okamoto, in *Abstracts of the 17th lnternational Conference on Amorphous and Microcrystalline Semiconductors: Science and Technology (ICAMS−17)*, Budapest, 1997, p. 209.
[7] T. Goto, N. Masui, M. Kondo, S. Nonomura, A. Matsuda, and S. Nitta, in *Abstracts of the 17th lnternational Conference on Amorphous and Microcrystalline Semiconductors: Science and Technology (ICAMS−17)*, Budapest, 1997, p. 210.
[8] O. A. Golikova and V. Kh. Kudoyarova, Fiz. Tekh. Poluprovodn. **29**, 1128 (1995) [Semiconductors **29**, 584 (1995)].
[9] O. A. Golikova, U. S. Babakhodzhaev, U. S. Dubro, M. M. Kazanin, M. M. Mezdrogina, and R. R. Yafaev, Fiz. Tekh. Poluprovodn. **24**, 1190 (1990) [Sov. Phys. Semicond. **24**, 751 (1990)].
[10] E. Sauvain, P. Pipos, A. Shah, and J. Hubin, J. Appl. Phys. **75**, 1722 (1994).
[11] A. P. Sokolov, A. P. Shebanin, O. A. Golikova, and M. M. Mezdrogina, J. Non-Cryst. Solids **137/138**, 99 (1991).
[12] A. H. Mahan, B. P. Nelson, S. Salomon, and R. S. Crandall, J. Non-Cryst. Solids **137/138**, 657 (1991).
[13] P. Stradins, H. Fritzsche, and M. Q. Tran, Mater. Res. Soc. Symp. Proc. **336**, 227 (1994).
[14] O. A. Golikova, Fiz. Tekh. Poluprovodn. **31**, 281 (1997) [Semiconductors **31**, 228 (1997)].

Translated by M. E. Alferieff

Effect of deposition and annealing conditions on the optical properties of amorphous silicon

A. I. Mashin,*) A. V. Ershov, and D. A. Khokhlov

N. I. Lobachevskiĭ Nizhniĭ Novgorod State University, 603600 Nizhniĭ Novgorod, Russia

(Submitted December 1, 1997; accepted for publication December 23, 1997)
Fiz. Tekh. Poluprovodn. **32**, 879–881 (July 1998)

The spectral characteristics of the refractive index and the extinction coefficient in the range 0.6–2.0 eV for amorphous silicon films prepared by electron-beam evaporation with variation of the substrate temperature, deposition rate, and annealing temperature in air are presented. The results obtained are discussed on the basis of the changes in the Penn gap energy as a function of the indicated preparation and treatment conditions. © *1998 American Institute of Physics.* [S1063-7826(98)02307-2]

Hydrogenated amorphous silicon (*a*-Si:H) is of interest mainly because it holds promise for the fabrication of inexpensive large-area film solar cells.[1] At the same time, investigators are devoting more and more attention to ''hydrogen-free'' amorphous silicon (*a*-Si) as a promising, high-refractive-index material for passive interference elements in near-IR fiber optics.[2,3]

Figure 1 shows typical spectral dependences of the refractive index n and the extinction coefficient k of *a*-Si films prepared by electron-beam evaporation in vacuum (see, for example, Ref. 4 for the technological details). The optical constants were determined by the method of Ref. 5. Just as in most published data,[6] in our case the values and variance of the refractive index of *a*-Si films (curve *1*) are higher than for crystalline silicon (*c*-Si) and *a*-Si:H in the experimental frequency interval. This fact can be explained by recalling that in amorphous silicon, besides destruction of the long-range order, there is a high concentration of matrix defects: dangling bonds, pores, extraneous impurities, etc. In the present paper we examine the influence of pores on the optical properties of *a*-Si films prepared with different substrate temperatures (T_s) and deposition rates (V_s) and annealed in air.

Depending on pore size, two cases can be studied.

1. If the pores are sufficiently large compared with the interatomic distance and slightly greater than or comparable to the wavelengths of visible light, then electromagnetic light waves undergo multiple scattering, and the optical properties of the material can be described within the effective-medium theory. According to Ref. 7, in the case when only pores are present in the material the following equation holds:

$$(1-x_v)[\hat{\varepsilon}_m(\omega)-\hat{\varepsilon}(\omega)]/[\hat{\varepsilon}m(\omega)+2\hat{\varepsilon}(\omega)] + x_v[\hat{\varepsilon}_v(\omega)-\hat{\varepsilon}(\omega)]/[\hat{\varepsilon}(\omega)+2\hat{\varepsilon}(\omega)]=0, \quad (1)$$

where x_v is the relative volume of the pores, $\hat{\varepsilon}_m(\omega)$ and $\hat{\varepsilon}_v(\omega)$ are the complex permittivities of the medium and the pores, and $\hat{\varepsilon}(\omega)$ is the effective complex permittivity of the system.

2. In the special case where the pores are very small (less than 1 nm), they can be treated as elements of a uniform network. Then the overall effect of the pores is to decrease the average strength of interatomic bonds and the plasma frequency of the material, and the optical properties can be calculated within the Penn model. According to Ref. 8, the static refractive index n_0 is related with the plasma frequency ω_p and the Penn gap energy $\hbar\omega_g$ by

$$n_0^2=1+(2/3)(\omega_p^2/\omega_g^2). \quad (2)$$

To a good approximation, the energy $\hbar\omega_g$ corresponds to the maximum of the spectrum $k(\omega)$, while

$$\omega_p^2=(4\pi e^2/m)(\rho L_A/A)n_V, \quad (3)$$

where e and m are the electron charge and mass, ρ is the density of the material, A is the molecular mass, and L_A is Avogadro's number. For *c*-Si, $n_V=4$.

The quantity $\hbar\omega_p$ is called the energy of a plasmon, which is a collective excitation of the electron gas localized mainly in dense regions of the random network and penetrating only very little into the pores, which in turn produce the density deficit in *a*-Si. Therefore, the plasmon energy can serve as a measure of the microscopic density of an amorphous semiconductor.

According to the data of Ref. 9, pores with diameter not exceeding 0.5 nm are characteristic for *a*-Si films. Then the pores can be treated as a cluster of atoms removed from the fully coordinated structure, and the expression (2) can be written as[10]

$$n=1+(2/3)(\omega_p^2/\omega_g^2)(\rho/\rho^0)^{1-4f}, \quad (4)$$

where $f=d\ln C/d\ln\rho$ is the fraction of the cluster bonds on the surface of a pore, C is the average coordination number, and the superscript 0 denotes a parameter of the fully coordinated material. The quantity f varies from 0 to 1, depending on the pore size. In the case of small pores (less than 2–3 coordination spheres) $f>0.25$, and the value of n for such a medium will likewise be greater than for a fully coordinated material.

 © 1998 American Institute of Physics

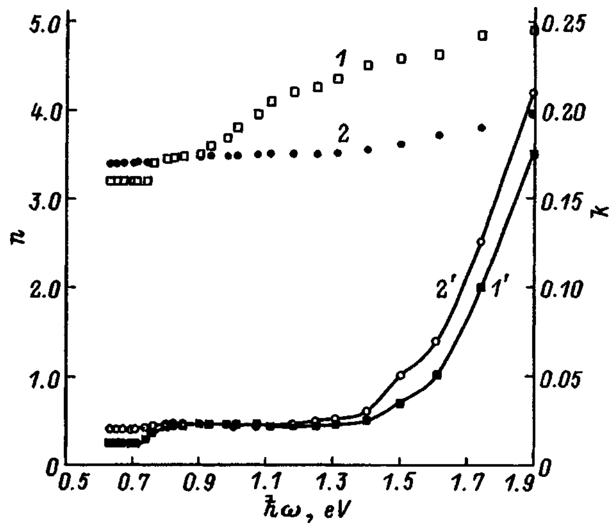

FIG. 1. Spectral dependences of the refractive index n (*1*, *2*) and the extinction coefficient k (*1*′, *2*′) of *a*-Si films produced by electron-beam evaporation with substrate temperatures $T_s = 250$ (*1*, *1*′) and 20 (*2*, *2*′) °C.

On the basis of these arguments we can say that in our case the *a*-Si films produced by electron-beam evaporation with $T_s = 250$ °C (Fig. 1) contain pores with diameters comparable to the first or second coordination radius and are accordingly characterized by a high refractive index.

Variation of the preparation conditions, specifically, decreases in T_s from 250 to 20 °C and in V_s by approximately a factor of 2 (Figs. 1 and 2), produces a qualitatively identical change in n in films — a decrease in n near the absorption edge. The dispersion of the refractive index also decreases under these conditions. As a result, the difference in the behavior of the curves *1* and *2* in the two figures is very substantial in the short-wavelength region. For example, for photon energy $\hbar\omega \simeq 1.9$ eV the difference between the refractive indices is ~1 (Fig. 1), whereas for $\hbar\omega \simeq 1.0$ eV this difference is ~0.4. For $\hbar\omega < 0.8$ eV the refractive index is virtually independent of these deposition conditions.

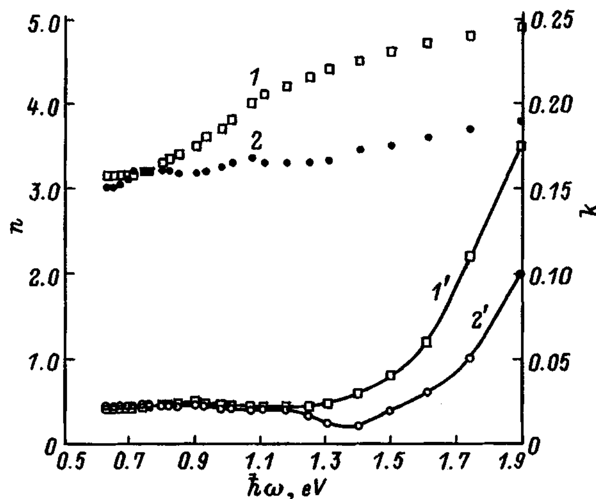

FIG. 2. Effect of the deposition rate on the spectral dependences of the refractive index n (*1*, *2*) and the extinction coefficient k (*1*′, *2*′) of *a*-Si films. Film deposition rate V_s, nm/s: *1*, *1*′ — 0.53, *2*, *2*′ — 0.30.

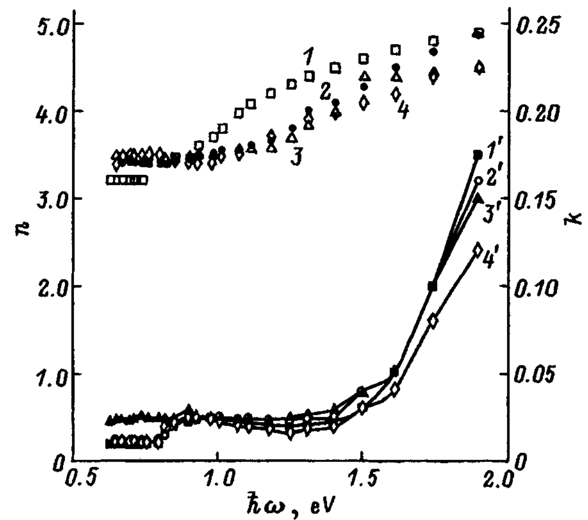

FIG. 3. Spectral dependences of the refractive index n (*1–4*) and the extinction coefficient k (*1*′*–4*′) of *a*-Si films prepared with $T_s = 250$ °C and annealed in air for 1 h at 20, 100, 150, and 250 °C (*1–4* or *1*′*–4*′, respectively).

Turning now to the frequency dependences of the extinction coefficient (curves *1*′ and *2*′ in Figs. 1 and 2), we can see that variations of T_s and V_s affect the behavior of $k(\omega)$ differently. Decreasing the substrate temperature (Fig. 1) shifts the absorption edge toward longer wavelengths, while decreasing V_s (Fig. 2) shifts the absorption edge of amorphous silicon toward higher energies. This fact suggests that the mechanism leading to a decrease in the refractive index as T_s decreases is different from the mechanism in the case when V_s decreases.

Evidently, as T_s decreases, the pore sizes in *a*-Si increase. In turn, this results in a decrease of n, which approaches the refractive index of *c*-Si, while for very large pores (50–100 nm) n achieves values which are lower than in the crystalline material. Since the Penn energy gap decreases in the process, the maximum of the function $k(\omega)$ and therefore the absorption edge shift toward longer wavelengths, as we observe on the experimental curves presented (Fig. 1). In this case the decrease in $\hbar\omega_g$ is explained by a decrease in the average coordination number.

Decreasing the deposition rate should decrease the porosity of the film, and according to Eq. (4) the refractive index should increase in this case. On the other hand, for low deposition rates the amount of extraneous impurities, such as oxygen, hydrogen, carbon, and so on, entering the film is larger. If we agree with Ref. 9 and assume that the pores in the original *a*-Si are approximately 0.5 nm in diameter, then it is difficult to imagine that the pore size will decrease further as the deposition rate decreases. Therefore, it is unlikely that a decrease in deposition rate will affect the optical characteristics of *a*-Si via a decrease in the pore size.

To isolate the effect of extraneous impurities, we thought it would be useful to consider the combined effect of the deposition rate and the subsequent annealing of *a*-Si in air, since in the latter case extraneous impurities should enter the film from the atmosphere. According to the experimental data, the annealing of *a*-Si in air, just as a decrease in the

deposition rate (Figs. 2 and 3), decreases the refractive index and shifts the absorption edge toward higher energies.

On this basis we believe that the character of the change produced in the optical properties of *a*-Si by variation of the preparation and heat-treatment conditions is described well within the Penn model. The Penn energy gap is determined both by the presence and the behavior of extraneous impurities in the film and by the structure of the short-range order in amorphous silicon. Thus, the diffusion of oxygen into the bulk of the material results in saturation of the dangling bonds and the formation of Si–O bonds instead of Si–Si bonds. Since the Si–O bond is energetically stronger than the Si–Si bond, the Penn energy gap $\hbar\omega_g$ increases and the maximum of $k(\omega)$ shifts toward shorter wavelengths. On the other hand, ''healing'' of the network, i.e., a decrease in the number of dangling bonds, increases the coordination number, while relaxation of an already fully connected network (a decrease in the spread of bond lengths and bond and dielectric angles) increases the Penn energy gap.

*)E-Mail: mashin@phys.unn.runnet.ru

[1] A. Madan and M. Shaw, *The Physics and Applications of Amorphous Semiconductors* (Academic Press, Boston-San Diego-N.Y.-London-Sydney-Tokyo-Toronto, 1988; Mir, Moscow, 1991, p. 670).

[2] K. Hamada, M. Wada, H. Shimizu, M. Kume, F. Susa, T. Shibutani, N. Yoshikawa, K. Itoh, G. Kano, and I. Teramoto, IEEE J. Quantum Electron. **QE-21**, 623 (1985).

[3] A. V. Ershov, N. B. Zvonkov, A. I. Mashin, and D. A. Khokhlov, in *Proceedings of the Russian Conference on the Structure and Properties of Crystalline and Amorphous Materials* [in Russian], Nizhniĭ Novgorod State University, Nizhniĭ Novgorod, 1996, p. 28.

[4] A. V. Ershov, A. I. Mashin, and A. F. Khokhlov, Vysokochist. Veshchestva **2**, 35 (1995).

[5] A. S. Valeev, Opt. Spektrosk. **15**, 500 (1963) [Opt. Spectrosc. **15**, 269 (1963)].

[6] M. H. Brodsky, R. S. Title, K. Weiser, and G. D. Pettit, Phys. Rev. B **1**, 2632 (1970).

[7] D. R. Penn, Phys. Rev. **128**, 2093 (1962).

[8] J. D. Joannopoulos and G. Lucovsky (Eds.), *The Physics of Hydrogenated Amorphous Silicon, Vol. 2: Electronic and Vibrational Properties*, (Springer-Verlag, Berlin–New York, 1984; Mir, Moscow, 1988, p. 447).

[9] N. J. Shevchik and W. Paul, J. Non-Cryst. Solids **16**, 55 (1974).

[10] J. C. Philips, Phys. Status Solidi B **44**, K1 (1971).

Translated by M. E. Alferieff

PHYSICS OF SEMICONDUCTOR DEVICES

Temperature dependence of the reverse current in Schottky barrier diodes

P. A. Pipinis, A. K. Rimeĭka, and V. A. Lapeĭka

Vilnius Pedagogic University, 2034 Vilnius, Lithuania

(Submitted June 16, 1997; accepted for publication July 31, 1997)
Fiz. Tekh. Poluprovodn. **32**, 882–885 (July 1998)

The temperature dependences of the current I in reverse-biased $Al/SiO_2/n$-Si, $Al/SiO_2/n$-GaAs and Al/n-GaAs (with the native oxide) structures are measured. It is established that these dependences all have the property that the thermal activation energy decreases with increasing applied voltage and that at higher voltages the plots of $\ln I$ versus $1/T$ deviate from straight lines. The results can be explained on the basis of the fact that the current through the barrier is due to electron tunneling from surface states into the conduction band of the semiconductor. The field intensity in the Schottky barrier and the density of surface electron states in the interfacial layer of the semiconductor are estimated by comparing the experimental results with a tunneling theory that takes into account the effect of the semiconductor lattice phonons on the tunneling probability. *© 1998 American Institute of Physics.* [S1063-7826(98)02407-7]

1. INTRODUCTION

Metal-semiconductor Schottky barrier diodes have been investigated by many researchers (see, for example, Ref. 1). The forward-bias currents — the forward branches of the current-voltage characteristics (IVC's) — have been explained by the theories of diffusion and thermionic emission,[2] as well as the tunneling processes of field and thermionic-field emission.[3,4] According to the thermionic-emission theory, the reverse current should saturate as the reverse bias voltage increases. However, since the expected current saturation is not observed at high reverse bias voltages in real Schottky diodes, the reverse branches of the IVC are explained by the fact that the barrier height decreases as the voltage increases[5,6] or by the fact that the current due to electron tunneling from the metal into the semiconductor is substantial at higher voltages.[7,8] For example, in Ref. 8 the reverse current of surface-barrier structures on GaAs ($n=10^{18}$ cm^{-3}) at $T=350$ K is explained by thermionic-field emission, which transforms into field emission at lower temperatures.

The theories of Schottky barriers and the current mechanism in them[9,10] take into account the influence of the surface states on the metal-semiconductor interface. The barrier characteristics and the main laws of current transport through the barrier, including the voltage dependence of the reverse current, can be explained by taking into account the effect of surface states on charge-carrier emission, as well as the voltage drop at the interface.[5,6] However, as one can see from the results of Refs. 5, 6, and 11, even the modern theories are incapable of explaining completely the temperature dependences of the current, especially at low bias voltages. In Ref. 11, to explain the IVC's obtained at different temperatures, the reverse branches of the IVC's of $CrSi_2/Si$ structures are attributed to the thermionic emission mechanism at low voltages and $T=200$ K and to thermionic-field emission at higher voltages and lower temperatures.

It seems to us that in many cases the temperature variation of the IVC's, as well as the observed features of the temperature dependence of the current for different reverse bias voltages, can be explained by a single theory of phonon-assisted electron tunneling from surface states through the barrier. In Ref. 12 the reverse branches of the IVC's obtained at different temperatures for diodes with an Al/n-GaAs Schottky barrier were explained on the basis of this mechanism.

This paper presents the temperature dependences of the reverse current at different voltages for certain metal-semiconductor diodes with a thin oxide layer. The experimental results are compared with theoretical expressions for the probability of tunneling from interfacial surface states through a barrier. The comparison makes it possible to estimate the maximum field intensity in the barrier and the charge density localized in interfacial defect levels.

2. SAMPLE CHARACTERISTICS AND MEASUREMENT METHODS

The experimental samples were prepared as follows. The $Al/SiO_2/n$-Si structure was based on an n-type Si ($n=2\times10^{16}$ cm^{-3}) wafer with (111) orientation. A thin SiO_2 layer was obtained on the Si surface by thermal oxidation of the surface in a dry-oxygen atmosphere at 700 °C. The oxide was no more than 4 nm thick. An aluminum disk of diameter 0.8 mm deposited on the oxide served as the barrier-forming electrode. An ohmic contact was deposited on the other side of the wafer.

The $Al/SiO_2/GaAs$ structures were prepared on an

 © 1998 American Institute of Physics

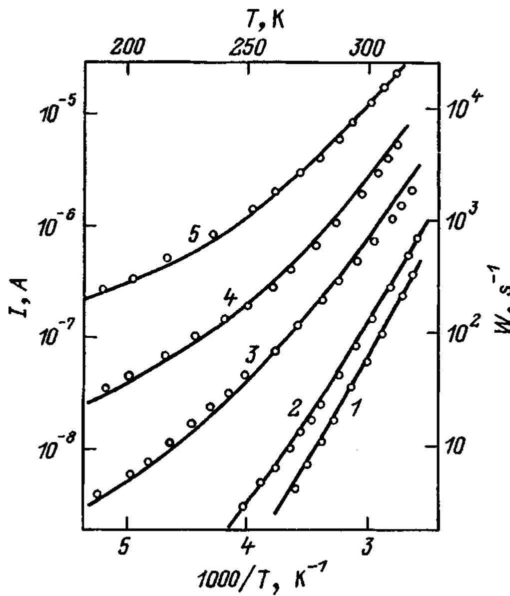

FIG. 1. Plots of the current I versus the temperature T at different reverse bias voltages (points) for $Al/SiO_2/n$-Si structures and theoretical dependences of the tunneling probability W on the electric field strength E (solid lines) calculated for a barrier height $\Delta=0.6$ eV, an electron-phonon interaction constant $a=6.0$, an electron effective mass (Si) $m^*=0.33m_e$, and a phonon energy (SiO_2) $\hbar\omega=0.063$ eV. The diffusion potential $U_0=0.4$ V. U, V: *1* — 0.05, *2* — 0.1, *3* — 0.5, *4* — 1, *5* — 5. E, 10^7 V/m: *1* — 5.5, *2* — 6, *3* — 7.2, *4* — 8, *5* — 9.

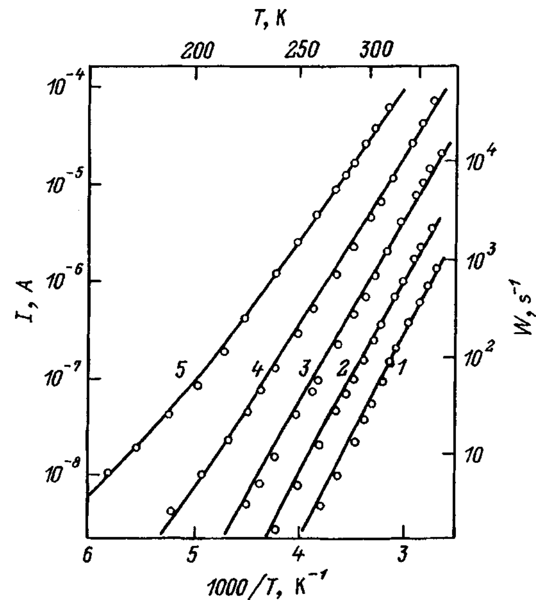

FIG. 2. Plots of the current I versus the temperature T at different reverse bias voltages (points) for $Al/SiO_2/n$-GaAs structures and theoretical dependences of the tunneling probability W on the electric field strength E (solid lines) calculated for a barrier height $\Delta=0.5$ eV, $a=8$, $m^*=0.068m_e$, and $\hbar\omega=0.036$ eV. The diffusion potential $U_0=0.3$ V. U, V: *1* — 0.2, *2* — 0.5, *3* — 1, *4* — 2, *5* — 4. E, 10^7 V/m: *1* — 0.7, *2* — 0.9, *3* — 1.3, *4* — 1.8, *5* — 2.3.

n-type (100) GaAs wafer ($n=5\times10^{16}$ cm^{-3}). After polishing and chemical treatment, a layer of silicon dioxide was deposited on one side of the wafer by a plasma-chemical method. An aluminum electrode of diameter 1.0 mm was deposited on the oxide surface at $T=100$ °C. An ohmic contact was created on the other side. Al/n-GaAs diodes with the native oxide were also studied. The GaAs surface was oxidized in an oxygen atmosphere for 40 min at 510 °C.

The measurements were performed in a vacuum cryostat that permitted varying the temperature from 100 to 400 K. The current was measured with an electrometer (the measurement range was $10^{-13}-10^{-9}$ A) or an $X-Y$ plotter.

3. RESULTS AND INTERPRETATION

The temperature dependence of the current at different reverse bias voltages were measured on these diodes. The experimental diodes exhibited a pronounced temperature dependence of the current. This dependence was identical for both types of diodes. More specifically, at low voltages the plots of $\ln I$ versus $1/T$ are straight lines with thermal activation energy 0.6 eV for the $Al/SiO_2/n$-Si diode and 0.5 eV for the $Al/SiO_2/n$-GaAs diode. At higher voltages the plots of $\ln I=f(1/T)$ deviate substantially from straight lines because of the weaker temperature dependence of the current at low temperatures (Figs. 1 and 2, curves *3–5*).

Such temperature dependences of the current are difficult to explain by the standard theories of current transport in Schottky diodes. For this reason, we shall explain them on the basis of the model proposed in Ref. 12 to explain the reverse-current current-voltage characteristics of Al/n-GaAs Schottky barrier diodes. It is assumed that the sources of current carriers in these diodes are electronic states in the semiconductor near the metal-semiconductor interface. Electrons enter the conduction band of the semiconductor as a result of phonon-assisted tunneling from these levels. Assuming that the tunneling electrons leave the depletion region without losses due to recombination and that they, therefore, all contribute to the measured current, the current through a reverse-biased barrier will be proportional to the tunneling probability W, i.e., $I=WeNS$, where N is the surface density of centers with localized electrons and S is the area of the barrier electrode. On this basis we shall compare the experimental temperature dependences of the current with the temperature dependence of the tunneling probability calculated according to the quantum-mechanical theory of phonon-assisted tunneling.

The temperature dependences of the tunneling probability depicted by the curves in Figs. 1–3 were calculated according to Eq. (16) from Ref. 13 for the values of the parameters indicated in the figure captions. In making the comparison, it was assumed that the maximum field intensity E in the barrier is proportional to the square root of the sum of the applied voltage U and the diffusion potential U_0. Therefore, we can take the ratio of the field intensity E to the square root of $U+U_0$ as a criterion for estimating the accuracy of the comparison. This ratio should not differ significantly for the curves being compared. The electron-phonon interaction constant a was chosen on just this basis; the other quantities required for the calculations were specified by the characteristics of the material. For a known tunneling probability (determined by comparison with the theoretical curve) the density of states in the surface layer can be determined from the measured current density. It is found to be

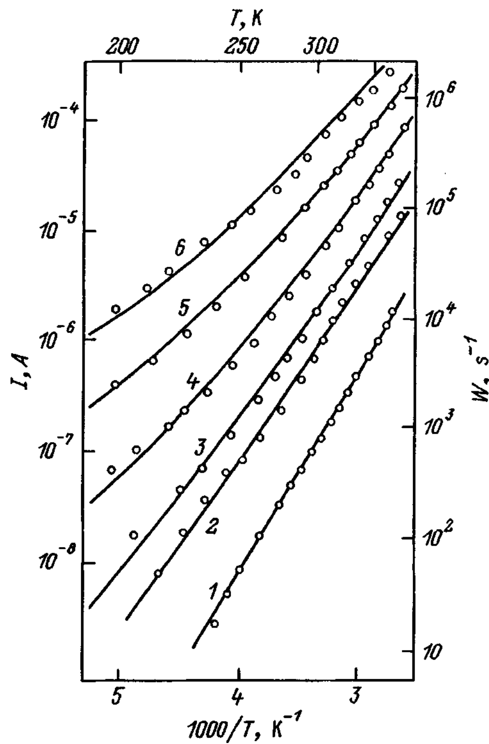

FIG. 3. Plots of the current I versus the temperature T at different reverse bias voltages (points) for Al/GaAs structures with the native oxide and theoretical dependences of the tunneling probability W on the electric field strength E (solid lines) calculated for a barrier height $\Delta=0.5$ eV, $a=8$, $m^*=0.068m_e$, and $\hbar\omega=0.036$ eV. The diffusion potential $U_0=0.4$ V. U, V: *1* — 0.1, *2* — 0.5, *3* — 1, *4* — 2, *5* — 4, *6* — 6. E, 10^7 V/m: *1* — 1.3, *2* — 1.8, *3* — 2.1, *4* — 2.5, *5* — 3.0, *6* — 3.3.

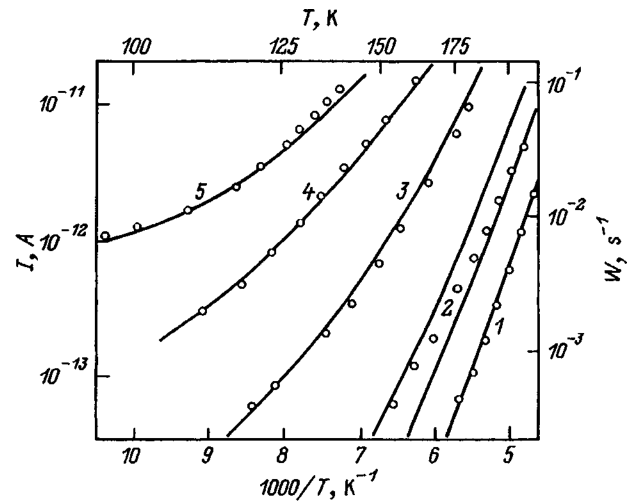

FIG. 4. Plots of the current I versus the temperature T at different reverse bias voltages (points) for Al/SiO_2/n-Si structures from Ref. 21 and theoretical dependences of the tunneling probability W on the electric field strength E (solid lines) calculated for barrier height $\Delta=0.5$ eV, $a=6.0$, $m^*=0.33m_e$, and $\hbar\omega=0.063$ eV. U, V: *1* — 5.2, *2* — 8.5, *3* — 11, *4* — 16, *5* — 18. E, 10^7 V/m: *1* — 2.6, *2* — 3.0–3.3, *3* — 3.9, *4* — 4.4, *5* — 4.7.

1.2×10^{12} cm^{-2} for the Al/SiO_2/n-Si sample, 2.8×10^{12} cm^{-2} for the Al/SiO_2/n-GaAs sample, and 3.7×10^{11} cm^{-2} for the Al/n-GaAs sample with the native oxide.

The interpretation presented above neglected the effect of the oxide layer on the current. The fact that emission occurs from somewhere other than the oxide is indicated by the small height of the barrier — 0.6 eV in Si and 0.5 eV in GaAs. In the case of electron emission from the metal into the oxide, the barrier would be approximately 3.2 eV.[14] Moreover, the capacitance-voltage characteristics in the form of plots of $1/C^2=f(U)$, where C is the capacitance and U is the reverse bias voltage, are straight lines, which also provide an important argument in favor of emission occurring through the space-charge region of the Schottky barrier. The small influence of the oxide layer on the passage of current through the structures studied can be explained by the fact that the oxide layer is not of uniform thickness and contains "pits," which become filled with the electrode metal. It is known[15,16] that such pits in an ultrathin oxide layer appear in the thermally grown oxide because of the nonuniformity of the surface. These micropits with patches of metal in the oxide are, in the opinion of many authors,[17–20] the locations where current passage occurs.

It should be noted that similar temperature dependences of the current through a barrier have also been observed by other authors. For example, in Ref. 6 the temperature dependences of the reverse current in Al/p-InP diodes with a thin oxide layer plotted in $\ln I=f(1/T)$ coordinates are straight lines at low voltages, while at higher voltages they deviate from straight lines as a result of the decrease in the thermal activation energy at low temperatures. In Ref. 21 the temperature dependences of the current in an Al/SiO_2/n-Si MIS structure exhibit a pronounced difference in the activation energy at low and higher temperatures, and the activation energy also decreases with increasing applied voltage. These structures were obtained by thermal oxidation of epitaxial silicon containing a large number of structural defects. The authors of the paper just cited attribute their results to the resonant tunneling of electrons from surface states through deep impurity levels in the band gap into the conduction band. The variation of the activation energy with temperature is explained by the fact that the surface states are distributed in a certain energy interval and their filling by the thermal ejection of electrons from the silicon valence band thus depends on the temperature. The variation of the activation energy with the temperature and voltage can be explained qualitatively on the basis of these assumptions.

Since the structures studied in Ref. 21 differed very little from our Al/SiO_2/n-Si diodes [except for the fact that the oxide thickness was greater (140 nm)], we offer the explanation for the temperature dependence of the current in Ref. 21 as an explanation for our results. We also suppose that tunneling occurs from interfacial centers through a 0.5-eV barrier. The theoretical curves of the tunneling probability calculated with the same parameters as in Fig. 1 for different values of the field intensity E are depicted in Fig. 4 by solid lines, while the experimental dependences of the current are represented by points. One can see that the temperature dependences of the current obtained in the voltage interval from 5.2 to 18 V agree well with the theoretical curves cal-

culated for values of E in the interval from 2.6 to 4.7×10^7 V/m.

Since, in the opinion of Litovskiĭ *et al.*,[21] the Si used contains a large number of defects, the oxide layer obtained apparently also has a nonuniform thickness, i.e., it contains micropits, where the oxide thickness is much smaller than the average oxide thickness, and it is through these micropits that current passes. According to a comparison of the theoretical and experimental curves, the total surface charge density giving rise to the current equals 2×10^{11} cm^{-2}. This value of the density of electronic surface states agrees with the estimate given by Litovskiĭ *et al.* Thus, even in this case the observed features of the temperature dependence of the reverse current in diodes can be explained by the phonon-assisted tunneling generation of free electrons.

In conclusion, we note that electron tunneling from surface levels in the semiconductor at the interface is apparently one of the main mechanisms of the reverse current observed in Schottky barrier diodes. Therefore, the quantum-mechanical theory of phonon-assisted tunneling provides good agreement with the experimental temperature dependences of the current. The effect of phonons on tunneling processes is manifested mainly in the fact that the interaction with phonons in the centers imparts a pronounced temperature dependence of the form observed experimentally to the tunneling processes.

[1] M. S. Tyagi, in *Metal-semiconductor Schottky Barrier Junctions and Their Applications*, edited by P. L. Sharma, N. Y., 1984.
[2] C. P. Crowel and S. M. Sze, Solid-State Electron. **9**, 1035 (1966).
[3] F. A. Padovani and R. Stratton, Solid-State Electron. **9**, 695 (1966).
[4] C. P. Crowel and V. L. Rideout, Solid-State Electron. **12**, 89 (1969).
[5] K. Maeda, I. Umzu, H. Ikoma, and T. Yoshimura, J. Appl. Phys. **68**, 2858 (1990).
[6] A. Singh and P. Cova, J. Appl. Phys. **74**, 2336 (1994).
[7] A. N. Korol', Fiz. Tekh. Poluprovodn. **14**, 1180 (1980) [Sov. Phys. Semicond. **14**, 698 (1980)].
[8] Yu. A. Gol'dberg and T. V. L'vova, Fiz. Tekh. Poluprovodn. **15**, 2339 (1981) [Sov. Phys. Semicond. **15**, 1359 (1981)].
[9] A. V. Chaplik and M. V. Éntin, Zh. Éksp. Teor. Fiz. **67**, 208 (1974) [Sov. Phys. JETP **40**, 106 (1974)].
[10] C. Y. Wu, J. Appl. Phys. **53**, 5947 (1982).
[11] B. Barus and D. Donoval, Solid-State Electron. **36**, 969 (1993).
[12] R. Brazis, P. Pipinys, A. Rimeika, and L. Gegznaite, Solid State Commun. **55**, 25 (1985).
[13] F. I. Dalidchik, Zh. Éksp. Teor. Fiz. **74**, 472 (1978) [Sov. Phys. JETP **47**, 247 (1978)].
[14] M. Lenzlinger and E. H. Snow, J. Appl. Phys. **40**, 278 (1969).
[15] J. M. Gibson and D. W. Dong, J. Electrochem. Soc. **127**, 27 212 (1980).
[16] S. I. Kirillova, V. E. Primachenko, O. V. Snitko, and O. S. Frolov, Mikroelektronika **13**, 239 (1984).
[17] S. J. Fonash and S. Ashok, Solid-State Electron. **24**, 427 (1981).
[18] A. Rothwarf and I. Pereyra, Solid-State Electron. **24**, 1067 (1981).
[19] P. Chattopadhyay and A. N. Daw, Solid-State Electron. **29**, 555 (1986).
[20] S. G. Dmitriev and Yu. V. Markin, Fiz. Tekh. Poluprovodn. **30**, 1231 (1996) [Semiconductors **30**, 649 (1996)].
[21] R. R. Litovskiĭ, V. S. Lysenko, A. N. Nazarov, and T. E. Rudenko, Mikroelektronika **16**, 427 (1987).

Translated by M. E. Alferieff

Use of direct wafer bonding of silicon for fabricating solar cell structures with vertical *p–n* junctions

V. B. Voronkov,*) E. G. Guk, V. A. Kozlov, M. Z. Shvarts, and V. B. Shuman

A. F. Ioffe Physicotechnical Institute, Russian Academy of Sciences, 194021 St. Petersburg, Russia
(Submitted December 9, 1997; accepted for publication December 23, 1997)
Fiz. Tekh. Poluprovodn. **32**, 886–888 (July 1998)

A technology based on ion implantation and the direct wafer bonding of p^+-p-n^+ structures has been developed for multijunction silicon solar cells. The internal quantum efficiency of such structures is close to unity in the wavelength range 350–900 nm. © *1998 American Institute of Physics.* [S1063-7826(98)02507-1]

One of the least developed variants of solar cells for use with solar radiation concentrators is a structure consisting of multijunction silicon solar cells with vertical *p–n* junctions [vertical multijunction (VMJ) silicon solar cells]. The advantages of VMJ silicon solar cells have been discussed repeatedly.[1–3] However, it has been noted that new technological solutions are required in order to implement these positive qualities in practice. The main difficulties are due to the need to ensure passivation of the working surface and a small series resistance. The characteristics of VMJ silicon solar cells produced by the diffusion welding of four silicon wafers with a n^+-p-p^+ structure were presented in Refs. 2 and 3. The diffusion welding was conducted in vacuum at 550 °C. In addition, aluminum was deposited on the wafer beforehand, while in a number of cases Silumin interlayers were used. After welding, the stack of wafers was cut into individual elements (Fig. 1a). The advantage of diffusion welding is that it makes it possible to join a large number of wafers without imposing special requirements being imposed on the wafer surface quality (for example, the surfaces can be etched in KOH). The drawback of such a complex structure is the presence of metal interlayers on the working surface. This produces shading (from 1 to 10%) and impedes chemical treatment and passivation of the surface. The best technological variant that makes it possible to avoid these drawbacks could be the direct bonding of silicon wafers. This comparatively new method[4] has been employed in microelectronics and technology of high-power semiconductor devices for bonding clean polished silicon wafers with different types of conduction or different resistivities, wafers coated with a layer of SiO_2, and Si wafers after ion implantation.

Our objective in the present work is to investigate the application of direct bonding for fabricating VMJ silicon solar cell structures.

Commercial, polished ⟨100⟩-oriented *p*-Si wafers with diameter 60 mm, thickness 350 μm, and resistivity 40 $\Omega\cdot$cm were used to fabricate the VMJ silicon solar cells. Some wafers were used to prepare VMJ silicon solar cells by diffusion welding using the method of Ref. 2. The rest of the wafers were used for direct bonding. In the latter case the ion implantation of boron atoms was conducted on one side of the wafers, and the implantation of phosphorus was conducted on the opposite side (for each impurity the dose equaled 8×10^{16}cm^{-2}). Annealing was not performed after ion implantation, since according to Ref. 5 amorphization of the surface promotes bonding.

Immediately before bonding, the wafers were etched in HF, after which they went through a standard cycle of acid-peroxide washings. In the final stage of the washings, the wafers were subjected to treatment in dilute 2% HF followed by hydroxylation of the surface in a $NH_4OH:H_2O_2:H_2O$ (0.05:1:5) solution and a final washing in deionized water with resistivity $\sim$18 M$\Omega\cdot$cm. The wafers were joined and bonded according to the method described in Ref. 6.

Bonded pairs were subjected to high-temperature heat treatment in air at 1100 °C for 2 h without applying an external pressure. The bonding continuity and the presence of ''bubbles'' at the interface were monitored by infrared (IR) photometry on a PTU-44 television system. The areal coordinate resolution of the system was $\sim$300 μm with a possibility of revealing bubbles with an optical gap $\geqslant$0.25 μm between the wafers. Monitoring of the bonding continuity showed that there are virtually no bubbles, and a narrow strip where bonding did not occur was present only at the edge of the wafers. The n^+ and p^+ layers were about 2 μm thick, and the surface boron and phosphorus densities were equal to 3×10^{19} and 6×10^{19} cm^{-3}, respectively. Next, aluminum was deposited on the exterior surfaces of the bonded wafers at 350 °C, and diffusion welding with low-resistivity silicon wafers, which served as heat compensators, was conducted. Next, the stack of wafers was cut into individual $5\times1.4\times1$ mm elements (Fig. 1b). The surface of the elements was worked on four sides by successively grinding, polishing, and etching with acid. A passivating coating — an 80 Å thick SiO_2 layer — and a two-layer antireflective coating consisting of Si_3N_4 and SiO_2 layers, 550 and 400 Å thick, respectively, were deposited in an ion-plasma reactive sputtering apparatus in a single vacuum cycle similarly to Ref. 3. The lifetime of the minority charge carriers was measured by Lax's method[7] and was equal to 48–50 μs for both methods of fabricating VMJ silicon solar cells. The spectral dependence of the reflection coefficient (R) for the bonded samples is presented in Fig. 2 (curve *1*). On account of the

 © 1998 American Institute of Physics

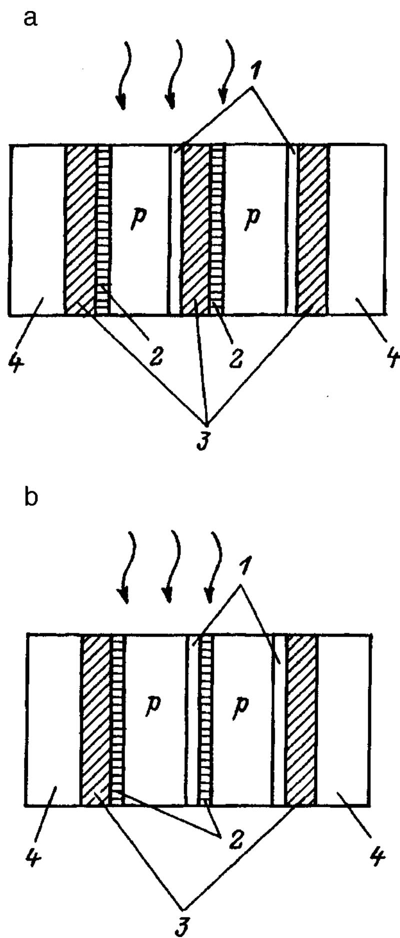

FIG. 1. Structures of silicon solar cells with vertical *p–n* junctions produced by diffusion welding (a) and direct bonding (b): *1* — p^+ layer, *2* — n^+ layer, *3* — Silumin, *4* — heat compensator.

two-layer antireflection coating $R<5\%$ in the wavelength range $\lambda = 550-850$ nm and minimum reflection occurs at $\lambda \approx 650$ nm. The spectral dependence of the carrier collection factor $Q(\lambda)$ for the same sample is presented in Fig. 2

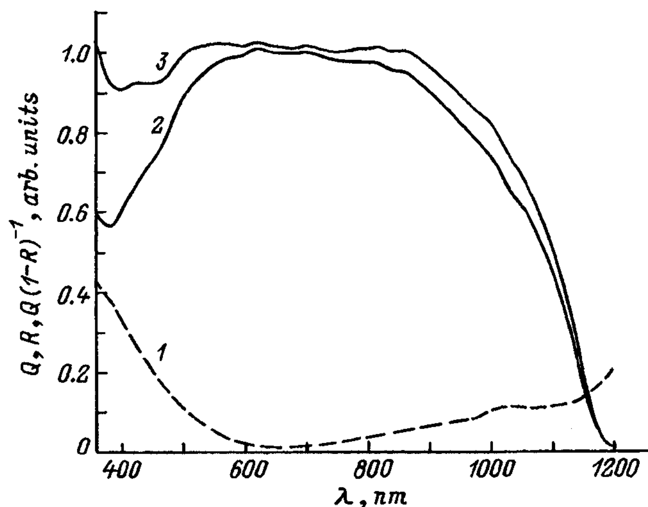

FIG. 2. Spectral characteristics of silicon solar cells produced by direct bonding: *1* — reflection coefficient *R* of the front surface; *2* — external collection factor *Q*, *3* — internal collection factor $Q/(1-R)$.

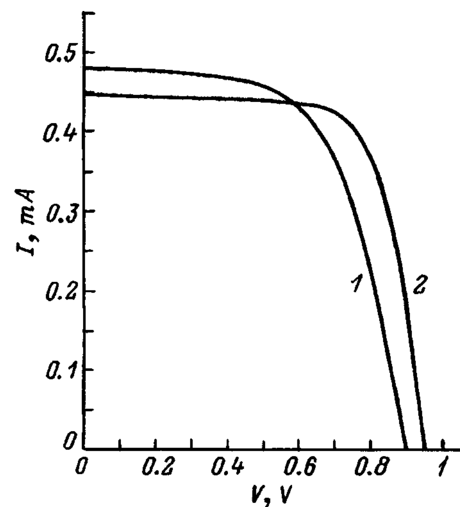

FIG. 3. Load characteristics of silicon solar cells with two *p–n* junctions under illumination intensity 100 mW/cm^2 (AM1.5). The solar cells were fabricated by direct bonding (*1*) and diffusion welding (*2*).

(curve *2*), and the spectral dependence of the internal quantum efficiency $Q(\lambda)/[1-R(\lambda)]$ is depicted by curve *3* in the same figure. The internal quantum efficiency is close to 1 in a wide wavelength range (350–900 nm).

The short-circuit current density (j_{sc}) was calculated from the spectral characteristics of the VMJ silicon solar cells for the AM1.5D solar radiation spectrum (1000 W/m^2) and found to be $j_{\mathrm{AM1.5D}}=39.43$ mA/cm^2. For exoatmospheric conditions $j_{\mathrm{AM0}}=48.14$ mA/cm^2. The spectral dependence of the internal quantum efficiency of the VMJ silicon solar cells is close to that presented in Ref. 8 for planar passivated-emitter solar cells (PESC's), which were fabricated from low-resistivity silicon and possessed a textured surface, a double antireflection coating, and shading of 4% of the area by the metal. Our values of j_{sc} (34–38.7 mA/cm^2) are also close to those presented in Ref. 8 $j_{sc}=36.7-37$ mA/cm^2 for AM1.5 conditions. The high sensitivity in the UV region of the spectrum makes it possible to estimate the surface recombination rate on the basis of the data in Ref. 9: it does not exceed 10^4 cm/s.

The load characteristics of VMJ silicon solar cells consisting of two *p–n* junctions connected in series were measured under a pulsed simulator of concentrated solar radiation for AM1.5D conditions. The load characteristic of one of the samples obtained by direct bonding for one-sun illumination is presented in Fig. 3 (curve *1*). For comparison the figure also shows the load characteristic for a diffusion-welded VMJ silicon solar cell with two *p–n* junctions (curve *2* in the same figure). For the ''welded'' silicon solar cell the short-circuit current density is somewhat lower ($j_{\mathrm{AM1.5D}}=34$ mA/cm^2) because the reflection minimum of the sample lies in the infrared region (≈ 800 nm). The dependences of the fill factor (FF) and the efficiency η on the degree of concentration of solar radiation for the same samples are presented in Fig. 4. One can see that the fill factor for the ''bonded'' sample is much smaller than for the ''welded'' sample, which had a surface density in the diffusion layers $\sim 10^{20}$ cm^{-3} and continuous surface metalliza-

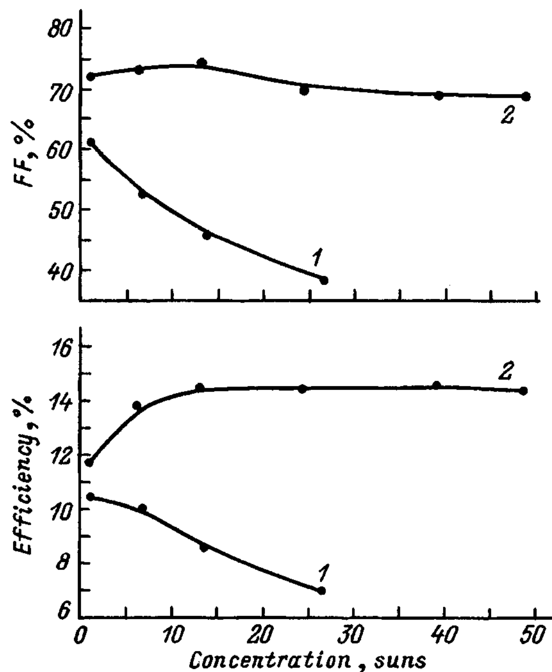

FIG. 4. Fill factor (FF) and efficiency η versus the degree of concentration of solar radiation (AM1.5) for solar cells fabricated by direct bonding (*1*) and diffusion welding (*2*).

tion at the interface. As a result of this, the efficiency of the first sample is also lower, while for the welded samples the fill factor reached 80–82% and the efficiency reached 14.5% (AM1.5). The low value of the FF is evidently due to the fact that ion doping did not give a sufficiently high surface density of the impurity at the interface, and this led to a high series resistance. To increase the fill factor it is necessary either to increase substantially the impurity implantation dose or to use silicon wafers with diffusion layers for direct bonding. However, in order to bond such wafers additional investigations are required, since diffusion does not preserve wafer surface quality.

In summary, vertical multijunction silicon solar cells, which have been produced for the first time by direct wafer bonding without the use of photolithography and surface texturing, make it possible to obtain spectral characteristics that are wavelength-independent in a wide range of wavelengths.

This work was supported by the Russian Fund for Fundamental Research under Grant No. 96-02-17902.

*)E-Mail: mevel@theory.ioffe.rssi.ru

[1] A. L. Fahrenbuch and R. H. Bube, *Fundamentals of Solar Cells*, Academic Press, New York, 1987 [Énergoatomizdat, Moscow, 1987, p. 182].

[2] E. G. Guk, N. S. Zimogorova, M. Z. Shvarts, and V. B. Shuman, Zh. Tekh. Fiz. **67** (2), 129 (1997) [Tech. Phys. **42**, 238 (1997)].

[3] E. G. Guk, T. A. Nalet, M. Z. Shvarts, and V. B. Shuman, Fiz. Tekh. Poluprovodn. **31**, 855 (1997) [Semiconductors **31**, 726 (1997)].

[4] J. B. Lasky, Appl. Phys. Lett. **48**, 78 (1986).

[5] F. Fujino, M. Matsui, T. Hattori, and Y. Hamakawa, Jpn. J. Appl. Phys. **34**, 1322 (1995).

[6] I. V. Grekhov, V. A. Kozlov, V. A. Volle, and V. B. Voronkov, in *Best of Soviet Semiconductor Physics and Technology, 1989–1990*, edited by M. Levinshtein and M. Shur, World Scientific, Singapore, 1995, p. 597.

[7] D. Lax and S. F. Neustadter, J. Appl. Phys. **25**, 1148 (1954).

[8] J. Zhao and M. A. Green, Trans. El. Rev. **ED-38** (8), 1925 (1991).

[9] K. Morita, T. Saitch, T. Uematsu, Y. Kida, S. Kokunai, and K. Matsukuma, Jpn. J. Appl. Phys. **26** (5), L547 (1987).

Translated by M. E. Alferieff

Pulsed investigations of diode structures based on silicon-hydrogen films

S. V. Belov and A. A. Lebedev

A. F. Ioffe Physicotechnical Institute, Russian Academy of Sciences, 194021 St. Petersburg, Russia
(Submitted December 17, 1997; accepted for publication December 23, 1997)
Fiz. Tekh. Poluprovodn. **32**, 889–891 (July 1998)

Me/silicon-hydrogen film/Si diode structures are investigated. The main features of the measurements performed are that, first, the method of paired voltage pulses applied to the sample is used and, second, the measurements are performed in the temperature range from 294 K up to 334 K. Reliable estimates of the main characteristics of silicon hydride films, such as the drift mobility, trap density, trap ionization energy, and carrier trapping cross section, are obtained by comparing the results obtained with data from previous work. © *1998 American Institute of Physics.* [S1063-7826(98)02607-6]

1. INTRODUCTION

Silicon-hydrogen films (SHF's) and porous silicon are kindred materials. Interest in SHF's increased substantially after the discovery of visible-range photoluminescence by R. W. Fathauer *et al.* in 1992.[1] Electroluminescence was also observed in Me/SHF/Si structures in that year.[2] Photodiodes sensitive in the range from 1.1 to 4.2 eV were fabricated and investigated in 1993.[3] However, the electrical properties of SHF's have been studied comparatively little. These films exhibit the properties of high-resistivity semiconductors with permittivity $\varepsilon = 3.9$.[4] Investigation of the static current-voltage characteristics (IVC's) of diode structures showed that they can be described satisfactorily on the basis of the theory of space-charge-limited (SCL) currents in the presence of traps.[5,6] The voltage at which rapid growth of the current J occurs is of the order of 0.4–1.0 V, and the trap density calculated from it is $10^{16}-10^{17}$ cm^{-3}. The carrier mobility calculated from the IVC's is of the order of 10^{-4} cm^2/V·s.

2. SAMPLES AND MEASUREMENT METHOD

Silicon hydride films are obtained by chemically etching silicon in HF, to which oxidizers (HNO_3, $NaNO_2$) are added. Films with thickness $L = 0.05 - 0.20$ μm form after 10–60 s. Their luminescence spectra are shown in Fig. 1.

Diodes were produced by depositing Al, Au, or Ag through a mask with openings 0.5–2.0 mm in diameter. Ohmic contacts to Si were obtained beforehand by diffusing P. The structures have diode IVC's with breakdown voltage >10 V and reverse currents of the order of several μA.

The measurements of the transient current characteristics $J(t)$ of the diodes were performed in the forward direction under the action of a paired voltage pulses with the same and different amplitudes U_1 and U_2 (Fig. 2).

3. MEASUREMENT RESULTS AND DISCUSSION

After a voltage pulse is switched on, the current through the diode rises rapidly (in a time $t_1 \simeq 0.1$ μs) up to a maximum value J_{m1} and then falls. The rise in current is due to the passage of free carriers through the SHF and the falloff of J is due to the capture of carriers in traps. The drift mobility of the carriers can be estimated from the rise time:

$$\mu = \frac{L^2}{t_1 U} \simeq 10^{-3} - 10^{-4} \text{ cm}^2/\text{V}\cdot\text{s}, \tag{1}$$

where U is the voltage on the diode. These values of μ agree well with the results of Ref. 6.

Let us estimate the order of magnitude of the free carrier density n. In the case of field transport the current is initially given by $J = q\mu n E$, and

$$J t_1 = q\mu E n \frac{L}{E\mu} \rightarrow n \simeq \frac{J t_1}{qL}, \tag{2}$$

where E is the electric field and q is the electron charge. Substituting the typical values $J = 2$ A/cm^2, $t_1 = 10^{-7}$ s, and $L = 10^{-5}$ cm into Eq. (2), we obtain $n \simeq 10^{17}$ cm^{-3}.

The current falloff is due to the capture of carriers by traps and occurs under the conditions of high electric fields ($E \simeq 10^5$ V/cm) and in response to a change in carrier density. However, the initial section of the falloff can be approximated by an exponential function (Fig. 3) with time constant $\tau_0 = \sigma v_T n$, where σ and v_T are the trapping cross section and the thermal velocity of the carriers, respectively; $\tau_0 = 10 - 50$ μs and does not depend on T. The cross section σ can be estimated from τ_0 and was found to be of the order of $10^{-19} - 10^{-20}$ cm^2 for different samples.

The traps in a SHF are filled during the first forward-current pulse, and after the pulse terminates, the traps are thermally emptied of trapped carriers. This process can be investigated with the aid of shifted voltage pulses.[7] Let us examine first the case when both pulses have the same amplitude and Δt is the time interval between the end of the first pulse and the start of the second pulse. As Δt increases, there is enough time for some traps to be thermally emptied of trapped carriers, and the current J_{m2} on the leading edge of the second voltage pulse increases. In Fig. 2a the dashed line shows the envelope of the function $J_{m2}(\Delta t)$. The difference $\Delta J_m = J_{m1} - J_{m2}$ on the initial section can be approximated by an exponential function. Figure 4 shows plots of

 © 1998 American Institute of Physics

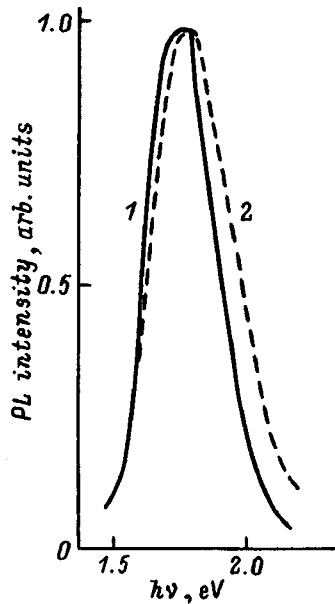

FIG. 1. Typical photoluminescence (PL) spectrum of the experimental SHF samples at 300 (*1*) and 77 K (*2*).

$\log \Delta J_m = f(\Delta t)$ for several values of T. The time constant τ_0 of carrier generation is related with the trap parameters by the well-known relation[8]

$$\tau_g = (v_T \sigma N_c)^{-1} \exp(E_t / v_T), \tag{3}$$

where N_c is the effective density of states in the closest allowed band. The Arrhenius dependence for τ_g is linear

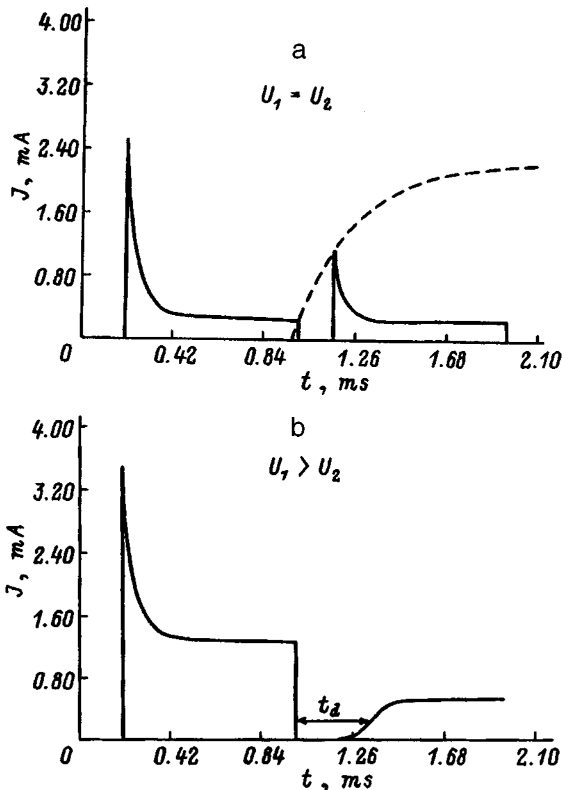

FIG. 2. Oscillograms of the current pulses of a typical sample with the same (a) and different (b) voltages in the first (U_1) and second (U_2) pulses.

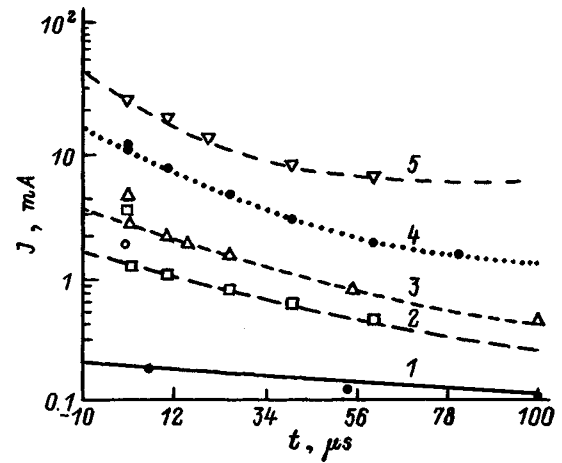

FIG. 3. Time dependences of the falloff of a current pulse with different voltages U (in V) on the sample: *1* — 1, *2* — 1.6, *3* — 2, *4* — 4, *5* — 7. $T = 294$ K.

(Fig. 5), and the trap activation energy determined from it is $E_t \simeq 0.2 \pm 0.02$ eV. The carrier trapping cross sections calculated from Eq. (3) with $E_t = 0.2$ eV, $N_c = 10^{19}$ cm^{-3}, and $\tau_g = 10^{-4}$ s were found to be of the order of $10^{-19} - 10^{-20}$ cm^2 and agree well with the data obtained from the carrier trapping kinetics of the traps.

Let us now consider the case when the voltage U_2 of the second pulse is less than that of the first pulse. For a certain value of U_2 it is possible to have a situation where there is virtually no forward current at the start of the second pulse, even when the second voltage pulse follows immediately after the first pulse, and the forward current increases after a time t_d equal to the time interval between the end of the first pulse and the onset of current growth (Fig. 2b). Such a form of the transient characteristic with a current step is due to the trapping of injected carriers by traps and the formation of an internal electric field in the SHF, which can be greater than the external field at the start of the pulse and can impede current flow through the diode. As carriers are thermally generated from traps, the internal field decreases, and current flow in the forward direction becomes possible. The experiments showed that t_d does not depend on whether or not an external field is applied to the SHF, i.e., t_d is the same in the

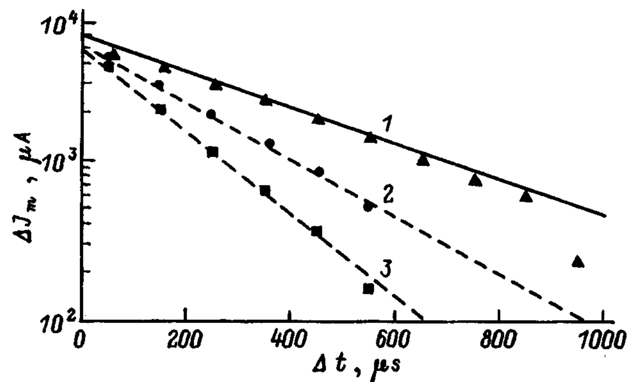

FIG. 4. Plots of $\Delta J_m = f(\Delta t)$ at various temperatures T, K: *1* — 294, *2* — 315, *3* — 334.

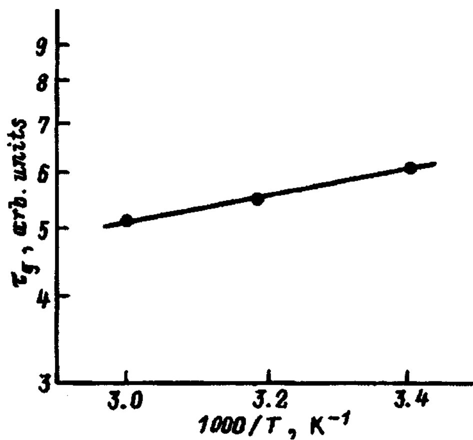

FIG. 5. Arrhenius plot for the thermal generation time constant τ_g.

cases when the second voltage pulse follows immediately after the first pulse and when the start of the second pulse is shifted by a time t_d.

The density N_t of charged traps can be estimated from the voltage of the second pulse at which the transient characteristic described above is observed. We know the trap distribution in an SHF and the degree to which the traps are filled by injection, but if it is assumed that the filling of the traps does not depend on the coordinate perpendicular to the plane of the SHF, then the Poisson equation yields

$$N_t \simeq \frac{2\varepsilon\varepsilon_0 U}{qL^2}, \tag{4}$$

where ε_0 is the permittivity. Substituting the known values[4] $U \simeq 1$ V, $L = 10^{-5}$ cm, and $\varepsilon = 3.9$ into Eq. (4) gives $N_t \simeq 4 \times 10^{16}$ cm^{-3}.

The quantity t_d depends on T, and the trap activation energy E_a can be calculated from it. The average value for several samples is $E_a = 0.21 \pm 0.08$ eV and agrees well with the values of E_t presented above.

Thus, the following estimates of the characteristics of SHF's can be made from static and pulsed measurements on Me/SHF/Si structures: the drift mobility $\mu = 10^{-3} - 10^{-4}$ cm^2/V·s; the trap density $N_t = 10^{16} - 10^{17}$ cm^{-3}; the trap ionization energy $E_a = 0.20 \pm 0.03$ eV; the trapping cross section of traps $\sigma = 10^{-19} - 10^{-20}$ cm^2.

4. CONCLUSIONS

It should be noted that Me/SHF/Si diodes have a complicated structure and that it has not yet been investigated adequately. A heterojunction is formed at the SHF/Si interface, and, according to the photoluminescence spectra of SHF's, the gap width in the SHF is at least 1.7–1.9 eV. Inclusions of nanosize silicon clusters with a large gap width are possible in the film. Material of a different nature can be present between such clusters. Surface states can form at the interface between a cluster and the material surrounding it. They can also form on the SHF/Si and SHF/metal interfaces. For this reason, the estimates made above are highly averaged, and in real structures the mechanism of current transport through an SHF is more complicated than the simplified model examined above.

This work was supported by the Russian Fund for Fundamental Research.

[1] R. W. Fathauer, T. George, A. Ksendsov, and R. P. Vasquez, Appl. Phys. Lett. **60**, 995 (1992).

[2] S. V. Belov, Pis'ma Zh. Tekh. Fiz. **18**(24), 16 (1992) [Sov. Tech. Phys. Lett. **18**, 800 (1992)].

[3] E. V. Astrova, S. V. Belov, O. A. Zaĭtsev, and A. A. Lebedev, Pis'ma Zh. Tekh. Fiz. **19**(24), 50 (1993) [Tech. Phys. Lett. **19**, 794 (1993)].

[4] E. V. Astrova, S. V. Belov, and A. A. Lebedev, Fiz. Tekh. Poluprovodn. **28**, 332 (1994) [Semiconductors **28**, 203 (1994)].

[5] M. Lampert and P. Mark, *Current Injection in Solids*, Academic Press, New York, 1970 [Mir, Moscow, 1973].

[6] S. V. Belov, O. A. Zaĭtsev, and A. A. Lebedev, Pis'ma Zh. Tekh. Fiz. **21**(3), 30 (1995) [Tech. Phys. Lett. **21**, 101 (1995)].

[7] L. M. Kapitonova, A. A. Lebedev, and N. A. Sultanov, Fiz. Tekh. Poluprovodn. **4**, 1130 (1970) [Sov. Phys. Semicond. **4**, 954 (1970)].

[8] L. S. Berman and A. A. Lebedev, *Capacitance Spectroscopy of Deep Centers in Semiconductors* [in Russian], Nauka, Leningrad, 1981.

Translated by M. E. Alferieff

Investigation of the device characteristics of a low-threshold quantum-dot laser emitting at 1.9 μm

A. E. Zhukov,*) A. Yu. Egorov, A. R. Kovsh, V. M. Ustinov, S. V. Zaĭtsev, N. Yu. Gordeev, V. I. Kopchatov, A. V. Lunev, A. F. Tsatsul'nikov, B. V. Volovik, N. N. Ledentsov, and P. S. Kop'ev

A. F. Ioffe Physicotechnical Institute, Russian Academy of Sciences, 194021 St. Petersburg, Russia

(Submitted December 24, 1997; accepted for publication December 30, 1997)
Fiz. Tekh. Poluprovodn. **32**, 892–895 (July 1998)

InAs quantum dots in a InGaAs matrix grown on an InP substrate by molecular-beam epitaxy are employed as the active region of an injection laser. Lasing via quantum-dot states is observed in the temperature range 77–200 K. At the lowest threshold current density 11 A/cm^2 the radiation wavelength is equal to 1.894 μm (77 K). © *1998 American Institute of Physics.* [S1063-7826(98)02707-0]

Quantum dot (QD) arrays are promising for use as the active region of an injection laser. In particular, an ultralow threshold current density and a sharp decrease in its temperature dependence,[1] as well as an increase in the specific gain,[2] have been predicted theoretically for them. An ultralow threshold current density of 60 A/cm^2, an internal quantum efficiency of 70%,[5] and continuous-wave lasing with output power of the order of 1 W (Ref. 6) have been reported for injection lasers based on QD's formed by the self-organization of three-dimensional islands in strongly strained systems of In(Ga)As/(Al)GaAs materials.[3,4]

However, the longest radiation wavelength achieved in QD-based structures of this type was 1.3 μm,[7] which greatly limits the possible applications in fields of practical importance, such as waveguide optical communication and monitoring of atmospheric pollution. We showed earlier that the range of radiation from QD's can be extended right up to 2 μm by using arrays of InAs quantum islands in a InGaAs matrix grown on an InP substrate.[8] The increase in the radiation wavelength as compared with (In,Ga)As QD's in a GaAs matrix in the present case is due, first and foremost, to the employment of a narrower-gap matrix. In the present paper we report the development of an injection laser on the basis of QD's in the InAs/InGaAs/InP system of materials and present the results of investigations of its optical and device characteristics.

The experimental structure was grown on an n^+-InP(100) substrate by molecular-beam epitaxy (MBE). A 0.6 μm thick waveguide layer of undoped InGaAs was deposited directly on the substrate, which functioned as the bottom emitter. An array of InAs QD's was placed at the midplane of the waveguide layer, which was bounded above by a 1.5 μm thick p-InAlAs emitter layer. The structure was completed by a 0.6 μm thick p^+-InGaAs contact layer. The InGaAs and InAlAs epitaxial layers were nominally lattice-matched with the InP substrate. All structures were grown at 500 °C.

The laser diodes shown schematically in Fig. 1 were formed in a geometry with four cleaved faces, which made it possible to reduce the exit losses of radiation to a minimum. A Ti/AuZn/Ni/Au alloy was used to form ohmic contacts to the p^+ layer, while Au:Te/Ni/Au was used for the contacts to the n^+-InP substrate. The laser characteristics were investigated under pulsed pumping with frequency 5 kHz and pulse duration 3 μs in the temperature range 77–300 K. The photoluminescence (PL) was investigated on structures with the top contact layer removed. The PL was excited by a GaAs/AlGaAs semiconductor laser and detected by a cooled InSb photodiode. The excitation power was 30 W/cm^2.

Since the number of charge carriers that can participate in lasing is limited by the QD density, the pump-current-density dependence of the gain achieved on the QD's should saturate when a certain value is reached. Gain saturation is manifested as a sharp superlinear increase in the threshold current density with increasing losses and has been observed in some lasers based on In(Ga)As QD's in a GaAs matrix.[9] To overcome gain saturation, it has been proposed that the QD density be increased by the repeated deposition of several arrays of QD's.[10,11]

The same technological method was used in the present work. The active region consisted of three arrays of InAs quantum dots separated by 5 nm thick InGaAs spacers. The transition from two- to three-dimensional growth was indicated directly during growth by the appearance of a streak RHEED pattern after the deposition of three InAs monolayers (ML) on an InGaAs(100) surface. The effective thickness of InAs deposited in each QD array was equal to 7 ML.

Transmission electron microscopy (TEM) data confirm the formation of coherently strained InAs islands in the InGaAs matrix when the effective thickness of the deposited InAs exceeds 3–3.3 ML.[8] The dimensions of the islands, which are characterized by a 50 nm base and a height of the order of 4–5 nm, are comparable to the exciton radius in this system of materials; this should lead to size quantization of charge carriers in all three directions.

It was observed after the repeated deposition of several QD arrays separated by InGaAs spacers with a thickness of the order of the characteristic height of the islands (5 nm)

 © 1998 American Institute of Physics

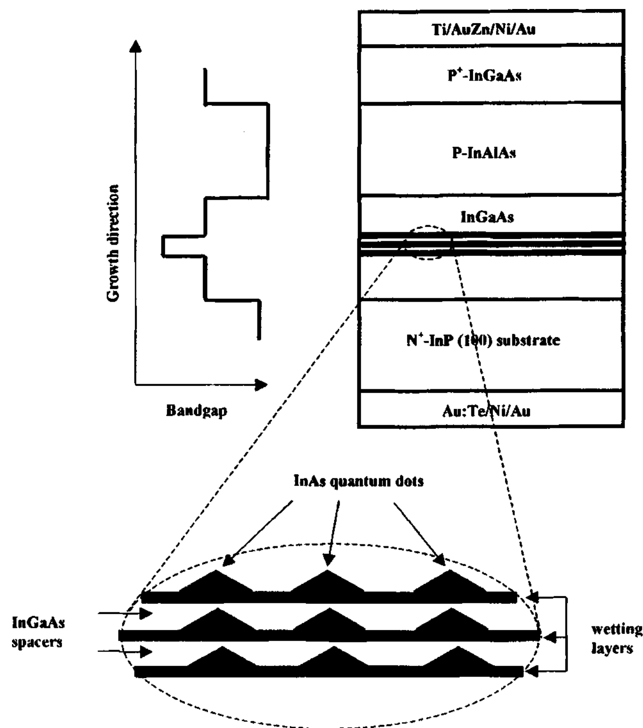

FIG. 1. Schematic representation of a section and band diagram of the experimental laser based on InAs quantum dots in an InGaAs matrix. Inset: schematic representation of the vertical alignment of QD's in neighboring arrays.

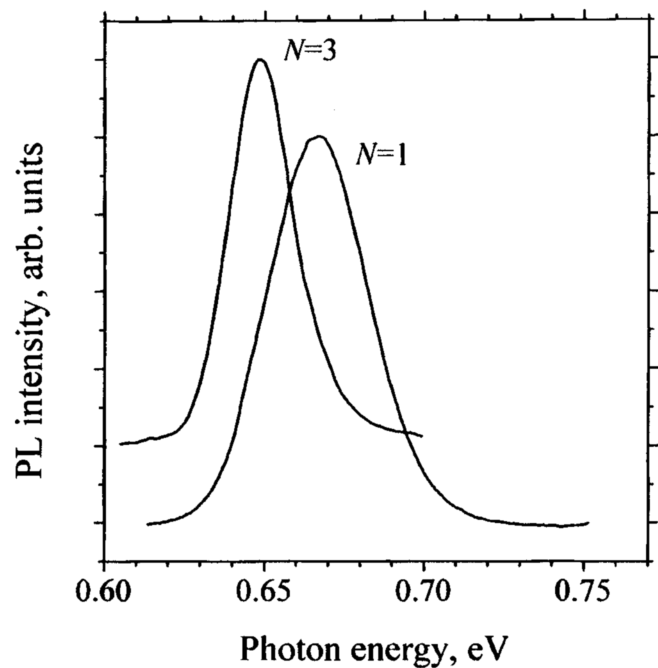

FIG. 2. PL spectra of structures obtained by single ($N=1$) and triple ($N=3$) deposition of InAs QD arrays separated by a 5 nm thick InGaAs spacers. The measurement temperature was 77 K.

that the islands in the second and subsequent arrays are formed precisely above islands of the preceding array, as shown schematically in the inset to Fig. 1. This same vertical alignment of QD's in neighboring arrays was observed earlier after the repeated deposition of InAs QD's in GaAs or AlGaAs matrices[12] and was attributed to the effect of inhomogeneous strain fields, arising as a result of the formation of the first array of dots, on the surface migration rates of Ga and In atoms.[13] We believe that this explanation is also valid in the case of InAs QD's in an InGaAs/InP matrix.

The PL data show that the radiation of strained InAs islands in an (In,Ga)As matrix at 77 K covers the wavelength range 1.65–1.944 μm, depending on the effective thickness of the deposited InAs, which controls the island sizes.[8] However, vertical alignment makes it possible to increase the radiation wavelength even more. Figure 2 shows the PL spectra at 77 K of structures differing in the number (N) of QD arrays in the active region. The effective thickness of InAs forming one QD array was the same in both samples and was equal to 7 ML. As one can see by comparing the spectra, the triple deposition ($N=3$) of QD's results in an appreciable shift (approximately 20 meV) of the maximum of the PL line toward lower energies as compared with the case of a single QD array ($N=1$). We believe that this is due to a decrease in the size-quantization energy in the system consisting of three vertically aligned QD's separated by tunneling-transparent barriers.[14]

The PL line of a QD array formed by self-organization is inhomogeneously broadened with a full width at half-height ordinarily of about 40–80 meV, reflecting a substantial spread of island sizes. As follows from the data in Fig. 2, vertical alignment of QD's is accompanied by narrowing of the PL line from 37 meV in the case of $N=1$ to 23 meV for $N=3$. It should be noted that such a small QD luminescence linewidth is one of the best reported values and provides indirect evidence of an improvement in the homogeneity of the QD sizes as a result of vertical alignment.

The electroluminescence (EL) spectra near the lasing threshold of the experimental laser structure are compared in Fig. 3 with the PL data. The excitation of an ultranarrow (less than 1 meV) line in the EL spectrum attests to a transition of the diode into the lasing regime at a pump current density $J_{th}=11.4$ A/cm^2. The lasing wavelength was equal to 1.894 μm. As far as we know, these values are the lowest threshold current density and the longest wavelength ever reported for QD lasers.

Mathematical modeling of the shape of the experimental PL spectrum distinguishes two Gaussian lines $PL1$ and $PL2$ (Fig. 3). The line with the longer wavelength ($PL1$) is due to recombination via the ground state of the QD's, while the line with the shorter wavelength ($PL2$) is apparently due to the excited state of the QD's. Two lines are also observed in the EL spectra. It is important to note that lasing arises right next to the maximum of the $PL1$ line, indicating that lasing occurs via the ground state of the QD's.

Figure 4 shows the temperature dependences of J_{th} and the integrated intensity of the PL line due to recombination in QD's. As one can see, the experimental laser structure demonstrates a very strong temperature dependence of the threshold current density, which can be described in terms of the characteristic temperature by the quantity T_0 of about 25 K. A sharp drop of the PL intensity described by an exponential dependence on the reciprocal temperature with acti-

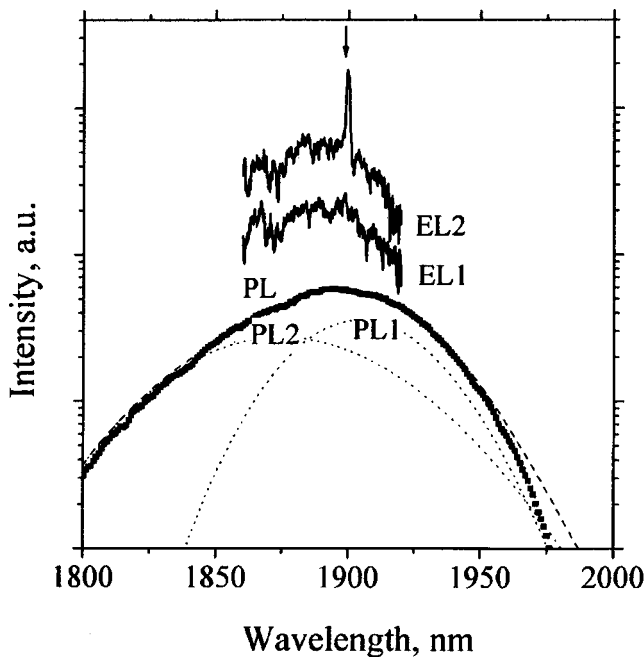

FIG. 3. Electroluminescence (*EL*1, *EL*2) and photoluminescence (*PL*) spectra of the laser structure. Spectra *EL*1 and *EL*2 were obtained with threshold current densities 10.8 and 12.5 A/cm^2, respectively (J_{th}= 11.4 A/cm^2). The arrow marks the lasing line. The dashed curve shows the PL line shape computed mathematically with two Gaussian curves *PL*1 and *PL*2.

vation energy 46 meV is observed at the same time. The highest temperature at which lasing was observed was equal to 200 K.

Similar behavior, though not so pronounced, has been observed before in lasers based on (In,Ga)As QD's in a GaAs matrix, and it has been shown that it is a consequence of the thermal transfer of carriers from QD states into the matrix and the wetting layer.[15] In the system of materials investigated in the present work, thermal transfer should apparently be much more pronounced because the energy separation between the QD levels and the band edges in the matrix is smaller. We believe that this problem can be partially overcome by using the wider-gap quaternary compound InGaAlAs as the matrix material.

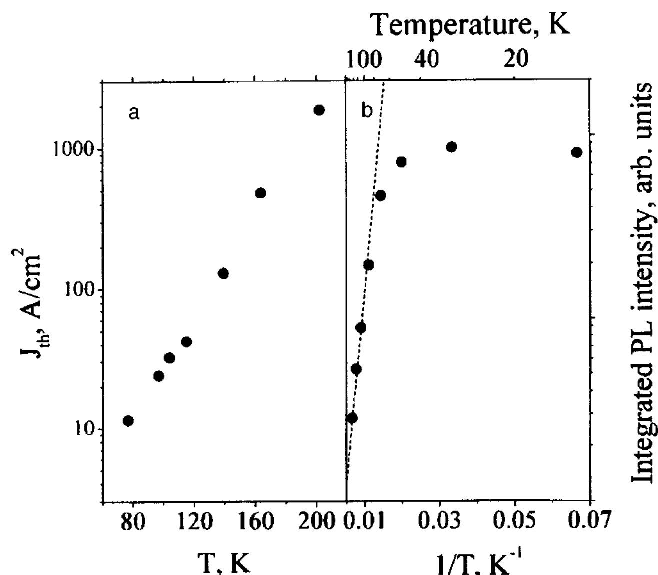

FIG. 4. Temperature dependences of the threshold current density for a sample with four cleaved faces (290×290 μm) (a) and the integrated PL line intensity (b). The dashed line in *b* shows an approximation of the falloff of the PL by an exponential function with activation energy 46 meV.

In summary, lasing has been demonstrated in a structure based on InAs quantum dots in an InGaAs matrix grown on an InP substrate. The threshold current density equals 11 A/cm^2, while the emission wavelength equals 1.894 μm at 77 K.

This work was supported by the Russian Fund for Fundamental Research (Grant 96-02-17824), the Ministry of Science of the Russian Federation (Project 2-001), the ''Physics of Solid-State Nanostructures'' program (Project 97-1090), and the Copernicus program (CP94/01180).

*)E-Mail: zhukov@beam.ioffe.rssi.ru

[1] Y. Arakawa and H. Sakaki, Appl. Phys. Lett. **40**, 939 (1982).
[2] M. Asada, Y. Miyamoto, and Y. Suematsu, J. Quantum Electron. **22**, 1915 (1986).
[3] L. Goldstein, F. Glas, J. Y. Marzin, M. N. Charasse, and G. Le Roux, Appl. Phys. Lett. **47**, 1099 (1985).
[4] D. Leonard, M. Krishnamurthy, L. M. Reaves, S. P. Den Baars, and P. M. Petroff, Appl. Phys. Lett. **63**, 3203 (1993).
[5] V. M. Ustinov, A. Yu. Egorov, A. R. Kovsh, A. E. Zhukov, M. V. Maksimov, A. F. Tsatsul'nikov, N. Yu. Gordeev, S. V. Zaitsev, Yu. M. Shernyakov, N. A. Bert, P. S. Kop'ev, Zh. I. Alferov, N. N. Ledentsov, J. Böhrer, D. Bimberg, A. O. Kosogov, P. Werner, and U. Gösele, J. Cryst. Growth **175/176**, 689 (1997).
[6] Yu. M. Shernyakov, A. Yu. Egorov, A. E. Zhukov, S. V. Zaĭtsev, A. R. Kovsh, I. L. Krestnikov, A. V. Lunev, N. N. Ledentsov, M. V. Maksimov, A. V. Sakharov, V. M. Ustinov, Chao Chen, P. S. Kop'ev, Zh. I. Alferov, and D. Bimberg, Pis'ma Zh. Tekh. Fiz. **23**, 51 (1997) [Tech. Phys. Lett. **23**, 149 (1997)].
[7] R. P. Mirin, J. P. Ibbetson, K. Nishi, A. C. Gossard, and J. E. Bowers, Appl. Phys. Lett. **67**, 3795 (1995).
[8] V. M. Ustinov, A. E. Zhukov, A. F. Tsatsul'nikov, A. Yu. Egorov, A. R. Kovsh, M. V. Maksimov, A. A. Suvorova, N. A. Bert, and P. S. Kop'ev, Fiz. Tekh. Poluprovodn. **31**, 1256 (1997) [Semiconductors **31**, 1080 (1997)].
[9] S. V. Zaitsev, N. Yu. Gordeev, Yu. M. Sherniakov, V. M. Ustinov, A. E. Zhukov, A. Yu. Egorov, M. V. Maximov, P. S. Kop'ev, Zh. I. Alferov, N. N. Ledentsov, N. Kirstaedter, and D. Bimberg, Superlattices Microstruct. **21**, 559 (1997).
[10] V. M. Ustinov, A. Yu. Egorov, A. E. Zhukov, N. N. Ledentsov, M. V. Maksimov, A. F. Tsatsul'nikov, N. A. Bert, A. O. Kosogov, P. S. Kop'ev, D. Bimberg, and Zh. I. Alferov, Mater. Res. Soc. Symp. Proc. **417**, 141 (1996).
[11] Q. Xie, A. Madhukar, P. Chen, and N. Kobayashi, Phys. Rev. Lett. **75**, 2542 (1995).
[12] A. Yu. Egorov, A. E. Zhukov, P. S. Kop'ev, N. N. Ledentsov, M. V. Maksimov, V. M. Ustinov, A. F. Tsatsul'nikov, N. A. Bert, A. O. Kosogov, D. Bimberg, and Zh. I. Alferov, Fiz. Tekh. Poluprovodn. **30**, 1682 (1996) [Semiconductors **30**, 879 (1996)].
[13] Q. Xie, P. Chen, and A. Madhukar, Appl. Phys. Lett. **65**, 2051 (1994).
[14] M. V. Maksimov, Yu. M. Shernyakov, S. V. Zaĭtsev, N. Yu. Gordeev, A. Yu. Egorov, A. E. Zhukov, P. S. Kop'ev, A. O. Kosogov, A. V. Sakharov, N. N. Ledentsov, V. M. Ustinov, A. F. Tsatsul'nikov, Zh. I. Alferov, A. Böhrer, and D. Bimberg, Fiz. Tekh. Poluprovodn. **31**, 670 (1997) [Semiconductors **31**, 571 (1997)].
[15] A. E. Zhukov, A. Yu. Egorov, A. R. Kovsh, V. M. Ustinov, N. N. Ledentsov, M. V. Maksimov, A. F. Tsatsul'nikov, S. V. Zaĭtsev, N. Yu. Gordeev, P. S. Kop'ev, D. Bimberg, and Zh. I. Alferov, Fiz. Tekh. Poluprovodn. **31**, 483 (1997) [Semiconductors **31**, 411 (1997)].

Translated by M. E. Alferieff